Dispersive analyses of three-body decays and scattering reactions

Dissertation
zur
Erlangung des Doktorgrades (Dr. rer. nat.)
der
Mathematisch-Naturwissenschaftlichen Fakultät
der
Rheinischen Friedrich-Wilhelms-Universität Bonn

vorgelegt von
Dominik Stamen
aus
Düsseldorf

Bonn, Oktober 2024

Angefertigt mit Genehmigung der Mathematisch-Naturwissenschaftlichen Fakultät
der Rheinischen Friedrich-Wilhelms-Universität Bonn.

Gutachter/Betreuer:	PD Dr. Bastian Kubis
Gutachter:	Prof. Dr. Christoph Hanhart
Tag der Promotion:	09.12.2024
Erscheinungsjahr:	2025

"I can't carry it for you,
but I can carry you [...]."

Samwise Gamgee [1]

Abstract

More than half a century after the discovery of quantum chromodynamics as the quantum-field-theoretical description of the strong interaction, its non-perturbative nature in the low-energy regime still poses a unique challenge. Particularly, the fundamental properties and scattering of light hadrons need to be studied precisely to unravel the structure of the strong interaction. In this thesis, we consider manifold applications of this kind using dispersive techniques that are based on the S-matrix principles of unitarity and analyticity.

We perform a study of rescattering effects in 3π final states, which are often described in terms of two-body resonances and a non-interacting spectator particle. Using Khuri–Treiman dispersion relations, we include crossed-channel effects and estimate the rescattering effects beyond the simplest isobar model for a selected set of quantum numbers. This allows for an estimate when rescattering effects become important and more complicated analysis techniques are needed to extract meaningful physical information from experiments.

However, Khuri–Treiman equations are limited to low energies as they are built from truncated partial-wave expansions. Therefore, a new parameterization is presented that can fulfill all theoretical expectations and connects the essential physics of hadron scattering both near threshold and in asymptotic limits. In this construction, dynamical information is entirely contained in Regge trajectories that generalize resonance poles in the complex-energy plane to poles in the angular-momentum plane. While the construction and first results are successfully presented in this thesis, this formalism allows for many extensions that can be explored in the future.

Properties of kaons are investigated using the kaon electromagnetic form factor and the Primakoff reactions $\gamma K \to K\pi$ and $\gamma K \to \gamma K$. These are constructed obeying the constraints of analyticity, which enables the extrapolation to unphysical energies or the pole positions on the second Riemann sheet. Using the kaon form factor allows for a calculation of the electromagnetic charge radius from a fit to experimental data in timelike and spacelike regions, while the Primakoff reactions can be used in the future to extract the chiral anomaly, radiative $K^*(892)$ couplings, and kaon polarizabilities. Additionally, there are several different applications for these results, e.g., the anomalous magnetic moment of the muon and corrections to Dashen's theorem.

List of publications

Part II of this thesis is published in the following article:

- D. Stamen, T. Isken, B. Kubis, M. Mikhasenko, and M. Niehus, *Analysis of rescattering effects in 3π final states*, Eur. Phys. J. C **83**, 510 (2023) [arXiv:2212.11767 [hep-ph]], [Erratum: Eur. Phys. J. C **83**, 586 (2023)] ,

while the results of Part III are based on the preprint

- D. Stamen, D. Winney, A. Rodas, C. Fernández-Ramírez, V. Mathieu, G. Montaña, A. Pilloni, and A. P. Szczepaniak, *Towards a unified description of hadron scattering at all energies*, (2024) [arXiv:2409.09172 [hep-ph]] ,

and Part IV on

- M. Dax, D. Stamen, and B. Kubis, *Dispersive analysis of the Primakoff reaction $\gamma K \to K\pi$*, Eur. Phys. J. C **81**, 221 (2021) [arXiv:2012.04655 [hep-ph]] ,
- D. Stamen, J. L. Dammann, Y. Korte, and B. Kubis, *Polarizabilities from kaon Compton scattering*, Eur. Phys. J. C **84**, 1267 (2024) [arXiv:2409.05955 [hep-ph]] ,
- D. Stamen, D. Hariharan, M. Hoferichter, B. Kubis, and P. Stoffer, *Kaon electromagnetic form factors in dispersion theory*, Eur. Phys. J. C **82**, 432 (2022) [arXiv:2202.11106 [hep-ph]] .

Results of this thesis were also incorporated in the following letter:

- M. Hoferichter, G. Colangelo, B.-L. Hoid, B. Kubis, J. Ruiz de Elvira, D. Schuh, D. Stamen, and P. Stoffer, *Phenomenological Estimate of Isospin Breaking in Hadronic Vacuum Polarization*, Phys. Rev. Lett. **131**, 161905 (2023) [arXiv:2307.02532 [hep-ph]] ,

which are summarized in Appendix 8.A. Furthermore, parts of the above have been published in the following proceedings:

- M. Hoferichter, G. Colangelo, B.-L. Hoid, B. Kubis, J. Ruiz de Elvira, D. Stamen, and P. Stoffer, *Chiral extrapolation of hadronic vacuum polarization and isospin-breaking corrections*, PoS **LATTICE2022**, 316 (2022) [arXiv:2210.11904 [hep-ph]] ,
- D. Stamen, M. Dax, and B. Kubis, *Dispersive analysis of the Primakoff reaction $\gamma K \to K\pi$*, PoS **CD2021**, 048 (2021) .

The code basis solving the Khuri–Treiman equations used in this thesis can be found in a public GitHub repository: github.com/HISKP-ph/khuri_treiman_solver.

Contents

Prologue

Chapter 1

Introduction

Physics as a fundamental natural science describes nature from very small to very large scales. There are many successful theories that have been tested by experiments and describe a vast amount of phenomena. Even though big revolutions do not come often, the human knowledge is advanced in tiny steps every day. There are still a lot of puzzling problems needed to be solved, and enormous efforts are taken striving for solutions. A few examples are: a unified and fully consistent theory including general relativity and the standard model of particle physics [10], dark matter [11], and the strong CP problem [12].

This thesis tries to improve the understanding of scattering reactions and decay processes of strongly interacting particles. We use two different types of concepts. First, we make predictions for planned experiments relying on input from theoretical constraints and other experimental results. Secondly, we analyze experimental data using theoretical tools for model-independent results. This is done in the very successful standard model of particle physics (SM), which is briefly introduced in the following section.

1.1 The standard model of particle physics

The SM[1] is the most successful quantum-field-theoretical description of particle physics. It contains the electromagnetic, weak, and strong interactions, with the gauge group reading

$$SU(3)_C \times SU(2)_L \times U(1)_Y \,. \tag{1.1}$$

The SM contains 17 elementary particles,[2] which can be grouped according to Fig. 1.1. While the electroweak sector is very well understood, the strong interaction still poses many problems. In contrast to the electroweak Lagrangian, the Lagrangian of quantum chromodynamics (QCD)

$$\mathcal{L}_{\text{QCD}} = \bar{q}\left(i\not{D} - m_q\right) q - \frac{1}{4} F^A_{\mu\nu} F^{A\mu\nu} - \theta \frac{g^2}{32\pi^2} F^A_{\mu\nu} \tilde{F}^{A\mu\nu} \,, \tag{1.2}$$

with the covariant derivative

$$D_\mu = \partial_\mu - ig\frac{1}{2}\lambda^A \mathcal{A}^A_\mu \,, \tag{1.3}$$

has the quark fields q and gluon fields $\mathcal{A}$, both carrying color charge, as degrees of freedom, while the measured spectrum consists of color neutral hadrons. The field strength tensor is defined as

$$F^A_{\mu\nu} = \partial_\mu \mathcal{A}^A_\nu - \partial_\nu \mathcal{A}^A_\mu + g f_{ABC} \mathcal{A}^B_\mu \mathcal{A}^C_\nu \,, \tag{1.4}$$

[1] Some of the most important articles that led to the development of the SM are Refs. [13–20]. For a nice historic overview, see Sec. 1 of Ref. [21] by Heinrich Leutwyler and Harald Fritzsch.

[2] Here, the corresponding antiparticles to the particles are not counted.

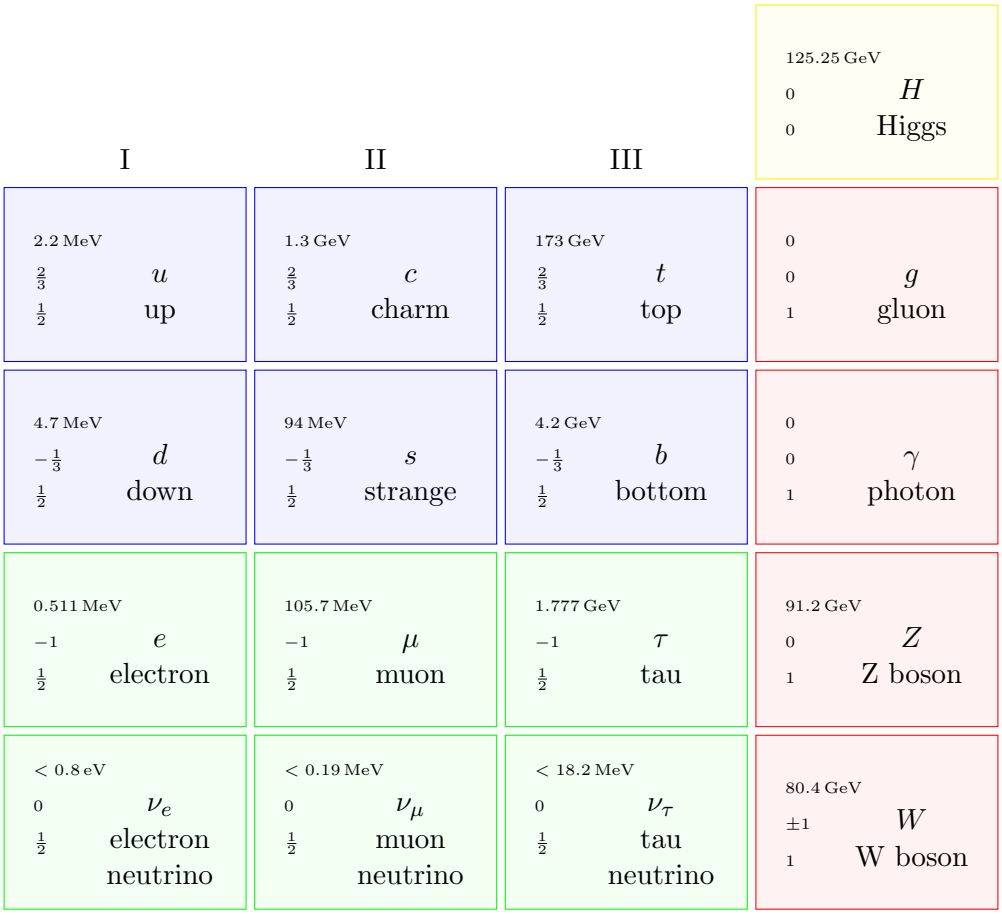

Figure 1.1: Elementary particles in the SM. They are grouped into quarks (blue), leptons (green), gauge bosons (red), and the Higgs boson (yellow). The left column in each node denotes the mass, the electric charge and the spin from top to bottom. The columns I, II, and III denote the three generations of the fermions. All masses are taken from Ref. [22], where the numbers shown here only serve the purpose of illustrating the involved scales.[3]

and the dual field strength tensor reads

$$\tilde{F}^A_{\mu\nu} = \frac{1}{2}\epsilon_{\mu\nu\alpha\beta}F^{A\alpha\beta}\,, \tag{1.5}$$

where f_{ABC} are the structure constants of $SU(3)$. Note that the flavor, spin, and color labels are suppressed.

[3]Note that the displayed masses should be interpreted very carefully. The light quark masses u, d, and s are the current-quark masses in the $\overline{\text{MS}}$ subtraction scheme at the renormalization scale $\mu = 2\,\text{GeV}$. Also, the other quark masses are scheme dependent, cf. Ref. [22] for details. Secondly, in the SM, neutrinos are assumed to be massless. However, in order to describe the observed phenomenon of neutrino oscillations, it is necessary that at least two generations of neutrinos have non-zero masses. These can be incorporated by extensions of the SM, where it is still disputed whether they are Dirac or Majorana fermions. The limits on the neutrino masses given here are for the weak eigenstates, which are superpositions of the mass eigenstates. For further reading, we refer to the literature, e.g., Ref. [23] and references therein.

The main difficulty of QCD is the running of the coupling constant g. Therefore, the theory cannot be solved perturbatively at low energies and we have to apply different methods in order to calculate processes. One of these methods, dispersion theory, is introduced in Part I. Other well established approaches are effective field theories and lattice QCD.

While the discrete symmetries charge conjugation (C), parity (P), and time reversal (T) are separately conserved in the electromagnetic and strong interactions,[4] only the combination CPT is preserved in the weak interaction. However, the θ-term in Eq. (1.2) induces P- and CP-violation. The size of the θ-term is strongly constrained by measurements of the neutron electric dipole moment [24] and can therefore not explain the matter–antimatter asymmetry in the universe.

1.2 Mesonic degrees of freedom

As mentioned in the previous section, the observable degrees of freedom are color-neutral hadrons. In this thesis, we focus on light mesons, a specific subclass built from a quark–antiquark pair. Light and heavy mesons are generally characterized by their quark content. The light sector consists of the up, down, and strange quarks, while the heavy sector includes the charm, bottom, and top quarks.[5] The goal is to gain information on the structure of QCD by decay and scattering processes of light mesons. The nonets for light pseudoscalar ($J^P = 0^-$) and vector ($J^P = 1^-$) mesons are grouped in Fig. 1.2. These nonets include almost all mesons that are studied in this thesis. Furthermore, the QCD Lagrangian is invariant under a $SU(2)$ transformation if the up- and down-quark mass are degenerate. This symmetry is called isospin due to its mathematical similarity to spin. It is approximately fulfilled in the strong interaction, since the quark-mass difference is small in nature compared to the QCD scale. Additionally, electromagnetic corrections break the isospin symmetry. However, it is useful to categorize mesons by their total isospin and its third component. Assuming perfect isospin symmetry, all particles in a multiplet are mass degenerate and processes violating isospin are not allowed in the strong interaction.

1.3 Effective field theories

The following section is based on Ref. [25]. One commonly used way to describe the strong interaction at low energies are effective field theories. The general idea of effective field theories is that for a given parameter range, the observed phenomena are not strongly influenced by scales far removed. For a set of light and heavy degrees of freedom L_i and H_i, respectively, their masses are separated by a scale Λ

$$m_{L_i} \ll \Lambda \lesssim m_{H_i} \,. \tag{1.6}$$

Then, for energies below the scale Λ, we are left with the effective Lagrangian with the heavy degrees of freedom integrated out,

$$\mathcal{L}(L_i, H_i) \xrightarrow{E \ll \Lambda} \mathcal{L}_{\text{eff}}(L_i) \,. \tag{1.7}$$

[4] This statement is only true for $\theta = 0$.

[5] Note that top quarks do not hadronize due to their extremely short lifetime.

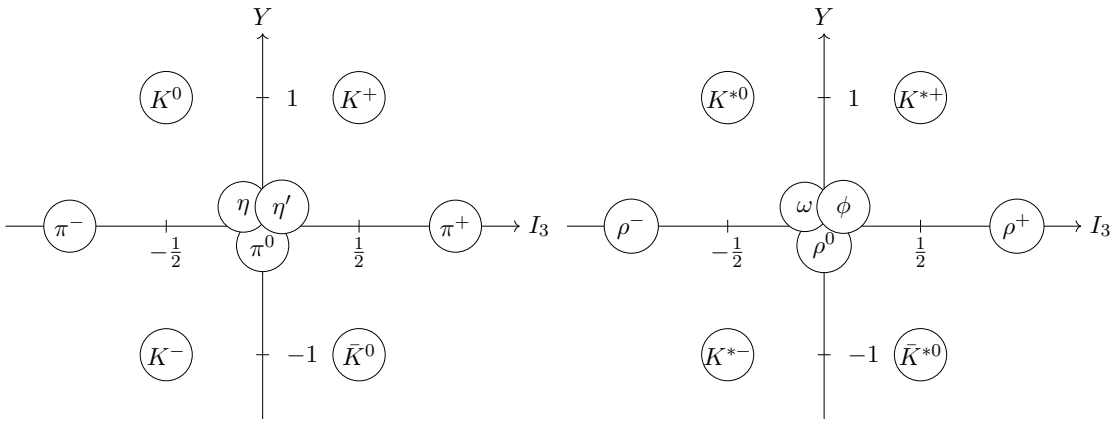

Figure 1.2: The nonets for the light pseudoscalar mesons (left) and vector mesons (right) in terms of the hypercharge $Y = 2\,(Q - I_3)$ and the third component of the isospin I_3.

1.3.1 Chiral perturbation theory

To construct an effective field theory for the strong interaction, we investigate the symmetries of the QCD Lagrangian. Furthermore, we restrict ourselves to the light sector with the quark fields $q^T = (u, d, s)$ and $m_q = \mathrm{diag}(m_u, m_d, m_s)$. One can split the quark fields into their chiral components using the projection operators

$$\begin{aligned} P_{R/L} &= \frac{1}{2}(1 \pm \gamma_5)\,, \\ q &= P_L q + P_R q = q_L + q_R\,. \end{aligned} \tag{1.8}$$

Therefore, we define the QCD Lagrangian for vanishing quark masses

$$\mathcal{L}^0_{\mathrm{QCD}} = i\bar{q}_L \not{D} q_L + i\bar{q}_R \not{D} q_R - \frac{1}{4} F^A_{\mu\nu} F^{A\mu\nu}\,, \tag{1.9}$$

which is additionally invariant under $U(3)_L \times U(3)_R$ transformations. This symmetry is explicitly broken by the mass terms, which mix left- and right-handed fields. As a result, one constructs chiral perturbation theory (ChPT), an effective field theory based on this chiral symmetry, which can be perturbatively expanded in the quark masses.

For the following discussion, it is helpful to factorize the symmetry group according to

$$U(3)_L \times U(3)_R = SU(3)_L \times SU(3)_R \times U(1)_V \times U(1)_A\,, \tag{1.10}$$

where vector $V = L + R$ and axial-vector $A = L - R$ transformations are used. Noether's theorem states that the symmetry is related to 18 conserved currents,

$$\begin{aligned} V^\mu &= \bar{q}\gamma^\mu q\,, & A^\mu &= \bar{q}\gamma^\mu\gamma_5 q\,, \\ V^\mu_a &= \bar{q}\gamma^\mu \frac{\lambda^a}{2} q\,, & A^\mu_a &= \bar{q}\gamma^\mu\gamma_5 \frac{\lambda^a}{2} q\,, \end{aligned}$$

where $a = 1, \ldots, 8$. The charge of the $U(1)_V$ current V^μ is conserved in the SM and is related to the quark or baryon number. The $U(1)_A$ current A^μ is anomalous due to quantum effects [26–30]. The $SU(3)_R \times SU(3)_L$ currents V^μ_a and A^μ_a are broken explicitly

by the quark masses.[6] However, in the chiral limit, the question remains if the symmetry group is realized in the Wigner–Weyl mode [31, 32], where the hadron spectrum consists of two degenerate parity multiplets, or the Nambu–Goldstone mode [33–35], where a massless spin-0 multiplet emerges in the hadron spectrum from the generators of the spontaneously broken symmetry. Phenomenologically, we do not find parity doubling, but $SU(3)_V$ multiplets. Therefore, if the chiral symmetry is realized in the Nambu–Goldstone mode, the Vafa–Witten theorem [36] states that the vector subgroup is unbroken, and the pattern of the spontaneous symmetry breaking (SSB) is

$$SU(3)_L \times SU(3)_R \xrightarrow{\text{SSB}} SU(3)_V \,. \tag{1.11}$$

The eight broken generators of the axial-vector symmetry correspond to the Nambu–Goldstone bosons: the pions, kaons, and the η.[7] For the construction of an effective Lagrangian with the Nambu–Goldstone bosons as degrees of freedom, we refer to the literature, cf., e.g., Ref. [25].

1.4 Thesis outline

This thesis is structured as follows: in Part I, the fundamental concepts that are used in this thesis are introduced. Therein, the properties of S-matrix theory and dispersion relations are presented in Chapter 2, while Chapter 3 focuses on basic concepts of Regge theory. In Part II and Chapter 4 therein, we investigate the importance of rescattering effects in three-pion final states. A hypergeometric isobar model including Regge trajectories is proposed in Part III and Chapter 5 therein. The projects including kaons are collected in Part IV. Chapter 6 calculates the $\gamma K \to K\pi$ amplitude dispersively, which is used as an input in the kaon Compton scattering analysis, Chapter 7, where a theoretical framework for the extraction of kaon polarizabilities from experiments is proposed. An analysis of $e^+e^- \to \bar{K}K$ data with the goal to extract the kaon electromagnetic form factors are performed in Chapter 8. Finally, a general conclusion and outlook are given in Chapter 9.

[6] Note that the octet vector currents are already conserved in the limit of equal quark masses, while the octet axial-vector currents are only conserved for vanishing quark masses.

[7] The η' corresponds to the pseudoscalar singlet state, where the mass gap can be explained by the $U(1)_A$ anomaly.

Part I

Foundations

Chapter 2

Dispersion theory

This chapter gives a short, but rather general introduction to S-matrix theory and dispersion relations, which will be used throughout this thesis. A recent pedagogical introduction to S-matrix theory can be found in Ref. [37]. The classic textbook Ref. [38] was written during the early days of S-matrix theory, which were more than half a century ago. S-matrix theory was developed as an approach to strong interactions during a time when QCD and its renormalization were not yet invented. The link to perturbation theory can be done via the Lehmann–Symanzik–Zimmermann-reduction formula [39]. In the low-energy regime, which is of major interest in this thesis, S-matrix theory in connection with dispersion relations is a powerful tool.

In Sec. 2.1, we introduce the main definitions of S-matrix theory and introduce the concepts of unitarity, analyticity, and crossing symmetry. The specifics of four-particle amplitudes are discussed in Sec. 2.2. The properties of dispersion relations with one and two cuts are presented in Sec. 2.3.

2.1 S-matrix theory

Assuming asymptotically free initial and final states $|i, \text{in}\rangle$ and $\langle f, \text{out}|$, the S-matrix can be defined between the free particle states $|i\rangle$ and $\langle f|$,

$$\langle f, \text{out}|i, \text{in}\rangle = \langle f| \mathcal{S} |i\rangle \ . \tag{2.1}$$

Therefore, the operator $\mathcal{S}$ represents the scattering information from initial to final states between $t = -\infty$ to $t = \infty$. The asymptotic states are treated as free particles that do not encounter any further scattering. We can separate the unity from the S-matrix to define the T-matrix via

$$\mathcal{S} = \mathbb{1} + i\mathcal{T} \, . \tag{2.2}$$

Consequently, all non-trivial information is contained in the T-matrix. Overall momentum conservation allows one to define the scattering amplitude $\mathcal{M}$ according to

$$\langle f| \mathcal{T} |i\rangle = (2\pi)^4 \delta^{(4)}(p_f - p_i) \mathcal{M}_{if} \, , \tag{2.3}$$

where the momenta p_f and p_i are the total four momenta of the final and initial state, respectively. The index if on the scattering amplitude is chosen to represent the transition from $i \to f$.

2.1.1 Unitarity

Probability conservation implies that the S-matrix is unitary. Therefore,

$$\mathcal{S}^\dagger \mathcal{S} = \mathcal{S}\mathcal{S}^\dagger = \mathbb{1} \tag{2.4}$$

holds, which, using Eq. (2.2), can be written as the unitarity condition for the T-matrix,

$$i\left(\mathcal{T}^\dagger - \mathcal{T}\right) = \mathcal{T}^\dagger\mathcal{T}\,. \tag{2.5}$$

Applying the initial and final states and inserting a complete set of intermediate states on the right-hand side of the equation leads to

$$i\left(\langle f|\,\mathcal{T}^\dagger\,|i\rangle - \langle f|\,\mathcal{T}\,|i\rangle\right) = \sum\!\!\!\!\!\!\int_n \langle f|\,\mathcal{T}^\dagger\,|n\rangle\,\langle n|\,\mathcal{T}\,|i\rangle\ . \tag{2.6}$$

Using Eq. (2.3) and since $\langle f|\,\mathcal{T}^\dagger\,|i\rangle = \langle i|\,\mathcal{T}\,|f\rangle^*$, we find

$$i\delta^{(4)}(p_f - p_i)\left(\mathcal{M}^*_{fi} - \mathcal{M}_{if}\right) = (2\pi)^4 \sum\!\!\!\!\!\!\int_n \delta^{(4)}(p_f - p_n)\delta^{(4)}(p_n - p_i)\mathcal{M}^*_{fn}\mathcal{M}_{in}\,, \tag{2.7}$$

where one can utilize $\delta^{(4)}(p_f - p_n)\delta^{(4)}(p_n - p_i) = \delta^{(4)}(p_f - p_i)\delta^{(4)}(p_n - p_i)$ under the integral. Then, both sides contain one delta function for the overall momentum conservation. This is dropped and overall momentum conservation is implied. The unitarity condition for a generic scattering amplitude reads

$$i\left(\mathcal{M}^*_{fi} - \mathcal{M}_{if}\right) = (2\pi)^4 \sum\!\!\!\!\!\!\int_n \delta^{(4)}(p_n - p_i)\mathcal{M}^*_{fn}\mathcal{M}_{in}\,. \tag{2.8}$$

2.1.2 Analyticity

A rigorous proof connecting analyticity and causality is still pending. Therefore, analyticity is typically defined as an axiom of S-matrix theory [38]. Maximal analyticity states that the scattering amplitude is holomorphic in all of its continuous variables. These are the four-momenta of the particles. Furthermore, one can also consider the angular momentum as a continuous complex variable; this feature is explored in Chapter 3 about Regge theory. Due to overall momentum conservation, not all momenta are independent. Then, a set of Mandelstam variables [40] can be chosen to represent the kinematical dependencies of the scattering amplitude. Typically, s denotes the total energy in the center-of-mass (CM) system. Imposing maximal analyticity, the scattering amplitude is holomorphic in s. The physical region is the domain where all kinematical variables take physically allowed values, i.e., real values above the scattering threshold for s.

There are two types of singularities allowed, namely poles and branch points. These are related to physical states of the chosen process. The scattering amplitude is defined for all complex variables except the positions of the singularities. Branch points, and therefore branch cuts, appear for multi-particle intermediate states, while poles are connected to bound states, virtual states, or resonances.

At first, we look at multi-particle states consisting of two or more particles. There exists a continuum of values of s where they can go on-shell. As an example, we consider a two-particle intermediate state, where

$$s = \left(\sqrt{|\vec{p}_1|^2 + M_1^2} + \sqrt{|\vec{p}_2|^2 + M_2^2}\right)^2\,, \tag{2.9}$$

with the masses M_i and the three momenta $\vec{p}_i$. All $|\vec{p}_i| \geq 0$ are allowed and therefore s can take all values from $(M_1 + M_2)^2$ to infinity. This continuum of singularities appears

as a branch cut, starting at the corresponding threshold, which is the branch point, and extending along the real axis to infinity.[1] As a consequence of a branch cut, the scattering amplitude is a multi-valued function for complex s. This can be cured by interpreting the scattering amplitude as a single-valued function on a Riemann surface. The branch cuts then determine how this surface is cut into different Riemann sheets. The physical scattering region is defined by approaching the cut from above with $s + i\epsilon$, $\epsilon \to 0^+$. In the simplest case with only one multi-particle intermediate state, the scattering amplitude has two Riemann sheets. They are smoothly connected and the physical region can be approached from the unphysical second Riemann sheet moving to the real axis from below with $s - i\epsilon$, $\epsilon \to 0^+$. In the general case with multiple multi-particle intermediate states, the scattering amplitude possesses multiple unphysical sheets.

The single-particle states, the poles of the scattering amplitude, can be grouped into three categories. A pole from a bound or virtual state is located below threshold on the real axis of s. Thereby, the bound state appears on the physical sheet and the virtual state is on an unphysical sheet. A resonance pole is in the complex plane on an unphysical sheet. The location defines the mass and the width of the resonance via

$$\sqrt{s_R} = M_R - \frac{i}{2}\Gamma_R \,. \tag{2.10}$$

2.1.3 Crossing symmetry

A direct consequence of the analyticity of the S-matrix is crossing symmetry. Hence, an arbitrary process with an incoming particle $\phi(p)$ can be related to a similar process with the incoming particle replaced by the outgoing antiparticle with opposite four-momentum $\bar{\phi}(-p)$. Expressing this statement in an equation, we find

$$\mathcal{T}(\phi(p) + \ldots \to \ldots) = \mathcal{T}(\ldots \to \ldots + \bar{\phi}(-p)) \,, \tag{2.11}$$

where the dots represent arbitrary incoming and outgoing particles. The connection of the different scattering amplitudes with the same particle content is found via analytic continuation in the respective four-momenta.

2.2 Four-particle amplitudes

In this section, we discuss the kinematics of generic $2 \to 2$ scattering and $1 \to 3$ decays. Thereby, the spin of the involved particles is not important, but we have 4 particles with masses M_i, $i \in \{1, 2, 3, 4\}$. We first look at an arbitrary $2 \to 2$ scattering process $\phi(p_1)\phi(p_2) \to \phi(p_3)\phi(p_4)$. In principle, the four four-momenta give rise to 16 kinematical degrees of freedom. However, not all of them are independent. Four degrees of freedom are fixed by the on-shell condition and another four are fixed by overall energy-momentum conservation. Furthermore, in the CM system, the three momenta are constrained, which removes another six degrees of freedom. This holds in general in all frames employing Lorentz transformations and therefore only 2 degrees of freedom survive. It is convenient

[1] The orientation of the cut in general is arbitrary since the second branch point is at infinity. However, the cut along the real axis is the typical choice.

to define the set of Lorentz-invariant Mandelstam variables [40]

$$\begin{aligned} s &= (p_1 + p_2)^2 = (p_3 + p_4)^2 \,, \\ t &= (p_1 - p_3)^2 = (p_2 - p_4)^2 \,, \\ u &= (p_1 - p_4)^2 = (p_2 - p_3)^2 \,. \end{aligned} \tag{2.12}$$

It can be shown that the sum of these variables is fixed by energy-momentum conservation,

$$s + t + u = \sum_i M_i^2 \,. \tag{2.13}$$

Therefore, only two of these are independent and can be chosen as the two independent degrees of freedom, and the scattering amplitude can be expressed in dependence of the Mandelstam variables. Another commonly used choice is to define the cosine of the scattering angle $z_s = \cos(\theta_s)$ in the CM system, where this angle is chosen between $\vec{p}_1$ and $\vec{p}_3$. Then, s and z_s are the free parameters and t and u can be expressed via

$$\begin{aligned} t(s, z_s) &= \frac{1}{2}\left(\sum_i M_i^2 - s - \frac{\Delta_{12}\Delta_{34}}{s} + \frac{\sqrt{\lambda(s, M_1^2, M_2^2)\lambda(s, M_3^2, M_4^2)}}{s} z_s \right) , \\ u(s, z_s) &= \frac{1}{2}\left(\sum_i M_i^2 - s + \frac{\Delta_{12}\Delta_{34}}{s} - \frac{\sqrt{\lambda(s, M_1^2, M_2^2)\lambda(s, M_3^2, M_4^2)}}{s} z_s \right) , \end{aligned} \tag{2.14}$$

where $\Delta_{ij} = M_i^2 - M_j^2$ and

$$\lambda(a, b, c) = a^2 + b^2 + c^2 - 2(ab + bc + ca) \tag{2.15}$$

is the Källén function [41]. The Källén function can be nicely rewritten for two special cases:

$$\begin{aligned} \lambda(s, M_1^2, M_2^2) &= \left(s - \left(M_1^2 + M_2^2 \right)^2 \right) \left(s - \left(M_1^2 - M_2^2 \right)^2 \right) , \\ \lambda(s, M^2, 0) &= \lambda(s, 0, M^2) = \left(s - M^2 \right)^2 . \end{aligned} \tag{2.16}$$

The definitions in Eq. (2.14) are for the s-channel process, where the CM energy is $\sqrt{s}$. The scattering process is physically allowed when s exceeds the incoming $(M_1 + M_2)^2$ and outgoing $(M_3 + M_4)^2$ masses and the cosine of the scattering angle is constrained to $-1 \leq z_s \leq 1$.

One can use crossing symmetry to relate this to the t- or u-channel processes by either replacing $(p_2 \leftrightarrow -p_3)$ or $(p_2 \leftrightarrow -p_4)$, respectively. The crossed definitions of Eq. (2.14) for the Mandelstam variables in terms of the angles θ_t or θ_u can, e.g., be found in Ref. [42].

The situation where one of the four particles can decay into the other three can again be found by crossing symmetry. Here, $M_1 \geq M_2 + M_3 + M_4$ and the decay process can be written as $\phi(p_1) \to \bar{\phi}(-p_2)\phi(p_3)\phi(p_4)$. The Mandelstam variables then describe the respective two-body subsystems of the final-state particles. For the physically allowed decay, they are bounded by

$$\begin{aligned} (M_3 + M_4)^2 \leq s \leq (M_1 - M_2)^2 \,, \\ (M_2 + M_4)^2 \leq t \leq (M_1 - M_3)^2 \,, \\ (M_2 + M_3)^2 \leq u \leq (M_1 - M_4)^2 \,, \end{aligned} \tag{2.17}$$

and the cosine of the scattering angles is $-1 \leq z_{s,t,u} \leq 1$. The upper bound of the Mandelstam variable is called the pseudothreshold.

2.2.1 Unitarity in 2 → 2 scattering

Considering $2 \to 2$ scattering, we want to simplify Eq. (2.8). This allows one to express the scattering amplitude in terms of the three Mandelstam variables. We consider the s-channel above threshold, but via crossing symmetry, we could in principle choose any Mandelstam variable. We can express our scattering amplitudes as

$$\begin{aligned} \mathcal{M}_{if} &= \lim_{\epsilon \to 0^+} \mathcal{M}_{if}(s + i\epsilon, t, u)\,, \\ \mathcal{M}^*_{fi} &= \lim_{\epsilon \to 0^+} \mathcal{M}^*_{fi}(s + i\epsilon, t, u)\,, \end{aligned} \tag{2.18}$$

where 0^+ denotes that the limit to zero is taken from above and we can use the property from Ref. [43] to write

$$\mathcal{M}^*_{fi}(s + i\epsilon, t, u) = \mathcal{M}_{if}(s - i\epsilon, t, u)\,. \tag{2.19}$$

The left-hand side of Eq. (2.8) can be written as the s-channel discontinuity

$$\begin{aligned} \mathcal{M}_{if} - \mathcal{M}^*_{fi} &= \lim_{\epsilon \to 0^+} \left(\mathcal{M}_{if}(s + i\epsilon, t, u) - \mathcal{M}_{if}(s - i\epsilon, t, u)\right) \\ &= \operatorname{disc}_s \mathcal{M}_{if}(s, t, u)\,. \end{aligned} \tag{2.20}$$

Therefore,

$$\operatorname{disc}_s \mathcal{M}_{if}(s, t, u) = i(2\pi)^4 \sum\!\!\!\!\!\!\int_n \delta^{(4)}(p_n - p_i) \mathcal{M}^*_{fn} \mathcal{M}_{in}\,, \tag{2.21}$$

where, in principle, all possible intermediate states are allowed. A process is denoted as *elastic* when the final-state and intermediate-state particles coincide. Moreover, invariance under time reversal implies $\mathcal{M}_{if} = \mathcal{M}_{fi}$, and together with Eq. (2.19) this leads to

$$\begin{aligned} \lim_{\epsilon \to 0^+} \mathcal{M}_{if}(s + i\epsilon, t, u) &= \lim_{\epsilon \to 0^+} \mathcal{M}_{if}(s - i\epsilon, t, u)^* \\ &= \lim_{\epsilon \to 0^+} \mathcal{M}_{if}((s + i\epsilon)^*, t, u)^*\,. \end{aligned} \tag{2.22}$$

Then, the scattering amplitude fulfills the Schwarz reflection principle[2] and the discontinuity can be expressed via the imaginary part

$$\operatorname{disc}_s \mathcal{M}_{if}(s, t, u) = 2i \lim_{\epsilon \to 0^+} \operatorname{Im} \mathcal{M}_{if}(s + i\epsilon, t, u)\,. \tag{2.23}$$

It is important to note that this derivation holds only for asymptotic initial and final states. However, an unstable particle that decays into three others does not fulfill this constraint. Therefore, Eq. (2.23) does not hold for $1 \to 3$ processes in the physical region, but one can, nevertheless, use analytic continuation. Considering a squared mass M^2 of the decaying particle that is below the three-particle production threshold, Eq. (2.21) still holds. Then, we perform an analytic continuation in the mass M^2 to a region where the decay is kinematically allowed. The additional cut structure in M^2 with a branch point at the three-particle threshold spoils the Schwarz reflection principle. Therefore, the identification in Eq. (2.23) is no longer valid and we need to use Eq. (2.21) with the discontinuity directly.

[2] The Schwarz reflection principle is introduced in Sec. 2.3.

2.3 Dispersion relations

This section serves as a brief introduction to dispersion relations that are extensively used within this thesis. An extensive and rather rigorous introduction can be found in Ref. [44]. We start the discussion using a function with a single cut in the following section. The more complicated structure of T-matrix elements for arbitrary $2 \to 2$ scattering is discussed in Sec. 2.3.2.

2.3.1 Single cut

We investigate an arbitrary complex function $f(s)$ that is holomorphic in the complex plane $\mathbb{C}$ excluding a branch cut $\mathbb{B}_+ = [s_{\text{th}}, \infty)$ along the real axis. Furthermore, f is real-valued for any $s \in \mathbb{R}\backslash\mathbb{B}_+$ and $f(s)$ does not grow faster than $\mathcal{O}(s^n)$ with $n \in \mathbb{R}$ for $|s| \to \infty$. This function then fulfills the Schwarz reflection principle $f^*(s) = f(s^*)$ for any $s \in \mathbb{C}\backslash\mathbb{B}_+$. Additionally, the discontinuity along the branch cut is given by

$$\operatorname{disc} f(s) = \lim_{\epsilon \to 0^+} \left(f(s + i\epsilon) - f(s - i\epsilon) \right) , \tag{2.24}$$

and for a function that fulfills the Schwarz reflection principle, the discontinuity can be related to the imaginary part via

$$\operatorname{disc} f(s) = \lim_{\epsilon \to 0^+} \left(f(s + i\epsilon) - f^*(s + i\epsilon) \right) = 2i \lim_{\epsilon \to 0^+} \operatorname{Im} f(s + i\epsilon) . \tag{2.25}$$

Cauchy's integral formula is given by

$$f(s) = \frac{1}{2\pi i} \oint_{\mathcal{C}} \mathrm{d}x \frac{f(x)}{x - s} , \tag{2.26}$$

where f is a holomorphic function in the complex plane excluding a branch cut $\mathbb{C}\backslash\mathbb{B}_+$ and $\mathcal{C}$ is a closed contour in counter-clockwise orientation. The contour must enclose the point s and cannot cross the branch cut. Two choices are represented in Fig. 2.1. We choose the dotted blue line in combination with the red solid line. Then, Eq. (2.26) can be written as

$$\begin{aligned} f(s) &= \frac{1}{2\pi i} \left(\lim_{\epsilon \to 0^+} \int_{s_{\text{th}}}^{\infty} \mathrm{d}x \frac{f(x + i\epsilon)}{x - s} - \lim_{\epsilon \to 0^+} \int_{s_{\text{th}}}^{\infty} \mathrm{d}x \frac{f(x - i\epsilon)}{x - s} + \int_{\gamma} \mathrm{d}x \frac{f(x)}{x - s} \right) \\ &= \frac{1}{2\pi i} \left(\int_{s_{\text{th}}}^{\infty} \mathrm{d}x \frac{\operatorname{disc} f(x)}{x - s} + \int_{\gamma} \mathrm{d}x \frac{f(x)}{x - s} \right) , \end{aligned} \tag{2.27}$$

where the arc γ is the blue dotted line in Fig. 2.1. This integral vanishes for $R \to \infty$ if $n < 0$. Therefore, we can write

$$f(s) = \frac{1}{2\pi i} \int_{s_{\text{th}}}^{\infty} \mathrm{d}x \frac{\operatorname{disc} f(x)}{x - s} , \tag{2.28}$$

which is called the dispersive representation or dispersion relation for $f(s)$. The function is determined by the discontinuity along the branch cut $\mathbb{B}_+$. It automatically gives an analytic continuation of f from a subset of the real axis, the branch cut, to the full complex plane.

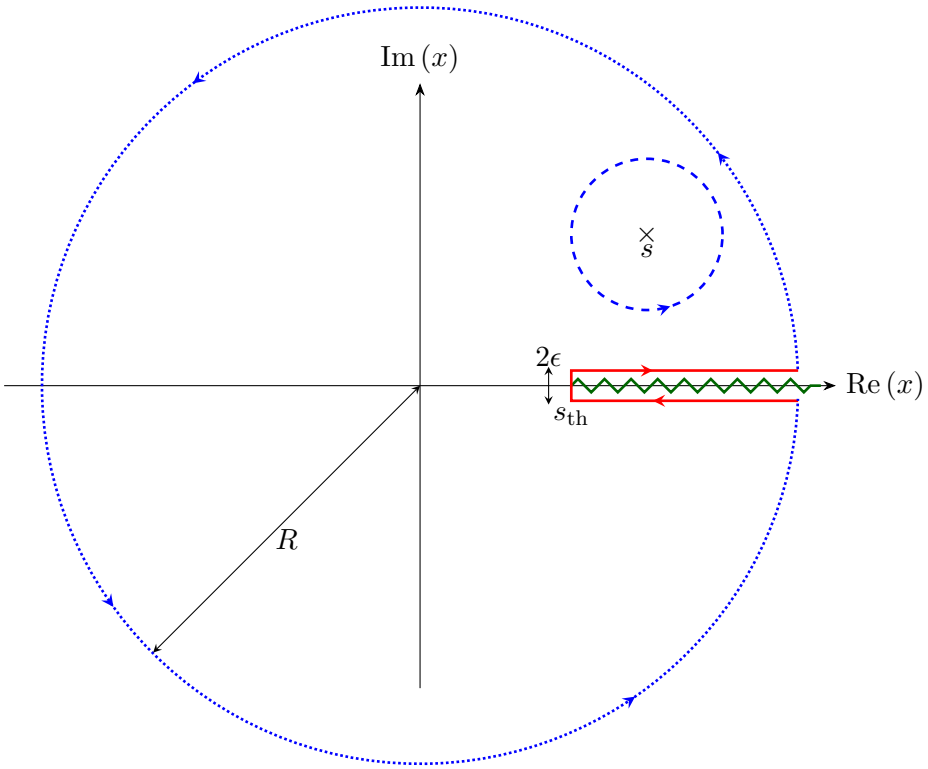

Figure 2.1: The green zigzag line represents the branch cut starting at s_{th} and extending to infinity. The point s is an arbitrary point in the complex plane, where the blue dashed line is a possible choice for the integration contour. The blue dotted and red solid line then represent the choice that encloses the branch cut, where the radius R goes to infinity.

To allow for functions f with less restrictive asymptotic behavior, $n \geq 0$, we introduce subtractions. Therefore, we define a polynomial of degree $m \geq \lfloor n \rfloor + 1$ with real coefficients $s_j < s_{\text{th}}$,

$$Q_m(x) = \prod_{j=1}^{m} (x - s_j)\,, \qquad Q_0(x) = 1\,, \tag{2.29}$$

where s_j are called subtraction points and $\lfloor n \rfloor = \max\{k \in \mathbb{Z} \,|\, k \leq n\}$ is the floor function. Using this, we can define the function

$$g(x) = \frac{f(x)}{Q_m(x)(x - s)}\,, \tag{2.30}$$

where g then again has the correct asymptotic behavior. Therefore, for g, the integration arc vanishes and we can solve for the function f to find

$$f(s) = P_{m-1}(s) + \frac{Q_m(s)}{2\pi i} \int_{s_{\text{th}}}^{\infty} \mathrm{d}x \frac{\operatorname{disc} f(x)}{Q_m(x)(x - s)}\,, \tag{2.31}$$

where P_{m-1} is an arbitrary polynomial of degree $m - 1$ and its constants are called sub-

traction constants.[3] Since $m = \lfloor n \rfloor + 1$ is sufficient to render the integral convergent, we can write for $k > m$

$$\begin{aligned} f(s) &= P_{m-1}(s) + \frac{s^m}{2\pi i} \int_{s_{\text{th}}}^{\infty} \mathrm{d}x \frac{\operatorname{disc} f(x)}{x^m (x-s)} \\ &= P_{k-1}(s) + \frac{s^k}{2\pi i} \int_{s_{\text{th}}}^{\infty} \mathrm{d}x \frac{\operatorname{disc} f(x)}{x^k (x-s)} \,, \end{aligned} \tag{2.32}$$

where for simplicity all $s_j = 0$. Since the polynomials are of different order, their asymptotic behavior differs, but the asymptotic behavior of the function f needs to remain the same. Therefore, we can find a relation between the two polynomials written as

$$P_{k-1}(s) = P_{m-1}(s) + \sum_{i=0}^{k-m-1} \frac{s^{m+i}}{2\pi i} \int_{s_{\text{th}}}^{\infty} \mathrm{d}x \frac{\operatorname{disc} f(x)}{x^{m+i+1}} \,. \tag{2.33}$$

This relation is called a sum rule, which keeps the overall asymptotic behavior unchanged. Via the sum rule, it is possible to increase the number of subtractions without introducing new subtraction constants. An improvement of the convergence behavior is only achieved when violating the sum rule.

Omnès function

While Eq. (2.31) holds for any function with the correct asymptotic behavior, there are certain cases where we can define other representations. Take a holomorphic function $\Omega(s)$, where $\ln \Omega(s)$ is holomorphic and $\Omega(s)$ does not possess any zeros. Furthermore, let $\Omega(s)$ be real on the real axis excluding a branch cut and $\ln \Omega(s)$ be bounded. Then, we can write a once-subtracted dispersion integral with $s_1 = 0$ for $\ln \Omega(s)$ as per

$$\ln \Omega(s) = c + \frac{s}{2\pi i} \int_{s_{\text{th}}}^{\infty} \mathrm{d}x \frac{\operatorname{disc} (\ln \Omega(x))}{x(x-s)} \,. \tag{2.34}$$

The function Ω and its logarithm fulfill the Schwarz reflection principle. Therefore, we can calculate the discontinuity explicitly,

$$\operatorname{disc} (\ln \Omega(s)) = 2i \lim_{\epsilon \to 0^+} \operatorname{Im} (\ln(\Omega(s + i\epsilon))) = 2i \lim_{\epsilon \to 0^+} \arg \Omega(s + i\epsilon) \,, \tag{2.35}$$

and write

$$\Omega(s) = \exp(c) \exp\left(\lim_{\epsilon \to 0^+} \frac{s}{\pi} \int_{s_{\text{th}}}^{\infty} \mathrm{d}x \frac{\arg \Omega(x + i\epsilon)}{x(x-s)} \right) . \tag{2.36}$$

Using the normalization condition $\Omega(0) = 1$ yields the Muskhelishvili–Omnès function [45, 46][4]

$$\Omega(s) = \exp\left(\lim_{\epsilon \to 0^+} \frac{s}{\pi} \int_{s_{\text{th}}}^{\infty} \mathrm{d}x \frac{\arg \Omega(x + i\epsilon)}{x(x-s)} \right) . \tag{2.37}$$

Therefore, the Omnès function is fixed purely by its argument along the cut. Since the argument is bounded, we can define $\lim_{s\to\infty} \lim_{\epsilon\to 0^+} \arg \Omega(s + i\epsilon) = k\pi$. Then, one can show that $\lim_{|s|\to\infty} \Omega(s) = \mathcal{O}\big(s^{-k}\big)$ [44].

[3] Note that for $m = 0$, the polynomial is zero and the function is purely given by the unsubtracted dispersion integral in Eq. (2.28).

[4] We use the common abbreviation from the literature and call this function "Omnès function" in this thesis.

Homogeneous Omnès problem

We now want to investigate a class of problems for a general function f that has the following properties:

1. f is holomorphic on $\mathbb{C}\backslash\mathbb{B}_+$;
2. f obeys the Schwarz reflection principle;
3. $\lim_{|s|\to\infty} f(s) = s^n$, $n \in \mathbb{R}$;
4. $\arg f(s)$ is bounded along $\mathbb{B}_+$ by $\lim_{s\to\infty} \delta(s) = k\pi$, with $\lim_{\epsilon\to 0^+} \arg f(s+i\epsilon) = \delta(s)$,

where we want to find a general solution for f. Since f fulfills the Schwarz reflection principle, the discontinuity can be written as

$$\begin{aligned}\operatorname{disc} f(s) &= 2i \lim_{\epsilon\to 0^+} \operatorname{Im} f(s+i\epsilon) \\ &= 2i \lim_{\epsilon\to 0^+} f(s+i\epsilon) \sin\delta(s) \exp(-i\delta(s))\,. \end{aligned} \tag{2.38}$$

This feature is not directly relevant for the solution of the problem but for the comparison with the next paragraph on the inhomogeneous solution. We can use the fact that there exists an Omnès function for which

$$\lim_{\epsilon\to 0^+} \arg f(s+i\epsilon) = \lim_{\epsilon\to 0^+} \arg \Omega(s+i\epsilon)\,. \tag{2.39}$$

Then, we consider the function

$$h(s) = \frac{f(s)}{\Omega(s)}\,, \tag{2.40}$$

where h is holomorphic on $\mathbb{C}\backslash\mathbb{B}_+$, since f and Ω are holomorphic on $\mathbb{C}\backslash\mathbb{B}_+$. Using that f and Ω fulfill the Schwarz reflection principle, the discontinuity of h can be calculated via

$$\begin{aligned}\operatorname{disc} h(s) &= 2i \lim_{\epsilon\to 0^+} \operatorname{Im} h(s+i\epsilon) = 2i \lim_{\epsilon\to 0^+} \operatorname{Im}\left(\frac{f(s+i\epsilon)}{\Omega(s+i\epsilon)}\right) \\ &= 2i \lim_{\epsilon\to 0^+} \operatorname{Im}\left(\frac{|f(s+i\epsilon)|\exp(i\arg f(s+i\epsilon))}{|\Omega(s+i\epsilon)|\exp(i\arg\Omega(s+i\epsilon))}\right) = 2i \lim_{\epsilon\to 0^+} \operatorname{Im}\left(\frac{|f(s+i\epsilon)|}{|\Omega(s+i\epsilon)|}\right) = 0\,. \end{aligned} \tag{2.41}$$

Therefore, h is free of branch cuts and due to the asymptotic behavior of f and Ω, it has to be a polynomial of order $\lfloor n+k \rfloor$. Solving for f then yields

$$f(s) = P_{\lfloor n+k\rfloor}(s)\Omega(s)\,, \tag{2.42}$$

where the coefficients of P have to be real to satisfy the Schwarz reflection principle.

Inhomogeneous Omnès problem

A further complication of the problem above is introduced via an inhomogeneity in the discontinuity equation. The requirements for a generic function f then read:

1. f is holomorphic on $\mathbb{C}\backslash\mathbb{B}_+$;

2. $\lim_{|s|\to\infty} f(s) = s^n$, $n \in \mathbb{R}$;

3. $\delta(s)$ is bounded along $\mathbb{B}_+$ by $\lim_{s\to\infty} \delta(s) = k\pi$, where δ is a real valued function;

4. the discontinuity of f is given by

$$\operatorname{disc} f(s) = 2i \lim_{\epsilon\to 0^+} \left(f(s+i\epsilon) + \widehat{f}(s) \right) \sin\delta(s) \exp(-i\delta(s)) \,; \tag{2.43}$$

5. the hat function $\widehat{f}$ is a complex-valued function and $\lim_{|s|\to\infty} \widehat{f}(s) = s^n$ is implied by the above conditions.

Note that $\lim_{\epsilon\to 0^+} \arg f(s+i\epsilon) = \delta(s)$ does not hold anymore and the Schwarz reflection principle is not satisfied. We use the same ansatz as in the previous paragraph, but the identification with the imaginary part does not hold anymore, therefore, the discontinuity of h is given by

$$\begin{aligned}
\operatorname{disc} h(s) &= \lim_{\epsilon\to 0^+} \left(\frac{f(s+i\epsilon)}{\Omega(s+i\epsilon)} - \frac{f(s-i\epsilon)}{\Omega(s-i\epsilon)} \right) = \lim_{\epsilon\to 0^+} \left(\frac{f(s+i\epsilon)}{\Omega(s+i\epsilon)} - \frac{f(s-i\epsilon)}{\Omega^*(s+i\epsilon)} \right) \\
&= \lim_{\epsilon\to 0^+} \left(\frac{f(s+i\epsilon)\exp(-i\delta(s)) - f(s-i\epsilon)\exp(i\delta(s))}{|\Omega(s+i\epsilon)|} \right) \\
&= \lim_{\epsilon\to 0^+} \left(\frac{[f(s+i\epsilon) - f(s-i\epsilon)]\exp(i\delta(s)) - 2if(s+i\epsilon)\sin\delta(s)}{|\Omega(s+i\epsilon)|} \right) \\
&= 2i \lim_{\epsilon\to 0^+} \frac{\widehat{f}(s)\sin\delta(s)}{|\Omega(s+i\epsilon)|} \,.
\end{aligned} \tag{2.44}$$

Note that Ω is generated by the function δ and it fulfills the Schwarz reflection principle, even though it is violated in f. Given the explicit form of the discontinuity, we can cast h into an m-times subtracted dispersion relation

$$h(s) = P_{m-1}(s) + \frac{Q_m(s)}{\pi} \lim_{\epsilon\to 0^+} \int_{s_{\text{th}}}^{\infty} \mathrm{d}x \frac{\widehat{f}(x)\sin\delta(x)}{|\Omega(x+i\epsilon)|Q_m(x)(x-s)} \,, \tag{2.45}$$

and solving for f yields

$$f(s) = \Omega(s) \left(P_{m-1}(s) + \frac{Q_m(s)}{\pi} \lim_{\epsilon\to 0^+} \int_{s_{\text{th}}}^{\infty} \mathrm{d}x \frac{\widehat{f}(x)\sin\delta(x)}{|\Omega(x+i\epsilon)|Q_m(x)(x-s)} \right) . \tag{2.46}$$

2.3.2 Two cuts

The abovementioned formalism can only be applied to functions that depend on one Mandelstam variable. Studying T-matrix elements of $2 \to 2$ scattering, which generally depend on two independent Mandelstam variables, is therefore not possible. In the following, we expand the formalism to allow for these more evolved dependencies. The $2 \to 2$ scattering T-matrix can be characterized by a scalar function $\mathcal{M}$ containing all the dynamical information. Note that for processes involving particles with spin, this $\mathcal{M}$ does not correspond to the one defined in Sec. 2.2, but there are additional kinematical factors and potentially

multiple scalar functions. For simplicity, we concentrate on one function $\mathcal{M}$ here. Using the constraint $s+t+u=3s_0$, we can write

$$\mathcal{M}(s,t,u)=\mathcal{M}(s,t,3s_0-s-t)\,. \tag{2.47}$$

Here, we have chosen s and t as our independent Mandelstam variables. One can simplify this to the former case by fixing t, and therefore the amplitude is only dependent on one variable

$$\mathcal{M}(s)=\mathcal{M}(s,t,3s_0-s-t)\,,\quad t \text{ fixed}\,. \tag{2.48}$$

In the following, we choose t below its scattering threshold. The s-channel again exhibits a branch cut starting at the threshold s_{th}. Additionally, the u-channel exceeds its threshold u_{th}. Then, the two-particle cut in the u-channel can be related to the variable s by

$$s\leq 3s_0-t-u_{\text{th}}=s_\ell\,, \tag{2.49}$$

where s_ℓ is the starting point of the left-hand branch cut $\mathbb{B}_-=(-\infty,s_\ell]$ in the complex s-plane. From now on, we require a kinematical setup so that $s_\ell<s_{\text{th}}$ and the branch cuts do not overlap. Consequently, the lower bound for t is

$$t>3s_0-s_{\text{th}}-u_{\text{th}}\,. \tag{2.50}$$

The amplitude $\mathcal{M}$ is holomorphic on $\mathbb{C}\backslash(\mathbb{B}_+\cup\mathbb{B}_-)$ and we assume the same properties as in Sec. 2.3.1. Then the fixed-t dispersion relation can be written as

$$\mathcal{M}(s)=P_{m-1}(s)+\frac{Q_m(s)}{2\pi i}\int_{s_{\text{th}}}^{\infty}\mathrm{d}x\frac{\operatorname{disc}\mathcal{M}(x)}{Q_m(x)(x-s)}+\frac{Q_m(s)}{2\pi i}\int_{-\infty}^{s_\ell}\mathrm{d}x\frac{\operatorname{disc}\mathcal{M}(x)}{Q_m(x)(x-s)}\,, \tag{2.51}$$

where the integration contour is shown in Fig. 2.2 and the subtraction points of Q are chosen between the two branch cuts. Since this dispersion relation implicitly depends on the choice of t, we write

$$\begin{aligned}\mathcal{M}(s,t,3s_0-s-t)=P^t_{m-1}(s)&+\frac{Q_m(s)}{2\pi i}\int_{s_{\text{th}}}^{\infty}\mathrm{d}x\frac{\operatorname{disc}_x\mathcal{M}(x,t,3s_0-t-x)}{Q_m(x)(x-s)}\\&+\frac{Q_m(s)}{2\pi i}\int_{-\infty}^{s_\ell}\mathrm{d}x\frac{\operatorname{disc}_x\mathcal{M}(x,t,3s_0-t-x)}{Q_m(x)(x-s)}\,,\end{aligned} \tag{2.52}$$

where the coefficients of the subtraction polynomials depend on t

$$P^t_{m-1}(s)=\sum_{i=0}^{m-1}c_i(t)s^i\,. \tag{2.53}$$

Furthermore, the discontinuity is defined as

$$\begin{aligned}\operatorname{disc}_x\mathcal{M}(x,t,3s_0-t-x)=\lim_{\epsilon\to0^+}\big[&\mathcal{M}(x+i\epsilon,t,3s_0-t-x-i\epsilon)\\&-\mathcal{M}(x-i\epsilon,t,3s_0-t-x+i\epsilon)\big]\,.\end{aligned} \tag{2.54}$$

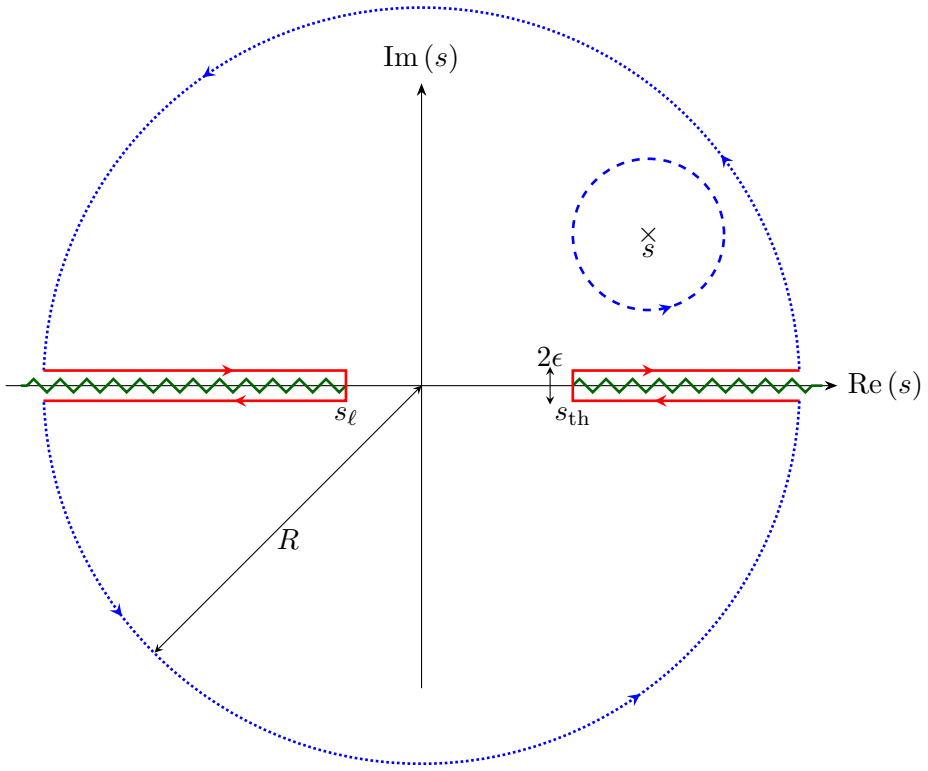

Figure 2.2: The green zigzag lines represent the branch cuts starting at s_{th} and s_ℓ and extending to $\pm\infty$, respectively. The point s is an arbitrary point in the complex plane, where the blue dashed line is a possible choice of the integration contour. The blue dotted and red solid lines then represent the choice that enclose the branch cuts, where the radius R goes to infinity.

The integral over the left-hand cut can be rewritten in terms of a right-hand-cut integral for the crossed channel u. This yields

$$\begin{aligned}\mathcal{M}(s,t,3s_0-s-t) = P^t_{m-1}(s) &+ \frac{Q_m(s)}{2\pi i}\int_{s_{\text{th}}}^{\infty}\mathrm{d}x\frac{\operatorname{disc}_x\mathcal{M}(x,t,3s_0-t-x)}{Q_m(x)(x-s)}\\ &+ \frac{Q_m(u)}{2\pi i}\int_{u_{\text{th}}}^{\infty}\mathrm{d}x\frac{\operatorname{disc}_x\mathcal{M}(3s_0-t-x,t,x)}{Q_m(x)(x-u)}\,. \end{aligned} \tag{2.55}$$

Note that the right-hand side of the equation is analytic in s, excluding the branch cuts. However, the derivation is only valid for real t and therefore not analytic in t, while the amplitude is required to be analytic in s and t. This property can be achieved by a reconstruction theorem [47–49]. It states that the $2 \to 2$ amplitude is reconstructed from the information on the partial-wave discontinuities. Therefore, we need to perform partial-wave expansions of the amplitude in the different scattering channels. This depends on the particles and their quantum numbers involved and we neither use a general nor a specific reconstruction theorem here. Some reconstruction theorems are known in the literature and two derivations can be found in the Appendices 4.A and 4.B. Note that these reconstruction theorems only hold for $2 \to 2$ scattering. However, one can use the

same analytic continuation of the decay mass already discussed in Sec. 2.1.1 to recover $1 \to 3$ decay amplitudes.

Chapter 3

Regge theory

This chapter serves as a short introduction to Regge theory and the way its concepts are presented here is based on Refs. [50–55]. Regge theory is used in Chapter 5. In Sec. 3.1, the Sommerfeld–Watson transform is introduced, which results in the asymptotic limit that is commonly known as Regge behavior. Sections 3.2, 3.3, and 3.4 briefly state other features used in Regge theory, and in Sec. 3.5 some properties of the Veneziano model, one of the earliest and most heavily used models to incorporate Regge physics, are shown.

The main idea of Regge theory was first introduced in 1959, where T. Regge considered the angular momentum j as a complex variable in Schrödinger equations for non-relativistic scattering [56]. It might seem unnatural to proceed this way, since angular momentum is physically restricted to positive integers. However, the analytic continuation to the complex-energy plane also gives rise to additional features of the scattering amplitude, albeit only real energies are measurable. Poles in the complex plane at positive integer j correspond to resonances or bound states. Phenomenologically, it is found that a sequence of particles of mass M_j and spin j lie on a linear Regge trajectory α, where $\alpha(M_j^2) = j$. This relation can be visualized in a Chew–Frautschi plot [57], where the primary example is the ρ trajectory, which is depicted in Fig. 3.1. Nowadays, Regge theory is applied to describe the high-energy behavior of scattering amplitudes in precision analyses [58–60]. Furthermore, using Regge theory, the first string theories were developed, where the trajectories are identified with vibrational modes of strings [61].

3.1 Sommerfeld–Watson transform

This section is mainly based on Ref. [50]. We consider the partial-wave expansion of an amplitude $A(s,t)$, for $2 \to 2$ scattering without spin and particles with equal mass M, in the physical t-channel, with $t > 4M^2$ and $s < 0$, which reads

$$A(s,t) = \sum_{j=0}^{\infty} (2j+1) f_j(t) P_j(z)\,, \tag{3.1}$$

where $f_j(t)$ is the partial-wave amplitude, $P_j(z)$ are the Legendre polynomials, and the cosine of the t-channel scattering angle is given by

$$z = 1 + \frac{2s}{t - 4M^2}\,. \tag{3.2}$$

Formally, the expansion in Eq. (3.1) will only converge within a limited region of the complex s-plane given by the Lehmann ellipse [62, 63]. Specifically, it diverges as $z \to \infty$ but one can use the Sommerfeld–Watson transform [64, 65] to find the proper analytic continuation. The partial-wave expansion is then valid in the entire s-plane, and we can properly investigate the limit $s \to \infty$ and fixed $t < 0$.

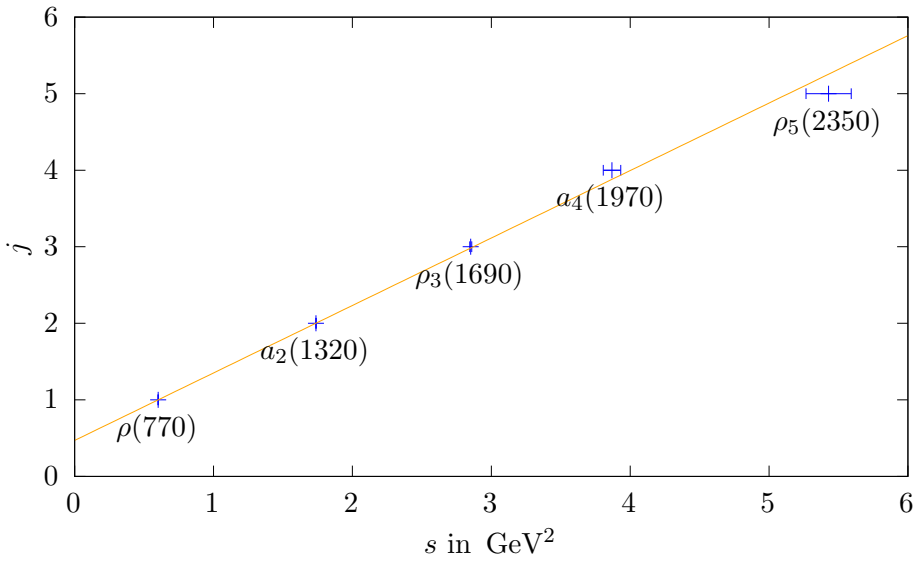

Figure 3.1: Chew–Frautschi plot [57] for the degenerate ρ–a_2 trajectory. The masses and their uncertainties are taken from Ref. [22]. The orange line represents a linear fit with $\alpha(s) = 0.47 + 0.88\,\mathrm{GeV}^{-2}s$.

First, we rewrite the sum as the Cauchy integral

$$A(s,t) = \frac{i}{2}\int_{C_1} \mathrm{d}j \frac{(2j+1)f(j,t)P_j(-z)}{\sin \pi j}\,, \tag{3.3}$$

with the contour shown in Fig. 3.2; here, $f(j,t)$ is the analytic continuation of the partial wave to complex j. Furthermore, $P_j(z)$ for complex j is defined as the Legendre function of the first kind [66]. The definition of the partial-wave amplitude is given by

$$f(j,t) = \frac{1}{2}\int_{-1}^{1} \mathrm{d}z P_j(z) A(s(z),t)\,, \tag{3.4}$$

which allows for an analytic continuation to complex j. However, the partial-wave amplitude in Eq. (3.4) does not fulfill the conditions of Carlson's theorem [67] and is therefore not unique. Furthermore, the asymptotic behavior of $P_j(z)$ in j is [66]

$$P_j(z) \approx j^{-1/2}\left(c_1 e^{ij\theta} + c_2 e^{-ij\theta}\right)\,, \tag{3.5}$$

where c_1 and c_2 are constants in j and z. Therefore, $P_j(z)$ diverges exponentially with increasing $|j|$ everywhere except for the real j axis.

There is an alternative definition of the partial-wave amplitudes that resolves these issues. It is derived via the Froissart–Gribov projection, cf. Ref. [50]. We define partial-wave amplitudes of odd and even signature and perform the Sommerfeld–Watson transform on each amplitude separately. The amplitudes read

$$A^{\pm}(s,t) \equiv A^{\pm}(t,z) = \sum_{j=0}^{\infty}(2j+1)f^{\pm}(j,t)P_j(z)\,, \tag{3.6}$$

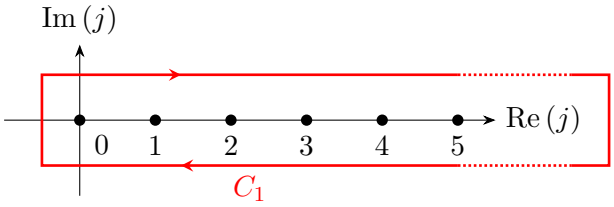

Figure 3.2: The contour C_1 of Eq. (3.3) and poles at real integers of j.

where the physical amplitude is the sum

$$A(t,z) = \frac{1}{2}\left(A^+(t,z) + A^+(t,-z) + A^-(t,z) - A^-(t,-z)\right) . \tag{3.7}$$

We now need to perform the contour integral, with the contour from Fig. 3.2, on each individual term. However, we deform the contour to C_2 shown in Fig. 3.3. Doing so, we also pick up potential poles, called Regge poles, in $f^\pm(j,t)$, which we classify by their position $\alpha^\pm(t)$ and residue $\beta^\pm(t)$.[1] Therefore, the signature amplitudes can be written as

$$A^\pm(t,z) = \frac{i}{2}\int_{C_2} \mathrm{d}j \frac{(2j+1) f^\pm(j,t) P_j(-z)}{\sin \pi j} - \sum_i \frac{\pi(2\alpha_i^\pm(t)+1)\beta_i^\pm(t) P_{\alpha_i^\pm}(-z)}{\sin \pi \alpha_i^\pm(t)} , \tag{3.8}$$

where the sum over i denotes the possible poles. If $f^\pm(j,t)$ falls fast enough for large j, the blue dotted arc of C_2 in Fig. 3.3 vanishes, and we are left with

$$\begin{aligned} A(s,t) = \frac{i}{2}\int_{-\frac{1}{2}-i\infty}^{-\frac{1}{2}+i\infty} \mathrm{d}j \frac{(2j+1)}{2\sin \pi j}\left(f^+(j,t)\left(P_j(-z)+P_j(z)\right) + f^-(j,t)\left(P_j(-z)-P_j(z)\right)\right) \\ - \sum_i \frac{\pi(2\alpha_i^\pm(t)+1)\beta_i^\pm(t)}{2\sin \pi \alpha_i^\pm(t)}\left(P_{\alpha_i^\pm}(-z) \pm P_{\alpha_i^\pm}(z)\right) . \end{aligned} \tag{3.9}$$

Note that the line integral is chosen at $\mathrm{Re}\, j = -1/2$, since it gives the most convergent behavior for the Legendre polynomials. However, in Ref. [68], it is shown how this point may be shifted to larger negative arguments.[2] Therefore, we include all Regge poles in the sum. Equation (3.9) enables us to analytically continue the amplitude from the physical t-channel region to high-energy s-channel scattering with $t < 0$. With the asymptotic behavior of the Legendre polynomials, we find

$$\begin{aligned} A(s,t) &\sim -\pi \sum_i \beta_i^\pm(t) \frac{1 \pm e^{-i\pi\alpha_i^\pm(t)}}{2\Gamma(\alpha_i^\pm(t)+1)\sin \pi\alpha_i^\pm(t)} s^{\alpha_i^\pm(t)} \\ &\sim \sum_i \frac{\beta_i^\pm(t)}{2}\Gamma(-\alpha_i^\pm(t))(1 \pm e^{-i\pi\alpha_i^\pm(t)}) s^{\alpha_i^\pm(t)} . \end{aligned} \tag{3.10}$$

The $s^{\alpha(t)}$ behavior for large s and small t is commonly called the Regge behavior and this also holds true in the crossed channels for all Mandelstam variables. Additionally, $\Gamma(-\alpha_i^\pm(t))$ produces poles for non-negative integers of $\alpha_i^\pm(t)$. They are further filtered to even and odd integers for the plus and minus signature, respectively.

[1] There also might appear additional effects due to branch cuts, which are ignored in this discussion. We refer the reader to Ref. [51] for further discussions.

[2] For further details, see the section on the Mandelstam–Sommerfeld–Watson transform in Ref. [51].

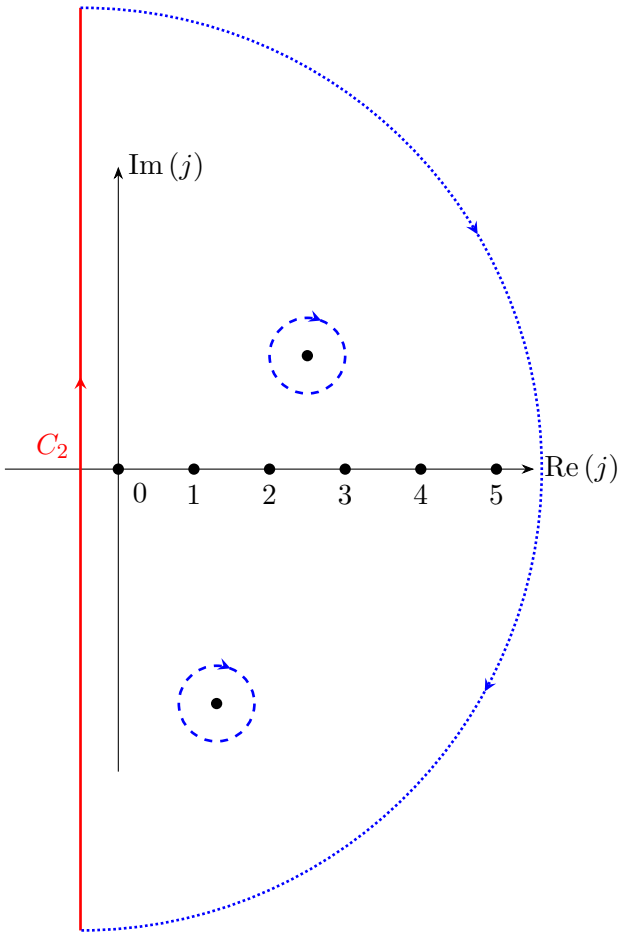

Figure 3.3: The contour C_2 of Eq. (3.8) and poles at real integers of j. Additionally, two poles are sketched in the complex j-plane that contribute to the second term in Eq. (3.8).

3.2 Pomeranchuk theorem

A phenomenon observed during the early stages of Regge theory is that all hadronic cross sections are remarkably constant at high energies. To achieve $\sigma^{\text{tot}}(s) \sim \text{const}$, a Regge trajectory with positive parity and $\alpha^{+}_{\mathbb{P}}(0) \sim 1$ was invented in Ref. [69], which is the maximum value permitted by the Froissart–Martin bound. This trajectory is called the Pomeron, named after I. Y. Pomeranchuk. He proved that the fraction of the cross sections for particle and antiparticle elastic scattering off the same target,

$$\frac{\sigma(A+B)}{\sigma(\bar{A}+B)} \to 1\,, \tag{3.11}$$

goes to unity if these cross sections are assumed to be constant at high energies [70, 71]. The Pomeron needs to have the quantum numbers of the vacuum, $J^{PC} = 0^{++}$, since it is exchanged in the t-channel of elastic scattering. The intersection at one saturates unitarity and there are no physical particles on this trajectory. However, it is still commonly parameterized as a pole. Some further details can be found in Sec. 5.2.3.

3.3 Froissart–Martin bound

In contrast to the previous section, the high-energy behavior of a cross section is restricted by the Froissart–Martin bound [72, 73]

$$\sigma^{\text{tot}}(s) \underset{s\to\infty}{\leq} \text{const} \cdot \ln^2(s)\,, \tag{3.12}$$

which is derived from the analytic properties of the scattering amplitude and unitarity. However, this theorem is only proven for $2 \to 2$ scattering with scalar particles. For all other processes, it is assumed to hold and most commonly used as an additional constraint. Relying on the Froissart–Martin bound and using the Regge behavior, with a phenomenologically motivated rising trajectory, we find that $\alpha(t) < 1$ for $t < 0$ and therefore $\alpha(0) \leq 1$. Additionally, in Refs. [52, 74, 75], it is shown that this behavior is limited by $A(s,t) \underset{s\to\infty}{>} s^{-1}$. Together with the Froissart–Martin bound, we find that the amplitude is constrained by

$$\frac{1}{s} < A(s,t) < s\ln^2(s)\,, \tag{3.13}$$

for $s \to \infty$ and arbitrary t.

3.4 Poles

Assuming we are close to an isolated Regge pole, we can write the amplitude as

$$A(t) = \frac{\beta(t)}{j - \alpha(t)}\,, \tag{3.14}$$

where α is a holomorphic function in the full complex plane except for a branch cut starting at t_{th}. Separating $\alpha(t) = \alpha_R(t) + i\alpha_I(t)$ and defining the point t_r where $\alpha_R(t_r) = j$, we can expand

$$\alpha(t) = j + \alpha_R'(t_r)(t - t_r) + i\alpha_I(t_r) + \dots\,. \tag{3.15}$$

Inserting this equation into Eq. (3.14), we find

$$A(t) = \frac{\beta(t)/\alpha_R'(t_r)}{t_r - t - i\alpha_I(t_r)/\alpha_R'(t_r)}\,, \tag{3.16}$$

and comparing to a simple Breit–Wigner formula, we can identify the mass $M_r = \sqrt{t_r}$ and width $\Gamma_r = \alpha_I(t_r)/(\alpha_R'(t_r)M_r)$. Note that below threshold, the imaginary part vanishes and we find a bound state on the real axis.

3.5 Veneziano model

In the low-energy region, it is useful to expand the scattering amplitude in s-channel partial-wave amplitudes. However, as s increases, the importance of higher partial waves grows and therefore this expansion is no longer meaningful in the high-energy region. On the contrary, one can also expand the amplitude in terms of t-channel Regge poles. This duality was used to construct the Veneziano model [76] for $2 \to 2$ scattering. Applying

this model to $\pi^+\pi^- \to \pi^+\pi^-$, the s- and t-channel contain $I = 0, 1$ resonances, while the u-channel is non-resonant with $I = 2$ [77–79]. Then, the amplitude can be written as

$$A(s,t) = \sum_n \frac{g_n(s,t)}{s - s_n} = \sum_m \frac{g_m(s,t)}{t - t_m}\,, \tag{3.17}$$

where the sums over all the s- and t-channel resonances are equal. Furthermore, the asymptotic Regge behavior should be fulfilled in both variables,

$$A(s,t) \underset{s\to\infty}{\sim} s^{\alpha(t)}\,, \tag{3.18}$$

$$A(s,t) \underset{t\to\infty}{\sim} t^{\alpha(s)}\,. \tag{3.19}$$

The simplest amplitude that fulfills these properties is the Veneziano formula

$$V(s,t) = g\frac{\Gamma(1-\alpha(s))\Gamma(1-\alpha(t))}{\Gamma(1-\alpha(s)-\alpha(t))}\,, \tag{3.20}$$

where g is the coupling strength and the denominator removes the double poles at the s–t points.[3] The Regge behavior for an increasing Regge trajectory $\alpha(s)$ and fixed t reads

$$V(s,t) \underset{s\to\infty}{\to} g\frac{\pi(-\alpha(s))^{\alpha(t)}}{\Gamma(\alpha(t))\sin\pi\alpha(t)}\,. \tag{3.21}$$

If the trajectory is assumed to be a real linear function $\alpha(s) = \alpha_0 + \alpha_1 s$, one finds the correct Regge asymptotics

$$V(s,t) \underset{s\to\infty}{\to} g\frac{\pi(\alpha_1 s)^{\alpha(t)}}{\Gamma(\alpha(t))\sin\pi\alpha(t)}e^{-i\pi\alpha(t)}\,, \tag{3.22}$$

where the same holds for $(s \leftrightarrow t)$.

In the s-channel close to a resonance pole s_n, one can expand the amplitude in the cosine of the s-channel scattering angle z_s

$$V(s,t) \underset{s\to s_n}{\to} \frac{g}{\alpha_1(s-s_n)(n-1)!}\left((2(s-s_{\text{th}})\alpha_1 z_s)^n + \mathcal{O}\big(z_s^{n-1}\big)\right)\,. \tag{3.23}$$

The residue can then be written in terms of a sum of Legendre polynomials of order 0 to n. The pole then corresponds to $n+1$ resonances with spin $0, \ldots, n$, the leading resonance and n daughters. The main disadvantage when using real linear trajectories is that the poles are on the real axis. Adding an imaginary part to the trajectory moves the poles to the second Riemann sheet. However, Eq. (3.23) is no longer valid and one produces ancestor poles with arbitrary high spin. Unitarization of single partial waves of the Veneziano model was unsuccessful. Nevertheless, the Veneziano model is a useful test model with many extensions to be used in different applications.

[3] Note that there are also other amplitudes where the summands of 1 in the arguments of the Gamma function are generalized to arbitrary integers.

Part II

Rescattering effects

Chapter 4

Analysis of rescattering effects in 3π final states

4.0 Prologue

The content of this chapter is based on the publication

- D. Stamen, T. Isken, B. Kubis, M. Mikhasenko, and M. Niehus, *Analysis of rescattering effects in* 3π *final states*, Eur. Phys. J. C **83**, 510 (2023) [arXiv:2212.11767 [hep-ph]], [Erratum: Eur. Phys. J. C **83**, 586 (2023)] .

Decays into three particles are often described in terms of two-body resonances and a non-interacting spectator particle. P-wave two-pion rescattering can be described in terms of an Omnès function, which incorporates the ρ resonance. Going beyond the simplest isobar model, crossed-channel rescattering effects need to be accounted for. We quantify the importance of these rescattering effects in three-pion systems for different decay masses and angular-momentum quantum numbers. Therefore, we provide amplitude decompositions, also known as reconstruction theorems, for the four decay processes with total $J^{PC} = 0^{--}$, 1^{--}, 1^{-+}, and 2^{++}, all of which decay predominantly as $\rho\pi$ states. Reconstruction theorems have been proven to a given order in chiral perturbation theory. For the derivation, we use fixed-variable dispersion relations and the symmetry properties of the amplitude, e.g., isospin and crossing symmetry. The decompositions for $J^{PC} = 0^{--}$ and 1^{--} were already known in the literature, cf. Ref. [80, 81]. For $J^{PC} = 1^{-+}$, the reconstruction theorem was first derived by Tobias Isken, and the final result can be found in Ref. [42]. The author of this thesis performed the calculation confirming the previous result, and the derivation is written down as part of this chapter. For $J^{PC} = 2^{++}$, the decomposition was not known. With helpful hints by Mikhail Mikhasenko and Bastian Kubis, the author of this thesis derived the decomposition. Note that, even though we neglect all partial waves higher than the P-waves, we get a contribution that behaves like a D-wave for numerical purposes. The derivation of the decomposition and the associated numerical treatment are part of this chapter.

The inclusion of crossed-channel effects is achieved by solving the Khuri–Treiman integral equations. For the solution of the Khuri–Treiman equations, a numerical code was developed by Hakan Akdag, Malwin Niehus, and the author of this thesis. It must be mentioned that prior to this, other versions existed, e.g., the code from Tobias Isken, which we used for cross checks. While Hakan Akdag mainly implemented the version for CP-violating $\eta^{(\prime)}$ decays with the "Pinocchio method" [81–84] and Malwin Niehus the Gasser–Rusetsky method [85–87] for $1^{-\mp}$, the author of this thesis simplified and generalized the code, which drastically reduced the effort for including new reconstruction theorems. This led to the current version, where all known reconstruction theorems for $\eta^{(\prime)} \to 3\pi$ and $\eta' \to \eta\pi\pi$ decays, as well as for the four quantum numbers mentioned

above, are implemented. Furthermore, numerical tools are available for matching around unstable points up to D-waves. Note that the numerical cure of D-waves had to be derived by the author of this thesis and is part of this chapter. The functions used therein are generalized and therefore the procedure for even higher partial waves can be derived. The Pinocchio method is implemented in C++ , and using `pybind11` [88] it is straightforward to use the classes and their respective member functions in Python. The author of this thesis also wrote main parts of the documentation and the code is now publicly available at github.com/HISKP-ph/khuri_treiman_solver [89].

This project has been an idea for a long time and it was clear that the single-variable amplitudes are not suitable for the desired comparison. Therefore, we needed a comparison on the Dalitz-plot level, but it remained unclear how to account for experimental binning. Mikhail Mikhasenko proposed the unbinned log-likelihood estimator to determine the significance of the rescattering effects beyond two-body resonances. Using this, we computed the minimum number of events necessary to unambiguously find these in future Dalitz-plot analyses. The calculation uses the Kullback–Leibler divergence and variance, and it was shown numerically that the assumption of a normal distribution is valid. First tests and the general idea are already sketched in Ref. [87]. The analysis was performed by the author of this thesis; additionally, all the plots that are part of this chapter were created by the author. Kinematic effects that enhance or dilute the rescattering were identified by the author in collaboration with Bastian Kubis and Mikhail Mikhasenko for the selected set of quantum numbers and various masses.

4.1 Introduction

Much of the modern-era precision in hadron spectroscopy is not gleaned from scattering reactions, but rather from production or decay processes [90–94]. For two-body states, the universality of final-state interactions [95] provides an important and fundamental link between scattering and production amplitudes, guaranteeing their phases to be identical in the region where scattering is elastic. The presence of a third strongly interacting decay product complicates rigorous analyses considerably. An approximation to the decay amplitude where the two-particle interaction is modeled by a resonant amplitude without accounting for the interaction with the spectators is referred to as the isobar model. The lineshape of the resonant pairwise interaction is often parameterized by the Breit–Wigner function [96]. While one might expect that under certain circumstances, the influence of spectator particles on the two-body resonance signal ought to be small—the resonance in question being narrow, or the spectators having large relative momenta—the impact of the spectator interaction on the resonance lineshape has only rarely been quantified. The goal of this chapter is to start the endeavor to survey such more complicated final-state interactions numerically, beginning with the simplest processes: decays into three pions.

A tool to perform a theoretically rigorous evaluation of three-body decays is given by the so-called Khuri–Treiman (KT) dispersion relations [97]. These are coupled integral equations that describe all sequential pairwise two-body rescattering, summed to all orders. While the two-body phase shifts are assumed to be known, the solutions of these equations depend on a set of free parameters, subtraction constants of the dispersion integrals, which can be fixed by comparison to experimental data or by matching to effective field theories. Instead of analyzing data for a particular process, we pose the question: how

much statistics needs to be collected in order for lineshape modifications due to a third pion to be discernible? We choose the processes to study based on the condition that their amplitude representations can be reduced to one single subtraction constant. This then serves as a mere normalization, and hence allows us to study subtle variations of the resonance lineshape in an unambiguous manner. In many three-pion decays, the ρ meson is the most prominent pion–pion resonance, and interactions of higher angular momentum are suppressed. An important criterion is therefore that we select decays in which S-waves are forbidden by conservation laws, reducing the problem to the P-wave interaction only. One process of significant interest disregarded here is the $\tau \to 3\pi\nu_\tau$ decay, in which the $a_1(1260)$ resonance with $J^{PC} = 1^{++}$ appears prominently; however, there are S-waves involved, whose strength relative to the P-waves cannot be fixed *a priori* without data (cf. a similar analysis in Ref. [98]).

The outline of this chapter is as follows: in Sec. 4.2, we introduce and discuss the KT equations and derive the amplitude decompositions of four different three-pion decays that are dominated by the $\rho\pi$ intermediate states. Subsequently, in Sec. 4.3, we describe the statistical method used to distinguish the KT solutions from the simpler Omnès model that neglects spectator interactions entirely. Section 4.4 shows our numerical results and discusses the dependence of the crossed-channel rescattering effects on mass and quantum numbers of the three-pion system in detail. Our findings are summarized in Sec. 4.5. Some technical details are relegated to the appendices.

4.2 Khuri–Treiman equations

The Khuri–Treiman equations [97] were first derived in the 1960s to analyze $K \to 3\pi$ decays. With the advent of very precise parameterizations of low-energy pion–pion ($\pi\pi$) phase shifts [49, 58, 99], the approach has experienced a remarkable renaissance and has been applied to various decays [80, 81, 100–116] and scattering processes [4, 117–120] since.

We here consider four different 3π decays with quantum numbers $J^{PC} = 0^{--}$, 1^{--}, 1^{-+}, and 2^{++}, which fulfill the criterion introduced in Sec. 4.1. For all these, the unpolarized distribution over the three-body phase space as represented by the Dalitz plot contains the full information on the decay dynamics, as only one helicity amplitude contributes in every case. In order to apply the KT equations, we decompose each amplitude into the so-called single-variable amplitudes (SVAs), which are complex functions with a right-hand cut only. These decompositions are known as reconstruction theorems, proven in chiral perturbation theory in a given order using fixed-variable dispersion relations [47, 48, 121]. Thereby, we restrict ourselves to P-waves and neglect all higher partial waves.

4.2.1 Reconstruction theorem for 1^{--} decay

We begin our discussion with the consideration of isoscalar vector quantum numbers, $I^G(J^{PC}) = 0^-(1^{--})$, where the isospin I is forced to be zero by the negative G-parity of the odd-pion system and negative C-parity. Decays into three neutral pions are forbidden by charge conjugation. The decays $\omega/\phi \to 3\pi$ have been studied extensively using the KT formalism [81, 102, 112, 113], as well as extended to the $J/\psi \to 3\pi$ decays [103, 115], and the general reactions $e^+e^- \to 3\pi$ [122–127]. Experimentally, the Dalitz plots both for $\omega \to 3\pi$ [128, 129] and $\phi \to 3\pi$ [130, 131] have been investigated in detail.

The decay reads

$$V(p) \to \pi^0(p_1)\pi^+(p_2)\pi^-(p_3)\,, \tag{4.1}$$

where p and p_i denote the four momenta of the decay particle V and the pions, respectively. The Mandelstam variables [40] are defined as $s = (p-p_1)^2$, $t = (p-p_2)^2$, and $u = (p-p_3)^2$. The amplitude $\mathcal{M}$ is decomposed into a scalar amplitude $\mathcal{F}$ and a kinematic factor in the following form:

$$\begin{aligned} \mathcal{M}(s,t,u) &= i\epsilon^\mu K_\mu \mathcal{F}(s,t,u)\,, \\ K_\mu &= \varepsilon_{\mu\nu\alpha\beta} p_1^\nu p_2^\alpha p_3^\beta\,, \end{aligned} \tag{4.2}$$

where the Levi-Civita tensor is employed due to the odd intrinsic parity. By squaring the matrix element and averaging over the initial polarization, one obtains

$$\overline{|\mathcal{M}|^2} = \mathcal{K}(s,t,u)|\mathcal{F}(s,t,u)|^2\,, \tag{4.3}$$

where $\mathcal{K}$ is a factor proportional to the Kibble function [132],

$$\mathcal{K}(s,t,u) = \frac{1}{4}\left(stu - M_\pi^2(M^2 - M_\pi^2)^2\right)\,. \tag{4.4}$$

Here, M denotes the mass of the decay particle, and M_π refers to the pion mass in the isospin limit. Using the fixed-variable dispersion relations, one can show that the scalar amplitude is decomposed into the P-wave SVAs, $\mathcal{F}(x)$ [42, 81, 83, 87]:

$$\mathcal{F}(s,t,u) = \mathcal{F}(s) + \mathcal{F}(t) + \mathcal{F}(u)\,, \tag{4.5}$$

where discontinuities in F- and higher partial waves have been neglected. The decay amplitude is invariant under a shift

$$\mathcal{F}(s) \to \mathcal{F}(s) + \alpha(s - s_0)\,, \tag{4.6}$$

where $3s_0 \equiv M^2 + 3M_\pi^2 = s + t + u$, and α is an arbitrary complex constant. This means that the decomposition in Eq. (4.5) only defines $\mathcal{F}(s)$ up to such a polynomial ambiguity. The strategy to eliminate the ambiguity is discussed in Sec. 4.2.5.

4.2.2 Reconstruction theorem for 1^{-+} decay

Mesons with quantum numbers $I^G(J^{PC}) = 1^-(1^{-+})$ are exotic in the quark model. The lightest candidate for such hybrid mesons is the $\pi_1(1600)$, which has been searched for experimentally in different final states such as $\eta\pi$ [133–137], $\eta'\pi$ [134, 135, 137], and the most relevant for the present study $\rho\pi$ [138].

The amplitude decomposition for the decays $\pi_1 \to 3\pi$ is very similar to the one for resonances with $I^G(J^{PC}) = 0^-(1^{--})$ discussed in the previous section, however, the positive charge conjugation implies odd isospin. For the isovector decay, the explicit decomposition of the decay amplitude in terms of isospin indices is required,

$$X^i(p) \to \pi^j(p_1)\pi^k(p_2)\pi^l(p_3)\,, \tag{4.7}$$

where i, j, k, and l are the isospin indices in the Cartesian basis. The decay is once more of odd intrinsic parity. The decomposition reads

$$\mathcal{M}^{ijkl}(s,t,u) = i\epsilon^{\mu} K_{\mu} \mathcal{H}^{ijkl}(s,t,u)\,, \tag{4.8}$$

with the isospin amplitude $\mathcal{H}^{ijkl}$ following from the well-known isospin relations for $\pi\pi$ scattering [139]:

$$\mathcal{H}^{ijkl}(s,t,u) = \delta^{ij}\delta^{kl}\mathcal{H}(s,t,u) + \delta^{ik}\delta^{jl}\mathcal{H}(t,u,s) + \delta^{il}\delta^{jk}\mathcal{H}(u,s,t)\,. \tag{4.9}$$

The reconstruction theorem retaining P-waves only, i.e., neglecting discontinuities in D-waves and higher, reads

$$\mathcal{H}(s,t,u) = \mathcal{H}(t) - \mathcal{H}(u)\,, \tag{4.10}$$

derived in Appendix 4.A. The decomposition is ambiguous by shifting

$$\mathcal{H}(s) \to \mathcal{H}(s) + \alpha\,. \tag{4.11}$$

This ambiguity in principle allows us to write down a twice-subtracted dispersion integral for $\mathcal{H}(s)$ that still depends on one subtraction constant only. Since the subtraction constants of these two representations are connected by a sum rule, the amplitude $\mathcal{H}(s,t,u)$ remains unchanged. The allowed charge configurations are

$$X^+ \to \pi^+\pi^0\pi^0\,,\quad X^+ \to \pi^+\pi^+\pi^-\,,\quad X^0 \to \pi^+\pi^-\pi^0\,,\quad X^- \to \pi^-\pi^0\pi^0\,,\quad X^- \to \pi^-\pi^-\pi^+\,,$$

which all lead to the same result for the absolute squared of the amplitude.[1] Due to the analogy between Eqs. (4.2) and (4.8), the latter can be written in the same form as Eq. (4.3).

4.2.3 Reconstruction theorem for 2^{++} decay

For isovector tensor mesons, $I^G(J^{PC}) = 1^-(2^{++})$, the lightest state is the $a_2(1320)$ that dominantly decays into 3π [22]. Hence, we need to consider isospin explicitly,

$$T^i(p) \to \pi^j(p_1)\pi^l(p_2)\pi^k(p_3)\,. \tag{4.12}$$

Due to the high spin of the decaying particle, the complete amplitude decomposition is considerably more complicated than for the vector decays and involves different helicity amplitudes; this is discussed in Appendix 4.B. The isospin decomposition of $\mathcal{M}^{ijkl}(s,t,u)$ involves invariant isospin amplitudes, which can be defined with respect to different Mandelstam variables. These are related to each other by crossing symmetry; see Appendix 4.B for details. The s-channel amplitude is given as

$$\mathcal{M}_s(s,t,u) = i\sqrt{2}\epsilon_{\mu\nu}K^{\mu}\left[(p_2+p_3)^{\nu}\mathcal{B}(s,t,u) + (p_2-p_3)^{\nu}\mathcal{C}(s,t,u)\right]\,. \tag{4.13}$$

The resulting spin-averaged squared amplitude then reads

$$\begin{aligned}\overline{|\mathcal{M}_s|^2} = \tilde{\mathcal{K}}_1(s,t,u)|\mathcal{B}(s,t,u)|^2 + 2\tilde{\mathcal{K}}_2(s,t,u)\,\mathrm{Re}\left(\mathcal{B}(s,t,u)\mathcal{C}(s,t,u)^*\right)\\ + \tilde{\mathcal{K}}_3(s,t,u)|\mathcal{C}(s,t,u)|^2\,,\end{aligned} \tag{4.14}$$

[1] The amplitudes for the charge configurations differ when including higher partial waves.

where

$$\begin{aligned}
\tilde{\mathcal{K}}_i(s,t,u) &= \frac{\mathcal{K}(s,t,u)}{40M^2} k_i(s,t,u)\,, \quad \forall i \in \{1,2,3\}\,,\\
k_1(s,t,u) &= \lambda(s,M^2,M_\pi^2)\,,\\
k_2(s,t,u) &= (s+M^2-M_\pi^2)(u-t)\,,\\
k_3(s,t,u) &= (t-u)^2 + 4M^2\left(s-4M_\pi^2\right)\,,
\end{aligned} \tag{4.15}$$

and $\lambda(a,b,c)$ is the standard Källén function defined in Eq. (2.15). The reconstruction theorem of the scalar functions has the form

$$\begin{aligned}
\mathcal{B}(s,t,u) &= \mathcal{B}(t) - \mathcal{B}(u)\,,\\
\mathcal{C}(s,t,u) &= \mathcal{B}(t) + \mathcal{B}(u)\,,
\end{aligned} \tag{4.16}$$

neglecting discontinuities that lead to $\pi\pi$ D-waves and higher. This decomposition is unambiguous.

4.2.4 Reconstruction theorem for 0^{--} decay

The decays of the $\eta^{(\prime)}$ mesons, $I^G(J^{PC}) = 0^+(0^{-+})$, into 3π necessarily violate G-parity. In the Standard Model, where both the strong and the electromagnetic interactions preserve charge conjugation, the decays proceed via breaking of isospin symmetry, while more exotic scenarios of physics beyond the Standard Model involving C-parity violation are suggested for the $\pi^+\pi^-\pi^0$ final state [80, 140, 141]. We here concentrate on the latter, with total three-pion isospin $I = 0$ and negative charge conjugation, which would be equally applicable for the three-pion decay of a quark-model-exotic resonance with $I^G(J^{PC}) = 0^-(0^{--})$ in QCD. Such states have been predicted as hybrid mesons with precisely this decay channel [142], although first lattice-QCD calculations at unphysically high pion masses suggest them to appear at higher masses than the 1^{-+} hybrids [143]; constituent-gluon models partly come to different conclusions [144]. The decay amplitude written in terms of P-waves only is given by

$$\mathcal{M}(s,t,u) = (t-u)\mathcal{G}(s) + (u-s)\mathcal{G}(t) + (s-t)\mathcal{G}(u)\,. \tag{4.17}$$

We note that due to the decaying particle being a (pseudo)scalar, there is no additional kinematic factor in the relation to the Dalitz-plot distribution. In contrast to the fully symmetric reconstruction theorem under pairwise exchange of Mandelstam variables for $J^{PC} = 1^{--}$, this one is fully antisymmetric.

The amplitude stays invariant under a three-parameter polynomial shift

$$\mathcal{G}(s) \to \mathcal{G}(s) + \alpha + \beta s + \gamma s^2(3s_0 - s)\,, \tag{4.18}$$

where α, β, and γ are arbitrary complex numbers. Similar to the discussion in Sec. 4.2.2, this ambiguity allows us to write $\mathcal{G}(s)$ as a twice- or three-times-subtracted dispersion integral, depending on a single subtraction constant.

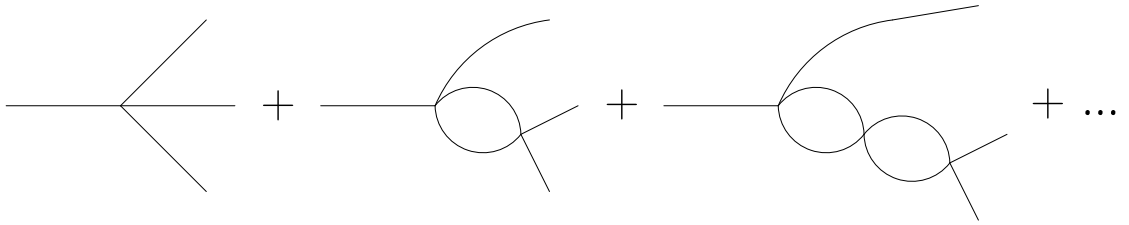

Figure 4.1: Diagrammatic representation of iterated bubble sums for the 2π subsystems, implemented by Omnès functions. In general, due to interchange of the rescattered pions, three different bubble sums may contribute.

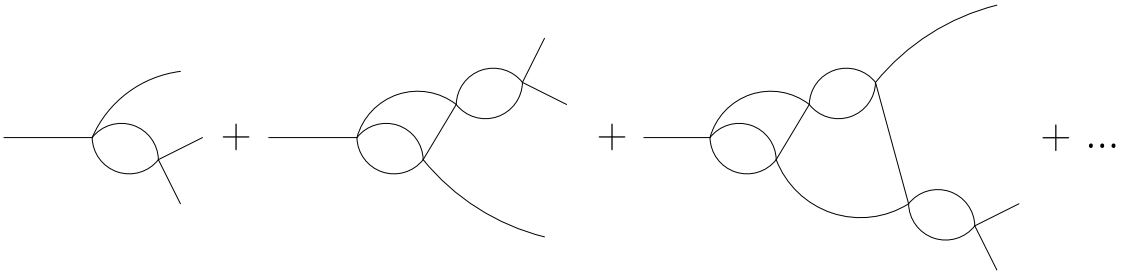

Figure 4.2: Diagrammatic representation of the amplitudes based on the full Khuri–Treiman equations.

4.2.5 Partial-wave unitarity, Omnès solutions

The form of the partial-wave series deviates due to the different spins of the decaying particles. While the one for the pseudoscalar decay in Eq. (4.17) proceeds in terms of standard Legendre polynomials, the one for the vector decays has the form [145]

$$\mathcal{F}(s,t,u) = \sum_{\ell=1} P'_\ell(z_s) f_\ell(s)\,, \tag{4.19}$$

and similarly for $\mathcal{H}(s,t,u)$, where $P'_\ell(z_s)$ refers to the derivatives of the Legendre polynomials. The cosine of the s-channel scattering angle, denoted by z_s, can be expressed via the Mandelstam variables

$$z_s = \frac{t-u}{\kappa(s)}\,, \quad \kappa(s) = \sqrt{1-\frac{4M_\pi^2}{s}}\lambda^{1/2}(s,M^2,M_\pi^2)\,. \tag{4.20}$$

In the s-channel center-of-mass system, t and u are related to the scattering angle via

$$t(s,z_s) = u(s,-z_s) = \frac{1}{2}\big(3s_0 - s + \kappa(s) z_s\big)\,. \tag{4.21}$$

The partial-wave expansion for the tensor-meson decay is slightly more cumbersome as discussed in Appendix 4.B.

We consider elastic unitarity for the two-pion states. The $\pi\pi$ P-wave phase shift $\delta(s) = \delta_1^1(s)$ is parameterized according to Ref. [146]. A partial wave $\chi_1(s)$ of angular momentum

$\ell = 1$ obeys a unitarity relation of the form

$$\begin{aligned}\operatorname{disc}\chi_1(s) &= \lim_{\epsilon\to 0}\left[\chi_1(s+i\epsilon) - \chi_1(s-i\epsilon)\right] \\ &= 2i\chi_1(s)\sin\delta(s)e^{-i\delta(s)}\theta\big(s-4M_\pi^2\big)\,. \end{aligned} \tag{4.22}$$

It can be decomposed into parts with right-hand and left-hand cuts only, $\chi_1(s) = \mathcal{X}(s) + \widehat{\mathcal{X}}(s)$, with $\mathcal{X} \in \{\mathcal{F}, \mathcal{H}, \mathcal{B}, \mathcal{G}\}$, where $\widehat{\mathcal{X}}$ is the so-called inhomogeneity that has no discontinuity along the right-hand cut. It results from the partial-wave projection of the t- and u-channel SVAs. The inhomogeneities are given by

$$\begin{aligned}
\widehat{\mathcal{F}}(s) &= 3\langle\big(1-z_s^2\big)\,\mathcal{F}\rangle && [J^{PC}=1^{--}]\,,\\
\widehat{\mathcal{H}}(s) &= -\frac{3}{2}\langle\big(1-z_s^2\big)\,\mathcal{H}\rangle && [J^{PC}=1^{-+}]\,,\\
\widehat{\mathcal{B}}(s) &= \frac{3}{4}\big[\langle\big(1-z_s^2\big)\,\mathcal{B}\rangle - \xi(s)\langle\big(1-z_s^2\big)\,z_s\mathcal{B}\rangle\big] && [J^{PC}=2^{++}]\,,\\
\widehat{\mathcal{G}}(s) &= -\frac{3}{\kappa(s)}\Big[3(s-s_0)\langle z_s\mathcal{G}\rangle + \kappa(s)\langle z_s^2\mathcal{G}\rangle\Big] && [J^{PC}=0^{--}]\,,
\end{aligned} \tag{4.23}$$

where we employ the notation

$$\langle z_s^n\mathcal{X}\rangle = \frac{1}{2}\int_{-1}^{1}\mathrm{d}z_s z_s^n\mathcal{X}\big(t(s,z_s)\big)\,, \tag{4.24}$$

and $\xi(s)$ is defined via

$$\xi(s) = \sqrt{1-\frac{4M_\pi^2}{s}}\,\frac{s+M^2-M_\pi^2}{\lambda^{1/2}(s,M^2,M_\pi^2)}\,. \tag{4.25}$$

As a consequence, the unitarity relations for the partial waves can be reduced to those for the SVAs $\mathcal{X}(s)$, which read

$$\operatorname{disc}\mathcal{X}(s) = 2i\Big(\mathcal{X}(s)+\widehat{\mathcal{X}}(s)\Big)\sin\delta(s)e^{-i\delta(s)}\theta\big(s-4M_\pi^2\big)\,. \tag{4.26}$$

The solution for the homogeneous problem, setting $\widehat{\mathcal{X}} = 0$, is given by the well-known Omnès function $\Omega(s)$ [45, 46]

$$\begin{aligned}\mathcal{X}_{\text{hom.}}(s) &= P(s)\Omega(s)\,,\\ \Omega(s) &= \exp\left(\frac{s}{\pi}\int_{4M_\pi^2}^{\infty}\mathrm{d}s'\frac{\delta(s')}{s'(s'-s)}\right)\,,\end{aligned} \tag{4.27}$$

where $P(s)$ is a polynomial and $\Omega(0) = 1$. Such representations are used, e.g., in descriptions of the pion vector form factor; see Ref. [146] and references therein. Using the Omnès function as an approximation for a SVA in a three-pion final state, we describe the rescattering of a two-pion subsystem only, with the third pion being a spectator, as shown in Fig. 4.1. To include the full rescattering effects, cf. Fig. 4.2, we need to solve the inhomogeneous equation. The solution is given by [101]

$$\mathcal{X}(s) = \Omega(s)\left(P_{n-1}(s) + \frac{s^n}{\pi}\int_{4M_\pi^2}^{\infty}\frac{\mathrm{d}s'}{s'^n}\frac{\sin\delta(s')\widehat{\mathcal{X}}(s')}{|\Omega(s')|(s'-s)}\right)\,, \tag{4.28}$$

where n determines the number of subtractions. As we aim for the most predictive model, without the need to fix the relative strength of various subtraction constants to concrete data, we set $n = 1$. The high-energy behavior of the SVAs is dictated by the one of the Omnès function, which in turn is given by the asymptotic limit of the input phase shift: $\delta(s \to \infty) \to \pi$ implies $\Omega(s \to \infty) \asymp s^{-1}$, and as a consequence, also the SVAs vanish asymptotically, $\mathcal{X}(s) \asymp s^{-1}$. As a result, none of the polynomial ambiguities discussed in the previous sections survive: they would alter this asymptotic behavior and violate the high-energy constraint imposed.

We note that the mass of the decay particle enters $\widehat{\mathcal{X}}$ via the partial-wave projection integral. Physically, $\widehat{\mathcal{X}}$ incorporates the crossed-channel effects, which depend on the relative momenta of all three final-state pions. The resulting differences are discussed in Sec. 4.2.6. The solution in Eq. (4.28) is generated iteratively for each process and decay mass, which can justify the diagrammatic representation in Fig. 4.2.

4.2.6 Comparison of different SVAs

In Fig. 4.3, we compare the KT solutions for the different SVAs to the Omnès solution, both for different decay masses (for the $J^{PC} = 1^{--}$ case; cf. also Ref. [83]) and comparing the SVAs with different reconstruction theorems or inhomogeneities at the same decay mass. These pictures suggest we already have an answer to the question to what extent the ρ lineshape and phase are modified by crossed-channel interactions, and how this modification varies with quantum numbers and decay mass. However, this impression is misleading to some extent, as can be seen by the following considerations.

1. As our reconstruction theorems all depend on one single SVA only, it is obvious that an overall shift of its phase by a constant is not observable. A significant part of the changes in phase compared to the input phase shift seen in Fig. 4.3 can already be undone by such a shift.

2. Although we have theoretically constrained our SVAs to fulfill a certain, restrictive, high-energy behavior, this still means that a polynomial shift according to the corresponding ambiguity is not observable in a finite Dalitz plot. This suggests that any change between Omnès and full KT solution that is, in fact, polynomial-like will not be experimentally verifiable.

3. Finally, the single subtraction or normalization constants of our dispersive amplitude representations are not *a priori* fixed; changes in the SVAs that can be absorbed in a change of normalization will therefore also not allow us to verify non-trivial rescattering effects. This is demonstrated in the bottom row of Fig. 4.3, where the SVAs are not commonly normalized at $s = 0$, but in the ρ peak: the differences between the different solutions already appear significantly muted.

All three points demonstrate that it is very difficult to quantify the observable changes by considering complex, interfering decay amplitudes only. We therefore choose a different, unambiguous, path in the following and immediately study the Dalitz-plot distributions, which are direct observables.

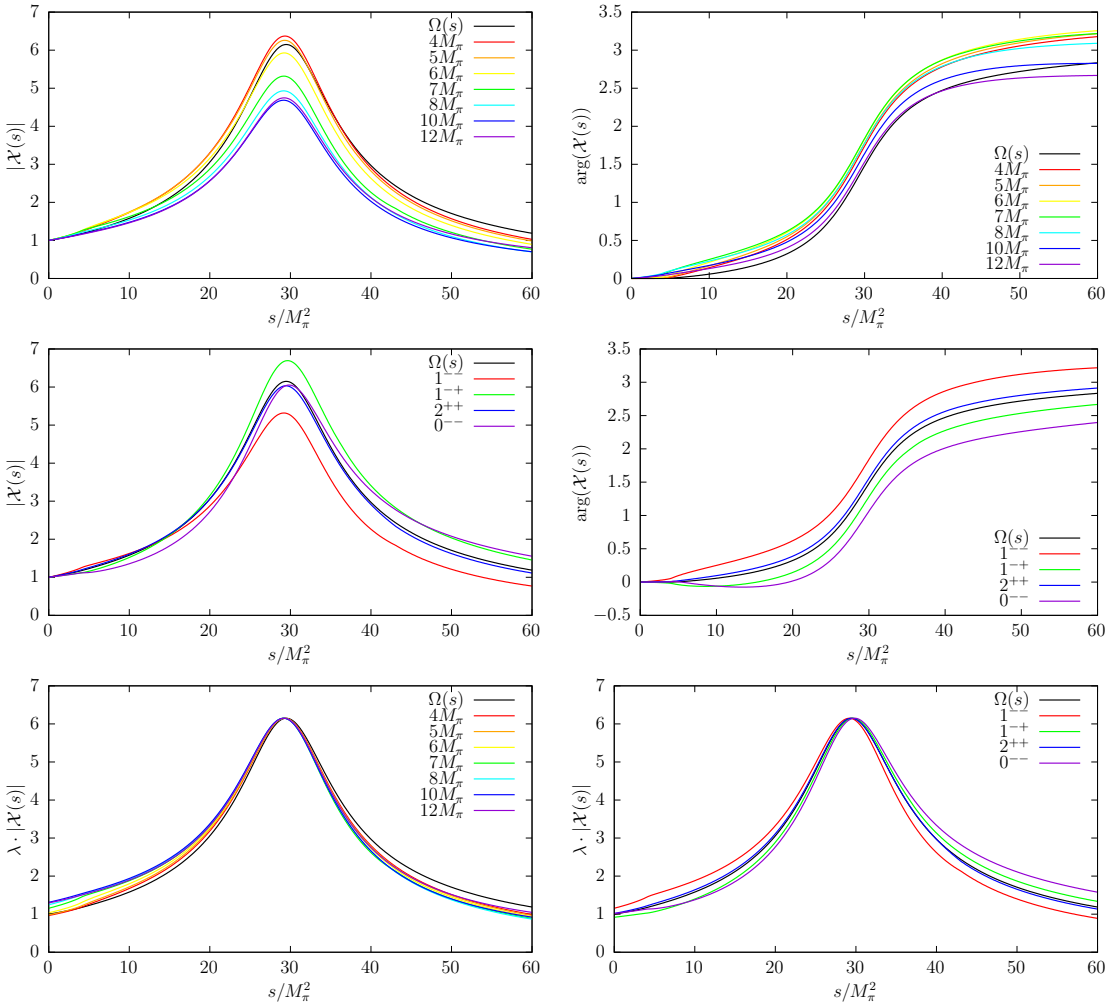

Figure 4.3: Absolute values (left) and phases (right) of the SVAs: for $J^{PC} = 1^{--}$ with different decay masses M (top), and at the same decay mass $M = 7M_\pi$ for the four different reconstruction theorems (middle). The two plots at the bottom show again the absolute values for both comparisons, but this time with the basis functions normalized to the peak of the Omnès function.

4.3 Log-likelihood estimator

In experiments measuring Dalitz plots, the data is often binned. The binning scheme is determined by each experiment individually to obtain distributions with reasonable statistical and systematic uncertainties; therefore, there is no unique prescription even for a given number of overall events. We thus seek an unbinned method to characterize the Dalitz-plot distribution, relying on the total number of events for the full Dalitz plot only. In the following, the deviations between the Omnès and KT solutions are quantified using the Kullback–Leibler (KL) divergence [147] based on the log-likelihood estimator.

As the description of the decay amplitudes in terms of KT equations is physically more complete, we interpret their outcome as the "truth" and test to which extent the Omnès

functions are capable of reproducing this. The decay amplitudes are denoted by $\mathcal{M}^{\mathrm{KT}}$ and $\mathcal{M}^{\mathrm{Omnès}}$ for the KT and Omnès solutions, respectively, where the isospin and helicity indices are suppressed for clarity. For the Omnès solution, we replace the SVAs by plain Omnès functions in the corresponding reconstruction theorems. We define the probability density function (pdf) as

$$f(s,t) = \frac{\overline{|\mathcal{M}|^2}(s,t,u)}{\int_D \overline{|\mathcal{M}|^2}(s,t,u)\mathrm{d}s\mathrm{d}t}\,. \tag{4.29}$$

Additionally, we explore an unphysical quantity defined by

$$\begin{aligned} |\tilde{\mathcal{M}}(s,t,u)|^2 &= \frac{\overline{|\mathcal{M}|^2}(s,t,u)}{\mathcal{K}(s,t,u)}\,, \\ \tilde{f}(s,t) &= \frac{|\tilde{\mathcal{M}}(s,t,u)|^2}{\int_D |\tilde{\mathcal{M}}(s,t,u)|^2\mathrm{d}s\mathrm{d}t}\,. \end{aligned} \tag{4.30}$$

This construct appears to be more sensitive to the distribution at the edge of the Dalitz plots and therefore visualizes the ρ bands discussed in Sec. 4.4. Our representation is fixed up to a normalization constant, therefore the pdf is free of any undetermined parameters. The integral region D is the three-body decay phase space, captured by the Dalitz plot. For the decay mass M and the pion mass M_π, its boundaries are determined by

$$\begin{aligned} 4M_\pi^2 \leq s &\leq (M - M_\pi)^2\,, \\ t(s, z_s = -1) \leq t &\leq t(s, z_s = 1)\,, \end{aligned} \tag{4.31}$$

where $t(s, z_s)$ is given by Eq. (4.21). We generate a sample $\mathbb{D}$ by drawing $N \in \mathbb{N}$ pairs (s_i, t_i) from f^{KT}. The likelihood function L of a pdf f with respect to the data sample $\mathbb{D}$ is defined as

$$L(\mathbb{D}, f) = \prod_{i=1}^{N} f(s_i, t_i)\,. \tag{4.32}$$

The likelihood ratio of the Omnès and KT solutions

$$\Delta L(\mathbb{D}) = \frac{L(\mathbb{D}, f^{\mathrm{Omnès}})}{L(\mathbb{D}, f^{\mathrm{KT}})} \tag{4.33}$$

indicates which one is favored. In the following, we will use the log-likelihood and its difference

$$\begin{aligned} \mathcal{L}(\mathbb{D}, f) &= \ln(L(\mathbb{D}, f))\,, \\ \Delta\mathcal{L}(\mathbb{D}) &= \ln\left(\Delta L(\mathbb{D})\right) = \mathcal{L}(\mathbb{D}, f^{\mathrm{Omnès}}) - \mathcal{L}(\mathbb{D}, f^{\mathrm{KT}})\,. \end{aligned} \tag{4.34}$$

We note that $\Delta\mathcal{L} > 0$ is possible despite drawing data from the KT solution, since N is finite. This gives us precisely the handle we need to determine the value of N to observe crossed-channel rescattering effects.

We can now perform $B \in \mathbb{N}$ runs, which generate B datasets $\mathbb{D}_b$, $b = 1, \ldots, B$, of size N. On each of these datasets, one can compute $\Delta\mathcal{L}$ and access its probabilistic distribution. For large values of B, this distribution is Gaussian, with the mean and variance given by

$$\begin{aligned} \mathrm{E}\left[\Delta\mathcal{L}(\mathbb{D})\right] &= -N d_{\mathrm{KL}}\,, \\ \mathrm{Var}\left[\Delta\mathcal{L}(\mathbb{D})\right] &= N\nu_{\mathrm{KL}}\,, \end{aligned} \tag{4.35}$$

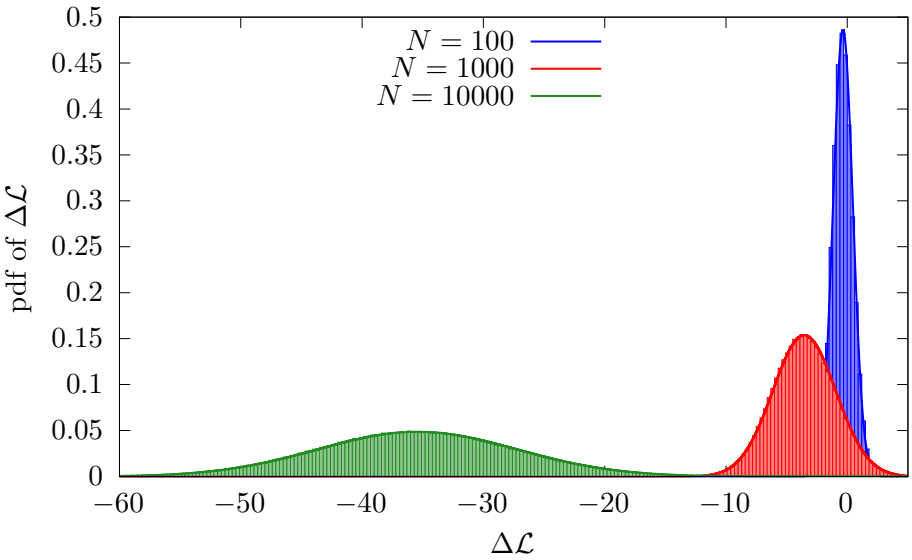

Figure 4.4: Histogram for $B = 10^6$ datasets of different sample size N. For this plot, the amplitudes are computed at $M = M_\phi$ and for $J^{PC} = 1^{--}$. Additionally, we plot Gaussians with the mean and standard deviation from Eq. (4.37).

where

$$\begin{aligned}
\tilde{d}_{\mathrm{KL}}(s,t) &= f^{\mathrm{KT}}(s,t)\ln\left(\frac{f^{\mathrm{KT}}(s,t)}{f^{\text{Omnès}}(s,t)}\right), \\
d_{\mathrm{KL}} &= \int_D \tilde{d}_{\mathrm{KL}}(s,t)\mathrm{d}s\mathrm{d}t\,, \\
\tilde{\nu}_{\mathrm{KL}}(s,t) &= f^{\mathrm{KT}}(s,t)\ln\left(\frac{f^{\mathrm{KT}}(s,t)}{f^{\text{Omnès}}(s,t)}\right)^2, \\
\nu_{\mathrm{KL}} &= \int_D \tilde{\nu}_{\mathrm{KL}}(s,t)\mathrm{d}s\mathrm{d}t - d_{\mathrm{KL}}^2\,.
\end{aligned} \tag{4.36}$$

The expressions are known as the Kullback–Leibler divergence [147] and variance. The cumulative distribution function reads

$$\begin{aligned}
\mathcal{N}(x,\mu(N),\sigma(N)) &= \frac{1}{2}\left(1+\mathrm{erf}\left(\frac{x-\mu(N)}{\sqrt{2}\sigma(N)}\right)\right) \\
\text{with}\quad \mu(N) &= -N d_{\mathrm{KL}}\,, \quad \sigma(N) = \sqrt{N\nu_{\mathrm{KL}}}\,,
\end{aligned} \tag{4.37}$$

where erf is the error function. To validate the assumption of a normal distribution, we use the comparison in Fig. 4.4, which indicates a very good description.[2] From here on we can calculate our results using the pdfs as defined in Eq. (4.29).

In the region $\Delta\mathcal{L} < 0$ we reject the hypothesis that the Omnès solutions are sufficient to describe the data. The probability that the hypothesis is not rejected then reads

$$q(N) = 1 - \mathcal{N}(0,\mu(N),\sigma(N))\,. \tag{4.38}$$

[2]Note that this is not an assumption for large N due to the central-limit theorem.

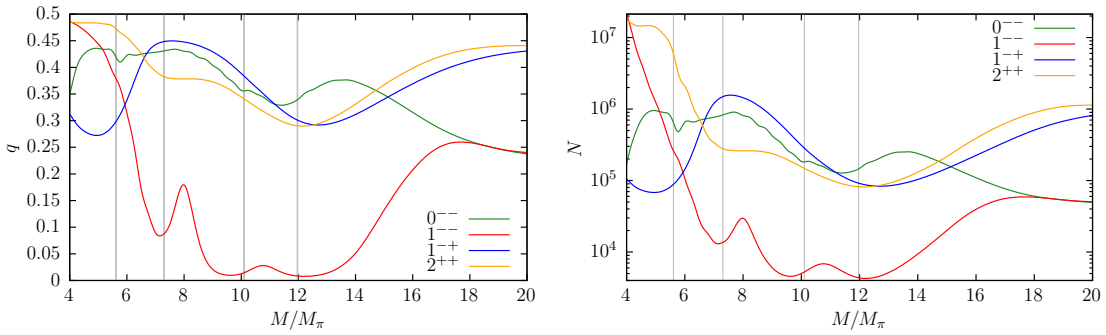

Figure 4.5: *Left panel:* Probability of the Omnès model not being rejected as a function of the mass of the decaying particle, for all four reconstruction theorems and $N = 1000$. *Right panel:* Statistics needed to set the probability that the Omnès model is not rejected to 5σ (right). The gray vertical lines, from left to right correspond to the masses of the ω, ϕ, $\omega(1420)$, and $\omega(1650)$ resonances.

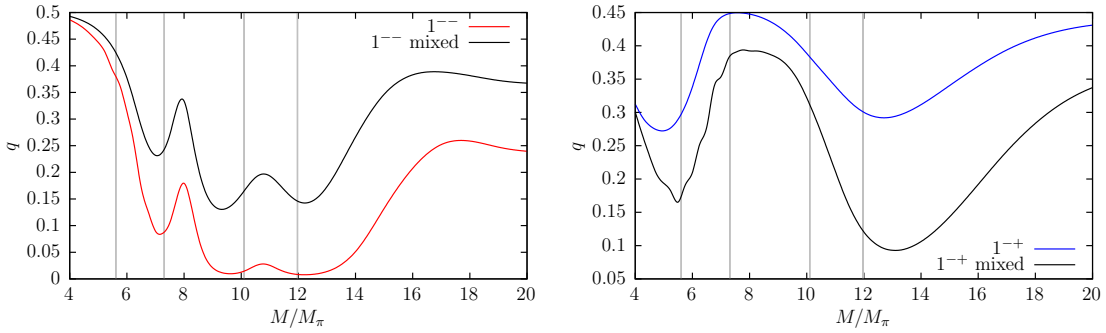

Figure 4.6: *Left panel:* Comparison for the 1^{--} reconstruction theorem with normal SVAs and 1^{-+} SVAs ("mixed"). *Right panel:* Comparison for 1^{-+} reconstruction theorem with normal SVAs and 1^{--} SVAs ("mixed"). We show the probability of the Omnès model not being rejected as a function of the mass of the decaying particle. Vertical gray lines as in Fig. 4.5.

The inversion of the equation gives the number of events with the confidence determined by q via

$$N(q) = 2\nu_{\mathrm{KL}} \left(\frac{\mathrm{erf}^{-1}(1-2q)}{d_{\mathrm{KL}}} \right)^2 . \tag{4.39}$$

For a 5σ confidence level we need to have $q = 2.87 \cdot 10^{-7}$ [22] and can now compute the resulting N.

4.4 Results

Among the three-pion decays studied in this chapter, only two Dalitz plots have been studied experimentally with sufficiently high statistics: $\omega \to 3\pi$ [128, 129], and $\phi \to 3\pi$ [130, 131].

For $\omega \to 3\pi$, WASA-at-COSY [128] has performed a Dalitz plot study with 44 080

events, while the analysis by BESIII [129] is based on 260 520 events. Both experiments parameterize the distribution by a polynomial expansion and present results testing one- and two-parameter models. Applying the formalism of the preceding section, we find that the statistics of WASA-at-COSY is sensitive to rescattering effects only at 2.1σ. On the other hand, in agreement with Ref. [113], BESIII reaches a 5σ level for the solution containing one subtraction. However, as pointed out by Ref. [113], an additional subtraction leads to a better agreement for the Dalitz plot parameters.

For $\phi \to 3\pi$, KLOE [130] provides a Dalitz plot analysis using $2 \cdot 10^6$ events, while CMD-2 [131] has studied almost $8 \cdot 10^4$ decays. For both, rescattering effects are clearly observable, as concluded by Ref. [81].

Using the statistical method explained above and the derived reconstruction theorems, we compute $q(N)$ and $N(q)$ for a large mass range as shown in Fig. 4.5. The mass dependence of N and q for the 1^{--} decay looks strikingly different from the 1^{-+} one, even though they share the same kinematic factor. To investigate the source of this difference in sensitivity between the two reconstruction theorems, we perform the following, unphysical, test. We plug the SVAs, calculated as KT solutions for the 1^{-+} decay, into the linear combination given by the reconstruction theorem for 1^{--}, see Eq. (4.5), and vice versa. These unphysical amplitudes are denoted by "mixed" in Fig. 4.6. We observe that this changes the absolute values of $q(N)$, while the qualitative behavior is the same. We therefore conclude that much of the sensitivity to rescattering effects is not actually due to the size of the lineshape modification of the SVAs, as shown in Fig. 4.3, but rather due to the specific linear combination in which they form the full decay amplitude.

In a log-plot for N (for fixed q) as a function of the decay mass, we find a similar form as for q (with fixed N); cf. left and right panels of Fig. 4.5. For large decay masses, the necessary number of events rises for all processes.[3] This is due to the fact that the KT solutions converge to the Omnès function in the infinite-mass limit. However, in the high-mass region, $M \gtrsim 15 M_\pi$, our approximations are no longer valid: inelastic effects and higher partial waves play a non-negligible role. For low decay masses, approaching the three-pion threshold, the necessary event numbers for the 1^{--}, 1^{-+}, and 2^{++} decays rise due to limited phase space and kinematic suppression of the Dalitz-plot borders, far away from the ρ resonance. For 0^{--} this is different, since here the amplitude does not vanish at the edge of the Dalitz plot.

The mass scan manifests several prominent features in the significance plot. For 1^{-+} decays, N starts at 10^5 events around the ω mass and then rises steeply to approximately $2 \cdot 10^6$ events at the ϕ mass. At higher masses, it falls off up to about $12 M_\pi$. The very high number of necessary events is mainly due to the fact that crossing symmetry requires a zero in the Dalitz plot along the line $t = u$, and hence any differences due to rescattering have to appear at the edge of the Dalitz plot, where the phase space is suppressed by the Kibble function. The Dalitz plots for decays of a particle with 1^{-+} quantum numbers are shown in Fig. 4.7 for different masses. Here, the difference decreases until the ρ bands are inside the Dalitz plot, and then falls off again when the size increases further.

For the 1^{--} decays, we find a different behavior. The event number N starts at high values for the ω resonance and then shows an overall decline with rising decay mass, with two small peaks between the ϕ and $\omega(1650)$. At the ϕ resonance mass, the ρ bands are completely inside the Dalitz plot. The Dalitz plots for different decay masses are shown in

[3] Note that this effect is not fully visualized by the mass range displayed in Fig. 4.5.

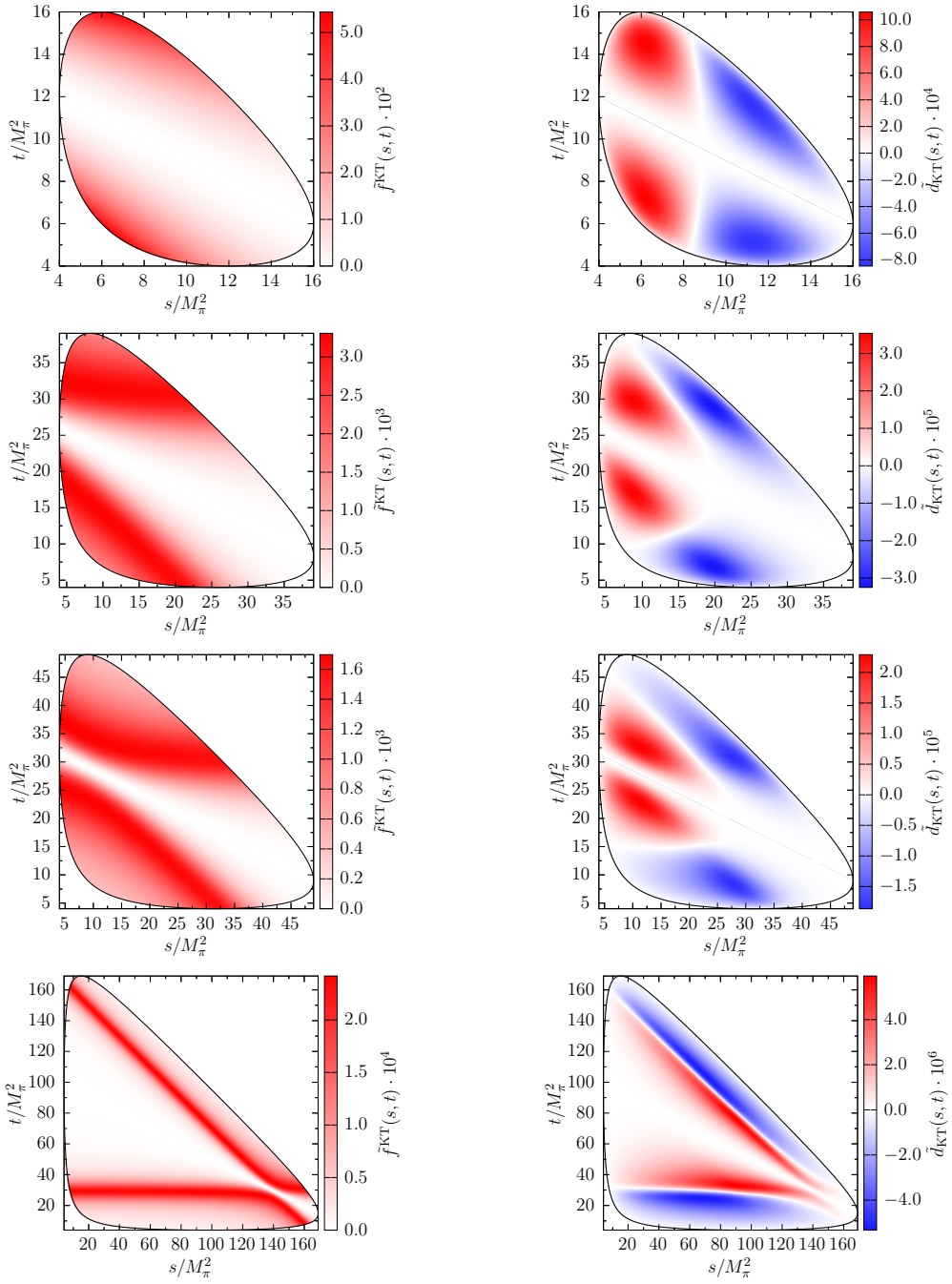

Figure 4.7: Dalitz plots for the $J^{PC} = 1^{-+}$ reconstruction theorem. From top to bottom the decay mass grows according to $M = 5/7.25/8/14\, M_\pi$, while the Dalitz plot without phase space $\tilde{f}(s,t)$ defined via Eq. (4.30) is shown in the left and $\tilde{d}_{\mathrm{KL}}(s,t)$ (Eq. (4.36)) in the right column.

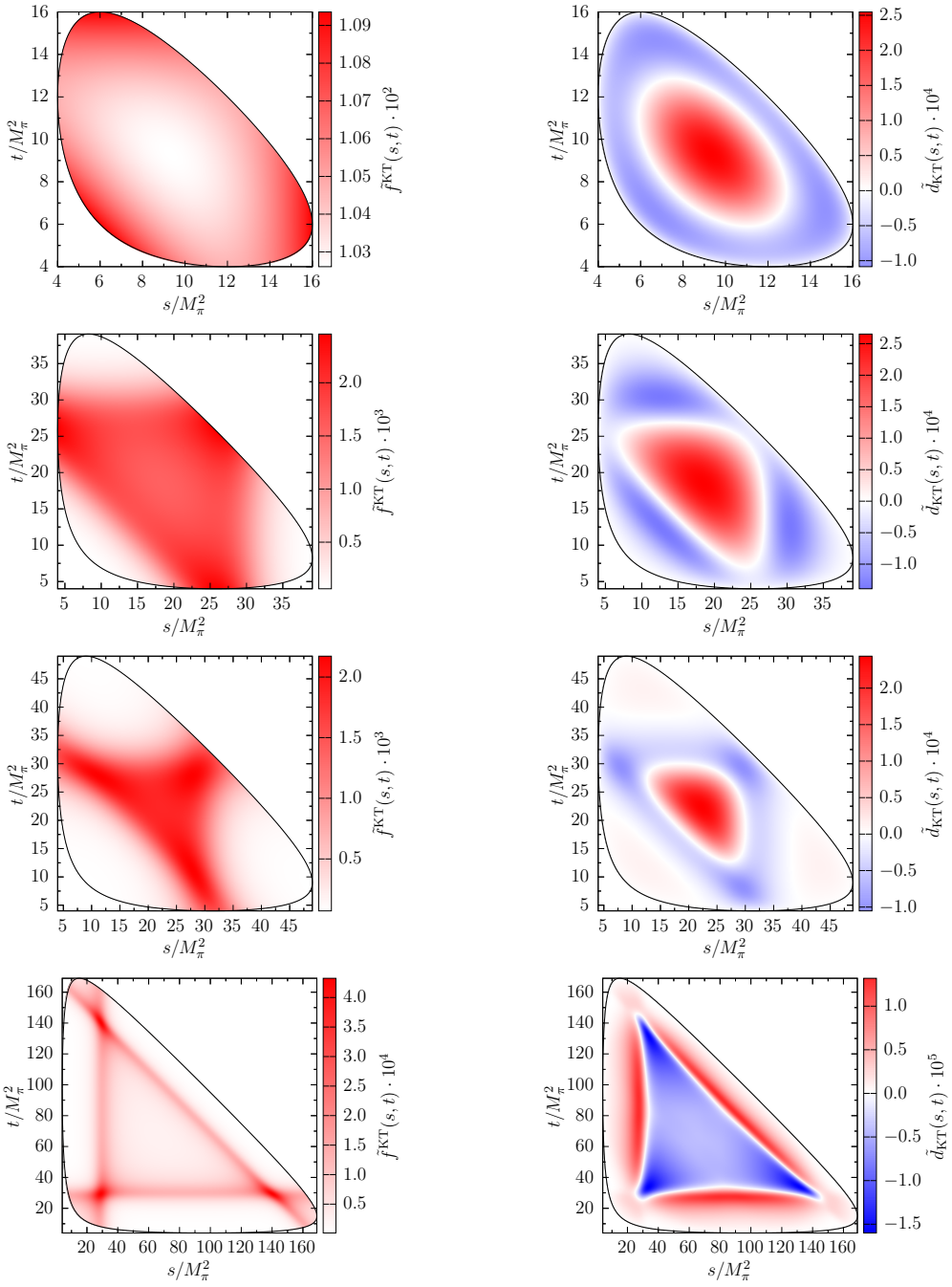

Figure 4.8: Dalitz plots for the $J^{PC} = 1^{--}$ reconstruction theorem. From top to bottom the decay mass grows according to $M = 5/7.25/8/14\, M_\pi$, while the Dalitz plot without phase space $\tilde{f}(s,t)$ defined via Eq. (4.30) is shown in the left and $\tilde{d}_{\mathrm{KL}}(s,t)$ (Eq. (4.36)) in the right column.

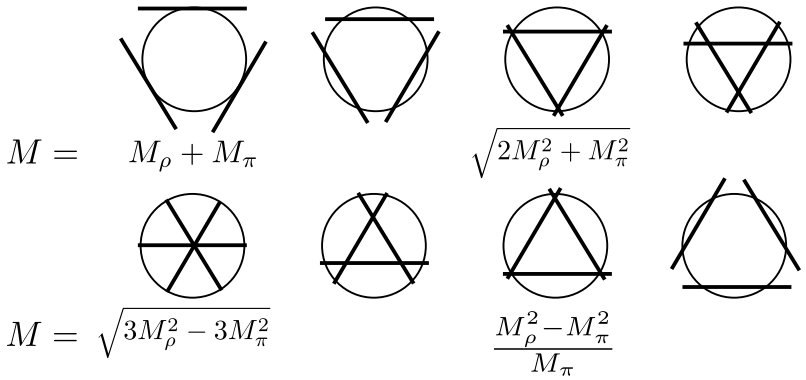

Figure 4.9: Sketches of different kinematic configurations for the 1^{--} decay with increasing decay mass. The straight lines denote the (qualitative) position of the three ρ bands in the Dalitz plot. The masses below the diagrams denote the decay masses for which the specific kinematic configurations are reached.

Fig. 4.8. The first peak occurs due to the third kinematic configuration of the Dalitz plot as shown in Fig. 4.9. The difference increases again when the three ρ bands cross in the middle of the Dalitz plot. The second peak is also due to a peculiar structure in the Dalitz plot: in this decay mass region we find a ring-shaped local minimum, clearly visible for an unphysically narrow ρ width; see Appendix 4.D. The ring affects the sensitivity even for the physical ρ width, and is responsible for the second peak.

In order to disentangle the origin of the various maxima and minima in the sensitivity of the 1^{--} decays in dependence on the decay mass a little better, we separate, somewhat unphysically, two different effects in Fig. 4.10: the size of the Dalitz plot, and modifications of the SVAs. We once keep the SVA basis function fixed as calculated for decay mass $M = 7.5M_\pi$ and only vary the size of the Dalitz plot; and secondly, we vice versa keep the Dalitz plot fixed at $M = 7.5M_\pi$, and only vary the SVA with its implicit decay-mass dependence. The precise plot depends heavily on the choice for the fixed mass, but we observe both peaks when using a SVA for a fixed mass and only varying the size of the Dalitz plot. Fixing the size of the Dalitz plot and only varying the SVAs, on the other hand, results in a rather smooth decrease of the difference towards higher masses. We therefore conclude that the peaks in the 1^{--} mass dependence are dominated by the structure of the Dalitz plot and not by the difference in the SVAs.

The main takeaway however is that with less than 10^5 events above the ϕ mass, rescattering effects will play an important role in analyses of Dalitz plot data. For the ω resonance and lower masses of the decaying particle, one requires more than 10^6 events to observe them.

For 0^{--} decays, we find some small numerical fluctuations in the low-mass region, which are due to the multiple regions where the total decay amplitude is kinematically suppressed in the Dalitz plots, shown in Fig. 4.11: it vanishes along the three lines of $s = t$, $s = u$, and $t = u$. The number of events slightly rises up to approximately $N = 10^6$ at the mass of the ω and stays constant up to $9M_\pi$. At higher masses, a slow decline sets in, including a small peak around $14M_\pi$. Due to the structure of the reconstruction theorem, the differences are located near the Dalitz plot boundaries. The six regions of intensity are then split into regions with larger pdfs for the KT equations and the Omnès solutions,

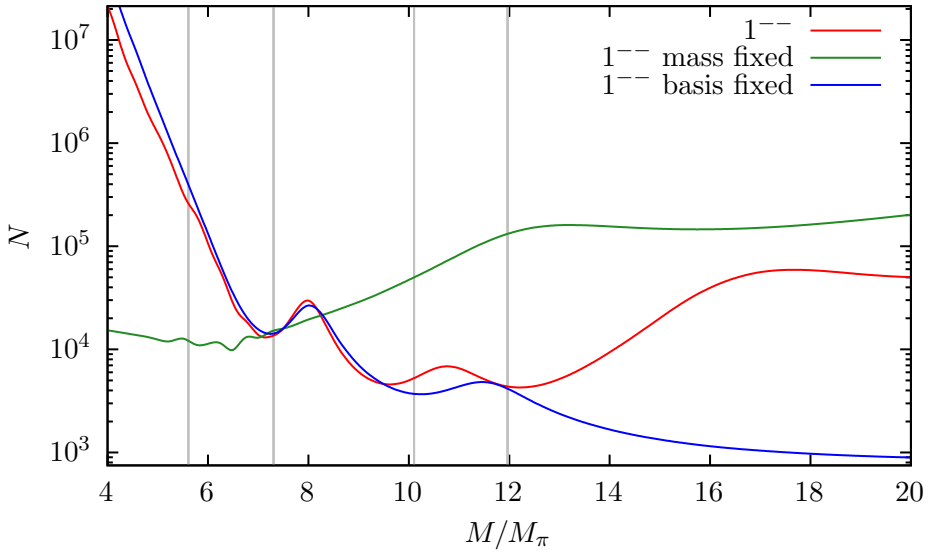

Figure 4.10: Minimal number of events N to exclude the Omnès model at 5σ significance for $J^{PC} = 1^{--}$, as a function of the decay mass decomposed into two different effects. The red line corresponds to the full solution from the right panel in Fig. 4.5. For the green line ("mass fixed"), we fix the size of the Dalitz plot to $M = 7.5M_\pi$ and only use the SVA varying with the running mass. For the blue line ("basis fixed"), we use the same SVA solution for $M = 7.5M_\pi$ for all masses and vary the size of the Dalitz plot. Vertical gray lines as in Fig. 4.5.

respectively.

For 2^{++} decays, the low-mass behavior looks similar to the 1^{--} decays. The difference, however, is that we find a small plateau up to the ω mass, such that the number of events is increased by orders of magnitude. Furthermore, the decline stops at the ϕ mass above 10^5 events, such that the behavior at larger masses is more similar to the other quantum numbers. The Dalitz plots in Fig. 4.12 suggest that we do not have any visible features of the ρ bands for the small decay masses. For larger masses we observe the two expected bands in t- and u-channel with one crossing point inside the Dalitz plot. Similar to the 1^{--} decays the Dalitz plot is split into two regions, where the pdfs for the KT equations and the Omnès functions are of different size. These regions vary in shape for the different decay masses.

Finally, to test the dependence of our findings on the ρ-resonance width, we repeat the above exercises using a phase shift extracted from a simple Breit–Wigner model with an energy-dependent width [148], whose nominal width we fix to the smaller value $\Gamma_\rho = 30\,\text{MeV}$. We find that the number of events required to distinguish rescattering effects is significantly increased by about two orders of magnitude. This confirms the expected trend that rescattering effects vanish in the limit of small widths. A short analytic derivation of this limit is presented in Appendix 4.E.

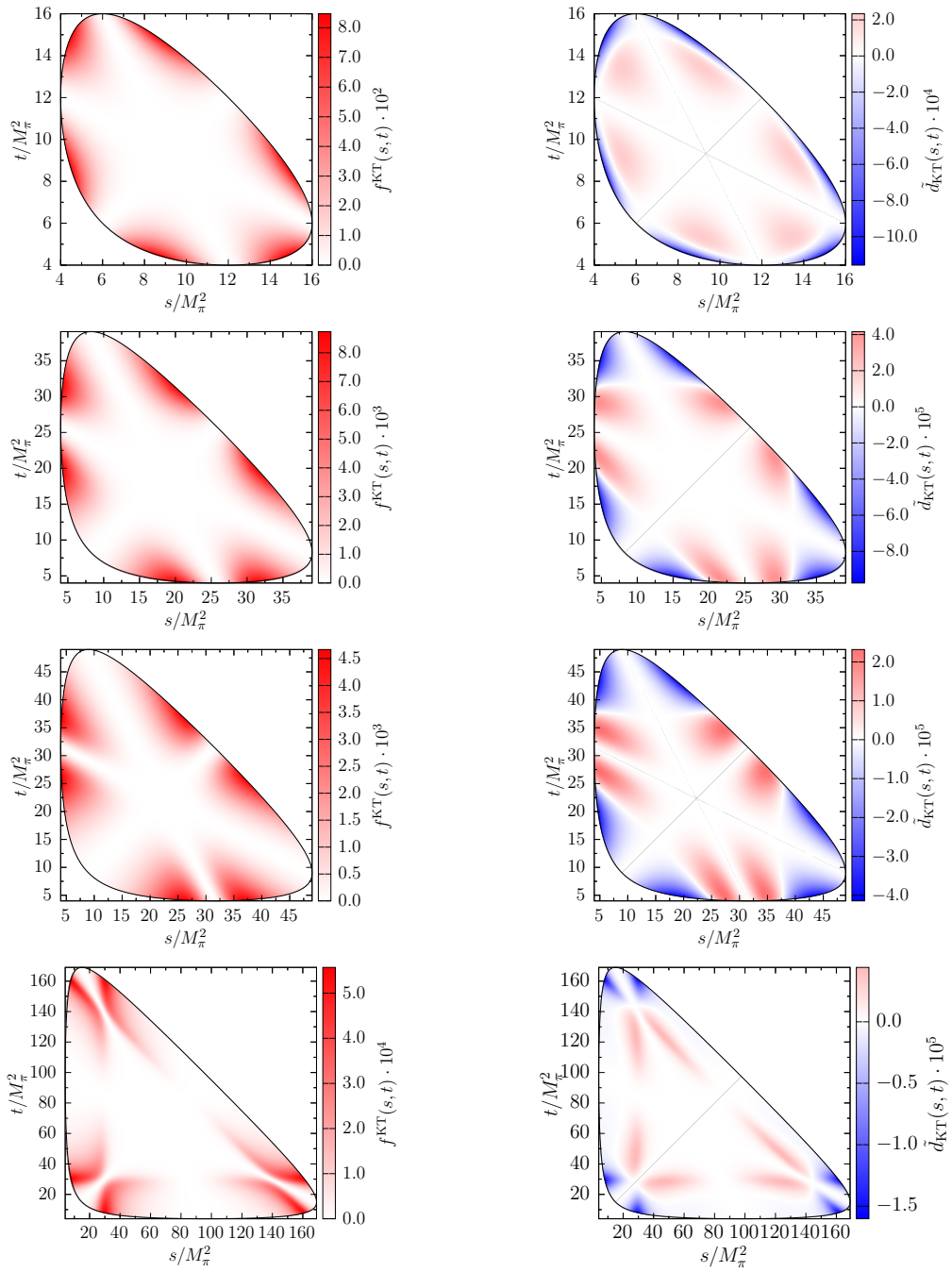

Figure 4.11: Dalitz plots for the $J^{PC} = 0^{--}$ reconstruction theorem. From top to bottom the decay mass grows according to $M = 5/7.25/8/14\, M_\pi$, while the Dalitz plot $f(s,t)$ defined via Eq. (4.29) is shown in the left and $\tilde{d}_{\mathrm{KL}}(s,t)$ (Eq. (4.36)) in the right column.

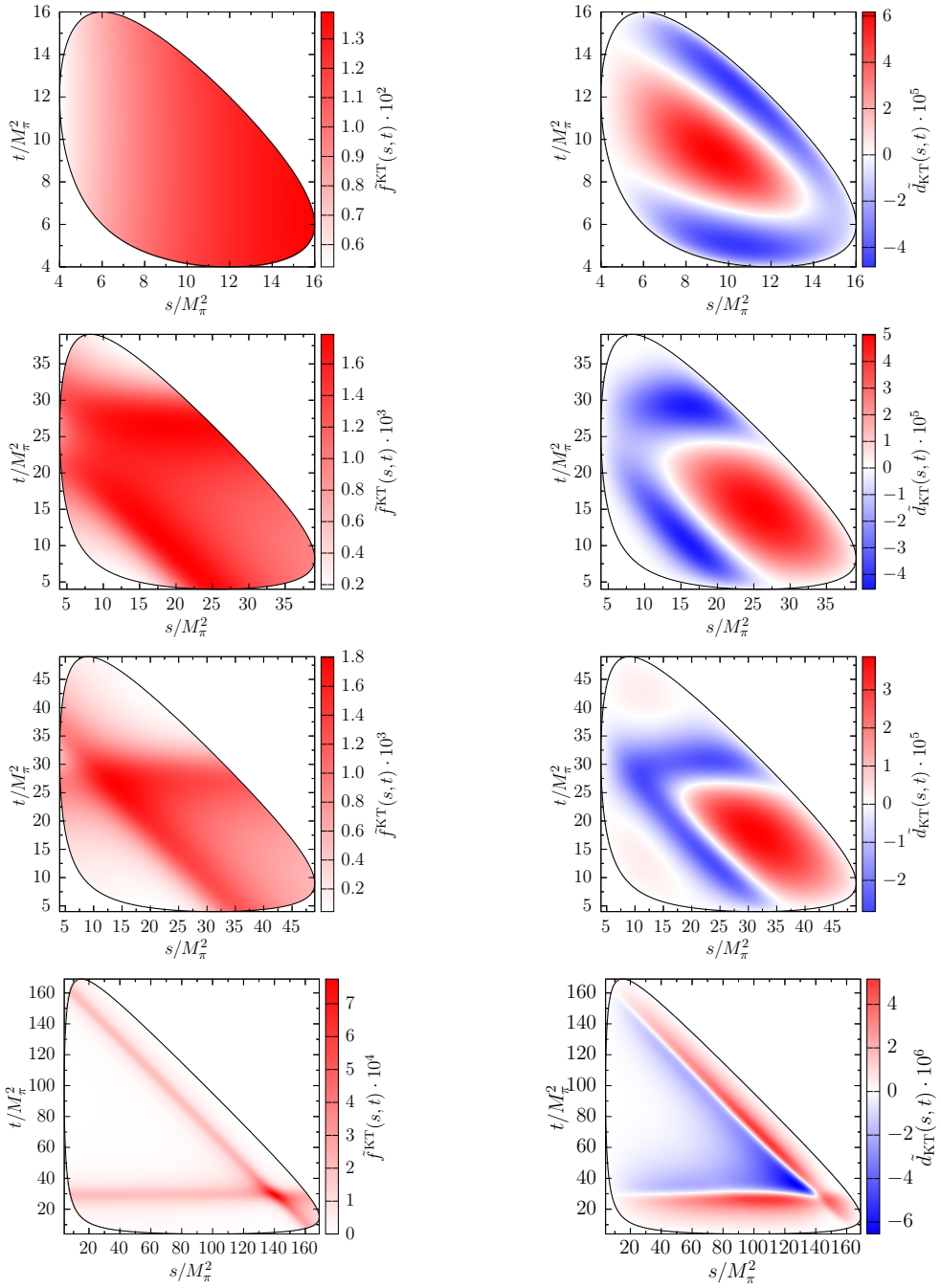

Figure 4.12: Dalitz plots for the $J^{PC} = 2^{++}$ reconstruction theorem. From top to bottom the decay mass grows according to $M = 5/7.25/8/14\, M_\pi$, while the Dalitz plot without the $\mathcal{K}(s,t,u)$ factor, $\tilde{f}(s,t)$, defined via Eq. (4.29) is shown in the left and $\tilde{d}_{\mathrm{KL}}(s,t)$ (Eq. (4.36)) in the right column.

4.5 Conclusion

In this chapter, we have investigated the feasibility of unambiguously identifying the crossed-channel rescattering effects beyond the simplest isobar model in three-pion decays dominated by $\rho\pi$ intermediate states. For four different quantum numbers of the decaying particles we have solved the Khuri–Treiman equations, integral equations that sum iterated two-pion rescattering in each pion pair to all orders. We have determined the minimal sample sizes for which Dalitz-plot distributions allow us to distinguish the KT solutions from the naive picture that ignores all effects beyond two-body resonances. The dependence on the mass of the decaying resonance has been studied in detail throughout.

The significance of the rescattering effects in 3π final states is heavily dependant on the decay kinematics. In particular, the appearance and position of the ρ bands in the Dalitz plots plays a major role. For $J^{PC} = 1^{--}$ we found a strong dependence on the mass of the decaying particle: rescattering effects are small for the ω resonance, where at least a few times 10^5 events in a Dalitz plot are necessary to identify them at 5σ significance, while they are easily observable for the ϕ resonance, with of the order of 10^4 Dalitz plot events sufficient; a similar sensitivity is expected for decaying isoscalar vector resonances up to almost 2 GeV. However, the predictive power for large masses, e.g., the three-pion decays of the vector charmonia J/ψ or ψ' [149], is clearly limited due to inelastic effects and higher partial waves.

In general, the processes with zeros in the amplitude due to crossing symmetry need more statistics to resolve rescattering effects. This is the case for the isovector 3π system with quantum numbers 1^{-+} and 2^{++},[4] as well as isoscalar 0^{--} states, where for a wide mass range up to 2 GeV, we predict necessary statistics between 10^5 and 10^6 events to identify non-trivial rescattering effects at 5σ significance.

Throughout, our investigation should be understood as a pilot study towards the thorough implementation of Dalitz plot fits beyond the simplest isobar models. Theoretical limitations at this point clearly concern the constraint to Khuri–Treiman systems with one single free parameter: it is by no means guaranteed that the neglect of additional subtraction constants, which inter alia allow us to absorb effects of inelastic intermediate states, is justified in all circumstances. Furthermore, decays with several relevant partial waves, in particular isoscalar $\pi\pi$ S-waves with their strong coupling to $K\bar{K}$ above 1 GeV, pose additional difficulties to pin down corrections to two-pion lineshapes unambiguously; these are known to play an important role in the interpretation of resonance signals in the a_1 spectrum [150–152]. The systematic study of such more complicated KT systems remains a both formidable and highly rewarding challenge for future research.

4.A 1^{-+} reconstruction theorem

This appendix is dedicated to the derivation of the 1^{-+} reconstruction theorem using fixed-t dispersion relations. We start by considering the decay process

$$X^i(p) \to \pi^j(p_1)\pi^k(p_2)\pi^l(p_3)\,, \tag{4.40}$$

[4] The 2^{++} system only has a zero in one of the two scalar functions.

where the T-matrix element is given by

$$\left\langle \pi^j(p_1)\pi^k(p_2)\pi^l(p_3)\right| T \left|X^i(p)\right\rangle = (2\pi)^4\delta^{(4)}(p-p_1-p_2-p_3)\mathcal{M}^{ijkl}(s,t,u)\,, \tag{4.41}$$

and the Mandelstam variables are defined as

$$\begin{aligned} s &= (p-p_1)^2 = (p_2+p_3)^2\,,\\ t &= (p-p_2)^2 = (p_1+p_3)^2\,,\\ u &= (p-p_3)^2 = (p_1+p_2)^2\,. \end{aligned} \tag{4.42}$$

The decomposition into the scalar amplitude and the kinematic prefactor due to the odd intrinsic parity can be found in Eq. (4.8). The isospin structure is identical to $\pi\pi$ scattering and the scalar amplitude therefore obeys the same decomposition

$$\mathcal{H}^{ijkl}(s,t,u) = \delta^{ij}\delta^{kl}\mathcal{H}_s(s,t,u) + \delta^{ik}\delta^{jl}\mathcal{H}_t(s,t,u) + \delta^{il}\delta^{jk}\mathcal{H}_u(s,t,u)\,. \tag{4.43}$$

Due to the symmetry of the process, the amplitude needs to stay invariant under simultaneous exchanges of isospin indices and momenta

$$\begin{aligned} &k \leftrightarrow l\,, && p_2 \leftrightarrow p_3\,, && t \leftrightarrow u\,;\\ &j \leftrightarrow l\,, && p_1 \leftrightarrow p_3\,, && s \leftrightarrow u\,;\\ &j \leftrightarrow k\,, && p_1 \leftrightarrow p_2\,, && s \leftrightarrow t\,, \end{aligned} \tag{4.44}$$

which relates $\mathcal{H}_s$, $\mathcal{H}_t$, and $\mathcal{H}_u$ and leads to

$$\mathcal{H}^{ijkl}(s,t,u) = \delta^{ij}\delta^{kl}\mathcal{H}(s,t,u) + \delta^{ik}\delta^{jl}\mathcal{H}(t,u,s) + \delta^{il}\delta^{jk}\mathcal{H}(u,s,t)\,, \tag{4.45}$$

where $\mathcal{H}$ is antisymmetric in its last two arguments. The isospin-projection operators are defined as

$$\begin{aligned} \mathcal{P}_0^{ijkl} &= \frac{1}{3}\delta^{ij}\delta^{kl}\,,\\ \mathcal{P}_1^{ijkl} &= \frac{1}{2}\left(\delta^{ik}\delta^{jl} - \delta^{il}\delta^{jk}\right)\,,\\ \mathcal{P}_2^{ijkl} &= \frac{1}{2}\left(\delta^{ik}\delta^{jk} + \delta^{il}\delta^{jk}\right) - \frac{1}{3}\delta^{ij}\delta^{kl}\,, \end{aligned} \tag{4.46}$$

which allow us to rewrite the isospin decomposition of the scalar amplitude according to

$$\mathcal{H}^{ijkl}(s,t,u) = \mathcal{P}_0^{ijkl}\mathcal{H}^0(s,t,u) + \mathcal{P}_1^{ijkl}\mathcal{H}^1(s,t,u) + \mathcal{P}_2^{ijkl}\mathcal{H}^2(s,t,u)\,, \tag{4.47}$$

resulting in

$$\begin{aligned} \mathcal{H}(s,t,u) &= \frac{1}{3}\left(\mathcal{H}^0(s,t,u) - \mathcal{H}^2(s,t,u)\right)\,,\\ \mathcal{H}(t,u,s) &= \frac{1}{2}\left(\mathcal{H}^1(s,t,u) + \mathcal{H}^2(s,t,u)\right)\,,\\ \mathcal{H}(u,s,t) &= \frac{1}{2}\left(\mathcal{H}^2(s,t,u) - \mathcal{H}^1(s,t,u)\right)\,. \end{aligned} \tag{4.48}$$

The partial-wave expansion of the isospin amplitudes proceeds via [145]

$$\mathcal{H}^I(s,z_s) = \sum_{\ell=1} P'_\ell(z_s) a^I_\ell(s)\,. \tag{4.49}$$

A fixed-t dispersion relation for $\mathcal{H}(s,t,u)$ yields

$$\begin{aligned}\mathcal{H}(s,t,u) = P^t_{n-1}(s,u) &+ \frac{s^n}{2\pi i}\int_{4M_\pi^2}^\infty \mathrm{d}s' \frac{\mathrm{disc}_{s'}\mathcal{H}(s',t,u(s'))}{s'^n(s'-s)} \\ &+ \frac{u^n}{2\pi i}\int_{4M_\pi^2}^\infty \mathrm{d}u' \frac{\mathrm{disc}_{u'}\mathcal{H}(s(u'),t,u')}{u'^n(u'-u)}\,,\end{aligned} \tag{4.50}$$

where n determines the number of subtractions and $P^t_{n-1}(s,u)$ is a polynomial in s and u of order $n-1$ with fixed t. We can insert the discontinuities according to

$$\begin{aligned}\mathrm{disc}_{s'}\,\mathcal{H}(s',t,u(s')) &= 0\,,\\ \mathrm{disc}_{u'}\,\mathcal{H}(s(u'),t,u') &= \frac{1}{2}\mathrm{disc}\,a^1_1(u')\,,\end{aligned} \tag{4.51}$$

neglecting all discontinuities in partial waves with $\ell \geq 2$. If we employ fixed-s and fixed-u dispersion relations in strict analogy to the above, we find that each fixed-variable dispersion relation misses the integral along the cut of the fixed Mandelstam variable. This missing integral can be subtracted from the polynomial if the number of subtraction constants is sufficiently high. This procedure is commonly referred to as symmetrizing the fixed-variable dispersion relations; details on general properties can be found in Ref. [87]. The result is given as

$$\mathcal{H}(s,t,u) = P_{n-1}(s,t,u) - \frac{t^n}{4\pi i}\int_{4M_\pi^2}^\infty \mathrm{d}t' \frac{\mathrm{disc}\,a^1_1(t')}{t'^n(t'-t)} + \frac{u^n}{4\pi i}\int_{4M_\pi^2}^\infty \mathrm{d}u' \frac{\mathrm{disc}\,a^1_1(u')}{u'^n(u'-u)}\,, \tag{4.52}$$

which can be simplified to

$$\mathcal{H}(s,t,u) = \mathcal{H}(t) - \mathcal{H}(u)\,, \tag{4.53}$$

where

$$\mathcal{H}(s) = P_{n-1}(s) - \frac{s^n}{4\pi i}\int_{4M_\pi^2}^\infty \mathrm{d}s' \frac{\mathrm{disc}\,a^1_1(s')}{s'^n(s'-s)}\,. \tag{4.54}$$

The ambiguity of this decomposition is discussed in Sec. 4.2.2. Note that in order to consistently define the SVAs from the symmetrized version of $\mathcal{H}(s,t,u)$, $n \leq 2$. The same holds true in the cases of 1^{--} and 2^{++} (neglecting angular momenta beyond P-waves). For the 0^{--} decays, $n \leq 3$ subtractions can be implemented.

4.B 2^{++} reconstruction theorem

In this appendix, we derive the reconstruction theorem for $J^{PC} = 2^{++}$, applying the approximations needed for our analysis. We start with the decay process

$$T^i(p) \to \pi^j(p_1)\pi^k(p_2)\pi^l(p_3)\,, \tag{4.55}$$

where the Mandelstam variables are defined in Eq. (4.42). We can write down the amplitude in terms of two scalar amplitudes $\mathcal{B}$ and $\mathcal{C}$ [153],

$$\begin{aligned}
\mathcal{M}^{ijkl}(s,t,u) &= \delta^{ij}\delta^{kl}\mathcal{M}_s(s,t,u) + \delta^{ik}\delta^{jl}\mathcal{M}_t(s,t,u) + \delta^{il}\delta^{jk}\mathcal{M}_u(s,t,u)\,, \\
\mathcal{M}_s(s,t,u) &= i\sqrt{2}\epsilon_{\mu\nu}K^\mu\left[(p_2+p_3)^\nu\mathcal{B}_s(s,t,u) + (p_2-p_3)^\nu\mathcal{C}_s(s,t,u)\right]\,, \\
\mathcal{M}_t(s,t,u) &= i\sqrt{2}\epsilon_{\mu\nu}K^\mu\left[(p_1+p_3)^\nu\mathcal{B}_t(s,t,u) + (p_1-p_3)^\nu\mathcal{C}_t(s,t,u)\right]\,, \\
\mathcal{M}_u(s,t,u) &= i\sqrt{2}\epsilon_{\mu\nu}K^\mu\left[(p_2+p_1)^\nu\mathcal{B}_u(s,t,u) + (p_2-p_1)^\nu\mathcal{C}_u(s,t,u)\right]\,,
\end{aligned} \tag{4.56}$$

with the isospin indices i, j, k, and l. The amplitude needs to be invariant under the symmetry transformations in Eq. (4.44), which gives us the following relations between the different $\mathcal{B}$ and $\mathcal{C}$ functions:

$$\begin{aligned}
\mathcal{B}_t(s,t,u) &= -\mathcal{B}_s(t,s,u)\,, & \mathcal{C}_t(s,t,u) &= -\mathcal{C}_s(t,s,u)\,, \\
\mathcal{B}_u(s,t,u) &= -\mathcal{B}_s(u,t,s)\,, & \mathcal{C}_u(s,t,u) &= -\mathcal{C}_s(u,t,s)\,.
\end{aligned} \tag{4.57}$$

We find that $\mathcal{B}_s$ is antisymmetric in the last two arguments, while $\mathcal{C}_s$ is symmetric. This helps us to rewrite the amplitude in terms of $\mathcal{B}_s$ and $\mathcal{C}_s$, and we drop the subscript s in the following. The isospin-projection operators are defined in Eq. (4.46). The corresponding isospin amplitude can be decomposed in analogy to Eq. (4.56) using

$$\begin{aligned}
\mathcal{M}^{ijkl}(s,t,u) &= \mathcal{P}_0^{ijkl}\mathcal{M}^0(s,t,u) + \mathcal{P}_1^{ijkl}\mathcal{M}^1(s,t,u) + \mathcal{P}_2^{ijkl}\mathcal{M}^2(s,t,u)\,, \\
\mathcal{M}^I(s,t,u) &= i\sqrt{2}\epsilon_{\mu\nu}K^\mu\left[(p_2+p_3)^\nu\mathcal{B}^I(s,t,u) + (p_2-p_3)^\nu\mathcal{C}^I(s,t,u)\right]\,,
\end{aligned} \tag{4.58}$$

where I denotes the s-channel isospin. This leads to the following relations including the scalar isospin amplitudes:

$$\begin{aligned}
\mathcal{B}(s,t,u) &= \frac{1}{3}\left[\mathcal{B}^0(s,t,u) - \mathcal{B}^2(s,t,u)\right]\,, \\
\mathcal{C}(s,t,u) &= \frac{1}{3}\left[\mathcal{C}^0(s,t,u) - \mathcal{C}^2(s,t,u)\right]\,, \\
\mathcal{B}(t,s,u) &= \frac{1}{4}\left[\mathcal{B}^1(s,t,u) + \mathcal{B}^2(s,t,u) + 3\mathcal{C}^1(s,t,u) + 3\mathcal{C}^2(s,t,u)\right]\,, \\
\mathcal{C}(t,s,u) &= \frac{1}{4}\left[\mathcal{B}^1(s,t,u) + \mathcal{B}^2(s,t,u) - \mathcal{C}^1(s,t,u) - \mathcal{C}^2(s,t,u)\right]\,, \\
\mathcal{B}(u,t,s) &= \frac{1}{4}\left[-\mathcal{B}^1(s,t,u) + \mathcal{B}^2(s,t,u) + 3\mathcal{C}^1(s,t,u) - 3\mathcal{C}^2(s,t,u)\right]\,, \\
\mathcal{C}(u,t,s) &= \frac{1}{4}\left[\mathcal{B}^1(s,t,u) - \mathcal{B}^2(s,t,u) + \mathcal{C}^1(s,t,u) - \mathcal{C}^2(s,t,u)\right]\,.
\end{aligned} \tag{4.59}$$

To find the relation between the scalar functions $\mathcal{B}(s,t,u)$, $\mathcal{C}(s,t,u)$ and partial-wave amplitudes, we evaluate the isospin-projected amplitude in the rest frame of the s-channel, resulting in

$$\begin{aligned}
\mathcal{M}^I_{\lambda=0}(s,t,u) &= 0\,, \\
\mathcal{M}^I_{\lambda=1}(s,t,u) &= \beta(s)\left[\mathcal{B}^I(s,t,u)\sin\theta_s - \xi(s)\mathcal{C}^I(s,t,u)\sin\theta_s\cos\theta_s\right]\,, \\
\mathcal{M}^I_{\lambda=2}(s,t,u) &= \alpha(s)\mathcal{C}^I(s,t,u)\sin^2\theta_s\,,
\end{aligned} \tag{4.60}$$

where the kinematic functions are defined as

$$\alpha(s) = -\frac{\lambda_T^{1/2}(s)\lambda_\pi(s)}{4\sqrt{2}\,s}\,, \qquad \beta(s) = -\frac{\lambda_T(s)\lambda_\pi^{1/2}(s)}{8\sqrt{2s}\,M}\,,$$
$$\xi(s) = \sqrt{1-\frac{4M_\pi^2}{s}}\,\frac{s+M^2-M_\pi^2}{\lambda_T^{1/2}(s)}\,, \tag{4.61}$$

and

$$\lambda_T(s) = \lambda(s, M^2, M_\pi^2)\,, \quad \lambda_\pi(s) = \lambda(s, M_\pi^2, M_\pi^2)\,. \tag{4.62}$$

Parity enforces the helicity-0 amplitude to vanish. We are therefore left with helicity-1 and helicity-2 amplitudes, whose partial-wave expansions start at P- and D-waves, respectively. The $\mathcal{M}_\lambda^I$ contain kinematic singularities, but have well-defined partial-wave expansions for fixed isospin I:

$$\begin{aligned}\mathcal{M}_\lambda^I(s,t,u) &= \sum_{j\geq|\lambda|}(2j+1)a_j^{\lambda I}(s)d_{\lambda 0}^j(z_s)\\ &= \sum_{j\geq|\lambda|}(2j+1)K_{j\lambda}(s,t,u)\hat{a}_j^{\lambda I}(s)\hat{d}_{\lambda 0}^j(z_s)\,,\end{aligned} \tag{4.63}$$

where in particular [51, 153]

$$\begin{aligned}K_{11}(s,t,u) &= \frac{1}{4\sqrt{s}}\sin\theta_s\lambda_\pi^{1/2}(s)\,,\\ K_{21}(s,t,u) &= \frac{1}{4\sqrt{s}}\sin\theta_s\lambda_\pi(s)\lambda_T^{1/2}(s)\,,\\ K_{22}(s,t,u) &= \frac{1}{16s}\sin^2\theta_s\lambda_\pi(s)\lambda_T^{1/2}(s)\,,\end{aligned} \tag{4.64}$$

and the Wigner d-matrices are given by

$$\begin{aligned}d_{\lambda 0}^j(z_s) &= \hat{d}_{\lambda 0}^j(z_s)\sin^{|\lambda|}\theta_s\,, \quad d_{10}^1(z_s) = -\frac{\sin\theta_s}{\sqrt{2}}\,,\\ d_{10}^2(z_s) &= -\frac{3}{\sqrt{6}}\sin\theta_s\cos\theta_s\,, \quad d_{20}^2(z_s) = \frac{3}{2\sqrt{6}}\sin^2\theta_s\,.\end{aligned} \tag{4.65}$$

Here, $\hat{a}_j^{\lambda I}(s)$ are the partial-wave amplitudes, which are however not yet free of kinematic constraints; see below. We use the relation between $\mathcal{M}_1^I$, $\mathcal{C}$, and $\mathcal{B}$ to reduce $\mathcal{B}$ to its leading partial waves. Neglecting all higher ones (denoted by ellipses), we find

$$\begin{aligned}\mathcal{B}^I(s,t,u) &= \frac{1}{\beta(s)\sin\theta_s}\mathcal{M}_1^I(s,t,u) + \xi(s)\cos\theta_s\mathcal{C}^I(s,t,u)\\ &= \frac{6M}{\lambda_T(s)}\hat{a}_1^{1I}(s) + \frac{16}{3\sqrt{3}}\lambda_\pi^{1/2}(s)\lambda_T^{1/2}(s)z_s\hat{a}_2^{1I}(s) + \xi(s)z_s\mathcal{C}^I(s,t,u) + \dots\\ &\equiv \tilde{a}_1^{1I}(s) + \chi(s)z_s\tilde{a}_2^{1I}(s) + \xi(s)z_s\mathcal{C}^I(s,t,u) + \dots\,.\end{aligned} \tag{4.66}$$

Note that a kinematic constraint needs to be enforced on $\hat{a}_1^{1I}$ to cancel the zeros of $\lambda_T(s)$. As a consequence, $\tilde{a}_1^{1I}$ is now a partial wave free of any kinematic singularities and zeros,

and is therefore suitable for a generalized Omnès representation. In strict analogy $\mathcal{C}^I$ can be expressed via

$$\begin{aligned}\mathcal{C}^I(s,t,u) &= \frac{1}{\alpha(s)\sin^2\theta_s}\mathcal{M}_2^I(s,t,u) = -\frac{5\sqrt{3}}{8}\hat{a}_2^{2I}(s)\\ &\equiv -\tilde{a}_2^{2I}(s)\,,\end{aligned} \tag{4.67}$$

employing the partial-wave expansion of $\mathcal{M}_2^I$. Using that the P-waves are pure isospin $I=1$ and D-waves need to be $I=0$ or $I=2$, we can give the relations for the discontinuities of $\mathcal{B}$ and $\mathcal{C}$, e.g.,

$$\begin{aligned}\mathrm{disc}_{s'}\,\mathcal{B}(s',t,u(s')) &= \frac{1}{3}\big(\chi(s')z_{s'}\mathrm{disc}\,\tilde{a}_2^{10}(s') - \xi(s')z_{s'}\mathrm{disc}\,\tilde{a}_2^{20}(s')\\ &\quad - \chi(s')z_{s'}\mathrm{disc}\,\tilde{a}_2^{12}(s') + \xi(s')z_{s'}\mathrm{disc}\,\tilde{a}_2^{22}(s')\big)\,,\\ \mathrm{disc}_{u'}\,\mathcal{B}(s(u'),t,u') &= \frac{1}{4}\big(-\mathrm{disc}\,\tilde{a}_1^{11}(u') + 3\mathrm{disc}\,\tilde{a}_2^{22}(u')\\ &\quad + \chi(u')z_{u'}\mathrm{disc}\,\tilde{a}_2^{12}(u') - \xi(u')z_{u'}\mathrm{disc}\,\tilde{a}_2^{22}(u')\big)\,.\end{aligned} \tag{4.68}$$

Writing down a fixed-t dispersion relation for $\mathcal{B}$

$$\begin{aligned}\mathcal{B}(s,t,u) &= P_{n-1}^t(s,u) + \frac{s^n}{2\pi i}\int_{4M_\pi^2}^\infty \mathrm{d}s'\frac{\mathrm{disc}_{s'}\,\mathcal{B}(s',t,u(s'))}{s'^n(s'-s)}\\ &\quad + \frac{u^n}{2\pi i}\int_{4M_\pi^2}^\infty \mathrm{d}u'\frac{\mathrm{disc}_{u'}\,\mathcal{B}(s(u'),t,u')}{u'^n(u'-u)}\,,\end{aligned} \tag{4.69}$$

and inserting the expansion from Eq. (4.66) into partial waves in fixed-s, -t, and -u dispersion relations and symmetrizing these equations yields

$$\begin{aligned}\mathcal{B}(s,t,u) &= \mathcal{B}_1(t) - \mathcal{B}_1(u) + (u-s)\mathcal{B}_2(t) + (s-t)\mathcal{B}_2(u)\\ &\quad - 3\mathcal{C}_2(t) + 3\mathcal{C}_2(u) + (t-u)\left(\mathcal{B}_0(s) - \frac{4}{3}\mathcal{B}_2(s)\right)\,,\\ \mathcal{C}(s,t,u) &= \mathcal{B}_1(t) + \mathcal{B}_1(u) + (u-s)\mathcal{B}_2(t) - (s-t)\mathcal{B}_2(u)\\ &\quad + \mathcal{C}_2(t) + \mathcal{C}_2(u) - \left(\mathcal{C}_0(s) - \frac{4}{3}\mathcal{C}_2(s)\right)\,,\end{aligned} \tag{4.70}$$

where

$$\begin{aligned}\mathcal{B}_1(s) &= P_{n-1}^{\mathcal{B}_1}(s) + \frac{s^n}{8\pi i}\int_{4M_\pi^2}^\infty \mathrm{d}s'\frac{\mathrm{disc}\,\tilde{a}_1^{11}(s')}{s'^n(s'-s)}\,,\\ \mathcal{B}_0(s) &= P_{n-2}^{\mathcal{B}_0}(s) + \frac{s^{n-1}}{6\pi i}\int_{4M_\pi^2}^\infty \mathrm{d}s'\frac{\chi(s')\mathrm{disc}\,\tilde{a}_2^{10}(s') - \xi(s')\mathrm{disc}\,\tilde{a}_2^{20}(s')}{\kappa(s')s'^{n-1}(s'-s)}\,,\\ \mathcal{B}_2(s) &= P_{n-2}^{\mathcal{B}_2}(s) + \frac{s^{n-1}}{8\pi i}\int_{4M_\pi^2}^\infty \mathrm{d}s'\frac{\chi(s')\mathrm{disc}\,\tilde{a}_2^{12}(s') - \xi(s')\mathrm{disc}\,\tilde{a}_2^{22}(s')}{\kappa(s')s'^{n-1}(s'-s)}\,,\\ \mathcal{C}_0(s) &= P_{n-1}^{\mathcal{C}_0}(s) + \frac{s^n}{6\pi i}\int_{4M_\pi^2}^\infty \mathrm{d}s'\frac{\mathrm{disc}\,\tilde{a}_2^{20}(s')}{s'^n(s'-s)}\,,\\ \mathcal{C}_2(s) &= P_{n-1}^{\mathcal{C}_2}(s) + \frac{s^n}{8\pi i}\int_{4M_\pi^2}^\infty \mathrm{d}s'\frac{\mathrm{disc}\,\tilde{a}_2^{22}(s')}{s'^n(s'-s)}\,.\end{aligned} \tag{4.71}$$

At this point we neglect all SVAs that contain discontinuities for D-waves. Therefore, only $\mathcal{B}_1$ is left, which contains the $I = 1$ P-wave. The inhomogeneity is defined via

$$\mathcal{B}_1(s) + \widehat{\mathcal{B}}_1(s) = \frac{1}{4}\tilde{a}_1^{11}(s)\,. \tag{4.72}$$

We can find the partial wave by projecting Eq. (4.66):

$$\tilde{a}_1^{1I}(s) = \frac{3}{4}\int_{-1}^{1} \mathrm{d}z_s(1-z_s^2)\big(\mathcal{B}^I(s,t,u) - \xi(s)z_s\mathcal{C}^I(s,t,u)\big)\,, \tag{4.73}$$

and therefore

$$\widehat{\mathcal{B}}_1(s) = \frac{3}{4}\left[\langle(1-z_s^2)\mathcal{B}_1\rangle - \xi(s)\langle(1-z_s^2)z_s\mathcal{B}_1\rangle\right]\,, \tag{4.74}$$

by inserting

$$\begin{aligned}
\mathcal{B}^1(s,t,u) &= \frac{1}{2}\big[\mathcal{B}(t,s,u) + 3\mathcal{C}(t,s,u) - \mathcal{B}(u,t,s) + 3\mathcal{C}(u,t,s)\big] \\
&= 4\mathcal{B}_1(s) + \mathcal{B}_1(t) + \mathcal{B}_1(u)\,, \\
\mathcal{C}^1(s,t,u) &= \frac{1}{2}\big[\mathcal{B}(t,s,u) - \mathcal{C}(t,s,u) + \mathcal{B}(u,t,s) + \mathcal{C}(u,t,s)\big] \\
&= \mathcal{B}_1(t) - \mathcal{B}_1(u)\,.
\end{aligned} \tag{4.75}$$

4.C *D*-wave projection

This appendix is an extension of the numerical treatment of Khuri–Treiman equations for S- and P-waves [82, 84, 154] to D-waves. Even though we do not introduce D-wave discontinuities in our analysis, the singularity structure of the inhomogeneity integral in the 2^{++} reconstruction theorem is of this type. The projection integrals from Appendix 4.B can be written in the form

$$\langle z_s^n\mathcal{B}\rangle = \frac{2^n}{\kappa^{n+1}(s)}\int_{s_-(s)}^{s_+(s)} \mathrm{d}s'(s'-\sigma)^n\mathcal{B}(s')\,, \tag{4.76}$$

where

$$\sigma = \frac{1}{2}(3s_0 - s)\,, \qquad z_s = \frac{2}{\kappa(s)}(s'-\sigma)\,, \qquad s_\pm(s) = \frac{1}{2}(3s_0 - s \pm \kappa(s))\,. \tag{4.77}$$

Therefore, the projection integral has a maximal singularity of degree 5/2 at the pseudothreshold $s_{\mathrm{III}} = (M - M_\pi)^2$.[5] The goal is to tame the effect of this singularity. Thereby, we rewrite the integrals into pieces that are analytically solvable and ones that are numerically stable. We start by explicitly rewriting

$$\tilde{\mathcal{B}}(s) = \kappa^5(s)\widehat{\mathcal{B}}(s)\,, \tag{4.78}$$

which leads to the following form of the dispersive integral:

$$I(s) = \int_{s_{\mathrm{th}}}^{\infty}\frac{\mathrm{d}s'}{s'^n}\frac{\sin\delta(s')\tilde{\mathcal{B}}(s')}{\kappa^5(s')|\Omega(s')|(s'-s\mp i\epsilon)}\,. \tag{4.79}$$

[5] Note the additional factor from the ξ function.

The singularities at the scattering thresholds $s_{\text{th}} = 4M_\pi^2$ and $s_{\text{IV}} = (M + M_\pi)^2$ are removable, since the integration path at these values is point-like. Furthermore, we define a function $\nu(s)$ to account for the correct analytic continuation:

$$\nu(s) = \begin{cases} \sqrt{1 - \frac{s_{\text{th}}}{s}}\sqrt{s_{\text{IV}} - s} & \text{for } s < s_{\text{IV}} \\ i\sqrt{1 - \frac{s_{\text{th}}}{s}}\sqrt{s - s_{\text{IV}}} & \text{for } s > s_{\text{IV}} \end{cases} . \tag{4.80}$$

We keep the singularity at the pseudothreshold explicit in the dispersion integral and define a function $T(s)$ containing all other functions,

$$T(s) = \frac{\sin\delta(s)\tilde{\mathcal{B}}(s)}{s^n \nu^5(s)|\Omega(s)|} . \tag{4.81}$$

The dispersion integral is then given by

$$I(s) = \int_{s_{\text{th}}}^{\infty} \mathrm{d}s' \frac{T(s')}{(s_{\text{III}} - s')^{5/2}(s' - s \mp i\epsilon)} . \tag{4.82}$$

Using this form we present the procedure to handle the Cauchy and the pseudothreshold singularities for D-waves. This is achieved by splitting the integrals into analytic parts and numerical integrals with removable singularities. In the following we consider two different regions for s:

1. $s \in \mathbb{R} \wedge s < s_{\text{th}}$ or $s \in \mathbb{C}$

   Here, s cannot hit the Cauchy singularity, since it is outside of the integration range. Therefore, we only need to handle the critical point $s' = s_{\text{III}}$. For this purpose we add and subtract an expansion of T up to the second derivative around the pseudothreshold:

$$\begin{aligned} I(s) = &\int_{s_{\text{th}}}^{\Lambda^2} \mathrm{d}s' \frac{\tilde{T}(s')}{(s_{\text{III}} - s')^{5/2}(s' - s)} + T(s_{\text{III}})\mathcal{Q}_{5/2}(s, s_{\text{th}}, \Lambda^2) \\ &+ T'(s_{\text{III}})\mathcal{Q}_{3/2}(s, s_{\text{th}}, \Lambda^2) + T''(s_{\text{III}})\mathcal{Q}_{1/2}(s, s_{\text{th}}, \Lambda^2) , \\ \tilde{T}(s) = &\, T(s) - T(s_{\text{III}}) - (s_{\text{III}} - s)T'(s_{\text{III}}) - (s_{\text{III}} - s)^2 T''(s_{\text{III}}) . \end{aligned} \tag{4.83}$$

   The procedure to calculate the derivatives is explained at the end of this appendix. Furthermore, we introduce a high-energy cutoff Λ^2. In this form the numerical integral converges and the $\mathcal{Q}$ functions are analytically given by

$$\begin{aligned} \mathcal{Q}_{\frac{2n+1}{2}}(s, x, y) &= \int_x^y \frac{\mathrm{d}s'}{\sqrt{s_{\text{III}} - s'}^{2n+1}(s' - s)} \\ &= \frac{1}{s_{\text{III}} - s}\left(\frac{-2i}{(2n-1)\sqrt{y - s_{\text{III}}}^{2n-1}} - \frac{2}{(2n-1)\sqrt{s_{\text{III}} - x}^{2n-1}} \right. \\ &\qquad \left. + \mathcal{Q}_{\frac{2n-1}{2}}(s, x, y) \right) \quad \forall n \in \mathbb{N}_{>0} , \end{aligned}$$

$$\mathcal{Q}_{\frac{1}{2}}(s,x,y) = \frac{1}{\sqrt{s_{\mathrm{III}}-s}}\left(\log\frac{\sqrt{s_{\mathrm{III}}-s}+\sqrt{s_{\mathrm{III}}-x}}{\sqrt{s_{\mathrm{III}}-s}-\sqrt{s_{\mathrm{III}}-x}} - 2i\arctan\frac{\sqrt{y-s_{\mathrm{III}}}}{\sqrt{s_{\mathrm{III}}-s}}\right). \quad (4.84)$$

This recursive relation is proven by induction.

2. $s \in \mathbb{R} \wedge s > s_{\mathrm{th}}$

Here, we introduce an artificial cutoff $p = (s_{\mathrm{III}}+s)/2$ to separate the two singularities into different integrals. First, we investigate $s < s_{\mathrm{III}}$, where the Cauchy singularity at $s' = s$ is in the integral from s_{th} to p and the pseudothreshold singularity is in the integral from p to Λ^2. We therefore rewrite the integral in the following form:

$$\begin{aligned} I(s) = &\int_{s_{\mathrm{th}}}^{p} \mathrm{d}s' \frac{T(s')-T(s)}{(s_{\mathrm{III}}-s')^{5/2}(s'-s)} + T(s)\mathcal{R}_{5/2}(s,s_{\mathrm{th}},p) \\ &+ \int_{p}^{\Lambda^2} \mathrm{d}s' \frac{\tilde{T}(s')}{(s_{\mathrm{III}}-s')^{5/2}(s'-s)} + T(s_{\mathrm{III}})\mathcal{Q}_{5/2}(s,p,\Lambda^2) \\ &+ T'(s_{\mathrm{III}})\mathcal{Q}_{3/2}(s,p,\Lambda^2) + T''(s_{\mathrm{III}})\mathcal{Q}_{1/2}(s,p,\Lambda^2), \end{aligned} \quad (4.85)$$

where the analytic form of $\mathcal{R}$ is given by

$$\begin{aligned} \mathcal{R}_{\frac{2n+1}{2}}(s,x,y) &= \int_x^y \frac{\mathrm{d}s'}{\sqrt{s_{\mathrm{III}}-s'}^{2n+1}(s'-s\mp i\epsilon)} \\ &= \frac{1}{s_{\mathrm{III}}-s}\left(\frac{2}{(2n-1)\sqrt{s_{\mathrm{III}}-y}^{2n-1}} - \frac{2}{(2n-1)\sqrt{s_{\mathrm{III}}-x}^{2n-1}} \right. \\ &\qquad \left. + \mathcal{R}_{\frac{2n-1}{2}}(s,x,y)\right) \quad \forall n \in \mathbb{N}_{>0}, \end{aligned}$$

$$\begin{aligned} \mathcal{R}_{\frac{1}{2}}(s,x,y) = \frac{1}{\sqrt{s_{\mathrm{III}}-s}}\Bigg(&\log\frac{\sqrt{s_{\mathrm{III}}-x}+\sqrt{s_{\mathrm{III}}-s}}{\sqrt{s_{\mathrm{III}}-x}-\sqrt{s_{\mathrm{III}}-s}} \\ &+ \log\frac{\sqrt{s_{\mathrm{III}}-s}-\sqrt{s_{\mathrm{III}}-y}}{\sqrt{s_{\mathrm{III}}-s}+\sqrt{s_{\mathrm{III}}-y}} \pm i\pi\Bigg). \end{aligned} \quad (4.86)$$

These equations are again proven by induction.

Next we investigate the case $s > s_{\mathrm{III}}$, where the Cauchy singularity at $s' = s$ is in the integral from p to Λ^2 and the pseudothreshold singularity is in the integral from s_{th} to p. Therefore, the integral can be rewritten as

$$\begin{aligned} I(s) = &\int_{p}^{\Lambda^2} \mathrm{d}s' \frac{T(s')-T(s)}{(s_{\mathrm{III}}-s'\mp i\epsilon)^{5/2}(s'-s)} + T(s)\mathcal{R}_{5/2}(s,p,\Lambda^2) \\ &+ \int_{s_{\mathrm{th}}}^{p} \mathrm{d}s' \frac{\tilde{T}(s')}{(s_{\mathrm{III}}-s')^{5/2}(s'-s)} + T(s_{\mathrm{III}})\mathcal{Q}_{5/2}(s,s_{\mathrm{th}},p) \\ &+ T'(s_{\mathrm{III}})\mathcal{Q}_{3/2}(s,s_{\mathrm{th}},p) + T''(s_{\mathrm{III}})\mathcal{Q}_{1/2}(s,s_{\mathrm{th}},p). \end{aligned} \quad (4.87)$$

The remaining integrals can be evaluated numerically. We therefore expand $T(s)$ in a series around the pseudothreshold:

$$\begin{aligned} T(s) &= T(s_{\mathrm{III}}) + (s_{\mathrm{III}} - s)T'(s_{\mathrm{III}}) + (s_{\mathrm{III}} - s)^2 T''(s_{\mathrm{III}}) \\ &\quad + \sqrt{s_{\mathrm{III}} - s}^5 d_D + (s_{\mathrm{III}} - s)^3 e_D + \dots \\ &= a_D + b_D(s_{\mathrm{III}} - s) + c_D(s_{\mathrm{III}} - s)^2 + d_D\sqrt{s_{\mathrm{III}} - s}^5 + e_D(s_{\mathrm{III}} - s)^3 + \dots , \\ \frac{\tilde{T}(s)}{\sqrt{s_{\mathrm{III}} - s}^5} &= d_D + e_D\sqrt{s_{\mathrm{III}} - s} + \dots . \end{aligned} \tag{4.88}$$

This expansion is matched both slightly above and below the pseudothreshold. For each of these the five constraints are fixed by the function at pseudothreshold s_{III} and two matching points $s_{\mathrm{III}} \pm \epsilon$ and $s_{\mathrm{III}} \pm 4\epsilon$ as well as the first and second derivatives at the matching point $s_{\mathrm{III}} \pm \epsilon$. The parameters are then evaluated via

$$f(x, i, j, k, l, m, n, p) = -\frac{1}{n\epsilon^p}\big(iT(x) + jT(4x - 3s_{\mathrm{III}}) + kT(s_{\mathrm{III}}) + l\epsilon T'(x) + m\epsilon^2 T''(x)\big) \tag{4.89}$$

and

$$\begin{aligned} a_D &= T(s_{\mathrm{III}}) , \\ b_D &= f(x, -112, 1, 111, -80, -32, 28, 1)\big|_{x=s_{\mathrm{III}}-\epsilon} , \\ c_D &= f(x, 126, -3, -123, 114, 68, 14, 2)\big|_{x=s_{\mathrm{III}}-\epsilon} , \\ d_D &= -2f(x, 28, -1, -27, 24, 18, 7, 5/2)\big|_{x=s_{\mathrm{III}}-\epsilon} , \\ e_D &= f(x, 56, -3, -53, 44, 40, 28, 3)\big|_{x=s_{\mathrm{III}}-\epsilon} \end{aligned} \tag{4.90}$$

below pseudothreshold and

$$\begin{aligned} a_D &= T(s_{\mathrm{III}}) , \\ b_D &= f(x, 112, -1, -111, -80, 32, 28, 1)\big|_{x=s_{\mathrm{III}}+\epsilon} , \\ c_D &= f(x, 126, -3, -123, -114, 68, 14, 2)\big|_{x=s_{\mathrm{III}}+\epsilon} , \\ d_D &= -2if(x, 28, -1, -27, -24, 18, 7, 5/2)\big|_{x=s_{\mathrm{III}}+\epsilon} , \\ e_D &= f(x, -56, 3, 53, 44, -40, 28, 3)\big|_{x=s_{\mathrm{III}}+\epsilon} \end{aligned} \tag{4.91}$$

above the pseudothreshold.

4.D Interference ring

When studying the Dalitz plots of the 1^{--} decays, we find a remarkable property induced by the symmetry of the process: a ring-shaped local minimum in the logarithmic intensity that crosses all three intersection points of the ρ bands. However, this only becomes visible when using an unphysically narrow ρ resonance. We again (cf. Sec. 4.4) employ a phase shift from a simple Breit–Wigner model with the energy-dependent width from Ref. [148] and the nominal width $\Gamma_\rho = 30\,\mathrm{MeV}$; therefore the resonance bands in the Dalitz plots are

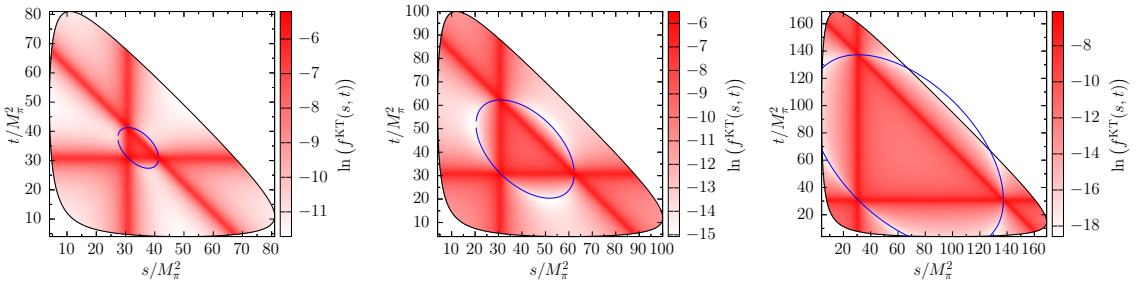

Figure 4.13: Logarithm of the intensity in the Dalitz plots for $J^{PC} = 1^{--}$ with smaller ρ width, see Appendix 4.D. From left to right, we show the decay masses $M = 10/11/14\, M_\pi$. The blue line is the solution of Eq. (4.95).

much narrower. When looking at plots with $M^2 > 3(M_\rho^2 - M_\pi^2)$, we obtain an interference ring that crosses all three intersection points of the three ρ bands. Transforming to the well-known Dalitz plot variables [155–157]

$$\begin{aligned} x &= \frac{\sqrt{3}}{2MQ}(t-u)\,, \\ y &= \frac{3}{2MQ}\left((M-M_\pi)^2 - s\right) - 1\,, \\ Q &= M - 3M_\pi \end{aligned} \tag{4.92}$$

renders the ring to a perfect circle. Using the three intersection points $s = t = M_\rho^2$, $s = u = M_\rho^2$, and $t = u = M_\rho^2$, we obtain three equations of the form

$$(x - x_c)^2 + (y - y_c)^2 - r^2 = 0\,. \tag{4.93}$$

These can be solved for the center and the radius of the circle in this parameterization:

$$\begin{aligned} x_c &= 0\,, \qquad y_c = 0\,, \\ r^2 &= \left(\frac{3(M_\rho^2 - M_\pi^2) - M^2}{MQ}\right)^2\,. \end{aligned} \tag{4.94}$$

Reverting back to the Mandelstam variables, we find that the ring can be determined using the formula for the circle $x^2 + y^2 - r^2 = 0$ and solving for

$$\begin{aligned} t(s) &= \frac{1}{2}\left(M^2 + 3M_\pi^2 - s \pm \sqrt{M_1(s) M_2(s)}\right)\,, \\ M_1(s) &= M^2 + 3M_\pi^2 - s - 2M_\rho^2\,, \\ M_2(s) &= M^2 + 3\left(M_\pi^2 + s - 2M_\rho^2\right)\,, \end{aligned} \tag{4.95}$$

in the s domain

$$-\frac{M^2}{3} - M_\pi^2 + 2M_\rho^2 \le s \le M^2 + 3M_\pi^2 - 2M_\rho^2\,. \tag{4.96}$$

This allows us to plot the interference ring in the Dalitz plot (cf. Fig. 4.13). For large masses, a sizeable part of it is outside of the Dalitz plot or close to its boundary, where the phase space is small. Using our realistic parameterization for the ρ resonance, this feature is washed out by the broadness of the ρ resonance.

4.E Rescattering effects for narrow resonances

We assume that for a narrow-width resonance, the Omnès function behaves approximately like a Breit–Wigner parameterization [96]

$$\Omega(s) = \frac{M^2}{M^2 - s - iM\Gamma}\,, \tag{4.97}$$

where the phase is given by

$$\delta(s) = \arctan\left(\frac{M\Gamma}{M^2 - s}\right)\,. \tag{4.98}$$

This assumption is justified since a zero-width phase given by

$$\delta(s) = \pi\theta(s - M^2)\,. \tag{4.99}$$

leads to

$$\Omega(s) = \frac{M^2}{M^2 - s}\,, \tag{4.100}$$

which is a Breit–Wigner function with zero width. By using Eqs. (4.97) and (4.98), the phase-shift-dependent fraction inside the dispersion integral over the inhomogeneity in Eq. (4.28) reads

$$\frac{\sin\delta(s)}{|\Omega(s)|} = \frac{\Gamma}{M}\,. \tag{4.101}$$

The general KT solution in Eq. (4.28) therefore reduces to

$$\mathcal{X}(s) = \Omega(s)\left(P_{n-1}(s) + \frac{\Gamma}{M}\cdot\frac{s^n}{\pi}\int_{4M_\pi^2}^{\infty}\frac{\mathrm{d}s'}{s'^n}\frac{\widehat{\mathcal{X}}(s')}{(s'-s)}\right)\,, \tag{4.102}$$

making it amply clear that all crossed-channel rescattering effects are suppressed in the limit of a narrow-width resonance for $\Gamma \to 0$.

Part III

Regge physics

Chapter 5

Towards a unified description of hadron scattering at all energies

5.0 Prologue

The content of this chapter is based on the preprint

- D. Stamen, D. Winney, A. Rodas, C. Fernández-Ramírez, V. Mathieu, G. Montaña, A. Pilloni, and A. P. Szczepaniak, *Towards a unified description of hadron scattering at all energies*, (2024) [arXiv:2409.09172 [hep-ph]] ,

which has been submitted for publication in Physical Review D.

This project originated during the "Scattering theory" course in the "Global Classroom Initiative" at Indiana University, where the idea to combine the properties of Khuri–Treiman equations at low energies with the high-energy behavior of Regge theory was proposed by Bastian Kubis and Adam Szczepaniak. In the beginning, the author of this thesis mainly worked with Miguel Albaladejo and Adam Szczepaniak on different possible models that might produce such a behavior. Thereby, especially the analytic properties of the gaussian hypergeometric functions were investigated.

The model that is presented in this chapter was developed by the author of this thesis in cooperation with Arkaitz Rodas, Adam Szczepaniak, and Daniel Winney. This happened over an extended period of time, where many different versions were tested and discussed.

While Khuri–Treiman equations fulfill unitarity, crossing symmetry, and analyticity in the Mandelstam variables, they are built from a truncated partial-wave expansion. Therefore, they are clearly not analytic in the j-plane and are only applicable at low energies.

We build a model of isobars that can be deployed in all three channels of $2 \to 2$ scattering. These isobars depend on a Regge trajectory in the direct channel and a combination of crossed-channel Mandelstam variables. Furthermore, we introduce a scale parameter that determines the position of the low- and high-energy regimes. The general isobar is based on Γ functions and the regularized Gaussian hypergeometric function. It is therefore analytic in all Mandelstam variables and, due to the Regge trajectory, it is analytic in the spin, as required from Regge theory. Crossing symmetry can be incorporated by splitting the total amplitude into a crossing-symmetric combination of isobars, which is appropriate for the investigated process. We show that in the high-energy region, above the chosen scale, the isobars behave exactly as expected from Regge theory if the Regge trajectories fulfill certain properties. Further, the low-energy region is dominated by an infinite sum of poles in the j-plane. We derive that the poles and residues show the expected behavior. Furthermore, a non-resonant isobar is introduced, which can resemble the Pomeron contribution.

It is shown that the Regge trajectories can fulfill all the properties that are needed for the Regge behavior of the isobars. Additionally, the trajectory is an analytic function in its Mandelstam variable via a once-subtracted dispersion relation. Unitarity is not built into the isobar model, but using an appropriate choice for the Regge trajectory, it can be incorporated approximately. Therefore, the real and imaginary parts of the Regge trajectories are connected via a coupled integral equation.

To demonstrate that this model is capable of reproducing the physical low-energy structure, we apply it to $\pi\pi \to \pi\pi$ scattering as an initial test. Thereby, we only employ the direct-channel contribution and neglect all crossed-channel effects. We fit the $I = 1$ P-wave and the $I = 0$ S-wave from the Madrid group [58]. The numerical results shown here are the ones obtained by Daniel Winney; they were, however, cross-checked by the author of this thesis and Arkaitz Rodas. The plots in Ref. [3] are produced by Daniel Winney, while the ones incorporated in this chapter are redone by the author of this thesis. For the P-wave fit, it is sufficient to use a single trajectory, while the S-wave fit needs more freedom in order to reproduce the Adler zero. This is achieved by additionally incorporating the f_2 and Pomeron trajectories. Furthermore, imposing unitarity on the trajectory level is more complicated than in the P-wave case. Solving the coupled integral equation is achieved by iteration. The first real part is modeled by an asymptotic square root function and the dispersion integral is recalculated, after which the partial waves are refitted iteratively until neither the parameters nor the resulting partial wave change. For the S-wave, the real and imaginary parts decouple, and we are able to find a solution that can be fitted directly with no need of employing the iterative procedure.

Since the Regge trajectories are analytic functions, we can search for roots in $|j - \alpha(s)|$ on the second Riemann sheet. Additionally, we are not only able to find the poles that are located close to the fit region, but we can also search for the location of excitations. The pole positions and residues are calculated by the author of this thesis and the results are cross-checked by Arkaitz Rodas and Daniel Winney.

The next—more complicated—test would involve a combined fit to the partial waves including all crossed-channel contributions. Also, further generalizations, as decay processes, coupled channels, unequal masses, and particles with spin, might be explored in the future.

The main parts of the following text are written by Daniel Winney and the author of this thesis. Arkaitz Rodas cross-checked all the equations presented here and helped to polish the presentation of the model. César Fernández-Ramírez, Vincent Mathieu, Glòria Montaña, Alessandro Pilloni, and Adam Szczepaniak made useful comments on the text and instructive discussions with them helped to further improve this project.

5.1 Introduction

In the middle of the twentieth century, a multitude of new strongly interacting particles that decay into pions and nucleons were discovered. To interpret this quickly growing spectrum, Chew, Frautschi, and contemporaries conjectured that these particles must all be bound states of an underlying force analogous to those from non-relativistic potential scattering [57, 69]. Crossing symmetry, however, requires that the force carriers of the relativistic theory, i.e., the particles being exchanged, should be those very same bound states and thus these particles must generate themselves through their own interactions.

This idea was at the heart of the original bootstrap program, which aimed to examine the structure of relativistic scattering amplitudes in hopes that, when constrained with all fundamental symmetries, a unique self-consistent theory remained [158–160].

Ultimately, the constraints of general S-matrix principles [37, 38] and discrete symmetries are not enough to define a unique theory of strong interactions [161–163]. It was realized that hadrons are indeed composite particles, and the underlying dynamics are actually of the quarks and gluons within quantum chromodynamics (QCD) and not of a self-generating bootstrap [164, 165]. Despite extensive theoretical developments since then [21, 166–174], the non-perturbative nature of QCD at low energies means a complete theory of hadronic resonances in terms of those constituents is still an open problem.

More than 50 years since the discovery of QCD, the primary toolkit of hadron phenomenology remains remarkably similar: general amplitudes, satisfying as many symmetries and basic S-matrix principles as possible, are constructed to extract meaningful physical information from experimental data [173]. The key difference is that these amplitudes are now employed to complement and test the predictions from QCD-based approaches such as lattice QCD [171, 175], chiral perturbation theory (ChPT) [176–179], and other effective field theories (EFTs) [170, 174, 180, 181].

The specific functional forms used to parameterize amplitudes typically depend on the energies of interest. In low-energy processes, for example, tools such as dispersion relations have allowed high-precision extraction of pole parameters, while including constraints of unitarity and crossing symmetry at the level of individual partial waves (PWs) (cf. Refs. [182, 183] and references therein). At high energies, on the other hand, Regge-based amplitudes, which incorporate an infinite number of PWs, are typically used to describe the phenomenology of peripheral scattering [184, 185].

Because QCD generates both the resonances at low energies as well as the exchanges at high energies, a complete theory of bound states in QCD should still be able to describe both resonance and Regge exchange phenomena, e.g., in the finite-energy sum rules [186]. Indeed, Regge inputs are often used to model high-energy contributions to constrain the low-energy PWs (cf., e.g., Ref. [182]), while resonance information informs the construction of Regge trajectories (RTs), which parameterize high-energy amplitudes (cf., e.g., Ref. [187–189]). A "complete" amplitude, however, which smoothly connects these scattering regimes, has never been satisfactorily established. Such an amplitude would provide a connection between resonances and their properties in the angular-momentum plane, which have been argued to give clues to its inner structure [190, 191], and thus give important complementary information to other theoretical approaches.

Historically, attempts at such an all-energies amplitude have fallen into the class of dual models, the most famous of which was proposed by Veneziano [76]. These amplitudes postulate that the poles in different channels are "dual" to each other, meaning the sum over poles in one channel will generate the poles in the crossed channel when analytically continued to a different kinematical region [192]. The resulting structure is fundamentally different than the typical construction of crossing symmetric "interference" or "isobar" amplitudes, where the poles of each channel are summed coherently such as in Feynman-diagram-based theories [193]. While dual amplitudes offered an appealing and relatively simple connection between low- and high-energy scattering, they were ultimately too restrictive to describe experimental data at any modern level of precision [53].

State-of-the-art formalisms that do allow high-precision parameterizations, such as those

based on Khuri–Treiman (KT) [97] equations, work with a truncated set of PWs. As a result, they no longer incorporate the constraints of analyticity in angular momentum and therefore have uncontrolled behavior at high energies. Usually, this problem is tackled by introducing subtractions, which suppress high-energy contributions and render the necessary dispersion integrals convergent. This requires fixing additional subtraction constants by fitting to data or matching to other theory predictions. These formalisms are thus typically restricted to limited ranges of kinematics and find most applications in meson decays, where the phase space is limited by the mass of the decaying particle [2, 80, 81, 100–116]. Other formalisms using Roy(-like) [58, 194] or Roy–Steiner [195] equations do incorporate an *a priori* known number of subtractions, but require a phenomenological matching between low- and high-energy regions. Starting from a full amplitude with the correct asymptotic behavior would, in principle, alleviate the need for such subtractions or matching.

In this chapter, we revisit the quest for an amplitude that satisfies all necessary constraints and simultaneously describes a wide breadth of scattering phenomena at all energies and scattering angles. We propose a new model for the $2 \to 2$ scattering amplitude of spinless particles which:

1. is crossing symmetric;
2. is analytic in all energy variables except for cuts at real values;
3. is analytic in angular momentum;
4. satisfies the Froissart–Martin bound [72, 73] and Mandelstam representation with a finite number of subtractions [40, 196];
5. has resonances appearing simultaneously as poles in the angular-momentum plane and on unphysical sheets of the energy plane;
6. exhibits Regge behavior at high energies with fixed momentum transfer;
7. and exhibits scaling behavior at high energies with fixed scattering angle.

This is accomplished by the interplay of two pieces: a model for the amplitude itself, which imposes structure expected from S-matrix and Regge theory, and a model for the RTs, which feed in the dynamical information of particle properties. This two-component formalism allows properties 1 to 7 to be satisfied by construction. Unitarity, on the other hand, is not manifestly satisfied and needs to be imposed numerically through the specific implementation of the RTs. As such, we propose a scheme in the same spirit as EFTs, which allows unitarity to be imposed for energies of interest via power counting in momentum barrier factors.

This chapter is organized as follows: the model for the amplitude is constructed from crossing symmetric combinations of "isobars", i.e., functions that contain the full tower of poles with any spin in a single energy variable. Each isobar is parameterized by RTs appearing in a hypergeometric function as discussed in Sec. 5.2. We thereby identify the requirements of the RTs to ensure the model has the desired properties in the limits of interest. In Sec. 5.3, we discuss the construction of RTs, which satisfy those requirements while being flexible enough to fit data. The utility of our model as a phenomenological

tool is demonstrated in Sec. 5.4 by applying it to elastic $\pi\pi$ scattering. We show how our model can be generalized to arbitrary isospin, extract the RTs of the $\rho(770)$ and $\sigma/f_0(500)$ mesons using elastic unitarity, and compare with existing literature. Finally, a summary including a discussion of future applications and generalizations is found in Sec. 5.5.

To streamline the presentation, several details are relegated to the appendices: a collection of useful formulae and identities relevant to the properties of the hypergeometric functions is included in Appendix 5.A. The high-energy limit at fixed scattering angle and the possible connection to inter-meson parton dynamics is explored in Appendix 5.B. In Appendix 5.C, we discuss general features of dual models and explore how our model fits to the usual notions of duality. An explicit demonstration of the crossing properties of the isobar decomposition when generalized to $\pi\pi$ scattering in the isospin limit is provided in Appendix 5.D. Lastly, Appendix 5.E contains technical details of extracting the pole locations and residues of resonances using this formalism.

5.2 Hypergeometric isobars

We first consider the elastic scattering of identical and spinless particles

$$\phi_1(p_1) + \phi_2(p_2) \to \phi_3(p_3) + \phi_4(p_4)\,, \tag{5.1}$$

with $p_i^2 = M^2$ and define the usual Mandelstam variables [40]

$$\begin{aligned} s &= (p_1+p_2)^2 = (p_3+p_4)^2\,,\\ t &= (p_1-p_3)^2 = (p_2-p_4)^2\,,\\ u &= (p_1-p_4)^2 = (p_2-p_3)^2\,, \end{aligned} \tag{5.2}$$

which satisfy the on-shell condition $s+t+u = 4M^2$. Because the particles are identical, crossing symmetry requires the single function $\mathcal{T}(s,t,u)$, denoting the scattering amplitude of the reaction Eq. (5.1), to also simultaneously describe the reactions $\phi_1 + \bar{\phi}_3 \to \bar{\phi}_2 + \phi_4$ and $\phi_1 + \bar{\phi}_4 \to \phi_3 + \bar{\phi}_2$ through the analytic continuation of momenta, or equivalently the interchange of Mandelstam variables.

The amplitude is expressible as an infinite sum of PWs in a given channel. For instance, we may write [51, 197]

$$\mathcal{T}(s,t,u) = \sum_{j=0}^{\infty} (2j+1)\, P_j(z_s)\, t_j(s)\,, \tag{5.3}$$

in terms of the cosine of the s-channel scattering angle z_s and the s-channel PWs [145],

$$t_j(s) = \frac{1}{2}\int_{-1}^{1} \mathrm{d}z_s\, P_j(z_s)\, \mathcal{T}(s, t(s,z_s), u(s,z_s))\,, \tag{5.4}$$

where $P_j(z_s)$ are the Legendre polynomials. The crossed-channel variables are related to the angular variable z_s via

$$t(s,z_s) = -2\,q_s^2\,(1-z_s)\,, \tag{5.5a}$$

$$u(s,z_s) = -2\,q_s^2\,(1+z_s)\,, \tag{5.5b}$$

where $q_s = \sqrt{s - 4M^2}/2$ is the modulus of the 3-momentum of the initial-state or final-state particles in the s-channel center-of-mass (CM) frame. Equation (5.5) can be inverted to express the angular variable in terms of the Mandelstam variables:

$$z_s = \frac{t - u}{4\, q_s^2}\,. \tag{5.6}$$

The PWs in Eq. (5.4) are analytic functions of energy, which contain branch cuts from the lowest multi-particle threshold, $s = 4M^2$ to infinity on the right-hand side of the complex s-plane and another from $s = 0$ to negative infinity on the left, referred to as right-hand cut (RHC) and left-hand cut (LHC), respectively. The RHC singularities arise from unitarity in the direct channel, in this case the s-channel, while the LHC is related to the dynamics of the crossed channels. Because the dependence on t and u enters only through the angular polynomials, the two-cut structure and the infinite number of terms in Eq. (5.3) are required to reconstruct the full amplitude and satisfy crossing symmetry. Specifically, while Eq. (5.4) is a general definition of the PW amplitude for any s, the expansion in Eq. (5.3) will only converge within a limited region of the complex z_s-plane (equivalently the t- or u-planes) given by the Lehmann ellipse [62, 63]. Recovering the crossed-channel PW expansion, i.e., Eq. (5.3) in terms of $t_j(t)$, thus involves a re-summation of the infinite sum outside this radius of convergence.

To simplify the introduction of the model, we restrict ourselves to the case of isoscalar particles and will generalize to isovectors in Sec. 5.4. In an isobar or interference model, the full amplitude is assumed to decompose into a crossing symmetric sum of terms describing individual scattering channels [193]:

$$\mathcal{T}(s,t,u) = \mathcal{F}^{+}(s,z_s) + \mathcal{F}^{+}(t,z_t) + \mathcal{F}^{+}(u,z_u)\,. \tag{5.7}$$

The superscript refers to the required symmetry of each term with the interchange of final-state particles, i.e., we require $\mathcal{F}^{\pm}(s,z_s) = \pm\,\mathcal{F}^{\pm}(s,-z_s)$. In the identical particle case all three channels enter with the same function $\mathcal{F}^{+}(x,z_x)$ for $x = s$, t or u, and it is straightforward to verify that Eq. (5.7) is fully invariant under the interchange of any two Mandelstam variables, thereby satisfying crossing symmetry.

$\mathcal{F}^{\pm}(s,z_s)$ is the s-channel isobar, which is assumed to contain poles only in s. Similarly, the isobars $\mathcal{F}^{\pm}(t,z_t)$ and $\mathcal{F}^{\pm}(u,z_u)$ only contain poles in t and u, respectively, and enter with the cosines of the crossed-channel scattering angles z_t and z_u. These angles are given by Eq. (5.6) with the interchange of $(s \leftrightarrow t)$ and $(s \leftrightarrow u)$, respectively.

In the s-channel physical region, then, the direct-channel isobar, i.e., $\mathcal{F}^{\pm}(s,z_s)$, produces the pole structure associated with the resonance spectrum. The other two terms contribute a smooth background associated with the exchanges of those same resonances in the crossed channels. This separation of poles in each variable means that the amplitude is primarily driven by the first term in Eq. (5.7) at low energies where s-channel resonances are observed. At high energies, it is instead dominated by the other two terms where the characteristic Regge behavior must emerge from the crossed channel.

For the construction in Eq. (5.7) to describe both poles and exchange behavior in the appropriate limits simultaneously, we parameterize the dynamics of each channel in terms of RTs. These are dynamical functions, which encode the properties of not only single resonances, but potentially infinite towers of particles at all energies by interpolating

their pole locations in the complex angular-momentum plane [56]. Guided by this, we decompose the isobars as

$$\mathcal{F}^{\pm}(s, z_s) = \sum_i \frac{g_i^2}{2} \left[F(\alpha_i(s),\, \nu_s) \pm (\nu_s \leftrightarrow -\nu_s) \right] , \tag{5.8}$$

where $\alpha_i(s)$ is a RT and g_i is a real coupling constant. The sum runs over all RTs, which are expected to contribute to the process. Each RT in the sum corresponds to a family of hadrons with increasing spin and the same quantum numbers. The natural parity, C-odd isovectors, for instance, i.e., the $\rho(770)$, $\rho_3(1690)$, etc., are all expected to lie on one trajectory, while isoscalars such as the $\sigma/f_0(500)$ and its possible excitations would be described by another RT. The properties and explicit construction of RTs will be explored in detail in Sec. 5.3, but for now it is sufficient to assume that each is an analytic function of s except for a RHC required by unitarity [51].

The angular dependence enters through the crossing variable ν_s, which depends only on crossed-channel Mandelstam variables

$$\nu_s = q_s^2\, z_s = \frac{t-u}{4} . \tag{5.9}$$

The two terms in Eq. (5.8) with respect to $\pm\nu_s$ manifestly satisfy the required symmetry with respect to $(z_s \leftrightarrow -z_s)$.

Finally, we define each term in Eq. (5.8) corresponding to the exchange of a single RT with the form

$$F(\alpha(s),\, \nu_s) = \Gamma(j_{\min} - \alpha(s))\, \hat{\nu}_s^{j_{\min}}\, {}_2\tilde{F}_1 \left[j_{\min}+1,\ j_{\min} - \alpha(s);\, j_{\min} + 1 - \alpha(s);\, \hat{\nu}_s \right] , \tag{5.10}$$

in terms of the Γ function and the regularized hypergeometric function ${}_2\tilde{F}_1$ defined from the usual one by

$${}_2\tilde{F}_1 \left[a,\ b;\, c;\, d \right] = \frac{{}_2F_1 \left[a,\ b;\, c;\, d \right]}{\Gamma(c)} . \tag{5.11}$$

The regularized hypergeometric function[1] is complex analytic with no pole singularities at finite values of its arguments and with a branch cut starting when its last argument is $d = 1$ and extending to infinity as long as a or b are not negative integers. We introduce a momentum scale Λ and define $\hat{q}_s^2 \equiv q_s^2/\Lambda^2$ and $\hat{\nu}_s \equiv \nu_s/\Lambda^2$. In Sec. 5.2.1, this scale will be identified as the characteristic scale of Regge physics. The remaining parameter $j_{\min} \geq 0$ is an integer, which corresponds to the lowest spin of a physical particle lying on the RT, e.g., the $\sigma/f_0(500)$ that has $j_{\min} = 0$ or the ρ whose trajectory has $j_{\min} = 1$.

The usefulness of the hypergeometric functions in modeling scattering amplitudes is well known, since the hypergeometric function provides an analytic continuation of angular polynomials beyond integer spins and therefore hints at a natural connection with Regge physics. Because of this, isobar models exploiting the analytic properties of hypergeometric functions were proposed as early as the seventies as an alternative to dual models [198, 199]. Hypergeometric functions also appear naturally in the modeling of multi-Regge processes [200, 201]. More recently, they were shown to be integral in elucidating the role

[1] General formulae regarding hypergeometric functions, which are relevant to our results, are collected in Appendix 5.A.

of Reggeized pion exchange in high-energy $\pi^{\pm}$ photoproduction via analytic continuation in angular momentum [202]. Thus, before looking at specific features of Eq. (5.10), we first consider its general analytic structure brought upon by the hypergeometric function.

Since both ${}_2\tilde{F}_1$ and Γ are analytic functions in all their arguments, $F(\alpha(s), \nu_s)$ is analytic in both the RT and crossed-channel variables. Further, at fixed t, because the s-dependence only implicitly enters through the RT (which is assumed to be analytic everywhere except for the RHC), the isobar is simultaneously analytic in both s and $\alpha(s)$. At fixed angle, additional dependence on s enters through q_s^2, which is polynomial, and therefore introduces no further singularities. As the other isobars, which enter in the crossed-channel terms, are related to $F(\alpha(s), \nu_s)$ by the interchange of Mandelstam variables, the full amplitude Eq. (5.7) will be analytic in all three energy variables, and the RT appearing in all three channels. Since the RT will be shown to be intimately related to spin, this property will be integral to the analyticity of the amplitude both in energy and in complex angular momentum.

If $\alpha(s)$ has a RHC,[2] then $F(\alpha(s), \nu_s)$ will also have a RHC. The $\Gamma(j_{\min} - \alpha(s))$ in Eq. (5.10) introduces poles at integer values of $\alpha(s)$ and will be discussed at length in Sec. 5.2.2. Similarly, the crossed-channel isobars with respect to $F(\alpha(t), \nu_t)$ contain poles in t and will develop a LHC associated with the RHC of $\alpha(t)$ as viewed from the s-channel physical region.

The aforementioned cut structure of the hypergeometric function will then split the behavior of the isobar into two distinct regimes below and above the secondary branch cut openings at each $\hat{\nu}_{s,t,u} = 1$. Specifically, because $\hat{\nu}_s$ involves the product of momentum and the scattering angle, the hypergeometric function contributing to the direct channel, Eq. (5.10), has a branch point, which depends on the value of z_s. Although this cut is unphysical, it will only affect how unitarity can be imposed. Provided Λ is large enough, the effects of these cuts are irrelevant in the resonance region. The values $z_s = \pm 1$ generate the lowest lying branch points, which occur at $q_s^2 = \pm\Lambda^2$ or equivalently at $s = \pm 4(\Lambda^2 \pm M^2)$. The symmetrized isobar $\mathcal{F}^{\pm}(s, z_s)$ will feature both of these cuts as shown diagrammatically in Fig. 5.1.

Because crossing symmetry requires that the same scale Λ also enters the crossed-channel isobars, we must calculate the location of the branch points of $\mathcal{F}^{\pm}(t, z_t)$ with respect to $\hat{\nu}_t = 1$ as a function of s and z_s. These can be found to appear at $s = \pm 2(\Lambda^2 \pm M^2)$ and therefore are lower lying than the secondary cuts of the direct channel. The cuts of the u-channel terms are identical. The cut structure of the crossed-channel isobars in the s-plane is also illustrated in Fig. 5.1. This two-cut structure of each isobar above a characteristic scale mimics that of the full amplitude, and will ensure that analyticity and unitarity constraints are still satisfied when Reggeized.

The first secondary cut in the s-channel physical region will thus be the right-hand cut coming from the hypergeometric function in the crossed-channel isobars and we define

$$\lambda^2 = 2(\Lambda^2 + M^2)\,. \tag{5.12}$$

The energy $s = \lambda^2$ is thus the maximal energy at which all terms in Eq. (5.7) lie below the branch points of the hypergeometric function for the entire physical range of the scattering angle in all three Mandelstam variables. Below this energy, each term only contains the

[2] In principle, $\alpha(s)$ should contain many branch points corresponding to every multi-particle threshold that the RT can couple to.

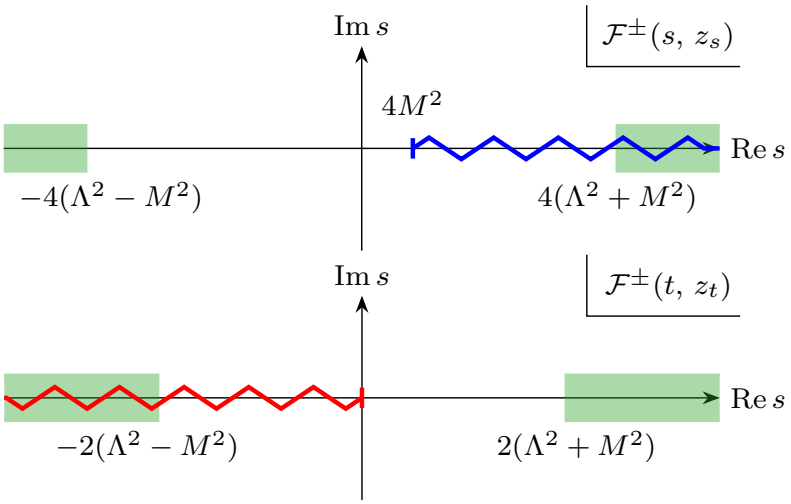

Figure 5.1: The cut structure of $\mathcal{F}^{\pm}(s, z_s)$ (top) and $\mathcal{F}^{\pm}(t, z_t)$ (bottom) in the complex s-plane for fixed $z_s = 1$. The zigzags denote cuts induced by the RTs. The RHC (blue) starting at threshold originates from $\alpha(s)$ and the LHC (red) from $\alpha(t)$ in the crossed channel. The green shaded regions denote where the secondary cuts of the regularized hypergeometric function begin to overlap those of the RTs.

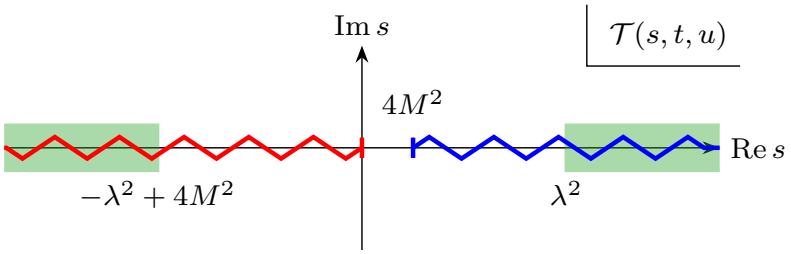

Figure 5.2: The cut structure of the full amplitude $\mathcal{T}(s,t,u)$ in the complex s-plane for fixed $z_s = 1$. Color scheme for the cuts as in Fig. 5.1.

RHC from the RT in its respective energy variable and the model resembles the structure of an isobar model in the KT dispersion representation [97, 153, 203, 204]. A diagrammatic representation of the cut structure for the full amplitude (i.e., the crossing symmetric sum of individual isobars) in the s-plane is shown in Fig. 5.2. The same cut structure will also appear in the t- and u-channel physical regions, respectively, due to crossing symmetry.

For energies $s > \lambda^2$, at least one isobar is evaluated above the additional branch points and the structure becomes more complicated. As we will explore in the following subsections, this transition point marks the energy at which the PW expansion diverges and must be re-summed into something that is Regge-behaved. In this way, these two kinematic regions reproduce the near-threshold resonance and asymptotic Regge regimes, respectively, which are connected via the complete analyticity of our isobars.

5.2.1 Regge region ($s \gg \lambda^2$)

We first consider the behavior of the isobars for energies above λ^2. For simplicity, we take $s \gg \lambda^2$ to study the Regge limit, i.e., $s, -u \to \infty$ with $t < 0$ fixed. A general crossing symmetric amplitude with the correct analytic properties is known to manifest Regge behavior in this limit and decomposes into a sum of terms of the form [51, 56, 185][3]

$$\mathbb{R}(s,t) = \beta(t)\,\xi_{\pm}(t)\,\Gamma(j_{\min} - \alpha(t))\left(\frac{s}{s_0}\right)^{\alpha(t)} . \tag{5.13}$$

This is the quintessential form of a Reggeon exchange, where $\beta(t)$ is an arbitrary real function of t referred to as the Regge residue. The signature factor, $\xi_{\pm}(t)$, is an oscillatory function of the form

$$\xi_{\pm}(t) = \frac{1}{2}\left[\pm 1 + e^{-i\pi\alpha(t)}\right] , \tag{5.14}$$

where the ± 1 denotes the signature of the RT $\alpha(t)$. The characteristic power-law behavior $s^{\alpha(t)}$ is associated with moving pole singularities, i.e., as a function of t, in the complex angular-momentum plane and arises from the re-summation of leading powers of s in the angular polynomials of the PW expansion, Eq. (5.3), outside its radius of convergence.

The Froissart–Martin bound [72, 73] limits the possible indefinite growth of the amplitude and restricts $\alpha(0) \leq 1$ for all RTs. The bound is saturated by the Pomeron with $\alpha_{\mathbb{P}}(0) \simeq 1$, while all other RTs corresponding to hadrons must be subleading, e.g., the ρ is found to have $\alpha_{\rho}(0) \simeq 0.5$ [205]. Crossed-channel unitarity fixes the imaginary part of the amplitude in this limit to be given by the signature factor.

We will show that the full amplitude constructed in Eq. (5.7) manifests the asymptotic behavior of Eq. (5.13), and thus the α that appears in Eq. (5.10) is indeed a RT in the usual sense. Further, identification of the RT as poles in the j-plane will be explored in the next subsection by demonstrating that the same function also generates resonances, i.e., poles in the PW amplitude.

We begin by considering the t-channel isobar, $\mathcal{F}^{\pm}(t, z_t)$. At fixed $t < 0$, i.e., below the RHC, $\alpha(t)$ is real and finite. Thus, taking the Regge limit only entails considering the hypergeometric function with $|\hat{\nu}_t| \to \infty$. Using Eq. (5.82) we must consider two cases for $\alpha(t) > -1$ and $\alpha(t) \leq -1$ when taking this limit, cf. Appendix 5.A. If $\alpha(t) > -1$ the isobar can be written as

$$F(\alpha(t) > -1, \nu_t \to \infty) = \left[\frac{\Gamma(1+\alpha(t))}{(-1)^{j_{\min}} j_{\min}!}\right]\ \Gamma(j_{\min} - \alpha(t))\left(\frac{u-s}{4\Lambda^2}\right)^{\alpha(t)} , \tag{5.15}$$

which resembles Eq. (5.13) without the signature factor. We already notice the emergence of a $\Gamma(j_{\min} - \alpha(t))$ factor, which would generate poles at *positive* integers $\alpha(t) = j \geq j_{\min}$. Because we are explicitly considering $t < 0$, which is below the RHC, these poles are never manifested and requiring $j_{\min} > \alpha(0)$ forbids the possibility of negative-energy poles appearing in the physical region.

We additionally note that the $\Gamma(1 + \alpha(t))$ factor appears to generate poles at *negative* integers $\alpha(t) = j \leq -1$. These poles, however, do not exist as, if $\alpha(t) < -1$, the amplitude

[3] Also compare to the Sommerfeld–Watson transform in Eq. (3.10).

is instead given by the second term in the asymptotic expansion in Eq. (5.82):

$$F(\alpha(t) < -1, \nu_t \to \infty) = \frac{(-1)^{j_{\min}}}{-1-\alpha(t)} \left(\frac{u-s}{4\Lambda^2}\right)^{-1} . \tag{5.16}$$

At the transition point $\alpha(t) = -1$, the hypergeometric function can be computed explicitly and shown to be finite with energy behavior of $s^{-1} \log s$ smoothly connecting the two limits in Eqs. (5.15) and (5.16), cf. Eq. (5.83).

The behavior of Eq. (5.16) means that at large s, the amplitude is always bounded from below by a fixed power and therefore satisfies the Cerulus–Martin bound [206]. The specific form of Eq. (5.16) is actually expected from Regge theory as unitarity prohibits amplitudes that only contain poles in the j-plane from falling faster than s^{-1} [74, 75] and can be attributed to the condensation of all Regge poles at $j = -1$ in the left-half angular-momentum plane [52, 185]. The asymptotic behavior of scattering amplitudes at fixed angles, that is, additionally taking $t \to -\infty$ with the ratio s/t kept finite, is closely related to the behavior in Eq. (5.16) and has been proposed to be connected with the microscopic dynamics of the partons exchanges. This connection is explored further in Appendix 5.B.

Inserting Eq. (5.15) into Eq. (5.8), we see that Bose symmetry with respect to z_t generates the signature factor and, using $s \sim -u$, yields a leading Regge behavior of

$$\frac{1}{2}\left[F(\alpha(t),\, \nu_t) \pm F(\alpha(t),\, -\nu_t)\right] = \left[\frac{\Gamma(1+\alpha(t))}{(-1)^{j_{\min}} j_{\min}!}\right] \xi_{\pm}(t)\, \Gamma(j_{\min} - \alpha(t)) \left(\frac{s}{2\Lambda^2}\right)^{\alpha(t)} , \tag{5.17}$$

so long as $\alpha(t) > -1$. Reading off the Regge residue by comparing Eqs. (5.7), (5.8), and (5.17) with Eq. (5.13) gives $\beta(t) = g^2\, \Gamma(1+\alpha(t))/((-1)^{j_{\min}} j_{\min}!)$ and the characteristic Regge scale $s_0 = 2\,\Lambda^2$. Note that this scale corresponds to the location of the secondary branch point $s_0 \approx \lambda^2$ in the limit $\Lambda^2 \gg M^2$. Because g and $\alpha(t)$ are both real, the imaginary part of Eq. (5.17) emerges solely from the signature factor $\xi_{\pm}(t)$ as expected from t-channel unitarity.

As we have shown, Regge behavior emerges in the t-channel isobar when taking $t < 0$ finite. Due to crossing symmetry, the same Regge behavior is found in all other similar limits, e.g., the s-channel isobar Reggeizes when $s < 0$ with $t, -u \to \infty$. However, precisely because all isobars contribute to the full amplitude, it is necessary to also show that all other isobars vanish faster than Eq. (5.17).

Because in the Regge limit $s, -u \to +\infty$, we must consider the behavior of the RTs at infinity. We will assume that the RTs are unbounded in both directions as this will ensure that the behavior of Eqs. (5.15) and (5.16) is always the leading power of s at finite t.

Looking at the u-channel term, because $u \to -\infty$ is below the RHC, $\alpha(u)$ is real and we require that $\alpha(u \to -\infty) \to -\infty$. If this is the case, the trajectory will eventually cross $\alpha(u) = -1$ and the isobar will behave as

$$F(\alpha(u) \to -\infty, \nu_u \to -\infty) = \frac{(-1)^{j_{\min}}}{\alpha(u)} \left(\frac{u}{4\Lambda^2}\right)^{-1} . \tag{5.18}$$

The factor of $\alpha(u)^{-1} \to 0$ ensures that this term will vanish faster than the leading Regge

term at any $t < 0$.[4] Computing the same limit for the other term appearing in Eq. (5.8), i.e., with $(\nu_u \leftrightarrow -\nu_u)$, proceeds identically.

The last term to consider is the s-channel isobar as $s \to \infty$, and this thus involves considering complex $\alpha(s)$ above the RHC. To demonstrate Regge behavior, it is sufficient to assume that the RT is unbounded, as before, but grows slower than s. While stronger bounds are possible, less-than-linear growth can be shown to be a requirement of RTs based on the most general analyticity principles [74] and is sufficient at this stage. With this in mind, we will identify additional requirements from our model on the asymptotic behavior of $\alpha(s)$ to be considered in Sec. 5.3. Because of the different power-law behavior in Eqs. (5.15) and (5.16), we need to consider the two different cases of $\operatorname{Re}\alpha(s) \to \pm\infty$ asymptotically.

If $\operatorname{Re}\alpha(s) \to -\infty$, the limit will be identical to that of the u-channel in Eq. (5.18) and will vanish faster than Regge behavior regardless of $\operatorname{Im}\alpha(s)$.

The more nuanced limit arises from RTs that rise indefinitely to positive infinity. Evaluating the Regge limit in this case yields an asymptotic behavior of the form

$$F(\alpha(s) \to \infty, \pm\nu_s \to \pm\infty) = \frac{\alpha(s)^{j_{\min}}}{j_{\min}!} \frac{-\pi}{\sin\pi\alpha(s)} \left(\frac{\mp s}{4\Lambda^2}\right)^{\alpha(s)} , \tag{5.19}$$

where we have used the Euler reflection formula and kept only the leading powers of the Pochhammer symbol, Eq. (5.77), at large arguments, i.e., $(x)_j \to x^j$.

Since $\alpha(s)$ is complex, we may separate the contributions from its real and imaginary parts such that, up to overall constants, the modulus of Eq. (5.19) is given by

$$\left|\frac{\alpha(s)^{j_{\min}}}{\sin\pi\alpha(s)} \left(\frac{s}{4\Lambda^2}\right)^{\alpha(s)}\right| \propto \exp\left[\operatorname{Re}\alpha(s)\log\left(s/4\Lambda^2\right) - \pi\operatorname{Im}\alpha(s)\right] . \tag{5.20}$$

The case involving $(-s)^{\alpha(s)}$ is subleading and not shown explicitly. Because we assume $|\alpha(s)| < s$ asymptotically, terms proportional to $\log|\alpha(s)|$ in the exponential are neglected. In this form, the s-channel isobar is exponentially suppressed if we require the RT to asymptotically satisfy

$$\operatorname{Im}\alpha(s) > \frac{1}{\pi}\operatorname{Re}\alpha(s)\log\left(\frac{s}{4\Lambda^2}\right) . \tag{5.21}$$

Such a condition is not new and naturally emerges in Regge-behaved models with complex rising RTs to ensure the amplitude is polynomial-bounded at infinity [54, 199, 207–210]. In particular, Ref. [199] shows that a model and RT satisfying Eqs. (5.19) and (5.21), respectively, are sufficient for the Mandelstam double dispersion representation to converge without subtractions. This property will guarantee that the amplitude has no essential singularities at infinity in any direction in the (complex) Mandelstam plane.

We note that Eq. (5.18) is trivially satisfied by Eq. (5.21) and thus is enough for both $\mathcal{F}^{\pm}(s, z_s) \to 0$ and $\mathcal{F}^{\pm}(u, z_u) \to 0$ faster than the Regge behavior of $\mathcal{F}^{\pm}(t, z_t)$ at arbitrary $t < 0$. Therefore, with a reasonably well-behaved $\alpha(s)$ whose imaginary part grows sufficiently fast, the full crossing symmetric amplitude Eq. (5.7) will be properly Regge-behaved in all channels.

[4] Satisfying this limit forbids considering the coupling g in Eq. (5.8) as a function of energy. If g is entire and $g < |\alpha(u)| < u$ then g is constant by Liouville's theorem.

5.2.2 Resonance region ($s < \lambda^2$)

The Regge behavior explored in the previous subsection is related to the presence of particles exchanged in the crossed channels at high energies. Crossing symmetry dictates that these same particles must be present in all other channels and, therefore, manifest as resonances when the CM energy is near the pole location. We explore the behavior of our isobar, Eq. (5.10), in the region below the secondary branch cuts, which manifests these resonant poles.

By construction, for $4M^2 \leq s < \lambda^2$, we have $0 \leq |\hat{\nu}_s| < 1$ and the isobar Eq. (5.10) can be expanded in powers of $\hat{\nu}_s$ with Eq. (5.78). For the discussion of poles in this section, we switch to using $\hat{\nu}_s = \hat{q}_s^2\, z_s$ to more easily identify the angular structure and write

$$F(\alpha(s),\, \nu_s) = \sum_{j=j_{\min}}^{\infty} n_j \, \frac{(\hat{q}_s^2\, z_s)^j}{j - \alpha(s)}\,, \tag{5.22}$$

with

$$n_j \equiv \frac{j!}{j_{\min}!\,(j - j_{\min})!}\,. \tag{5.23}$$

Clearly, Eq. (5.22) is the sum of simple poles whose residues are polynomials in the crossed-channel variables. The analytic structure of Eq. (5.22) is thus entirely determined by that of $\alpha(s)$. In the absence of bound states, having no poles on the physical Riemann sheet means any point s_j satisfying $(j - \alpha(s_j)) = 0$ must appear on the unphysical Riemann sheet in the lower-half complex s-plane.

To interpret the residue of these poles, we decompose the monomial in z_s into Legendre polynomials as

$$z_s^j = \sum_{j'=0}^{j} (2j'+1) P_{j'}(z_s)\, \mu_{jj'}\, \tau_{j+j'}\,, \tag{5.24}$$

with

$$\mu_{jj'} \equiv \frac{j!}{(j-j')!!\,(j+j'+1)!!}\,. \tag{5.25}$$

Since the monomial has definite parity with respect to z_s, the only non-zero terms in the expansion involve Legendre polynomials of the same parity as j and we can define the parity symbol

$$\tau_k \equiv \frac{1}{2}\left[1 + (-1)^k\right]\,, \tag{5.26}$$

which is 0 and 1 for odd and even indices, respectively.

Combining Eqs. (5.22) and (5.24), as $\alpha(s) \to j$, a single term will dominate and can be written as

$$F(\alpha(s) \to j,\, \nu_s) = \frac{\hat{q}_s^{2j}}{j - \alpha(s)} \left[\sum_{j'=0}^{j} (2j'+1)\; P_{j'}(z_s)\, n_j\, \tau_{j+j'}\, \mu_{jj'}\right]\,. \tag{5.27}$$

Here we see the pole at $\alpha(s_j) = j$ describes not only a single resonance of spin j, i.e., the residue is proportional to $P_j(z_s)$, but also resonances of all possible same-parity spins $j' < j$ at the same mass. This coincidence of masses for particles of decreasing spin is

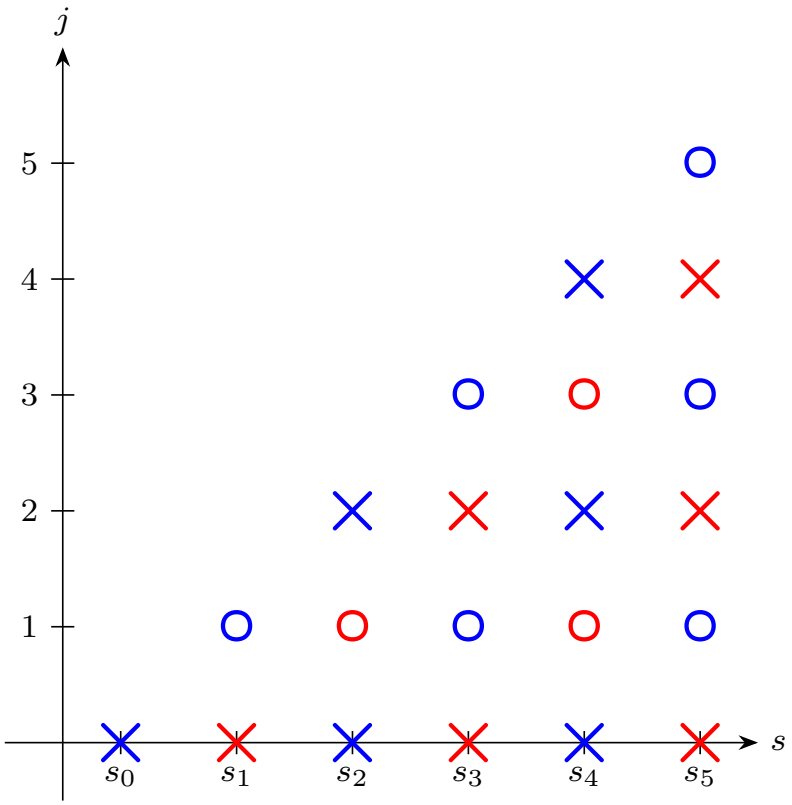

Figure 5.3: Chew–Frautschi plot illustrating the schematic pole structure of Eq. (5.8) with a generic, indefinitely rising trajectory. Isobars will have poles at each energy s_j in the complex plane satisfying $\alpha(s_j) = j$. The horizontal axis thus schematically represents *complex pole locations* that do not require the RT to be real or linear. We show poles from two terms both with $j_{\min} = 0$: the leading trajectory $\alpha(s)$ (blue) and the first daughter trajectory $\alpha(s) - 1$ (red). Crosses (circles) are poles appearing in the isobars with even (odd) signature.

observed in the Chew–Frautschi plots of many meson families [57] and referred to as the spectrum of "daughter poles" [51, 211]. These are typically understood as resonances lying on RTs parallel to $\alpha(s)$ but shifted down by integer units of angular momentum, e.g., the k-th daughter appears on the trajectory $\alpha(s) - k$. The resulting pole structure of the isobars is illustrated by the Chew–Frautschi plot in Fig. 5.3. It is important to note that the spectrum resembles that of the Veneziano model [53, 212], however, as mentioned above, the pole must be located in the complex s-plane and the RTs are not required to be real or linear.

If a pole is sufficiently narrow (i.e., with $\mathrm{Re}\, s_j \gg \mathrm{Im}\, s_j$) and isolated, the trajectory may be expanded around the projection of the pole position on the real axis recovering a Breit–Wigner (BW) form [52, 96, 213]. In principle, however, arbitrary lineshapes can be implemented with an appropriately chosen parameterization for $\alpha(s)$.

The structure of Eq. (5.22) is robust for complex and non-linear $\alpha(s)$, with the residue of each term always appearing as a fixed-order polynomial of the crossed-channel variables and thus avoids the appearance of ancestor poles [214]. Furthermore, the "parent pole",

i.e., the term with $j' = j$, always appears with the correct angular-momentum barrier factor q_s^{2j} as required to remove kinematic singularities in the angular variable and the factorization of Regge pole residues [75, 185]. The same barrier factor multiplies daughter poles, which will also be free of kinematic singularities, but vanish faster at threshold than required by analyticity. Since any number of trajectories can be added in Eq. (5.8), this problem can be remedied by adding the daughter trajectory itself into the sum, i.e., including terms with $F(\alpha(s) - k, \nu_s)$.

Because every pole term in Eq. (5.10) has a definite parity, when inserted into Eq. (5.8), Bose symmetry acts as a filter with the even-signature combination

$$\mathcal{F}^+(s, z_s) = \sum_i \sum_{j=j_{\min}}^{\infty} \tau_j \left[g_i^2 \, n_{ij} \, \frac{(\hat{q}_s^2 \, z_s)^j}{j - \alpha_i(s)} \right] \tag{5.28}$$

only containing poles at even integers.[5] Similarly, the antisymmetric combination will only have poles at odd values of j, i.e., $\mathcal{F}^-(s, z_s)$ contains a factor of τ_{j+1}. In this way, τ is the restriction of the signature factor in Eq. (5.14) to integer values of angular momentum, and enforces that only particles of a definite parity/signature appear on each RT.

Turning to the t-channel isobars, since $|\hat{\nu}_t| < 1$, we find the identical structure to Eq. (5.28), but with $(s \leftrightarrow t)$. Therefore, the dependence of s will be a polynomial and the only possible cut comes from $\alpha(t)$. Since in the s-channel physical region, $t \leq 0$ is below the RHC of $\alpha(t)$, the entire contribution from $\mathcal{F}^{\pm}(t, z_t)$ is a real and smooth background to the direct channel. The u-channel isobar follows analogously.

Combining all three isobars to the full amplitude we can conclude that in the s-channel physical region, with $4M^2 \leq s < \lambda^2$, Eq. (5.7) will only have poles in s and the imaginary part arises only by the s-channel isobar

$$\operatorname{Im} \mathcal{T}(s, t, u) = \operatorname{Im} \mathcal{F}^+(s, \, z_s) = \sum_i \left[\sum_{j=j_{\min}}^{\infty} \frac{n_{ij} \, \tau_j \, (\hat{q}_s^2 \, z_s)^j}{|j - \alpha_i(s)|^2} \right] \, g_i^2 \operatorname{Im} \alpha_i(s) \, . \tag{5.29}$$

Although we have ignored unitarity thus far, we see that the imaginary part of the amplitude (and therefore of the PWs) comes from the interplay of the different RTs. As the RTs are, in principle, complicated functions correlating information of all PWs and inelastic channels simultaneously, it is likely impossible to construct a finite set of trajectories that exactly unitarize Eq. (5.29) at all energies. However, since the term in the brackets is a convergent expansion in momentum (divided by the energy scale Λ),[6] one can impose unitarity up to some energy of interest by power counting factors of $\hat{q}_s^2$ as we will show in Sec. 5.4.

A similar structure to Eq. (5.29) emerges in the KT formalism, i.e., the discontinuity of the full amplitude along the RHC is also that of the direct-channel isobar. One crucial difference with a typical KT decomposition is that the sum in Eq. (5.22) is necessarily infinite and each isobar will contribute to all allowed PWs owing to its analyticity in j. In this energy range, the series in $\hat{q}_s$ in Eq. (5.29) converges but will diverge at $s > \lambda^2$ and

[5] Because n_{ij} depends on $j_{\min}$ it implicitly depends on $\alpha_i(s)$. This is the same quantity as in Eq. (5.23) where, since only one RT was considered, the index i was omitted.

[6] Since there is additional s-dependence in the RT, this is not a true expansion in momentum. Instead, this is analogous to the suppression of higher PWs below the radius of interaction [185].

must be re-summed into the Regge-behaved contributions of the previous subsection. In this way, the momentum scale Λ mimics the radius of interaction [185]. Because each isobar is an infinite sum of simple one-particle exchanges, Eq. (5.7) is a crossing symmetric sum of Reggeons each realized by a van-Hove-like model [215]. Furthermore, Λ also marks the divergence of the crossed-channel PW series and therefore plays the role of the semi-major axis of the (small) Lehmann ellipse [62].

As shown, the amplitude given by Eqs. (5.7), (5.8), and (5.10) corresponds to the sum of three terms each of which is responsible for the resonances and the Regge behavior in a specific channel. This deviates from the usually held notions of duality, which argue instead for a decomposition in which the Regge behavior in one channel is dual to the resonances in another. More general definitions, such as proposed by Ref. [216], i.e., that duality only requires resonances and Reggeons to emerge from the same function $\alpha(s)$, are still satisfied. A more detailed discussion and comparison with dual models is provided in Appendix 5.C.

5.2.3 The Pomeron isobar

Before concluding the discussion on the general properties of our hypergeometric isobars, we consider how the Pomeron trajectory may be incorporated in our model. The Pomeron shares the quantum numbers of the vacuum and is typically ascribed to the exchange of gluonic degrees of freedom [217]. The Pomeron is phenomenologically well established and required to describe diffractive peaks in a wide array of hadronic scattering at high energies (cf. Ref. [218] and references therein). In the low-energy regime, these gluonic exchanges could correspond to glueballs, i.e., resonances made entirely of gluons. Although the existence of glueballs has long been conjectured to lie on the Pomeron trajectory [219–222], no state has been unambiguously identified by experiment. Alternative interpretations of the Pomeron trajectory emerging from purely non-resonant exchanges have also been proposed [223, 224].

As such, we construct a special non-resonant isobar, which allows the Pomeron trajectory $\alpha_{\mathbb{P}}(s)$ to contribute to the Regge behavior at high energies without adding direct-channel poles at low energies.[7] In practice, this includes making the assumption that the Pomeron is a simple Regge pole. While this is a phenomenologically reasonable assumption, the true nature of the Pomeron with respect to the complex j-plane may be more complicated [218, 225].

We define the non-resonant isobar as

$$F_{\mathrm{NR}}(\alpha_{\mathbb{P}}(s),\, \nu_s) = \frac{{}_2\tilde{F}_1\left[1,\ -\alpha_{\mathbb{P}}(s);\, 1-\alpha_{\mathbb{P}}(s);\, \hat{\nu}_s\right]}{\alpha_{\mathbb{P}}(s)-1}\,. \tag{5.30}$$

This is Eq. (5.10) with $j_{\min} = 0$ and the $\Gamma(-\alpha(s))$ prefactor replaced by a single pole at $\alpha_{\mathbb{P}}(s) = 1$. Through the direct calculation of the Regge limit, this will yield the Regge behavior (cf. Eq. (5.13)),

$$\mathbb{P}(s,t) = \frac{\beta_{\mathbb{P}}(t)\,\xi_+(t)}{\alpha_{\mathbb{P}}(t)-1}\,\left(\frac{s}{2\Lambda^2}\right)^{\alpha_{\mathbb{P}}(t)}\,, \tag{5.31}$$

[7] We will only discuss the leading trajectory and do not discard the possibility of glueballs appearing from daughter trajectories.

with $\beta_{\mathbb{P}}(t) = g_{\mathbb{P}}^2\,\Gamma(1+\alpha_{\mathbb{P}}(t))$. Since the Pomeron has positive signature and $\alpha_{\mathbb{P}}(0) \sim 1$, the trajectory can be expanded around the forward peak at $t = 0$,

$$\mathbb{P}(s, t \to 0) = \frac{i\pi}{2}\, g_{\mathbb{P}}^2 \left(\frac{s}{2\Lambda^2}\right) , \tag{5.32}$$

which is entirely imaginary as expected from high-energy phenomenology. Because the pole at $\alpha_{\mathbb{P}}(s) = 1$ occurs at a wrong-signature value of j, it is canceled by a zero of the signature factor $\xi_+(t)$ to give a finite contribution at forward t.

Checking the behavior of the other isobars in the Regge limit, it is straightforward to see the usual assumption of $\alpha_{\mathbb{P}}(u) \to -\infty$ as $u \to -\infty$ retains vanishing behavior faster than Eq. (5.16). Similar to Eq. (5.19), ensuring the s-channel isobar vanishes entails a requirement on the real and imaginary parts of $\alpha_{\mathbb{P}}(s)$. Following the analogous derivation to obtain Eq. (5.21), one can show that if $|\alpha_{\mathbb{P}}(s)| \leq s^{1-\epsilon}$ is bounded above for some $0 \leq \epsilon < 1$ then the s-channel isobar will be exponentially suppressed if asymptotically

$$\operatorname{Im}\alpha_{\mathbb{P}}(s) > \left(\frac{4-2\epsilon}{\pi}\right) \operatorname{Re}\alpha_{\mathbb{P}}(s)\, \log\left(\frac{s}{4\Lambda^2}\right) . \tag{5.33}$$

In the resonance region, we expand in ν_s and write the expansion

$$F_{\mathrm{NR}}(\alpha_{\mathbb{P}}(s),\, \nu_s) = \frac{\alpha_{\mathbb{P}}(s)}{\Gamma(2-\alpha_{\mathbb{P}}(s))} \sum_{j=0}^{\infty} \frac{(\hat{q}_s^2\, z_s)^j}{j - \alpha_{\mathbb{P}}(s)} . \tag{5.34}$$

At $\alpha_{\mathbb{P}}(s) = 0$, the pole in the first term of the sum is canceled by the numerator of the prefactor. Similarly, for all integer $\alpha_{\mathbb{P}}(s) = j \geq 2$, the poles are canceled by the Γ factor in the denominator. Thus, the only pole contained in Eq. (5.34) arises from the $j = 1$ term, which will be removed by the parity factor τ_j in the positive signature combination $\mathcal{F}^+(s, z_s)$, cf. Eqs. (5.8) and (5.28).[8] The isobar Eq. (5.30) therefore introduces no poles and is consistent with phenomenological expectations of the Pomeron.

5.3 Dispersive trajectories

As we have demonstrated, Eqs. (5.8) and (5.10) will recover many appealing features of amplitudes in both the resonance and asymptotic regimes if certain assumptions on the RTs are made. The isobar model is ultimately ineffective, however, unless RTs can be constructed to satisfy all requirements while remaining flexible enough to fit scattering data. In this section, we explore plausible models for this purpose.

The assumption that $\alpha(s)$ is an analytic function with only a RHC and bounded above by s means it can be written as a once-subtracted dispersion relation

$$\alpha(s) = \alpha(0) + \frac{s}{\pi} \int_{4m^2}^{\infty} \mathrm{d}s' \frac{\operatorname{Im}\alpha(s')}{s'\,(s'-s)} , \tag{5.35}$$

in terms of its imaginary part, since $\alpha(s)$ fulfills the Schwarz reflection principle. Dispersion relations have long been a starting point for constructing Regge trajectories as they provide

[8] Note that an arbitrary number of poles at different *odd* values of j can be introduced and will be canceled by the signature factor. Thus, Eq. (5.31) is a minimal choice of t-dependence for the Regge residue.

an effective way to incorporate dynamical input while preserving analyticity [191, 209, 226–231]. We disallow a linear term, i.e., a second subtraction, not only because it would violate previously mentioned asymptotic bounds, but it would mean the slope of $\mathrm{Re}\,\alpha(s)$ and therefore the particle spectrum is determined by parameters external to the reaction dynamics [232]. We must thus reconcile the phenomenologically observed linearity of $\mathrm{Re}\,\alpha(s)$ for many mesons with a RT given by the form in Eq. (5.35).

As seen in Eq. (5.29), unitarity must be implemented in our model through $\mathrm{Im}\,\alpha(s)$ and can thus help guide the functional form of the imaginary part. Taking the j-th PW projection of Eq. (5.29) gives

$$\mathrm{Im}\; t_j(s) = \sum_i g_i^2\, n_{ij}\, \tau_j\, \mu_{jj}\, \hat{q}_s^{2j}\, \frac{\mathrm{Im}\,\alpha_i(s)}{|j-\alpha_i(s)|^2} + \mathcal{O}\left(\hat{q}_s^{2(j+2)}\right), \tag{5.36}$$

where all contributions of poles at $\alpha(s) > j$ appear with higher powers of momentum. Approaching threshold, these higher terms vanish faster than the leading pole, and the imaginary part of the full amplitude will be dominated by Eq. (5.36) with j replaced by the lowest physical spin. Similarly, since the first pole in each isobar term, Eq. (5.22), occurs at $\alpha(s) = j_{\min}$, the lowest PW to which each $\alpha(s)$ will contribute also has $j = j_{\min}$.[9] Thus, examining Eq. (5.36) together with the unitarity condition of PWs [51]

$$\mathrm{Im}\, t_j(s) = \rho(s)\, |t_j(s)|^2\,, \tag{5.37}$$

where $\rho(s) = 2q_s/\sqrt{s}$ is the relativistic two-body phase space, each RT must satisfy

$$\mathrm{Im}\,\alpha_i(s \to 4M^2) \propto \rho(s)\, \hat{q}_s^{2j_{\min}}\, g_i^2\,, \tag{5.38}$$

for the lowest PWs to fulfill unitarity at threshold. Note that even if there are multiple poles or crossed-channel contributions, Eq. (5.38) must still hold to ensure each pole term has the required powers of momentum. Although not considered here, in a coupled-channel scenario similar limits could be derived for each multi-particle threshold.

In addition to constraining the behavior near threshold, analyticity and unitarity principles can be used to constrain the asymptotic behavior. Along fairly general arguments, for instance, the asymptotic growth of any complex trajectory should be bounded by a square root up to possibly arbitrary $\log s$ factors [207]. Combined with Eq. (5.21) to ensure polynomial boundedness [54, 208], however, this bound becomes stricter with

$$|\alpha(s \to \infty)| \leq \sqrt{s}\, \log s\,. \tag{5.39}$$

Because Eq. (5.35) is defined through a once-subtracted dispersion relation, the positivity and unboundedness of $\mathrm{Im}\,\alpha(s \geq 4M^2)$ will guarantee $\alpha(s \to -\infty) \to -\infty$ [74].

The construction of RTs that satisfy conditions like Eqs. (5.35), (5.38), and (5.39) is not entirely new. For example, Ref. [230] constructs a model for the imaginary part of $\alpha(s)$ built up from terms of the form:

$$\mathrm{Im}\,\alpha(s) = \sum_i g_i^2\, \sqrt{s-s_i}\, \left(\frac{s-s_i}{s}\right)^{\lambda_i} \theta(s-s_i)\,. \tag{5.40}$$

[9] Because of the parity factor τ_j, $j_{\min}$ can technically be selected as a wrong-signature value and the sum will effectively start at $j = j_{\min} + 1$. For simplicity, here we assume that $j_{\min}$ and j have the same parity.

Here, the sum refers to the openings of multi-particle thresholds located at s_i. The exponents λ_i determine the vanishing behavior at each threshold and are used to enforce unitarity constraints, e.g., by taking $\lambda_i = \operatorname{Re}\alpha(s_i)$ or, in the case of Eq. (5.38), choosing the lowest threshold to satisfy $\lambda_0 = j_{\min}$.

Because Eq. (5.40) behaves as $\sqrt{s}$ asymptotically, the real part of the trajectory from evaluating Eq. (5.35) will asymptotically approach a constant for s greater than the highest considered threshold. Therefore, any trajectory of this type will trivially satisfy the bounds in Eqs. (5.21) and (5.33). Achieving the quasi-linear behavior observed in the particle mass spectra, however, requires adding multiple higher thresholds. In addition, while the form Eq. (5.40) can reproduce the branch point structure required by unitarity and analyticity, the precise s behavior is fairly rigid and does not allow much flexibility to unitarize PWs of the form Eq. (5.36). Thus, we seek a different functional form with which to describe resonances in conjunction with the isobar model in Sec. 5.2.

We will parameterize the RTs with a logarithmic form

$$\operatorname{Im}\alpha(s) = \frac{\gamma}{\pi}\log\left(1 + \frac{\pi}{\gamma}\,\rho(s)\,r(s)\right)\theta(s - 4M^2)\,, \tag{5.41}$$

with a constant $\gamma > 0$ and a real function $r(s)$. At $s \to 4M^2$ and $\rho(s) \to 0$ we may expand the logarithm,

$$\operatorname{Im}\alpha(s \to 4M^2) = \rho(s)\,r(s)\,, \tag{5.42}$$

which is independent of γ. The function $r(s)$ is assumed to be free of singularities along real $s \geq 4M^2$ but is otherwise completely general. It can thus be used to help us enforce unitarity constraints. For a single isolated pole with $j = j_{\min}$, for instance, Eqs. (5.38) and (5.42) would imply

$$r(s) = g^2\,\mu_{j_{\min}j_{\min}}\,\hat{q}_s^{2j_{\min}} + \mathcal{O}\left(\hat{q}_s^{2j_{\min}+1}\right)\,, \tag{5.43}$$

where the coupling g and momentum scale Λ should be the same as those appearing in the isobars.[10] We will thus assume that $r(s)$ can be written as

$$r(s) = \sum_{k=0}^{N} c_k\,\hat{q}_s^{2k} + c_\alpha\,\hat{q}_s^{2\operatorname{Re}\alpha(s)}\,. \tag{5.44}$$

This is a general, but still fairly minimal, parameterization of the possible function $r(s)$. For example, Eq. (5.44) can be multiplied by any overall power of s or $\log s$, but this is omitted for simplicity. The first term in Eq. (5.44) allows energy behavior bounded by an arbitrary finite-order polynomial of $\hat{q}_s^2$, or equivalently of s, with real coefficients c_k. The second term, on the other hand, enforces a Regge-like power-law behavior. The overall logarithm in Eq. (5.41) means any fixed power behavior in s can be added without having exponential growth and thus the first term allows the trajectory to be flexible enough to parameterize amplitudes at finite s when expanded for $\hat{q}_s^2 < 1$, e.g., through Eq. (5.42). Individual c's in Eq. (5.44) can be negative, but for $\operatorname{Im}\alpha(s)$ to be real and positive on the real axis we require $r(s) > 0$ for all $s \geq 4M^2$.

[10] Note that Λ enters through $\hat{q}_s^2$.

Taking the limit $s \to \infty$ of Eq. (5.41) with Eq. (5.44), we see

$$\operatorname{Im}\alpha(s \to \infty) = \frac{\gamma}{\pi} \log\left(c_N\, \hat{q}_s^{2N} + c_\alpha\, \hat{q}_s^{2\operatorname{Re}\alpha(s)}\right) , \tag{5.45}$$

where the asymptotic behavior is dictated by the behavior of the last term. Because $\operatorname{Re}\alpha(s)$ is assumed to be unbounded, we have two possibilities depending on $\operatorname{Re}\alpha(s) \to \pm\infty$. If $\operatorname{Re}\alpha(s) \to -\infty$ the Regge-like term will quickly vanish as $\hat{q}_s^2 > 1$ and we have

$$\operatorname{Im}\alpha(s \to \infty) = (\gamma/\pi)\, N\, \log\bigl(s/4\Lambda^2\bigr) . \tag{5.46a}$$

If instead $\operatorname{Re}\alpha(s) \to +\infty$, then

$$\operatorname{Im}\alpha(s \to \infty) = (\gamma/\pi)\operatorname{Re}\alpha(s)\, \log\bigl(s/4\Lambda^2\bigr) , \tag{5.46b}$$

and the bound in Eq. (5.21) can be encoded by requiring $\gamma > 1$. The trade-off, however, is that when inserted in Eq. (5.35), $\alpha(s)$ is now defined through a non-linear integral equation, which must be solved numerically.

Although it is not obvious, this integral equation admits stable solutions, which satisfy $\operatorname{Re}\alpha(s) \sim \sqrt{s}$ and $\operatorname{Im}\alpha(s) \sim \sqrt{s}\log s$ asymptotically and thus saturate the bound in Eq. (5.39). To illustrate this point, we will solve the integral equation by fitting the masses of particles on the exchange degenerate ρ–a_2 RT. This is intended as a proof-of-concept and the ρ trajectory will be revisited in Sec. 5.4.1 when considering $\pi\pi$ scattering using more in-depth unitarity constraints combined with the isobar model of Eq. (5.10).

Analogous to the analysis in Ref. [230], we adopt an iterative fitting procedure, where we start with an initial guess for $\operatorname{Re}\alpha(s)$ and fix free parameters by fitting Eq. (5.35) with a least squares minimization

$$d^2 = \sum_i \left[\bigl(\operatorname{Re}\alpha(M_i^2) - j_i\bigr)^2 + \bigl(\Gamma(M_i^2) - \Gamma_i\bigr)^2\right] , \tag{5.47}$$

where M_i, Γ_i, and j_i are the masses, widths, and spins of the ρ/a_2 mesons and their orbital excitations. To connect the width with the RT we expand the width function for narrow resonances given by [52]

$$\Gamma(s) = \frac{\operatorname{Im}\alpha(s)}{\sqrt{s}\operatorname{Re}\alpha'(s)} , \tag{5.48}$$

cf. Sec. 3.4. As our primary interest is in the existence and properties of a solution and not the numerical values of parameters, we will ignore any errors associated with the input masses and widths. After a good fit is found, the initial guess of $\operatorname{Re}\alpha(s)$ is updated with an interpolation of the previous best-fit real part and the trajectory is fit again. This procedure is continued until a stable solution is found.

We consider the masses and widths of isovectors of both signatures up to $j \leq 6$ from the Review of Particle Physics (RPP) [22]. In the absence of individual PWs, only the last term in Eq. (5.44) is kept, i.e., all $c_k = 0$, and we fix $\alpha(0) = 0.5$ and $\Lambda = \sqrt{2}\,\text{GeV}$ for simplicity. This latter value is chosen such that $\sqrt{s} = \lambda \approx \sqrt{2}\Lambda \approx 2\,\text{GeV}$ coincides with the energy at which Regge behavior appears to begin in the $\pi\pi$ total cross section [59, 233, 234]. We start with the initial guess

$$\operatorname{Re}\alpha(s) = \frac{0.5 + 0.9\,\text{GeV}^{-2}s}{\sqrt{1 + s/(20\,\text{GeV}^2)}} , \tag{5.49}$$

i	γ	c_α
0	1.345	4.953
1	1.101	3.100
2	1.072	3.612
3	1.083	3.565
4	1.085	3.566
5	1.082	3.573
10	1.082	3.571
15	1.083	3.570
20	1.083	3.569

Table 5.1: Results for the iterative fitting procedure for the exchange degenerate ρ–a_2 trajectory. The fit value at the i-th fit iteration is shown for the two free parameters γ and c_α.

and fit the remaining two parameters γ and c_α. A reasonably stable solution is found after about four iterations of the integral equation as seen in the best-fit parameters tabulated in Table 5.1.

In Figs. 5.4 and 5.5 the resulting RT after 20 iterations is plotted compared to both the phenomenological linear trajectory $(0.5 + 0.9\,\mathrm{GeV}^{-2}s)$ [51] and the results of Ref. [230]. In this comparison, we note several things: first, both Eqs. (5.40) and (5.41) achieve approximate linearity in the resonance region, however, this is accomplished by completely different mechanisms. For Eq. (5.40), effective multi-body threshold openings are required to enhance the imaginary part and prevent the real part from saturating to a constant. The linearity of Regge trajectories is therefore assumed to be an inherently inelastic phenomenon. Equation (5.41), however, accomplishes the quasi-linear behavior using only a single threshold. Although we do not explore this here, considering additional thresholds can modify the slope of the trajectory and possibly lead to an asymptotically constant real part. In this way, it is actually the termination of resonances that is a multi-threshold effect. Since the termination of the infinite tower of excited resonances is proposed to be related to screening from coupled channels [235, 236], the interpretation of the latter mechanism seems more plausible.

Second, $\mathrm{Re}\,\alpha(s)$ continues to grow indefinitely, but slows from approximately linear to square-root behaved. A model with infinitely many poles, such as in Eq. (5.22), will thus indeed have infinitely many resonances appearing as orbital excitations. Note that, unlike narrow resonance models, $\mathrm{Im}\,\alpha(s)$ also grows indefinitely and at a faster rate. This has the effect of moving higher-j poles deeper and deeper into the complex plane, such that the infinite tower of resonances is indiscernible from a non-resonant background above some energy scale.

Finally, we note that the best-fit value of $\gamma \approx 1.08 > 1$ means the asymptotic behavior of $\alpha(s)$ satisfies the bounds in Eqs. (5.21) and (5.39). A crossing symmetric combination of isobar terms of the form in Eq. (5.8) with the trajectory as in Figs. 5.4 and 5.5 will thus be properly Regge-behaved at high energies.

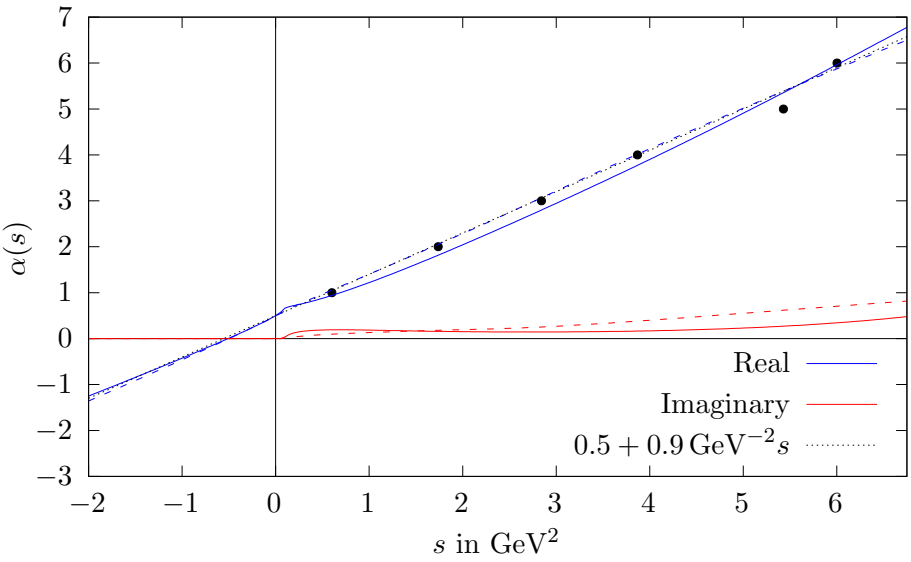

Figure 5.4: Results for the exchange degenerate ρ–a_2 trajectory in the resonance region. The results using Eqs. (5.41) and (5.44) (solid) are compared to the model of Ref. [230] using Eq. (5.40) (dashed) as well as the canonical linear ρ trajectory (black dotted).

5.4 Application to $\pi\pi$ scattering

As we have demonstrated, the isobar model constructed in Sec. 5.2 offers a unified description of low-energy resonances and high-energy Regge behavior through analyticity in both energy and angular momentum. The key ingredients to accomplish this are RTs, which encode all the relevant dynamical information. In Sec. 5.3, a RT model that satisfies all the requirements to realize the isobar model in Eq. (5.7) is discussed. In this section, we now combine the results of the previous sections to consider $\pi\pi$ scattering and study the ρ and $\sigma/f_0(500)$ resonances as a benchmark of the presented theoretical framework using as few parameters as possible. This is not intended to be a precision study of these resonances.

Because the pion is an isovector, Eq. (5.7) must be generalized to accommodate the scattering of different isospin states. Since the isobars in Eq. (5.8) already have definite signature, such a generalization is trivially accomplished by defining isobars with a definite isospin $I = 0,\ 1,\ 2$ as:

$$\mathcal{F}^I(s, z_s) = \sum_i \frac{g_i^2}{2} \left[F(\alpha_i^I(s), \nu_s) + (-1)^I\, F(\alpha_i^I(s), -\nu_s) \right] . \tag{5.50}$$

This isobar transforms as $\mathcal{F}^I(s, z_s) = (-1)^I\, \mathcal{F}^I(s, -z_s)$, which is required by Bose symmetry. We assume that the RTs, which are summed over, also carry a definite isospin. While exchange degeneracy, i.e., the approximate equality of RTs with similar quantum numbers [237], can still be imposed, we will not require it. In general, each trajectory is only responsible for generating the resonances of a single signature and isospin.

The analog of Eq. (5.7) for the s-channel isospin amplitudes can be written by con-

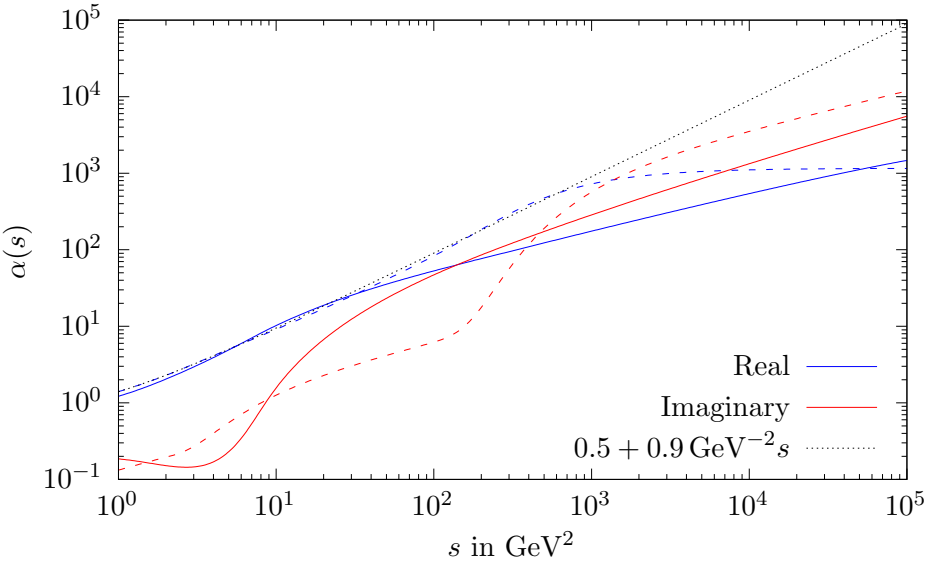

Figure 5.5: Results for the exchange degenerate ρ–a_2 trajectory at asymptotic energies. Legend is the same as in Fig. 5.4.

structing a crossing symmetric combination of terms given by Eq. (5.50) [119, 153]

$$\mathcal{T}^I(s,t,u) = \mathcal{F}^I(s,z_s) + \sum_{I'} C_{st}^{II'} \left[\mathcal{F}^{I'}(t,z_t) + (-1)^{I+I'}\,\mathcal{F}^{I'}(u,z_u)\right] , \tag{5.51}$$

where $C_{st}^{II'}$ are the elements of the isospin crossing matrix [238, 239]

$$C_{st} = \begin{pmatrix} \frac{1}{3} & 1 & \frac{5}{3} \\ \frac{1}{3} & \frac{1}{2} & -\frac{5}{6} \\ \frac{1}{3} & -\frac{1}{2} & \frac{1}{6} \end{pmatrix} . \tag{5.52}$$

An explicit demonstration that Eq. (5.51) is crossing symmetric, i.e., the decomposition with respect to isospin defined in the t- or u-channels is identical, is relegated to Appendix 5.D.

Since each isobar will only have poles in its energy variable, Eq. (5.51) will only have s-channel resonances of isospin I coming from the first term. The remaining terms thus represent the exchange of all isospin particles in the t- and u-channels. Assuming well-behaved RTs in each channel, taking the $s \to \infty$ limit with fixed $t < 0$, Eq. (5.51) yields the Regge-behavior

$$\mathcal{T}^I(s,t,u) \to \sum_{I'} C_{st}^{II'} \left[\sum_i \mathbb{R}_i^{I'}(s,t)\right] , \tag{5.53}$$

with each $\mathbb{R}_i^{I'}$ given by Eq. (5.13) with respect to $\alpha_i^{I'}(t)$. Clearly, Eq. (5.53) represents the exchange of Reggeons of all isospins in the t-channel with the correct coefficients from crossing as expected from high-energy $\pi\pi$ scattering [49, 59, 233].

Although the exploratory ρ trajectory in Figs. 5.4 and 5.5 reasonably reproduces the resonance region with only a single threshold, this result should be interpreted with caution. Beyond the mass of the lowest-lying ρ, inelastic thresholds become increasingly important, e.g., the $\rho_3(1690)$ decays primarily into 4π. Constraining a RT in a broad range of energies is thus inherently a coupled-channel problem. For this first study, then, we will restrict ourselves to the $\pi\pi$ scattering in the isospin limit below the $K\bar{K}$ threshold. In these energies, the primary contributions come from two-body dynamics and the RTs contain only one relevant branch point [51]. The amplitude can thus be effectively constrained with elastic unitarity in order to benchmark the extraction of the RTs of mesons in this mass region.

Fixing $\Lambda = \sqrt{2}\,\mathrm{GeV}$ (and therefore $\lambda \simeq \sqrt{2}\,\Lambda = 2\,\mathrm{GeV}$) at the observed scale of Regge physics in $\pi\pi$ scattering as before, the elastic region lies well within the boundary $s < \lambda^2$ where our amplitude is a genuine isobar model as discussed in Sec. 5.2.2. We can thus take the j-th PW projection, which is decomposed into separate contributions from direct-channel and crossed-channel isobars:

$$t_j^I(s) = f_j^I(s) + \sum_{I'} C_{st}^{II'}\, \tilde{f}_j^{I'}(s)\,. \tag{5.54}$$

The direct-channel term contains the RHC and is given by the projection of all the s-channel poles, the projection of which can be written explicitly using Eq. (5.28)

$$f_j^I(s) = \tau_{I+j} \sum_i \sum_{k=0}^{\infty} \hat{q}_s^{2(j+2k)} \left[\frac{g_i^2\, n_{i,j+2k}\, \mu_{j+2k,j}}{j - (\alpha_i^I(s) - 2k)}\right]. \tag{5.55}$$

The inhomogeneous term on the other hand is given by the projection of the crossed-channel isobars:

$$\tilde{f}_j^I(s) = \int_{-1}^{1} \mathrm{d}z_s\, P_j(z_s)\, \mathcal{F}^I(t(s,z_s), z_t(s,z_s))\,, \tag{5.56}$$

which will generate the LHC of $t_j^I(s)$ and cannot be done in closed form. The structure of the PW in Eq. (5.54) is intentionally written to mirror the structure of the KT decomposition [2, 97, 153].

Since imposing unitarity in the KT formalism requires solving systems of coupled integral equations for each isospin simultaneously, they are typically very challenging. In our formalism, the analogous integral equations will be non-linear. Because of this, we first demonstrate that unitarity can be imposed by solving the homogeneous equation

$$\mathrm{Im}\, t_j^I(s) = \mathrm{Im}\, f_j^I(s) = \rho(s)\, |f_j^I(s)|^2\,, \tag{5.57}$$

which ignores the contribution from the crossed channels in the second term of Eq. (5.54). In the conventional KT formalism, this reduces to an Omnès problem and is readily solved in terms of the scattering phase shift [45, 46]. In the language of Eq. (5.54), on the other hand, the homogeneous solutions will decouple the different isospins and yield RTs without corrections from final-state interactions. Thus, despite not involving the full crossing symmetric model in Eq. (5.51), solving the homogeneous problem is a highly non-trivial and necessary first step towards a full "KT with Regge poles" analysis to be done in the future.[11]

[11] We have chosen to implement unitarity at the level of individual PWs, but because our isobars incorporate the infinite tower of increasing spin, one could, in principle, try to unitarize the full amplitude.

As described in Sec. 5.2.2, the imaginary part of the amplitude arises from the imaginary part of the RTs. Using Eq. (5.41), the degrees of freedom with which to incorporate unitarity are the coefficients of the $\hat{q}_s^2$ polynomial contained within Eq. (5.44). In practice, because this polynomial is of fixed order, unitarity can only be imposed up to a certain momentum scale corresponding to the first power of $\hat{q}_s^2$ which is not considered. Luckily, with the scale parameter $\Lambda = \sqrt{2}\,\text{GeV}$, the region below the $K\bar{K}$ threshold, i.e., with $s \lesssim 1\,\text{GeV}^2$, has $\hat{q}_s^2 \lesssim 0.12$ and the sums over powers of momentum in Eq. (5.55) converge very quickly. Elastic unitarity can thus be implemented numerically with only a few terms.

As our primary focus is the application to hadron spectroscopy, we will focus on the $I = 0$ and 1 channels. Resonances with $I = 2$ would correspond to doubly-charged mesons and are not observed in nature. From Eq. (5.29), we see that PWs in our formalism can only achieve a non-zero imaginary part with an explicit RT in the direct channel and thus parameterizing any $I = 2$ amplitude would indeed require constructing at least one $\alpha^{I=2}(s)$. Exotic mesons can be avoided with a RT that never crosses positive even integers or through a non-resonant isobar analogous to that in Sec. 5.2.3. We, however, do not pursue this further.

5.4.1 $I = 1$ and $\alpha_\rho(s)$

The isospin $I = 1$ channel of the elastic $\pi\pi$ spectrum is well known to be dominated by the ρ resonance in the P-wave. As such, we include only a single trajectory $\alpha_\rho(s) \equiv \alpha^{I=1}(s)$ with $j_{\text{min}} = 1$, such that the isobar Eq. (5.50) takes the form

$$\mathcal{F}^1(s, z_s) = \frac{g_\rho^2}{2}\left[F(\alpha_\rho(s),\, \nu_s) - F(\alpha_\rho(s),\, -\nu_s)\right] . \tag{5.58}$$

We use a trajectory given by Eqs. (5.35) and (5.41) with Eq. (5.44) containing two terms

$$r_\rho(s) = \frac{g_\rho^2}{3}\,\hat{q}_s^2 + c_\rho\,\hat{q}_s^{2(1+\text{Re}\,\alpha_\rho(s))} , \tag{5.59}$$

in order to unitarize up to order $\mathcal{O}\left(\hat{q}_s^2\right)$, which encompasses only the P-wave (i.e., the F-wave is $\mathcal{O}\left(\hat{q}_s^6\right)$). Expanding the logarithm around small $\hat{q}_s^2$ with Eq. (5.42), the P-wave projection of Eq. (5.58) is given by

$$\text{Im}\, f_1^1(s) = \rho(s)\left|f_1^1(s)\right|^2 + \mathcal{O}\left(\hat{q}_s^{2(2+\text{Re}\,\alpha_\rho(s))}\right) . \tag{5.60}$$

Since $\text{Re}\,\alpha_\rho(s) \gtrsim 0.5$ is expected above threshold, e.g., similar to Fig. 5.4, the second term will always be subleading and Eq. (5.60) reproduces Eq. (5.57) to leading order.

The first higher-order term in Eq. (5.60) scales with $\text{Re}\,\alpha_\rho(s)$ and will be the dominant correction at small and intermediate s. However, as s increases, and $\text{Re}\,\alpha_\rho(s) > 2$, the next-to-leading order term will instead be the next fixed power of $\hat{q}_s^2$ in Eq. (5.55). The constant c_ρ in Eq. (5.59) is thus left as a free parameter to incorporate the small contributions from these terms in the unitarity equation at low energies. We fix $\alpha_\rho(0) = 0.491$ to the value extracted from charge-exchange πN scattering in Ref. [205] and thus have three parameters left to be determined: g_ρ^2, γ_ρ, and c_ρ. We adopt an iterative fitting procedure as in Sec. 5.3 to simultaneously solve the integral equation for $\alpha_\rho(s)$ as well as fix parameters by comparing them to data. Using the same initial guess in Eq. (5.49),

i	g_ρ^2	γ_ρ	c_ρ
0	4.269	1.302	2.818
1	4.262	1.074	3.231
2	4.263	1.071	3.241
3	4.263	1.079	3.142
4	4.263	1.080	3.212
5	4.263	1.077	3.221
10	4.263	1.077	3.221
15	4.263	1.078	3.219
20	4.263	1.078	3.218

Table 5.2: Results for the iterative fitting procedure of the ρ trajectory using low-energy unitarity.

we now minimize the distance squared of the resulting P-wave projection of Eq. (5.58) to known $\pi\pi$ PWs

$$(d^2)_j^I = \sum_i \left| f_j^I(s_i) - (t_{\mathrm{GKPY}})_j^I(s_i) \right|^2 . \tag{5.61}$$

Here $(t_{\mathrm{GKPY}})_j^I$ is the central value of PWs with a given isospin as determined by the Madrid group (GKPY) [58]. Once again, as an exploratory study, we ignore the errors associated with these PWs. By fitting both real and imaginary parts of the PWs simultaneously, the constraint of elastic unitarity is incorporated into the RT. For the present case of the ρ trajectory, $f_1^1(s_i)$ is given by projecting Eq. (5.58) onto the P-wave and we choose 10 evenly spaced points between $4M_\pi^2$ and $1\,\mathrm{GeV}^2$ as the sampled energies s_i.

The resulting P-wave is plotted in Fig. 5.6 with parameters in Table 5.2, where we see generally good agreement with unitarity and the GKPY amplitude. The resulting trajectory $\alpha_\rho(s)$ is plotted in the resonance region in Fig. 5.7, where $\alpha_\rho(s)$ crosses through the point $\mathrm{Re}\,\alpha(M_\rho^2) = 1$ as well as $\mathrm{Im}\,\alpha(M_\rho^2) = M_\rho\,\Gamma_\rho\,\mathrm{Re}\,\alpha'(M_\rho^2)$, which is expected of the nearly BW nature of the ρ lineshape. Note, however, that compared to the prototypical linear trajectory, the slope begins to decrease well within the fit region with deviations beginning just after the ρ mass, i.e., $s \gtrsim 0.5\,\mathrm{GeV}^2$. We may also compare with other dispersive trajectories that incorporate unitarity, in particular the ρ RT calculated in Ref. [191] using a constrained Regge pole (CRP) model [227, 228]. We see a similar trend with the two coinciding near the ρ mass. We do note that the CRP trajectory has a larger imaginary part near threshold, in a region where the authors already observed that the PW amplitude is overestimated. This trajectory is calculated fixing only the complex pole position and not with a fit to the PW (i.e., the opposite approach to this analysis). Comparing the two methods, thus suggests that constraining the energy dependence of the residues in the numerator is important for extracting the RT in the denominator from fits to the PW amplitude.

Because our RT is analytic, it can also be evaluated for spacelike energies below threshold, which is shown in Fig. 5.8. We compare $\alpha_\rho(s)$ with the experimental extraction of the effective RT in charge-exchange πN scattering [205], which first observed the non-linearity of ρ exchange at large momentum transfers. Remarkably, despite not being included in the fit, $\alpha_\rho(s)$, as constrained by elastic unitarity, is compatible with all data points.

Finally, because the RT contains all the relevant information on the particle spectrum,

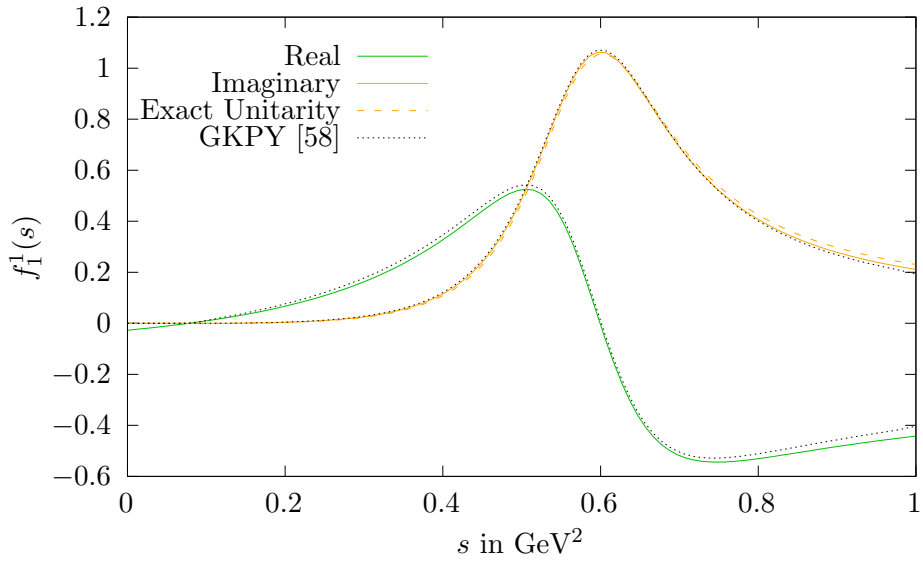

Figure 5.6: Best-fit of the P-wave projection of Eq. (5.58) in the elastic region (solid). For comparison, the GKPY PW (black dotted) is plotted and the expectation of elastic unitarity if it were satisfied exactly, i.e., Eq. (5.57) (orange dashed).

	This work		RPP [22]	
	$\alpha_\rho(s_j)$	$\sqrt{s_j}$ in MeV	M_j in MeV	$\Gamma_j/2$ in MeV
$\rho(770)$	1	$760 - i\,70$	(761 – 765)	(71 – 74)
$\rho(1450)$	2	$1380 - i\,120$	1465 ± 25	200 ± 30
$\rho_3(1690)$	3	$1800 - i\,130$	1688 ± 2.1	80 ± 5
$\rho(1700)$			1720 ± 20	125 ± 50

Table 5.3: Comparison of extracted complex roots of $\alpha_\rho(s_j) = j$ with the masses and widths of the observed ρ spectrum. Only the RPP values for the $\rho(770)$ correspond to T-matrix pole parameters. The remaining quoted values are BW masses and widths.

$\alpha_\rho(s)$ can be used to examine the locations of resonance poles in the complex plane by searching for roots of $(j - \alpha(s))$ for *any* positive integer j. Thus, in addition to the $\rho(770)$, we can extrapolate outside the fit range to extract the pole positions of the first radial excitation, $\rho(1450)$ or ρ', and first orbital excitation ρ_3, which are located at $\alpha_\rho(s_2) = 2$ and $\alpha_\rho(s_3) = 3$, respectively. In the case of the former, the minimal model considered in Eq. (5.58) does not contain an explicit pole for this state as the $j = 2$ term gets canceled by the signature factor. Ultimately, resonance masses and widths will only depend on the RT on which they appear and we can use the RT constrained around the $\rho(770)$ to predict the location of higher states. The structure of daughter poles in Fig. 5.3 means that the pole located at $\sqrt{s_3}$ will be degenerate with the second radial excitation, the $\rho(1700)$ or ρ'', which we also compare against. Details of the pole extraction are provided in Appendix 5.E.

The resulting pole positions are tabulated in Table 5.3, where we see the parameters of the $\rho(770)$ are generally in good agreement with more detailed dispersive analyses [240–

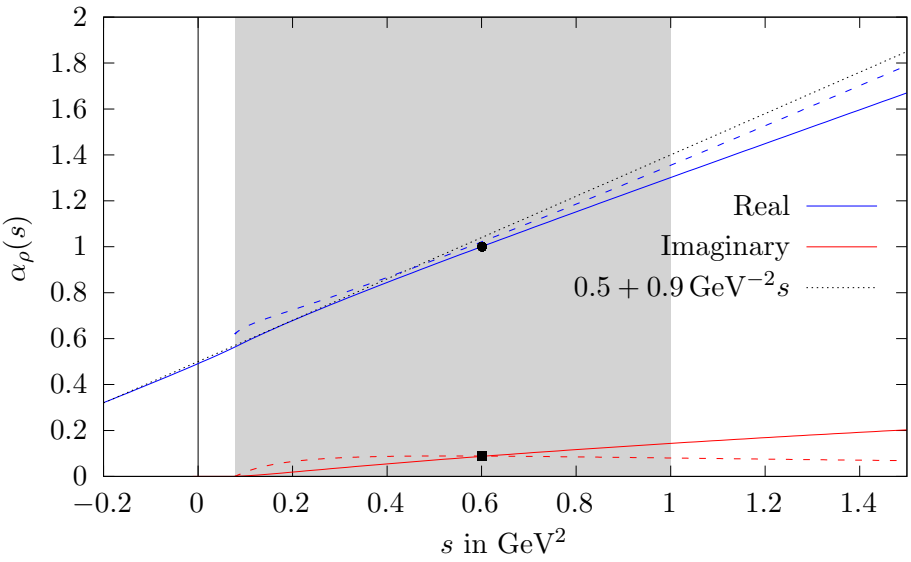

Figure 5.7: Best-fit trajectory $\alpha_\rho(s)$ after the iterative fitting procedure in the resonance region (solid) compared to the CRP trajectory from [191] (dashed). The fitted region is shaded and the phenomenological trajectory $(0.5 + 0.9\,\mathrm{GeV}^{-2}s)$ (black dotted) is also plotted for comparison. The points correspond to $\mathrm{Re}\,\alpha(M_\rho^2) = 1$ (circle) and $\mathrm{Im}\,\alpha(M_\rho^2) = M_\rho\,\Gamma_\rho\,\mathrm{Re}\,\alpha'(M_\rho^2)$ (square) at the nominal BW ρ mass $M_\rho = 775\,\mathrm{MeV}$ and width $\Gamma_\rho = 148\,\mathrm{MeV}$.

242]. In addition, using Eq. (5.109) we extract the modulus and phase of the residue

$$|g_{\rho\pi\pi}| = 5.8 \quad \text{and} \quad \phi_{\rho\pi\pi} = -6.2^\circ\,, \tag{5.62}$$

which are also in qualitatively good agreement [240–242]. We present these values as well as the pole positions without error analysis as we aim only for an exploratory benchmark of the isobar and trajectory models. Furthermore, the pole positions are rounded to 5 MeV.

The higher poles of the ρ', ρ'', and ρ_3 also compare reasonably well with the RPP masses and widths in Table 5.3, but deviate more than the ground state ρ. This could be due to several factors: first, the quoted RPP values for these states correspond to BW masses and widths. Since these states are generally broader and harder to extract than the ρ, there may be substantial deviations from the genuine pole location. Second, the model in Eq. (5.28) is not unitary by construction and thus extrapolating far outside the fit range may suffer violations from unitarity. Finally, as previously mentioned, higher ρ resonances couple primarily to inelastic channels such as 4π. Since the RT couples to multi-body channels in a possibly non-trivial way, our trajectory may be ignoring important effects from inelastic thresholds.

We do not attempt to quantify the uncertainties from these effects here. Nevertheless, finding resonance poles located in generally the right place in the complex plane, even when extrapolated far from the fit region, is reassuring and a first step to a more in-depth exploration of these poles in the future.

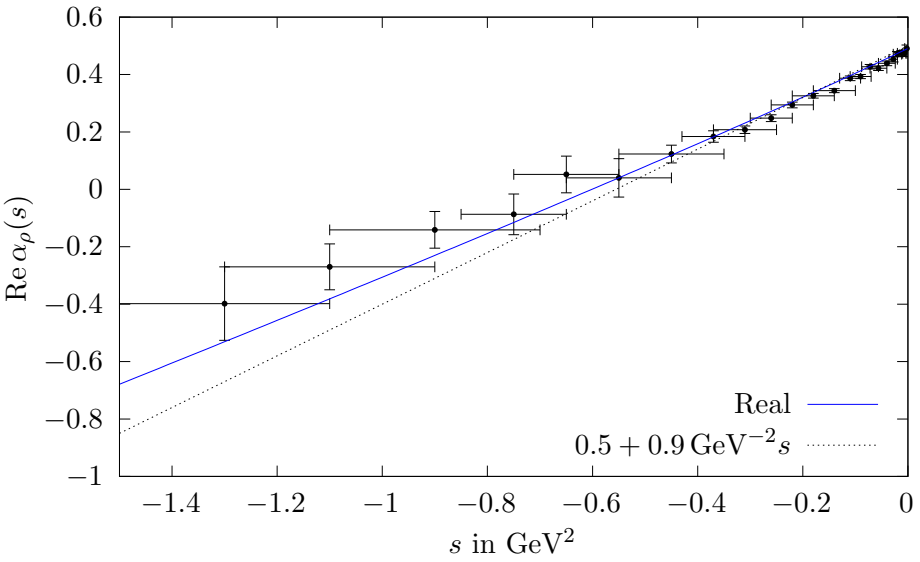

Figure 5.8: Best-fit trajectory $\alpha_\rho(s)$ plotted for spacelike energies. The curves are the same as Fig. 5.7. Data points are the effective ρ trajectory as extracted from charge-exchange πN scattering at high energies [205]. These data points are shown for comparison but were not included in the fit.

5.4.2 $I = 0$ and $\alpha_\sigma(s)$

Turning to the isospin $I = 0$ amplitude, we wish to investigate the $\sigma/f_0(500)$ resonance, which is seen in the S-wave near threshold alongside the narrow $f_0(980)$. In our formalism, this channel will receive contributions from all RTs of similar quantum numbers and one must also account for the f_2 and $\mathbb{P}$ trajectories. We therefore write

$$\mathcal{F}^0(s, z_s) = \frac{1}{2}\Big[g_\sigma^2\, F(\alpha_\sigma(s),\, \nu_s) + g_{f_2}^2\, F(\alpha_{f_2}(s),\, \nu_s) + g_{\mathbb{P}}^2\, F_{\mathrm{NR}}(\alpha_{\mathbb{P}}(s),\, \nu_s)\Big] + (\nu_s \leftrightarrow -\nu_s)\,, \tag{5.63}$$

where the σ and f_2 use the resonant isobar in Eq. (5.10) and the Pomeron is non-resonant using Eq. (5.30). Only a single trajectory for the scalar resonances is included as we will restrict our fitting to energies close to threshold in order to focus on the σ. Follow-up investigations about the $f_0(980)$ can be conducted by including an additional term in Eq. (5.63).

We first discuss the f_2 trajectory, which is expected to yield the largest contribution resulting from $I = 0$ hadron exchanges at high energies, subleading only to the exchange of a Pomeron. The smallness of the $\pi\pi$ scattering cross sections at maximal isospin is often explained by cancellations between the Reggeons in the crossed channel due to the (approximate) exchange degeneracy of the ρ and f_2 trajectories [243]. Specifically, if

$$\alpha_\rho(s) \approx \alpha_{f_2}(s) \quad \text{and} \quad g_{f_2}^2 \approx \frac{3}{2}\, g_\rho^2\,, \tag{5.64}$$

then the sum of imaginary parts from the ρ and f_2 in Eq. (5.53) will vanish asymptotically. We may do a simple test of exchange degeneracy using the $\alpha_\rho(s)$ as calculated in

the previous subsection by comparing the quoted T-matrix poles of the $f_2(1270)$ and its degenerate daughter pole $f_0(1370)$ [22]

$$\sqrt{s_{f_2(1270)}} = ((1260 - 1283) - i\,(90 - 110))\ \text{MeV}\,, \tag{5.65a}$$

$$\sqrt{s_{f_0(1370)}} = ((1250 - 1440) - i\,(60 - 300))\ \text{MeV}\,. \tag{5.65b}$$

Equation (5.64) suggests these should be compared with the $\alpha_\rho(s_2) = 2$ entry in Table 5.3, which once again compare rather well, but without a detailed error analysis no definite conclusions can be drawn. In any case, because the first physical resonance on the f_2 trajectory has spin 2, this isobar must have $j_{\min} = 1$ or 2 in order to avoid the pole at $j = 0$. At low energies the contributions of the f_2 Regge pole will always be $\mathcal{O}\left(\hat{q}_s^4\right)$ as dictated by Eq. (5.28), and details of the trajectory and coupling are largely suppressed when considering very near threshold energies. Thus, taking the S-wave PW projection of Eq. (5.63) and considering only leading order in the momentum expansion yields

$$f_0^0(s) = \frac{g_\sigma^2}{-\alpha_\sigma(s)} - \frac{g_{\mathbb{P}}^2}{\Gamma(2 - \alpha_{\mathbb{P}}(s))} + \mathcal{O}\left(\hat{q}_s^4\right)\,, \tag{5.66}$$

without a contribution from the f_2. Because we are ignoring the crossed channels in the homogeneous unitarity equation, the Pomeron coupling and trajectory are largely unconstrained. For simplicity then, given the limited energy range considered, we will assume $\alpha_{\mathbb{P}}(s) \approx \alpha_{\mathbb{P}}(0) \simeq 1$ and fit the coupling $g_{\mathbb{P}}^2$. Since our primary goal is the extraction of $\alpha_\sigma(s)$, we keep the full tower of poles in the hypergeometric function for $F(\alpha_\sigma(s), \nu_s)$ and absorb all other $\mathcal{O}\left(\hat{q}_s^4\right)$ and higher contributions of both the $\mathbb{P}$ and f_2 in Eq. (5.63) into the fitted coupling $g_{\mathbb{P}}^2$. In a fully crossing symmetric analysis, the value of the coupling $g_{\mathbb{P}}^2$ should instead be compared with the total $\pi^+\pi^-$ cross section at high energies using Eq. (5.53).

With these simplifications in mind, we approximate Eq. (5.63) as

$$\mathcal{F}^0(s, z_s) = \frac{1}{2}\left[g_\sigma^2\, F(\alpha_\sigma(s),\, \nu_s) - g_{\mathbb{P}}^2\right] + (\nu_s \leftrightarrow -\nu_s)\,, \tag{5.67}$$

such that the resulting S-wave projection is written as

$$f_0^0(s) = \frac{g_\sigma^2 + g_{\mathbb{P}}^2\ \alpha_\sigma(s)}{-\alpha_\sigma(s)} + \mathcal{O}\left(\hat{q}_s^4\right)\,. \tag{5.68}$$

Note that because g_σ^2 and $g_{\mathbb{P}}^2$ are both real and positive, the numerator will manifest a zero if for some real $s_A < 4\,M_\pi^2$, the trajectory satisfies $\alpha_\sigma(s_A) = -(g_\sigma/g_{\mathbb{P}})^2$. This is the Adler zero, required by chiral symmetry [244, 245]. We remark that the existence of such a zero in the chiral limit, i.e., at $s_A = 0$, requires $\alpha_\sigma(0) \leq 0$ and would be consistent with a quickly vanishing Regge exchange contribution at high energies, but we make no *a priori* assumptions about the location of the zero.

We briefly comment on how the Adler zero arises in Eq. (5.68) as compared to the Veneziano–Lovelace–Shapiro (VLS) model [76–78]. In the latter, requiring a zero implies a relation between the trajectories appearing in different channels. Since only a single trajectory was considered (i.e., that of the exchange degenerate ρ–f_2 mesons), this required $\alpha(s) + \alpha(t) = 1$ and fixes $\alpha(0) = 1/2$ in the chiral limit. From this perspective, the zero is

a manifestly crossing symmetric phenomenon with the direct-channel and crossed-channel RTs interfering near the Adler point. In Eq. (5.68), the zero arises from the interplay of purely $I = 0$ trajectories in the direct channel and necessitates a trajectory with negative intercept, a typical feature of scalar resonances, interfering with the Pomeron. Considering subleading terms in the momentum expansion, more trajectories, or the fully crossing symmetric combination Eq. (5.51) can modify the location of the zero, but will not change the basic mechanism of Eq. (5.68). While the original VLS model cannot accommodate the Pomeron, extensions to include its effects concluded it should play an important role in satisfying chiral constraints [246, 247]. As such, we find the interpretation of the zero in terms of $\sigma/\mathbb{P}$ interference in the direct channel particularly appealing.[12]

Further, since unitarity will only affect the shape of the RT, the amplitude Eq. (5.68) will contain an Adler zero even if we only consider the homogeneous unitarity equation without requiring the inverse amplitude, in this case $\alpha_\sigma(s)$, to have a sub-threshold pole. This is unlike the typical Omnès function approach, which requires introducing *ad hoc* parameters, i.e., subtraction polynomials [248], when considering homogeneous unitarity.

We may enforce Eq. (5.57) at leading order of Eq. (5.68) if

$$\operatorname{Im}\alpha_\sigma(s) = \rho(s)\left[g_\sigma^2\left|1+\frac{g_{\mathbb{P}}^2}{g_\sigma^2}\alpha_\sigma(s)\right|^2 + \mathcal{O}\left(\hat{q}_s^4\right)\right]. \tag{5.69}$$

Since by assumption $|\alpha_\sigma(s)| < s$, Eq. (5.69) is still of the form in Eqs. (5.42) and (5.44), albeit no longer a simple polynomial in momentum.

We begin by assuming that the σ RT admits a solution similar to the ρ as considered in Sec. 5.4.1. If this is the case, $\operatorname{Re}\alpha_\sigma \sim \sqrt{s} \to +\infty$ with known asymptotic limits for both real and imaginary parts and one may choose

$$r_\sigma(s) = g_\sigma^2\left|1+\frac{g_{\mathbb{P}}^2}{g_\sigma^2}\,\alpha_\sigma(s)\right|^2 + c_\sigma\,\hat{q}_s^{2(1+\operatorname{Re}\alpha_\sigma(s))}, \tag{5.70}$$

such that

$$\operatorname{Im} f_0^0(s) = \rho(s)\,|f_0^0(s)|^2 + \mathcal{O}\left(\hat{q}_s^{2(1+\operatorname{Re}\alpha_\sigma(s))}\right), \tag{5.71}$$

satisfies Eq. (5.57) at leading order assuming $\operatorname{Re}\alpha_\sigma(s \gtrsim 4M_\pi^2)$ is not too negative. Since very little is known about the σ trajectory from measurements, we have more parameters, i.e., $\alpha_\sigma(0)$, g_σ^2, $g_{\mathbb{P}}^2$, γ_σ, and c_σ, to determine by minimizing Eq. (5.61) with our iterative fitting procedure. We choose an initial guess of

$$\alpha_\sigma(s) = \frac{-0.2 + 0.1\,\mathrm{GeV}^{-2}s}{\sqrt{1+s/(20\,\mathrm{GeV}^2)}} \tag{5.72}$$

and fit evenly spaced points from $4M_\pi^2$ to $0.5\,\mathrm{GeV}^2$. This fitting range is selected to minimize the effect of the $f_0(980)$, which is not included.

The first two iterations are plotted in Fig. 5.9, where we see a dramatically different behavior than in Fig. 5.7. Specifically, subsequent iterations have the effect of reducing the

[12] The $I = 2$ S-wave is also predicted to have an Adler zero as a consequence of chiral symmetry. In our formalism, this zero must come from a different mechanism than that of $I = 0$ as, in the former, the Pomeron only contributes indirectly through the crossed channel. We do not investigate plausible alternatives for this channel here.

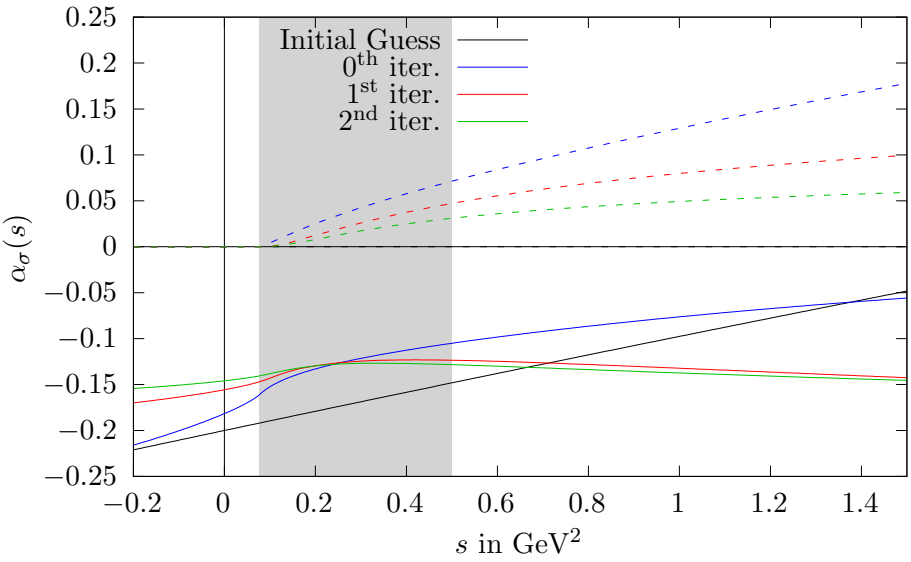

Figure 5.9: First three iterations of the integral equation for $\mathrm{Re}\,\alpha_\sigma(s)$ (solid) and $\mathrm{Im}\,\alpha_\sigma(s)$ (dashed) using Eq. (5.70). The fitted region is shaded and we see a trend towards negative $\mathrm{Re}\,\alpha_\sigma(s)$ with subsequent iterations.

i	$\alpha(0)$	g_σ^2	$g_{\mathbb{P}}^2$	γ_σ	c_σ	c'_σ
			[Eq. (5.70)]			
0	-0.182	0.228	1.170	0.523	1.053	
1	-0.156	0.362	2.243	0.111	$3.78 \cdot 10^{-3}$	
2	-0.146	0.533	3.586	0.082	$2.11 \cdot 10^{-5}$	
			[Eq. (5.73)]			
		0.137	1.886			0.014

Table 5.4: Fit parameters for the $\sigma/f_0(500)$ trajectory. We tabulate the first two iterations resulting from using Eq. (5.70) as well as the non-iterative solution using Eq. (5.73).

slope of $\mathrm{Re}\,\alpha_\sigma(s)$ as it tends to negative values. At the same time, the parameters at each iteration tabulated in Table 5.4 reveal c_σ approaches zero and, thus, the term $\propto \hat{q}_s^{2\mathrm{Re}\,\alpha_\sigma(s)}$, which is responsible for the indefinite rise of the real part of the RT, decouples from the integral equation. This implies that elastic unitarity disfavors stable solutions for the σ of the same type as for the ρ, with the former preferring an imaginary part that grows like some power of $\log s$ and $\mathrm{Re}\,\alpha_\sigma(s) \to -\infty$. Different choices of the initial guess change the other parameters and rate of $c_\sigma \to 0$, but ultimately reach the same conclusion.

Already, we can see that the shape being approached in Fig. 5.9 is highly non-linear and resembles the RTs from potential theory in non-relativistic quantum mechanics rather than the quintessential "stringy" dynamics of a relativistic confined quark model [249]. In addition, none of the iterations in Fig. 5.9 cross zero near threshold implying that, if these contain the σ pole, it is located deep in the complex plane and unlike a typical BW resonacne.

With the previous considerations, it is possible to choose a different parameterization

by setting $c_\sigma = 0$ in Eq. (5.70) from the beginning. Since we anticipate $\mathrm{Re}\,\alpha(s) \to -\infty$, Eq. (5.21) will be trivially satisfied and it is no longer required to find a stable iterative solution with $\gamma_\sigma > 1$. In fact, no iterative solution is needed at all, by choosing

$$\mathrm{Im}\,\alpha_\sigma(s) = \rho(s)\, g_\sigma^2 \left(1 + \frac{g_{\mathbb{P}}^2}{g_\sigma^2}\left[\alpha_\sigma(4M_\pi^2) + c'_\sigma\, \rho(s)\, \log\left(\frac{s}{4M_\pi^2}\right)\right]\right)^2 , \tag{5.73}$$

which is derived from Eqs. (5.41) and (5.70) by taking $\gamma_\sigma \to \infty$. This limit is taken because, with $c_\sigma = 0$, the trajectory will be asymptotically logarithmic (cf. Eq. (5.45)) and having $\mathrm{Im}\,\alpha_\sigma(s) \propto |\alpha_\sigma(s)|^2$ will no longer spoil the convergence of Eq. (5.35). We may thus remove the overall logarithm of Eq. (5.41) and dependence on γ_σ with the aforementioned limit. By shifting the subtraction point of the dispersion integral to $s = 4M_\pi^2$, we may further approximate the factor of $\alpha_\sigma(s)$ on the right-hand side of Eq. (5.69) by $\alpha_\sigma(s) \simeq \alpha_\sigma(4M_\pi^2) + c'_\sigma\, \rho(s)\, \log\big(s/4M_\pi^2\big)$,[13] which empirically describes the near-threshold behavior. Strictly speaking, since $\alpha_\sigma(s)$ is complex-valued above threshold, the parameter c'_σ should also be complex. The imaginary part must be a real function, however, and we keep c'_σ as a real parameter in Eq. (5.73), to be determined by the fit, and drop the absolute value.

Using Eq. (5.73), in principle, four free parameters are left to be determined by fit: $g_{\mathbb{P}}^2$, g_σ^2, $\alpha_\sigma(4M_\pi^2)$, and c'_σ. Note, however, that because the RT is now given in terms of fixed parameters instead of an iterative interpolation, up to an overall constant, the PW in Eq. (5.68) will only depend on the ratios $\alpha_\sigma(4M_\pi^2)/g_\sigma^2$ and c'_σ/g_σ^2. Then, since these are all *a priori* undetermined, at least one will be redundant and we fix $\alpha(4M_\pi^2) = -0.064$. This is the threshold value of the σ RT as calculated using the CRP model in Ref. [191], allowing for a direct comparison between the two approaches. When considering the fully crossing symmetric model, which is left for a future extension of this work, the parameters of the isobars in the crossed channel, i.e., the ρ coupling, will set a scale to break this ambiguity and allow a determination of $\alpha_\sigma(4M_\pi^2)$ (or equivalently $\alpha_\sigma(0)$).

The resulting S-wave amplitude and its parameters are shown in Fig. 5.10 and Table 5.4, respectively. Generally good agreement with unitarity within the fit range is observed, but significant deviations appear when extrapolating outside. As discussed before, higher-order terms in momentum, the presence of the $f_0(980)$, and the $K\bar{K}$ threshold become important at $s \geq 0.5\,\mathrm{GeV}^2$ and are beyond the scope of our minimal model.

Examining the RT in Fig. 5.11, we see a very similar shape to that being approached in Fig. 5.9: a nearly flat real part, which eventually turns downward before diverging to $\mathrm{Re}\,\alpha(s) \to -\infty$ logarithmically. We compare explicitly with the real and imaginary parts of the CRP $\alpha_\sigma(s)$ in Ref. [191]. Therein, a twice-subtracted dispersion relation, the S-wave PW with a single pole, and elastic unitarity are used and are in qualitatively good agreement with the GKPY amplitude. The CRP analysis concluded that the σ pole was consistent with a RT with a very small slope. In comparison, our trajectory in Fig. 5.11, grows even slower and is thus also consistent with a σ meson featuring a non-ordinary Regge behavior. Another indication of this is the observation that the real part of neither RT in Fig. 5.11 crosses the real axis in the vicinity of the σ meson. As was seen with the ρ resonance, the mass and width of narrow resonances lying on conventional rising

[13] Note that the Eq. (5.73) vanishes at threshold as $\mathrm{Im}\,\alpha_\sigma(s) \propto \rho(s) \propto \sqrt{s - 4M_\pi^2}$ and, thus, $\mathrm{Re}\,\alpha_\sigma(s) \to \alpha_\sigma(4M_\pi^2)$ linearly in $(s - 4M_\pi^2)$. The empirical simplification converges to the threshold value faster, but this does not affect the analytic properties of $\alpha_\sigma(s)$.

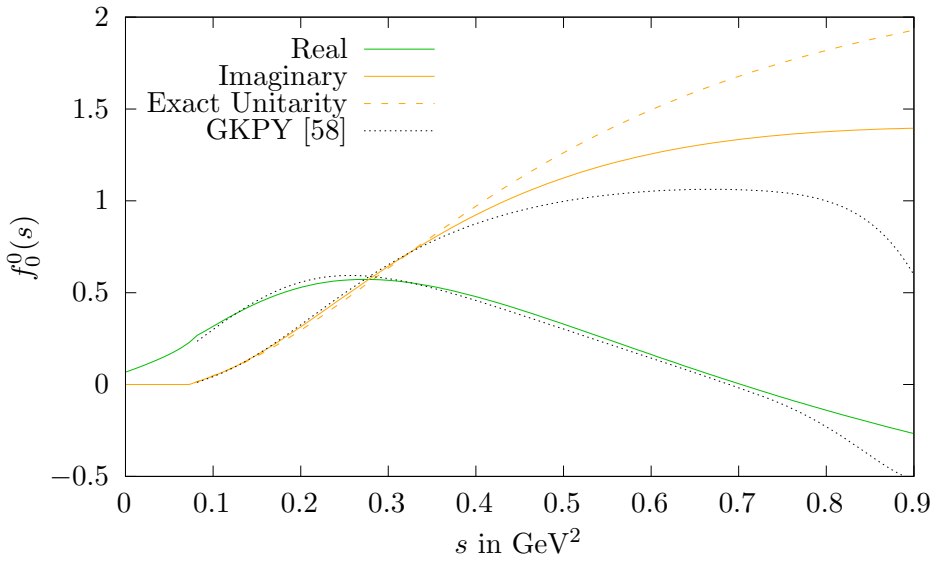

Figure 5.10: The S-wave PW projection for the $I = 0$ amplitude using Eq. (5.67) as described in the text. Legend is the same as in Fig. 5.6.

trajectories can be well estimated by expanding the RT around the integer values of the real part. This is clearly not the case for the σ whose real part has no zero crossing.

While our free parameters are determined by fitting the PWs, the CRP trajectory was calculated by ensuring that the σ pole and residue in the complex plane are consistent with those quoted in Ref. [58]. In order to compare, we also continue our trajectory to the second Riemann sheet where a single root satisfying $\alpha(s_\sigma) = 0$ is found with

$$\sqrt{s_\sigma} = (500 - i\,470)\,\text{MeV}\,, \tag{5.74}$$

and a residue in the PW of

$$|g_{\sigma\pi\pi}| = 7.9\,\text{GeV} \quad \text{and} \quad \phi_{\sigma\pi\pi} = -72^\circ\,. \tag{5.75}$$

While the mass and phase are in qualitatively good agreement with typical results extracted from precision studies [240, 241, 250–252], the width and size of the coupling deviate by about a factor of two. This is not entirely unexpected, as we recall that the model in Eq. (5.68), which is used to constrain the RT, is devoid of s-dependence except that coming from the $\alpha_\sigma(s)$. More specifically, using the homogeneous unitarity equation Eq. (5.57), we ignore any contribution from LHCs, which are well known to be important contributions to σ pole determinations [248, 253–255]. Because of this, $\alpha_\sigma(s)$ and therefore the width of the σ, must encompass the entire s-dependence of the PW, leading to this overestimation.

Another indication of this effect is the location of the Adler zero, which is located at $s_A = -0.05\,\text{GeV}^2$. From ChPT predictions, we should expect the Adler zero to be some *positive* factor of M_π^2 below threshold [248]. While the leading-order prediction places the zero at $s_A = M_\pi^2/2$ [139], its precise location is typically sensitive to the implementation of the LHC given the close proximity of the branch point at $s = 0$ as well as that of the

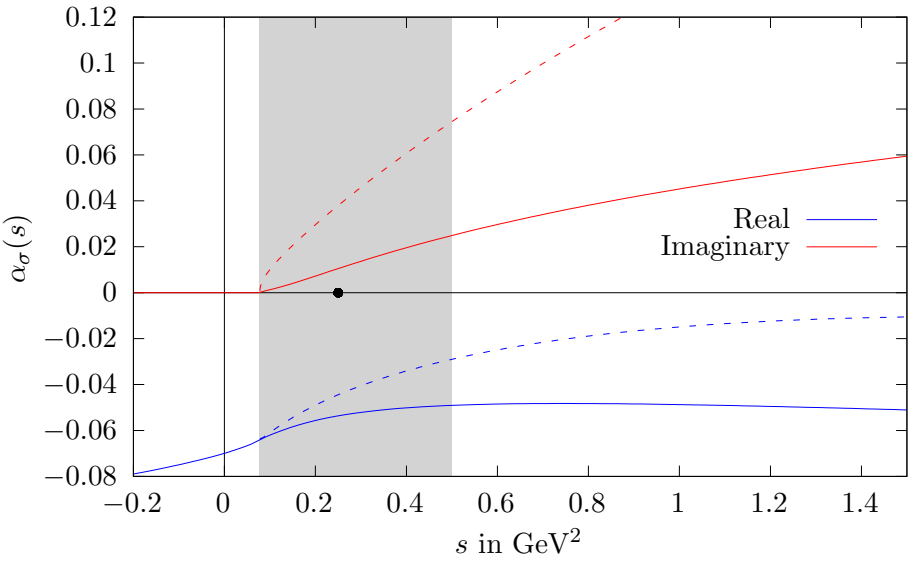

Figure 5.11: The σ trajectory as constrained by homogeneous elastic unitarity in Eq. (5.57) using Eq. (5.73) (solid). The fitted region is shaded and we compare with $\alpha_\sigma(s)$ as calculated in Ref. [191] (dashed) as well as with the expectation of a BW-like σ satisfying $\mathrm{Re}\,\alpha_\sigma(M_\sigma^2 \sim (0.5\,\mathrm{GeV})^2) = 0$ (grey dot). Unlike Fig. 5.7, no corresponding point calculating $\mathrm{Im}\,\alpha_\sigma(s)$ via Eq. (5.48) is shown.

RHC at $s = 4M_\pi^2$ [242, 248]. Our Adler zero at $s < 0$ would, in principle, overlap with the LHC if it were included and we thus expect a more in-depth analysis, which includes the crossed-channel contributions, to shift both pole and zero to values more consistent with other approaches. Regardless, we consider finding a pole (and zero) in the correct mass range with such a simple model and with few parameters provides reassurance that the formalism presented here is capable of describing more than just the classical examples of "simple" resonances such as the ρ.

One obvious advantage of working with RTs is that one can examine other properties about the σ, which would not be possible with typical PW analyses. Specifically, just like the extraction of the ρ' and ρ_3 in Sec. 5.4.1, the existence of radial and orbital excitations of the σ can be examined. These would-be σ' and σ_2 mesons correspond to the roots $\alpha_\sigma(s_{\sigma'}) - 1 = 0$ and $\alpha_\sigma(s_{\sigma_2}) - 2 = 0$, respectively, and can be searched in the same way as the ground state σ. Calculating $\alpha_\sigma(s)$ in the complex plane, we notice that on the unphysical sheet $\mathrm{Re}\,\alpha_\sigma(s) \to -\infty$ monotonically (and logarithmically) in every direction in the lower-half complex plane. Because of this, there are no positive integer values of $\alpha_\sigma(s)$ in the complex plane and we can conclude that the σ does not have any excitations. This is once again more akin to the RT of a non-relativistic potential with finitely many bound states as opposed to a conventional Reggeon [191, 249]. While it may be possible that coupling to higher thresholds can produce a RT that turns around above some energy, such a scenario would entail the excitations are somehow "induced" by inelastic thresholds, which we find highly unlikely.

5.5 Summary and outlook

To summarize, in this chapter we presented a parameterization for scattering amplitudes that recovers many expectations of S-matrix principles both at low energies and in the asymptotic limit. Since analyticity and crossing necessarily correlate the physics of hadron interactions at all energies and in all partial waves, our proposed formalism in terms of hypergeometric isobars and Regge trajectories allows these constraints to be rigorously imposed by using relatively simple functional forms. In this way, our model is a realization of the unification of a wide array of QCD phenomena: resonances in the complex-energy plane, existence of orbital/radial excitations, Reggeon exchanges in peripheral reactions, and even the scaling behavior emerging from parton exchanges in perturbative regimes. Here, we focused on the scattering of identical, spinless particles, but this constitutes a starting point for further applications, generalizations, and improvements on the basic formalism.

As first-order validation of the feasibility of our model, we examined low-energy $\pi\pi$ scattering. We showed the flexibility of our formalism to generalize for different isospins and meson families. A numerical method to enforce unitarity up to some momentum scale of interest, which parallels the implementation of the KT equations, was proposed and the Regge trajectories of the ρ and σ mesons were examined. Our results compared reasonably to existing literature and highlighted future improvements, which can lead to better extractions of these Regge trajectories. Specifically, we have paved the way towards generalizing the unitarization scheme to include the full effect of left-hand cuts in a crossing symmetric KT-like or Roy-like analysis using Regge poles. Because our formalism aims to describe scattering at all energies, such an analysis can also include experimental high-energy data directly to further constrain the amplitude.

Further generalizations to decay processes, coupled channels, unequal masses, and particles with spin will greatly increase the applicability of our model and allow a much more constrained determination of Regge trajectories. Since these are generalizations of poles in the relativistic S-matrix, Regge trajectories can be an important tool for the study of hadronic resonances.

5.A Hypergeometric formulae

We provide a summary of relevant properties of the hypergeometric function and its regularized form. The identities used here are expounded upon in Ref. [256].

The Gaussian hypergeometric function is defined for $|d| < 1$ through its power series

$$ {}_2F_1\left[a,\ b;\ c;\ d\right] = \sum_{n=0}^{\infty} \frac{(a)_n\,(b)_n}{(c)_n}\,\frac{d^n}{n!}\,, \tag{5.76} $$

where

$$ (x)_n = \frac{\Gamma(x+n)}{\Gamma(x)}\,, \tag{5.77} $$

is the Pochhammer symbol. Equation (5.76) manifests poles when c is a negative integer and thus we work with the regularized hypergeometric function defined in Eq. (5.11),

which is pole-free for all values of its arguments. For $|d| < 1$ the regularized power series reads:

$$ {}_2\tilde{F}_1\left[a,\ b;\, c;\, d\right] = \sum_{n=0}^{\infty} \frac{(a)_n\,(b)_n}{\Gamma(c+n)}\,\frac{d^n}{n!}\,. \tag{5.78} $$

The regularized hypergeometric function is also often represented in an integral form via

$$ {}_2\tilde{F}_1\left[a,\ b;\, c;\, d\right] = \frac{1}{\Gamma(b)\Gamma(c-b)}\int_0^1 \mathrm{d}x\, x^{b-1}(1-x)^{c-b-1}(1-xd)^{-a}\,, \tag{5.79} $$

which converges only for $\mathrm{Re}\,(c) > \mathrm{Re}\,(b) > 0$ and $|\arg(1-d)| < \pi$.

To consider asymptotic limits, the power series representation of ${}_2\tilde{F}_1$ in $1/d$ converges as $|d| \to \infty$ and with $a > b$ reads

$$ {}_2\tilde{F}_1\left[a,\ b;\, c;\, d\right] \to \frac{\Gamma(b-a)}{\Gamma(b)\Gamma(c-a)}(-d)^{-a} + \frac{\Gamma(a-b)}{\Gamma(a)\Gamma(c-b)}(-d)^{-b}\,, \tag{5.80} $$

as long as $b-a$ is not an integer. This latter caveat is important as there are apparent poles emerging from the Γ functions in the numerators of both terms in the expansion. As we approach one of these apparent poles, taking $b \to a+n$ for integer $n \geq 1$, the leading term becomes

$$ {}_2\tilde{F}_1\left[a,\ a+n;\, c;\, d\to\infty\right] \to \frac{(n-1)!}{\Gamma(a+n)\,\Gamma(c-a)}\,(-d)^{-a} \tag{5.81} $$

without a pole. The specific form of the asymptotic limit that we require is multiplied by additional powers of the parameter d (cf. Eq. (5.10)) and we write this particular case as

$$ \begin{aligned} d^j\,{}_2\tilde{F}_1\left[1+j,\ j-\alpha;\, 1+j-\alpha;\, d\to\infty\right] \\ \to (-1)^j\left(\frac{1}{\Gamma(j-\alpha)(-1-\alpha)}\,(-d)^{-1} + \frac{\Gamma(1+\alpha)}{\Gamma(1+j)}(-d)^{\alpha}\right)\,. \end{aligned} \tag{5.82} $$

Finally, Eq. (5.82) seems to manifest a pole in both terms at $\alpha \to -1$, but when taking the limit we see that the result is free of poles:

$$ d^j\,{}_2\tilde{F}_1\left[1+j,\ 1+j;\, 2+j;\, d\to\infty\right] \to \frac{(-1)^j}{j!}\,\log d\,(-d)^{-1}\,. \tag{5.83} $$

Although we do not compute the limits for $\alpha \to -j$ for any integer $j > 1$, similar expressions may be derived and Eq. (5.82) is finite and pole-free everywhere.

5.B Fixed-angle scattering

While the Regge limit explored in Sec. 5.2.1 is of more immediate interest as it relates to the properties of hadrons in different channels, the limit of large s with fixed angle z_s, i.e., large $-t$ with the ratio t/s fixed, connects the hadron level amplitude with the inter-meson dynamics of parton exchanges [257, 258]. In particular, while the behavior $s^{\alpha(t)}$ is characteristic in the Regge limit, at fixed angles, hadronic cross sections exhibit scaling properties of the form

$$ \frac{\mathrm{d}\sigma}{\mathrm{d}t} \simeq \frac{1}{s^2}\,|\mathcal{T}(s,t,u)|^2 \propto s^{-N}\,, \tag{5.84} $$

where the power N is constant and argued to be related to the number of constituent partons involved in the scattering process [259–261].

In this limit, Veneziano-based amplitudes with linear trajectories fall exponentially and are thus entirely unable to reproduce the power-law scaling in Eq. (5.84) [54, 262]. More sophisticated dual models such as dual amplitudes with Mandelstam analyticity (DAMA) can be made to exhibit fixed-angle scaling, but at the cost of logarithmically bounded Regge trajectories [263, 264]. While a DAMA model of this form can provide a unified description of both fixed-angle and Regge phenomena, the slowly growing RTs make it difficult to also simultaneously describe the resonance spectra at timelike energies. Of note, however, is that DAMA with a logarithmic trajectory allows a microscopic interpretation of its integral representation in terms of meson wave functions and the loop momentum of exchanged partons [262].

To investigate under which assumptions the model in Sec. 5.2 exhibits the scaling behavior, we will use a slightly generalized form of the isobar function with $j_{\min} = 0$,

$$F(\alpha(s), \nu_s) = \Gamma(-\alpha(s))\, {}_2\tilde{F}_1\left[\eta,\ -\alpha(s);\ 1-\alpha(s);\ \hat{\nu}_s\right], \tag{5.85}$$

which reduces to Eq. (5.10) with $\eta = 1$. In the large energy limit at fixed s-channel scattering angle θ_s, all three Mandelstam variables are large and we may use

$$t \to -s\,\cos^2\frac{\theta_s}{2} \quad \text{and} \quad u \to -s\,\sin^2\frac{\theta_s}{2}. \tag{5.86}$$

We will ignore fixed angular factors and consider only the powers of s. This limit thus involves considering $s \to +\infty$ while both t and $u \to -\infty$. With the usual assumptions on the RTs in Sec. 5.2.1, the s-channel isobar $\mathcal{F}^{\pm}(s, z_s) \to 0$ exponentially as in Eq. (5.20). The leading powers of s will thus be given by the t- and u-channel isobars, which decrease proportional to $t^{-\eta}/\alpha(t)$ and $u^{-\eta}/\alpha(u)$, respectively (cf. Eq. (5.18)). Since the RTs we consider are unbounded in both directions, as $t, u \to -\infty$, both RTs $\alpha(t)$ and $\alpha(u) \to -\infty$, and the term of Eq. (5.18) becomes the leading s behavior. Since these will scale with the same powers of s, it is sufficient to examine one of these terms.

Because $\alpha(t)$ is assumed to satisfy the once-subtracted dispersion relation of Eq. (5.35), there is an $0 \leq \epsilon < 1$ such that $|\alpha(t \to -\infty)| \lesssim s^{1-\epsilon}$. This means that in the high-energy limit at fixed angle, the amplitude Eq. (5.7) will scale as

$$|\mathcal{T}(s,t,u)|^2 \propto \left|\frac{t^{-\eta}}{\alpha(t)}\right|^2 \propto s^{-2(\eta+1-\epsilon)}, \tag{5.87}$$

and the resulting differential cross section as

$$\frac{\mathrm{d}\sigma}{\mathrm{d}t} \propto s^{-2(\eta+2-\epsilon)}. \tag{5.88}$$

Here, we see that regardless of the exact behavior of $\alpha(t)$, as long as it is unbounded in the negative direction, the cross section exhibits fixed power-law scaling behavior with any combination of isobars of the form Eq. (5.85). The parameter η can be used to change the leading power of s to accommodate theoretical predictions or experimental data. In this way, this isobar model smoothly connects the hadronic component of the isobars, i.e., as encoded through $\alpha(s)$, to the parton-level dynamics, which are governed by η.

In the case of $\pi\pi$ scattering, fixed-angle high-energy scattering is not experimentally possible and we thus do not attempt to fine-tune η. Instead, we look at the expectation from Regge phenomenology as described in Sec. 5.2.1 as well as predictions of hadron scattering processes at large transverse momentum from perturbative QCD (pQCD). Specifically, Refs. [257, 265] argue that because the large s- and $|t|$-regime of exclusive hadron processes should be dominated by constituent parton exchanges, all hadron RTs will couple to a lower RT that encodes hard physics and is effectively constant. Such a trajectory would correspond to that of a Reggeized *quark* and satisfies $\alpha_q(t \to -\infty) = -1$ [231]. We thus fix $\eta = -\alpha_q(t) \approx 1$. Identifying the lower bounding behavior of Eq. (5.16) as arising from a lower-lying quark RT can be trivially considered by generalizing η to a function of t but is not considered here.

With the specific form of Eq. (5.10) and with η fixed as above, the scaling of Eq. (5.84) is $N = 6 - 2\epsilon$. Simple dimensional counting arguments from pQCD predict the elastic scattering of mesons each with two constituents, i.e., a quark–antiquark pair, have $N = 6$ [260, 261]. With the trajectories fitted in Sec. 5.4, the scaling will be dominated by the slowest trajectory, which is that of the σ. Since our $\alpha_\sigma(s)$ grows logarithmically, it is bounded by any power of s and we can set $\epsilon = 1$ (minus a positive infinitesimal) giving our $\pi\pi$ amplitude a scaling with $N = 4$. As discussed above, the connection of this scaling behavior and pQCD offers an enticing connection between the σ and quark exchange dynamics and may offer clues into the internal structure of the former.

5.C Duality

In this appendix, we briefly compare the isobar model constructed in Sec. 5.2 with commonly held notions of resonance–Regge duality. The concept that s-channel poles are "dual" to t-channel poles was first encountered by considering the finite-energy sum rules (FESRs) resulting from the analyticity of scattering amplitudes [186, 266]. If an amplitude is analytic and satisfies crossing symmetry then one may write a dispersion relation up to some finite energy N and derive a self-consistency relation of the form

$$\frac{1}{2}\int_{-N}^{N} \mathrm{d}s' \,\mathrm{disc}\,\mathcal{T}(s',\,t,\,u) \simeq \sum_i \mathbb{R}_i(N,t)\,. \tag{5.89}$$

Here, an integral over the discontinuities along both LHC and RHC is related to a sum over Regge terms given by Eq. (5.13) on the right-hand side. For simplicity, we have ignored the contributions of the background integral and the possible presence of Regge cuts.

Considering Eq. (5.89) in the narrow-width approximation leads to the observation that an amplitude that contains resonances and Regge behavior separately, i.e.,

$$\mathcal{T}(s,t,u) = \mathcal{T}_{\mathrm{Res}}(s,t,u) + \mathcal{T}_{\mathrm{Regge}}(s,t,u)\,, \tag{5.90}$$

leads to violations of the FESRs (and therefore analyticity) in intermediate energies where the two terms can interfere, i.e., the "double counting" problem [186, 267]. A proposed solution was that the resonance and Regge behaviors are dual to each other, in the Dolen–Horn–Schmid (DHS) sense, meaning they must arise from a single function when evaluated in different limits and there is therefore no second term with which to interfere. This led

to the general conception that amplitudes will fall into one of two distinct categories: dual models, which realize this DHS duality, or interference models, which sum direct-channel and crossed-channel processes like in a Feynman-diagram-based approach. Since only the former is thought to satisfy the FESRs, it is believed to be more fundamental.

The isobar model constructed in Sec. 5.2 belongs in the latter category with explicit sums of poles in the s-, t-, and u-channels. The model in Eq. (5.7), however, also satisfies the FESRs by construction as evident by the analyticity of Eq. (5.10), the cut structure in Fig. 5.2, and the Regge asymptotics in Sec. 5.2.1. Indeed, whether satisfying the FESRs requires amplitudes to be dual in the DHS sense has been criticized in Refs. [216, 268–271], since interference models can be constructed to satisfy Eq. (5.89) when going beyond the narrow-resonance approximation and introducing cuts. Our model is one realization of these ideas, with the cuts of the RTs playing a pivotal role in the Regge asymptotics (cf. Eq. (5.20)).

Other works further criticized the distinction between dual and interference with proofs that, under general assumptions, amplitudes can always be decomposed into separate resonance and Regge terms akin to an interference model [193, 272, 273]. In light of this seemingly blurry boundary between the two classes of models, Ref. [216] suggests an unambiguous statement of duality. It states that resonances and Regge behavior are dual if they both arise from the same function $\alpha(s)$ with respect to poles in the complex j-plane. As explored in Secs. 5.2.1 and 5.2.2, this is the case for our model.

In addition to the general considerations above, we can explicitly compare the implementation of our model to $\pi\pi$ scattering, discussed in Sec. 5.4 and expressed in the charge basis in Appendix 5.D, to dual amplitudes for the same reaction, particularly the VLS model [76–78] and the broader class of DAMA models (for a general survey of the latter, see Refs. [54, 274, 275] and references therein).

In a generic dual model, the charge basis $\pi\pi$ amplitude of Eq. (5.107) is decomposed in terms of a single function of two variables [78]:

$$\mathcal{M}(s,t,u) = V(s,t) + V(s,u) - V(t,u)\,, \tag{5.91}$$

where $V(s,t) = V(t,s)$ contains resonances in either the s- or t-channel in different limits. The structure of Eq. (5.91) is fairly rigid to ensure the absence of $I = 2$ resonances when constructing isospin amplitudes with Eq. (5.106) [53]. The choice of the function $V(s,t)$, however, can be shown to be fairly general and, in the language of DAMA, typically defined in terms of an integral of the form

$$V(s,t) = \int_0^1 dx\, x^{-\alpha(s)-1}\,(1-x)^{-\alpha(t)-1}\,g(s,t,x)\,, \tag{5.92}$$

with a kernel function $g(s,t,x) = g(t,s,1-x)$, which is regular at the end points of integration. A classical choice of the kernel is a constant, i.e., $g(s,t,x) = g^2$, which reproduces the Euler beta function:

$$V(s,t) = g^2\,\frac{\Gamma(-\alpha(s))\,\Gamma(-\alpha(t))}{\Gamma(-\alpha(s)-\alpha(t))}\,, \tag{5.93}$$

and is the basis of the VLS model. More complicated functions have also been considered, cf. Ref. [276]. The integral in Eq. (5.92) does not typically converge for all s and t and must be extended, e.g., to the resonance region $\alpha(s) > 0$, through analytic continuation [54].

We want to consider whether the isobar model constructed in Sec. 5.4 can recover the structure of Eqs. (5.91) and (5.92), despite not appearing as a dual model. First, the absence of $I = 2$ is trivially achieved in Eq. (5.51) by decoupling any s-channel RTs in that channel. Thus, we set all couplings in $I = 2$ to zero such that Eq. (5.107) reduces to:

$$\mathcal{M}(s,t,u) = \frac{1}{3}\mathcal{F}^0(s,z_s) + \frac{1}{2}\left[\mathcal{F}^1(t,z_t) - \mathcal{F}^1(u,z_u)\right] . \tag{5.94}$$

The remaining $I = 0$ and 1 isobars can then be assumed to be given by a single exchange degenerate trajectory $\alpha(s)$ with $j_{\min} = 0$ and the couplings in the different isospins related to a universal coupling by $g^2 = g_0^2/3 = g_1^2/2$ (cf. the exchange degeneracy assumptions in Eq. (5.64)). With Eq. (5.50) and these choices, Eq. (5.94) can be cast in the same form as Eq. (5.91) using:

$$\begin{aligned} V(s,t) &= \frac{g^2}{2}\left[F(\alpha(s),\,\nu_s) + F(\alpha(t),\,\nu_t)\right] , \\ V(s,u) &= \frac{g^2}{2}\left[F(\alpha(s),\,-\nu_s) + F(\alpha(u),\,-\nu_u)\right] , \\ V(t,u) &= \frac{g^2}{2}\left[F(\alpha(t),\,-\nu_t) + F(\alpha(u),\,\nu_u)\right] , \end{aligned} \tag{5.95}$$

in terms of the isobar functions in Eq. (5.10). These functions are symmetric in their arguments and related only by the interchange of Mandelstam variables. As discussed in Sec. 5.2.2, near a resonance pole in the complex plane, $V(s \to s_j, t) \propto P_j(z_s)/(j - \alpha(s))$, while simultaneously $V(s, t \to t_j) \propto P_j(z_t)/(j - \alpha(t))$. Further, the spectrum of the Chew–Frautschi plot of Eq. (5.95) matches that of Eq. (5.93) (albeit not on linear, real trajectories), since $V(s,t)$ is not yet symmetrized with a definite parity. When evaluating the Regge limits with the usual assumptions in Sec. 5.2.1, we have $V(s \to \infty, t) \propto s^{\alpha(t)}$ and $V(s, t \to \infty) \propto t^{\alpha(s)}$, once again as in Eq. (5.93).

Unlike Eq. (5.93), however, these limits are achieved through the sum of infinitely many terms in both $(j-\alpha(s))^{-1}$ and $(j-\alpha(t))^{-1}$. Thus, a limiting case of our model can recover all the same phenomenological features of the VLS amplitude, but without DHS duality. Moreover, our amplitude easily loosens the assumptions of exchange degeneracy, zero-width resonances, and linear trajectories, which have been notorious difficult challenges for Veneziano-like amplitudes to overcome.

We can also compare Eq. (5.95) to the more general class of DAMA models given by Eq. (5.92). Using the integral form of the regularized hypergeometric function, Eq. (5.79), we can write the isobar in Eq. (5.10) as:

$$F(\alpha(s),\,\nu_s) = \int_0^1 \mathrm{d}x\, \frac{x^{-\alpha(s)-1}}{1-\hat{\nu}_s\, x} , \tag{5.96}$$

which converges so long as $\mathrm{Re}\,\alpha(s) < 0$. With this representation, Eq. (5.95) is of the form Eq. (5.92) with the choice

$$g(s,t,x) = \frac{g^2}{2}\left[\frac{(1-x)^{\alpha(t)+1}}{1-\hat{\nu}_s\, x} + \frac{x^{\alpha(s)+1}}{1-\hat{\nu}_t\,(1-x)}\right] , \tag{5.97}$$

which satisfies the necessary symmetries and is regular at $x = 0$ and 1. This seems to suggest a close connection between our amplitude and DAMA, albeit with a choice of a

kernel that separates s- and t-channel components and thus breaks the intrinsic duality. Such a splitting of DAMA into an interference-like representation has been considered in Refs. [54, 273], although with different model constructions. Equation (5.97) is a particularly convenient choice as it allows the analytic continuation to arbitrary $\alpha(s)$ and $\alpha(t)$ to be done in closed form via the hypergeometric function in Eq. (5.10).

Because we are able to write the isobars in the form of the DAMA integral and have scaling properties as explored in Appendix 5.B, we conjecture a similar microscopic interpretation of the kernel in Eq. (5.97) in terms of meson wave functions and interchanged parton momentum as in Ref. [257] but do not explore this here.

5.D Isospin structure

Here, we show that Eq. (5.51) is indeed crossing symmetric by computing the amplitudes projected onto the t- and u-channel isospin bases. The s–t isospin crossing matrix is already defined in Eq. (5.52) and we define two more matrices [49]

$$C_{su} = \begin{pmatrix} \frac{1}{3} & -1 & \frac{5}{3} \\ -\frac{1}{3} & \frac{1}{2} & \frac{5}{6} \\ \frac{1}{3} & \frac{1}{2} & \frac{1}{6} \end{pmatrix} \tag{5.98a}$$

and

$$C_{tu} = \begin{pmatrix} 1 & 0 & 0 \\ 0 & -1 & 0 \\ 0 & 0 & 1 \end{pmatrix} . \tag{5.98b}$$

The elements of Eq. (5.98a) are related to those in Eq. (5.52) by $C_{st}^{II'} = (-1)^{I+I'} C_{su}^{II'}$. Each matrix obeys $C_{st}^2 = C_{su}^2 = C_{tu}^2 = 1$ as well as the cyclic relations

$$C_{st}\, C_{tu} = C_{tu}\, C_{su} = C_{su}\, C_{st} \tag{5.99a}$$

and

$$C_{su}\, C_{tu} = C_{tu}\, C_{st} = C_{st}\, C_{su} . \tag{5.99b}$$

These matrices arise as coefficients when considering isospin amplitudes in different frames. For example, defining a vector with respect to isospin components,

$$\vec{\mathcal{T}}(s,t,u) = \begin{pmatrix} \mathcal{T}^0(s,t,u) \\ \mathcal{T}^1(s,t,u) \\ \mathcal{T}^2(s,t,u) \end{pmatrix} , \tag{5.100}$$

crossing symmetry requires the t-channel isospin amplitudes to fulfill

$$\vec{\mathcal{T}}(t,s,u) = C_{st}\, \vec{\mathcal{T}}(s,t,u) , \tag{5.101a}$$

and similarly for the u-channel

$$\vec{\mathcal{T}}(u,t,s) = C_{su}\, \vec{\mathcal{T}}(s,t,u) . \tag{5.101b}$$

Defining an analogous vector for the isospin-definite isobars in Eq. (5.50),

$$\vec{\mathcal{F}}(s,z_s) = \begin{pmatrix} \mathcal{F}^0(s,z_s) \\ \mathcal{F}^1(s,z_s) \\ \mathcal{F}^2(s,z_s) \end{pmatrix} , \tag{5.102}$$

we can write Eq. (5.51) compactly as:

$$\vec{\mathcal{T}}(s,t,u) = \vec{\mathcal{F}}(s,z_s) + C_{st}\,\vec{\mathcal{F}}(t,z_t) + C_{su}\,\vec{\mathcal{F}}(u,z_u)\,. \tag{5.103}$$

Then, we calculate

$$\begin{aligned} C_{st}\,\vec{\mathcal{T}}(s,t,u) &= C_{st}\,\vec{\mathcal{F}}(s,z_s) + \vec{\mathcal{F}}(t,z_t) + C_{su}\,C_{tu}\,\vec{\mathcal{F}}(u,z_u) \\ &= C_{st}\,\vec{\mathcal{F}}(s,z_s) + \vec{\mathcal{F}}(t,z_t) + C_{su}\,\vec{\mathcal{F}}(u,-z_u) \\ &= \vec{\mathcal{T}}(t,s,u)\,, \end{aligned} \tag{5.104a}$$

where $C_{tu}\,\vec{\mathcal{F}}(x,z_x) = \vec{\mathcal{F}}(x,-z_x)$ is used. For the u-channel, the calculation proceeds identically:

$$\begin{aligned} C_{su}\,\vec{\mathcal{T}}(s,t,u) &= C_{su}\,\vec{\mathcal{F}}(s,z_s) + C_{st}\,\vec{\mathcal{F}}(t,-z_t) + \vec{\mathcal{F}}(u,z_u) \\ &= \vec{\mathcal{T}}(u,t,s)\,, \end{aligned} \tag{5.104b}$$

and thus Eq. (5.103) indeed satisfies Eq. (5.101).

The starting point of our construction Eq. (5.51) are isobars that already carry definite isospin. However, we may also compare to the charge basis, which is the traditional starting point of narrow-resonance models, such as in Refs. [77, 78]. By defining the generic isospin amplitude

$$\mathcal{M}^{ijkl}(s,t,u) = \delta^{ij}\delta^{kl}\,\mathcal{M}(s,t,u) + \delta^{ik}\delta^{jl}\,\mathcal{M}(t,s,u) + \delta^{il}\delta^{jk}\,\mathcal{M}(u,t,s)\,, \tag{5.105}$$

with isospin indices i, j, k, and l in the Cartesian basis, the amplitude $\mathcal{M}(s,t,u)$ can be related to Eq. (5.51) by

$$\begin{pmatrix} \mathcal{T}^0(s,t,u) \\ \mathcal{T}^1(s,t,u) \\ \mathcal{T}^2(s,t,u) \end{pmatrix} = \begin{pmatrix} 3 & 1 & 1 \\ 0 & 1 & -1 \\ 0 & 1 & 1 \end{pmatrix} \begin{pmatrix} \mathcal{M}(s,t,u) \\ \mathcal{M}(t,s,u) \\ \mathcal{M}(u,t,s) \end{pmatrix} . \tag{5.106}$$

This relation may be inverted yielding the charge basis amplitude in terms of isobars:

$$\begin{aligned} \mathcal{M}(s,t,u) = \frac{1}{3}\,\mathcal{F}^0(s,z_s) + \frac{1}{2}\left[\mathcal{F}^1(t,z_t) - \mathcal{F}^1(u,z_u)\right] \\ - \frac{1}{3}\left[\mathcal{F}^2(s,z_s) - \frac{3}{2}\left(\mathcal{F}^2(t,z_t) + \mathcal{F}^2(u,z_u)\right)\right] . \end{aligned} \tag{5.107}$$

5.E Pole positions

In this appendix, we describe the procedure to extract the pole positions using the RTs constructed in the text. The resonances of a given isobar Eq. (5.10) correspond to integer values of $\alpha(s)$ in the complex s-plane. Thus, determining the location for a resonance

with spin j on a trajectory $\alpha(s)$ entails searching for roots of $(j - \alpha(s))$ on the second Riemann sheet in the lower-half complex plane. Because the trajectories are defined through Eq. (5.35), they are evaluated on the first Riemann sheet and must be continued to the unphysical sheet. This can be accomplished in a number of ways, but we use the Schlessinger Point Method (SPM) [277–281].[14] From $\alpha(s)$ evaluated through Eq. (5.35), we construct the continued fraction:

$$\tilde{\alpha}_N(s) = \alpha(s_1) \Big/ \left(1 + \frac{a_1(s-s_1)}{1 + \frac{a_2(s-s_2)}{\ddots_{a_N(s-s_N)}}}\right), \tag{5.108}$$

where the coefficients a_k for $k = 1, \ldots, N$ are chosen such that $\tilde{\alpha}_N(s_k) = \alpha(s_k)$ at $N+1$ energy points on the real line s_k. We refer to the appendix of Ref. [277] for the explicit formula to calculate each a_k recursively. If the points s_k interpolate a segment above threshold, then the resulting $\tilde{\alpha}_N(s)$ can be used to probe the unphysical Riemann sheet in the lower-half plane, which will be smoothly connected to the first Riemann sheet in the upper-half plane.

The interpolated s_k's are chosen to be evenly spaced points from threshold to some $s_{\max}$. For a given N and $s_{\max}$, then, poles are found by minimizing $|j - \tilde{\alpha}_N(s)|$ for the desired value of j. Once poles are found, their stability upon varying N and $s_{\max}$ must be verified as an analytic continuation using the SPM may introduce spurious singularities [290–292].

The above procedure can be done with the trajectory alone. In order to also extract the residue of the poles, however, we need to use the RT in conjunction with the fitted isobar model. Since the pole at $\alpha(s_j) = j$ will appear in the PW projection of the direct-channel isobar $f_j^I(s)$ in Eq. (5.55), the residue can be extracted by evaluating

$$g^2 = -16\pi \lim_{s \to s_j} (s - s_j) \frac{(2j+1)}{(2q_s)^{2j}} f_j^I(s)\,. \tag{5.109}$$

The PW projected isobar must also be continued to the second Riemann sheet, which can be accomplished using the SPM as above, or directly from Eq. (5.55) by replacing $\alpha(s)$ with Eq. (5.108). Once again, the stability of the residue must be checked by varying N and $s_{\max}$.

Because the RTs naturally sort resonances into different particle families each entering through a separate $F(\alpha_i(s), \nu_s)$ in Eq. (5.8), as we approach the pole, the residue in Eq. (5.109) will actually only depend on a single term in the sum of Eq. (5.55). This means the extraction of pole parameters in situations involving multiple resonances appearing on different RTs can be simplified, since, after the amplitude is fit to data, one only needs to examine a single trajectory at a time.

[14] Other methods that could be used are conformal expansions [254, 282], Laurent–Pietarinen expansions [283–285], or sequences of Padé approximants [286–289].

Part IV

Kaon processes

Chapter 6

Dispersive analysis of the Primakoff reaction $\gamma K \to K\pi$

6.0 Prologue

The content of this chapter is a short summary of the publication

- M. Dax, D. Stamen, and B. Kubis, *Dispersive analysis of the Primakoff reaction* $\gamma K \to K\pi$, Eur. Phys. J. C **81**, 221 (2021) [arXiv:2012.04655 [hep-ph]] ,

the two Master's theses

- M. Dax, Master's thesis, Bonn University (2020) ,
- D. Stamen, Master's thesis, Bonn University (2020) ,

and the proceeding

- D. Stamen, M. Dax, and B. Kubis, *Dispersive analysis of the Primakoff reaction* $\gamma K \to K\pi$, PoS **CD2021**, 048 (2021) .

The project extends the analyses of Refs. [117, 118], where the Primakoff process $\gamma\pi \to \pi\pi$ is investigated. This representation of the amplitude is currently used to analyze the pion COMPASS data to extract the chiral anomaly as well as the $\rho \to \pi\gamma$ coupling [295]. The idea is to provide a similar framework for the upcoming run on charged $\gamma K \to K\pi$ processes at the same facility. It is, however, expected that the statistics in the kaon case are decreased by roughly a factor of 8, while accounting for a longer run time [296].

Therefore, we provide a dispersion-theoretical representation of the Primakoff reaction amplitudes $\gamma K \to K\pi$ in all charge channels, including the neutral ones. The K-Long Facility (KLF) [297] in principle allows to measure these Primakoff events for a neutral kaon beam, but major experimental challenges remain and the expected event rate might be very small.

The main input to our analysis is a modern pion–kaon P-wave phase shift taken from Ref. [60]. We derive the respective reconstruction theorems for all charge channels to use Khuri–Treiman equations for the resulting single-variable amplitudes. Crossed-channel singularities in $\gamma\pi \to \bar{K}K$ are fixed from phenomenology wherever possible. Thereby, the narrow resonances ω and ϕ are described via a vector-meson dominance model and their respective couplings to $\pi\gamma$ and $\bar{K}K$. The decay $\omega \to \bar{K}K$ cannot be fixed directly from data; consequently, we use the output of an analysis of the timelike kaon form factor. This is compatible with fixing it from the $\phi \to \bar{K}K$ coupling and $SU(3)$ symmetry. Furthermore, the broad ρ is dispersively reconstructed via the $\pi\pi$ intermediate state.

Note that the $\gamma\pi \to \pi\pi$ amplitude is therefore used as an input for the crossed-channel contributions. We demonstrate how the subtraction constants can be matched to a low-energy theorem and radiative couplings of the $K^*(892)$ resonances, where the couplings are defined as the residues of the pole on the second Riemann sheet. The amplitude at the pole position is given in terms of the subtraction constants, allowing for a determination of the radiative couplings from a fit to experimental data. Altogether, we provide a model-independent framework for future analyses of high-precision kaon Primakoff data.

All these steps and main results were developed in the Master's theses of Maximilian Dax [293] and the author of this thesis [294] in fruitful cooperation. However, the publication [4] was only written later. Therefore, all figures were created and the main text parts therein were written by the author of this thesis. Prominently, the cross section results were only carried out during this time and are not part of the Master's theses. Therefore, the following chapter contains a short version of the technical details, since they are already explained greatly in the given references. However, the motivation for this project, the results, and discussions are kept in more detail. Furthermore, some other results are included that were only calculated or published in the literature after the publication. One of these is the calculation done in Ref. [298], where the next higher partial wave, the resonant D-wave including the $K_2^*(1430)$ resonance is calculated. It confirms the previous estimate of the applicable energy range for the dispersive treatment. Additionally, the analysis in Chapter 8 gives access to the $\omega \to \bar{K}K$ coupling. However, the uncertainties are larger than from the method used before, so that our analysis remains unchanged.

The following chapter provides an insight into the work done by the author of this thesis in the context of this project after the completion of the Master's theses, while giving enough details to make this chapter self-consistent and readable.

6.1 Introduction

The Wess–Zumino–Witten anomaly [299, 300] provides QCD predictions for processes of odd intrinsic parity at low energies. The textbook example is the two-photon decay of the neutral pion [26, 28, 29], which is determined, at zero quark masses, by the elementary charge, e, and the pion decay constant, F_π. The next-more-complicated reactions involving strong and electromagnetic interactions only are three-pseudoscalars–photon processes [301] such as $\gamma\pi \to \pi\pi$, or $\eta \to \pi\pi\gamma$. Low-energy theorems for these are of a very similar structure, i.e., they provide parameter-free predictions in terms of e and F_π, e.g.,

$$F_{3\pi} = \frac{e}{4\pi^2 F_\pi^3} \tag{6.1}$$

for $\gamma\pi \to \pi\pi$ [302–304]. This reaction can be investigated experimentally in a Primakoff reaction [305], with a charged-pion beam scattered off the Coulomb field of a heavy nucleus. Such experiments have been performed, with the objective to test the prediction of Eq. (6.1), at Serpukhov [306], or are being analyzed at COMPASS [295, 307].

The generalization of such Primakoff reactions to beams of charged kaons was conceived as early as in the 1960s [308], and put into practice in the 1970s both at the CERN Proton Synchrotron [309] and at AGS in Brookhaven [310], with refined experiments conducted in the 1980s at Fermilab [311–314]. The motivation here was mainly the exploration of radiative couplings of strange resonances, predominantly the $K^*(892)$, and the supposed relation of these (magnetic) radiative transitions, in the quark model, to quark

magnetic moments [311, 313]. KTeV has investigated Primakoff production of neutral strange resonances with a K_L beam [315], concentrating on radiative widths of heavier kaon resonances. Currently, the OKA experiment [316, 317] analyzes data on charged-kaon Primakoff reactions. In the future, high-precision data is expected from the upgrade to a kaon beam at AMBER [318–320]. Furthermore, the KLF collaboration plans a neutral kaon beam [297], where theoretically the Primakoff process could be measured, which will become experimentally very challenging due to the weaker Coulomb field compared to AMBER.

It was realized in Refs. [117, 118] for the anomalous photon–pion reaction that both aspects, low-energy theorem and chiral anomaly on the one hand, and radiative resonance couplings on the other, are intimately related to each other. Unitarity implies a close link between the amplitude $\gamma\pi \to \pi\pi$, at zero energy and in the chiral limit, and its behavior in the resonance peak region of the $\rho(770)$. This has the practical consequence that the prediction due to the anomaly can be tested with much better statistics [117]. In addition, using a dispersion-theoretical representation, the radiative coupling $\rho \to \pi\gamma$ can be extracted in a model-independent way, from the residue of the pole on the second Riemann sheet [118]. Furthermore, such dispersive amplitudes will also help to link lattice QCD calculations [321–323] to physical parameters [86, 120]. The overarching interest in $\gamma\pi \to \pi\pi$ is also justified by its role in the dispersive reconstruction of the neutral-pion transition form factor [122–124] and the latter's role for hadronic light-by-light scattering and the muon's anomalous magnetic moment [324, 325].

In this chapter, we construct a dispersion-theoretical representation for $\gamma K \to K\pi$ (in all possible charge configurations) that fulfills a similar feat. The chiral anomaly predicts the amplitudes for π^0 production to have the exact same value in the chiral limit and at zero energy as the analogous photon–pion reaction, see Eq. (6.1); based on the fundamental principles of analyticity and unitarity, the anomaly can also here be related to the radiative couplings of $K^*(892) \to K\gamma$ [313, 314, 326]. In this manner, our analysis provides a consistent framework to analyze future data, from OKA or AMBER, in a theoretically sound setting. The radiative K^* coupling constants are, inter alia, important input quantities for coupled-channel descriptions of photon–photon fusion reactions $\gamma\gamma \to \pi\pi/K\bar{K}$ [327, 328] and $\gamma\gamma \to \pi\eta/K\bar{K}$ [329, 330]. On a similar note, the full $\gamma K \to K\pi$ amplitudes might serve as a building block for an advanced analysis of Compton scattering on kaons, from which the kaon polarizabilities [331] can be extracted, the main motivation of the COMPASS kaon Primakoff program [332]. This will be explored in Chapter 7.

Previous theoretical work on these reactions is rather elusive. The channels with incoming charged kaons were calculated in Ref. [333] in a tree-level model based on effective Lagrangians for vector exchanges. For $\gamma K^- \to K^-\pi^0$ only, one-loop corrections in the chiral expansion have been considered [334, 335]. Here we derive Khuri–Treiman-type equations [97] for all possible charge configurations and solve these self-consistently for the (crossing-symmetric) s- and u-channels, while t-channel singularities are fixed from data and symmetry arguments as much as possible. To guarantee an accurate description of the universal kaon–pion final-state interactions, we employ phase shift input from corresponding Roy–Steiner analyses [60, 336, 337]. After the publication of Ref. [4] the Hadron Spectrum Collaboration calculated $\gamma K \to K\pi$ in lattice QCD with unphysical pion masses of 284 MeV [338].

The outline of this chapter is as follows: we introduce the necessary kinematics as well

as partial-wave and isospin formalism in Sec. 6.2, leading to the amplitude decomposition in terms of so-called reconstruction theorems. The fixed t-channel amplitudes are determined in Sec. 6.3. Section 6.4 is devoted to derivation and solution of the Khuri–Treiman equations for $\gamma K \to K\pi$. In Sec. 6.5, we discuss the matching of the subtraction constants, the free parameters of the dispersive representation, to the chiral anomaly and the radiative K^* couplings. Results for the cross sections are shown in Sec. 6.6. We summarize and conclude our study in Sec. 6.7.

6.2 Decomposition of the amplitude

We decompose the amplitude for the reaction $\gamma(q)K(p_1) \to K(p_2)\pi(p_0)$ in terms of a kinematic prefactor of odd intrinsic parity and the scalar amplitude $\mathcal{F}(s,t,u)$ according to

$$\mathcal{M} = i\epsilon_{\mu\nu\alpha\beta}\varepsilon^\mu p_1^\nu p_2^\alpha p_0^\beta \mathcal{F}(s,t,u)\,, \tag{6.2}$$

where ε^μ is the polarization vector of the photon and the Mandelstam variables [40] are given by $s = (q+p_1)^2$, $t = (q-p_0)^2$, and $u = (q-p_2)^2$. In the isospin limit with $M_\pi = M_{\pi^\pm}$ and $M_K = 0.496\,\text{GeV}$ (the convention used in the pion–kaon scattering analysis of Ref. [60]), the on-shell condition reads $s+t+u = 2M_K^2 + M_\pi^2 = 3s_0$ and the elastic threshold is given by $s_\text{th} = (M_K + M_\pi)^2$. The total cross section is given by

$$\sigma(s) = \frac{(s-M_K^2)\lambda^{3/2}(s,M_\pi^2,M_K^2)}{1024\pi s^2}\int_{-1}^{1}\mathrm{d}z_s(1-z_s^2)|\mathcal{F}(s,t,u)|^2\,. \tag{6.3}$$

In terms of isospin, the reaction $\gamma K \to K\pi$ is equivalent to pion photoproduction off a nucleon $\gamma N \to N\pi$ studied, e.g., in Refs. [339, 340]. For dispersion-theoretical analyses of scattering or (three-body) decay amplitudes, it is highly advantageous to decompose these in terms of single-variable amplitudes (SVAs). Decompositions of such a kind are commonly referred to as reconstruction theorems [47, 48, 121]. With one exception, we neglect discontinuities of partial waves with $\ell \geq 2$, resulting in the reconstruction theorems for $\mathcal{F}$ in the four different charge channels [4].

Despite the (potentially) very high accuracy of the representation at low energies, the range of applicability towards higher energies is clearly limited. One of the main limiting factors for a description of cross-section data in the direct or s-channel is the appearance of a resonant $K\pi$ D-wave around the $K_2^*(1430)$. Given a width of $\Gamma_{K_2^*(1430)} = 100(2)\,\text{MeV}$, this suggests our representation to be applicable up to well below $\sqrt{s} = 1.3\,\text{GeV}$ [298]. Furthermore, for the dominant $K\pi$ P-wave, we will stick to the implementation of elastic unitarity with $K\pi$ intermediate states only, which will break down around the $K^*(1410)$ resonance ($\Gamma_{K^*(1410)} = 232(21)\,\text{MeV}$) with its large inelastic coupling mainly to $K\pi\pi$. For this reason, the dispersive amplitude representation we aim for is supposed to be valid to good approximation up to $\sqrt{s} \approx 1.2\,\text{GeV}$.

6.3 Singularities in the *t*-channel

The usual approach to analyzing Khuri–Treiman-type systems is to solve the unitarity relations for the single-variable amplitudes in all three channels fully self-consistently. This is an obvious strategy for perfectly crossing-symmetric systems such as $\gamma\pi \to \pi\pi$ [117, 120],

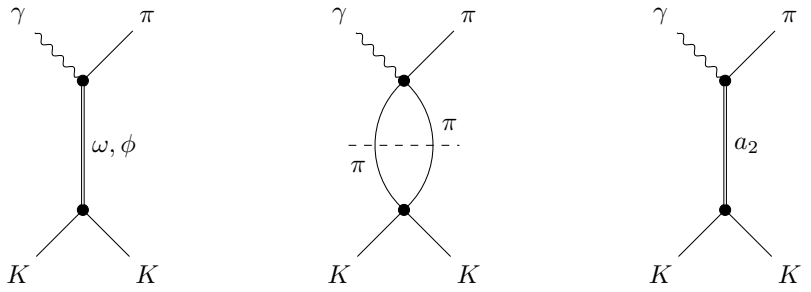

Figure 6.1: t-channel contributions to $\gamma K \to K\pi$; see main text for the individual terms.

related three-pion decays [2, 81], or even pion–pion scattering [119], but has also been followed for less symmetric processes such as $\eta \to \pi^+\pi^-\pi^0$ [111], $\eta' \to \eta\pi\pi$ [109], or $D \to \bar{K}\pi\pi$ [105, 110]. We do not pursue this approach here as far as the t-channel is concerned, for the following reasons: the t-channel singularities in $\gamma K \to K\pi$ are either dominantly inelastic (ρ, a_2), or consist of very narrow poles (ϕ), or both (ω); see Fig. 6.1. For this reason, in our analysis we approximate these by fixed t-channel contributions, similar in spirit, e.g., to various analyses of $\gamma\gamma \to \pi\pi$ [327, 341] or the description of left-hand cuts in $\eta^{(\prime)} \to \pi^+\pi^-\gamma$ [342].

The isospin $I = 0$ P-wave amplitude $\mathcal{G}^{(+)}(t)$ is dominated by the ω and ϕ vector mesons. We calculate this SVA via tree-level exchanges with intermediate vector resonances $V \in \{\omega, \phi\}$, see Fig. 6.1. To this end we use the effective Lagrangian from Ref. [343].

The $\omega \to K\bar{K}$ coupling required for the dominant ω-exchange contribution cannot be determined from a direct decay. One option is to simply fix it using $SU(3)$ symmetry, with plausible guesses at best of the uncertainty attached. A somewhat more data-driven access to this coupling can be obtained by relying on a vector-meson-dominance (VMD) model fitted to timelike kaon form factor data from $e^+e^- \to K^+K^-$, K_SK_L, and $\tau^- \to K^-K_S\nu_\tau$, see Model II in Ref. [344]. Together with the ω–photon coupling from $\omega \to e^+e^-$ [118] we obtain $g_\omega = 7.1(0.8)$. The error is dominated by the fit value from Ref. [344]; within uncertainties, g_ω is indeed compatible with $SU(3)$ symmetry. Furthermore, a combined analysis of the spacelike and timelike kaon form factors can be used to determine $g_{\omega_n} = 5.7(1.9)$ and $g_{\omega_c} = 8.1(1.9)$ in the neutral and charged case, hence compatible, but with larger uncertainties [6], cf. Chapter 8.

Adding the ω and ϕ tree-level contributions, we obtain the SVA

$$\mathcal{G}^{(+)}(t) = e\left[\frac{g_\omega d_\omega}{M_\omega^2 - t} - \frac{\sqrt{2} g_\phi^c \bar{d}_\phi}{M_\phi^2 - t}\right]. \tag{6.4}$$

We use zero-width propagators for the vector mesons as t is negative in $\gamma K \to K\pi$.

The isospin $I = 1$ $\gamma\pi \to K\bar{K}$ P-wave $\mathcal{G}^{(0)}(t)$ is dominated by the rather broad $\rho(770)$. Since the ρ is a $\pi\pi$ P-wave resonance, we can employ a more sophisticated approach than the VMD approximation and compute this SVA dispersively, taking into account intermediate $\pi\pi$ states; cf. Fig. 6.1. The corresponding unitarity relation reads

$$\operatorname{disc} \mathcal{G}^{(0)}(t) = -i\frac{t}{2\sqrt{2}}\sigma_\pi^3(t)\big[g_1^1(t)\big]^* h_1^1(t)\,, \tag{6.5}$$

with the isospin $I = 1$ P-waves $h_1^1(t)$ for $\gamma\pi \to \pi\pi$ [117] and $g_1^1(t)$ for $\pi\pi \to K\bar{K}$ [345]. We cast $\mathcal{G}^{(0)}$ into a dispersion integral

$$\mathcal{G}^{(0)}(t) = \frac{-1}{4\sqrt{2}\pi} \int_{4M_\pi^2}^{\infty} \mathrm{d}t' \frac{t'\sigma_\pi^3(t')\left[g_1^1(t')\right]^* h_1^1(t')}{t'-t} \,. \tag{6.6}$$

We retain $\mathcal{H}^{(-)}$ since the corresponding P-wave is forbidden by charge conjugation, such that the D-wave represents the leading t-channel discontinuity for this SVA. Moreover, $\mathcal{H}^{(-)}$ is enhanced due to the resonant $a_2(1320)$ contribution. We follow the approach of Ref. [342] and compute the SVA $\mathcal{H}^{(-)}$ via the tree-level diagram with an intermediate $a_2(1320)$ tensor meson, see Fig. 6.1. For the interaction vertices, we use the formalism presented in Ref. [346]. The coupling g_T for the $a_2 K\bar{K}$ vertex is related to the partial width via

$$\Gamma(a_2 \to K\bar{K}) = \frac{g_T^2 M_{a_2}^3}{120\pi F_\pi^4} \sigma_K^5\left(M_{a_2}^2\right) . \tag{6.7}$$

Similarly, the coupling c_T for the $a_2\gamma\pi$ vertex can be determined via the partial width of radiative a_2 decays [347] (updated compared to Ref. [342] due to the inclusion of the new COMPASS measurement [348]),

$$\Gamma\left(a_2 \to \gamma\pi\right) = \frac{e^2 c_T^2}{160\pi F_\pi^2} \frac{\left(M_{a_2}^2 - M_\pi^2\right)^5}{M_{a_2}^5} \,. \tag{6.8}$$

The tree-level contribution of the a_2 meson reads

$$\mathcal{H}^{(-)}(t) = \frac{2\sqrt{2} e c_T g_T}{F_\pi^3} \frac{1}{M_{a_2}^2 - t} \,. \tag{6.9}$$

Following the arguments presented in Ref. [342] we fix the signs of the coupling constants via

$$c_T g_T = +|c_T g_T| \,. \tag{6.10}$$

6.4 Dispersive representations and Khuri–Treiman solutions

We now discuss the main part of the dispersive representation of the $\gamma K \to K\pi$ amplitudes, the reconstruction of the s- and u-channel partial waves or SVAs. This consistently incorporates $K\pi$ P-wave rescattering in the elastic approximation. From the reconstruction theorems [4], we can obtain the relevant partial waves, i.e., the P-waves of different isospins with the result

$$f_1^{(i)}(s) = \mathcal{F}^{(i)}(s) + \widehat{\mathcal{F}}^{(i)}(s) \,, \quad i = 0,\, 1/2,\, 3/2 \,. \tag{6.11}$$

Here, the functions $\widehat{\mathcal{F}}^{(i)}(s)$ originate from the t- and u-channel SVAs; they only contribute left-hand cuts to the partial waves and hence have no discontinuities along the right-hand cut. The $\widehat{\mathcal{F}}^{(i)}(s)$ can be collected from appropriate linear combinations of the different reconstruction theorems [4].

In the approximation of elastic unitarity, a right-hand cut in the amplitude is induced by intermediate $K\pi$ states. Here, the partial waves for $i = 0,\, 1/2$ are both associated with

$I = 1/2$, while $i = 3/2$ requires $I = 3/2$. Note that $i = 0$ is related to the isoscalar photon component, while $i = 1/2,\, 3/2$ corresponds to an isovector photon. The unitarity relation implies Watson's final-state theorem, which states that the phase of $f_1^{(i)}(s)$ coincides with $\delta_1^I(s)$ [95]. Remembering that the $\widehat{\mathcal{F}}^{(i)}(s)$ are free of right-hand-cut discontinuities, we find a unitarity relation for the SVAs,

$$\operatorname{Im}\mathcal{F}^{(i)}(s) = \left(\mathcal{F}^{(i)}(s) + \widehat{\mathcal{F}}^{(i)}(s)\right) e^{-i\delta_1^I(s)} \sin\delta_1^I(s)\,. \tag{6.12}$$

Due to Eq. (6.12), the functions $\widehat{\mathcal{F}}^{(i)}(s)$ are usually referred to as inhomogeneities, as they constitute the inhomogeneous contributions to the unitarity relations for $\mathcal{F}^{(i)}(s)$. The solution of the full, inhomogeneous unitarity relation (6.12) for the single-variable amplitudes is subsequently obtained using a separation ansatz with the Omnès function. The input for the latter is taken from Ref. [60]. The results are the Khuri–Treiman equations [97] for the SVAs

$$\begin{aligned}\mathcal{F}^{(0,1/2)}(s) &= \Omega(s)\left(P_{n-1}^{(0,1/2)}(s) + \frac{s^n}{\pi}\int_{s_\text{th}}^{\infty}\frac{\mathrm{d}s'}{s'^n}\frac{\widehat{\mathcal{F}}^{(0,1/2)}(s')\sin\delta_1^{1/2}(s')}{|\Omega(s')|(s'-s)}\right),\\ \mathcal{F}^{(3/2)}(s) &= P_{n'-1}^{(3/2)}(s)\,.\end{aligned} \tag{6.13}$$

Note that we approximate the $I = 3/2$ phase shift to be zero since it is negligibly small, and therefore the solution for $\mathcal{F}^{(3/2)}$ reduces to Eq. (6.13). We can solve for the SVAs by inserting the fixed t-channel contributions from Sec. 6.3 into the inhomogeneities and then solving Eq. (6.13) iteratively. The system is linear in the subtraction constants, so that it is possible to construct basis functions. The calculation of the latter converges very quickly, such that they remain practically unchanged after at most five iterations.

6.5 Matching

Next, we discuss how to fix the free parameters of the dispersive representation, the subtraction constants, by matching them to the chiral anomaly on the one hand, and the radiative couplings of the $K^*(892)$ resonances on the other.

6.5.1 Chiral anomaly

The Wess–Zumino–Witten anomaly [299, 300] yields low-energy theorems for the different $\gamma K \to K\pi$ amplitudes in the limit of vanishing energies ($s = t = u = 0$) and vanishing (light as well as strange) quark masses. It contributes to the neutral-pion-production amplitudes, but not to the charge-exchange processes:

$$\mathcal{F}^{-0/00}(0,0,0) = F_{KK\pi}\,, \quad \mathcal{F}^{0-/-+}(0,0,0) = 0\,, \tag{6.14}$$

where [334, 335]

$$F_{KK\pi} = \frac{e}{4\pi^2 F_\pi^3} = 9.8\,\text{GeV}^{-3}\,, \tag{6.15}$$

is given in terms of the pion decay constant $F_\pi = 92.28(3)\,\text{MeV}$ and the electric charge e, and is actually identical to the similarly defined anomaly $F_{3\pi}$ for $\gamma\pi \to \pi\pi$ [302–304].

Since it is hard to estimate the correlations between all the higher-order corrections, we simply estimate a resulting uncertainty of 25% on $F_{KK\pi}$. A complete next-to-leading-order calculation of all $\gamma K \to K\pi$ channels in chiral perturbation theory would certainly be highly desirable (see Refs. [334, 335] for partial results).

Obviously, also the vanishing charge-exchange amplitude will be modified due to higher-order corrections. Since a relative error estimate is not meaningful here, we use the absolute uncertainty given for the anomaly also for the charge-exchange amplitudes. Our combined assumption on the different amplitude normalizations in the soft-meson limits is therefore

$$\mathcal{F}^{-0/00}(0,0,0) = 9.8(2.4)\,\text{GeV}^{-3}\,, \quad \mathcal{F}^{0-/-+}(0,0,0) = 0.0(2.4)\,\text{GeV}^{-3}\,. \tag{6.16}$$

6.5.2 Radiative couplings of the $K^*(892)$

In the narrow-width approximation, the radiative widths of the $K^*(892)$ vector mesons are given by

$$\frac{1}{4}\Gamma_{K^{*0}\to K^0\gamma} = \Gamma_{K^{*\pm}\to K^\pm\gamma} = \frac{e^2 d_{K^*}^2}{864\pi}\left(\frac{M_{K^*}^2 - M_K^2}{M_{K^*}}\right)^3\,. \tag{6.17}$$

The Review of Particle Physics (RPP) [347] lists only three measurements from which these radiative widths have been extracted, one for $K^{*0} \to K^0\gamma$ [314] and two for $K^{*\pm} \to K^\pm\gamma$ [313, 326]. The extracted charged and neutral radiative couplings read $d_{K^*}^{\text{c}} = 2.50(12)\,\text{GeV}^{-1}$, $d_{K^*}^{\text{n}} = 1.93(8)\,\text{GeV}^{-1}$, and thus violate $SU(3)$ symmetry at the 20% level.

For a model-independent extraction of the radiative K^* coupling constants, we have to analytically continue the $\gamma K \to K\pi$ amplitudes onto the second Riemann sheet and connect them to the residues of the corresponding poles. The continuation to the second sheet can be found from the discontinuity,

$$f_{1,I}^{(i)}(s) - f_{1,II}^{(i)}(s) = -2\hat{\kappa}(s)t_{1,II}^{1/2}(s)f_{1,I}^{(i)}(s)\,, \tag{6.18}$$

where I (II) denotes the first (second) Riemann sheet, and

$$\hat{\kappa}(s) = \frac{\sqrt{-\lambda(s, M_\pi^2, M_K^2)}}{s}\,, \quad \hat{\kappa}(s \pm i\epsilon) = \mp i\kappa(s)\,, \tag{6.19}$$

which leads to the correct analytic structure including the branch cut and where $\lambda(a,b,c)$ is the Källén function defined in Eq. (2.15).

6.6 Discussion and results

We begin the discussion of numerical results with the minimal subtraction scheme, which contains two subtractions constants. According to the discussion of the previous section, we can choose to fix these in two different ways: via matching to the chiral anomaly or by reproducing the experimentally measured radiative K^* couplings. We start with the first option and match the subtraction constants to the low-energy theorems; see Figs. 6.2 and 6.3 (left). Obviously, the error bands are huge. This illustrates the very strong dependence

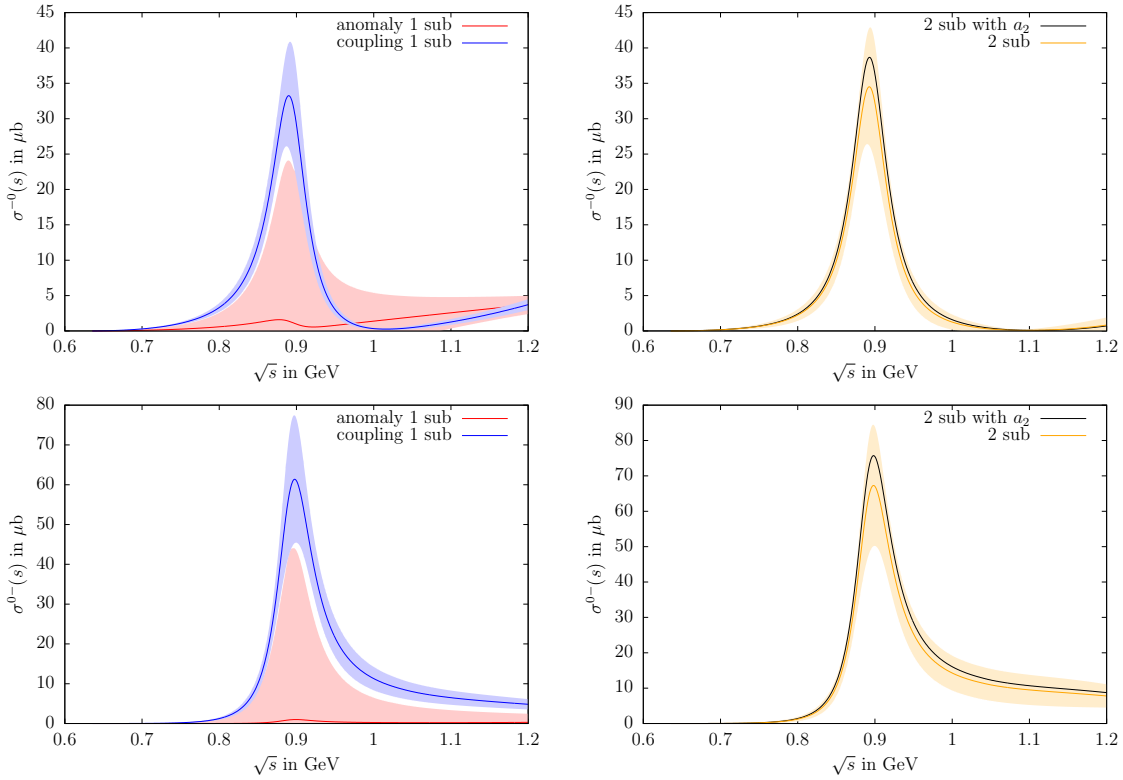

Figure 6.2: Cross section results for $\gamma K^- \to K^-\pi^0$ (top) and $\gamma K^- \to \bar{K}^0\pi^-$ (bottom) including P-wave amplitudes. Left panels: minimal subtraction scheme, matched to the chiral anomaly and the K^* radiative couplings separately. Right panels: twice subtracted scheme, matched to anomaly and radiative couplings simultaneously, with and without the a_2 contribution. The error bands correspond the propagated error of the real and imaginary parts.

of the partial waves, and in particular the $K^*(892)$ resonance signals, on the amplitudes in the low-energy limit. By reversing the argument, a concise measurement of the cross section around the resonance peak will help determine the anomaly and, potentially, its higher-order corrections very accurately if the minimal subtraction scheme can be validated experimentally to be sufficient. This is in strict analogy to the argument of Ref. [117] that the full resonance signal of the $\rho(770)$ can be employed to extract the chiral anomaly in $\gamma\pi \to \pi\pi$.

As the second approach, we fix the real subtraction constants in the minimal subtraction scheme using the radiative K^* couplings derived from experiment. We observe that the uncertainties are much smaller in this scheme. To obtain a larger degree of flexibility for the description of future high-precision cross-section data, we can apply the twice subtracted version with four degrees of freedom. This allows us to include both constraints, low-energy theorems and resonance couplings, and combine them into a prediction for experiment. Furthermore, in the twice subtracted representation it is possible to include the a_2 t-channel contribution, which changes the isovector part of the photon only. The corresponding plots are also included in Figs. 6.2 and 6.3. Comparing the two solutions

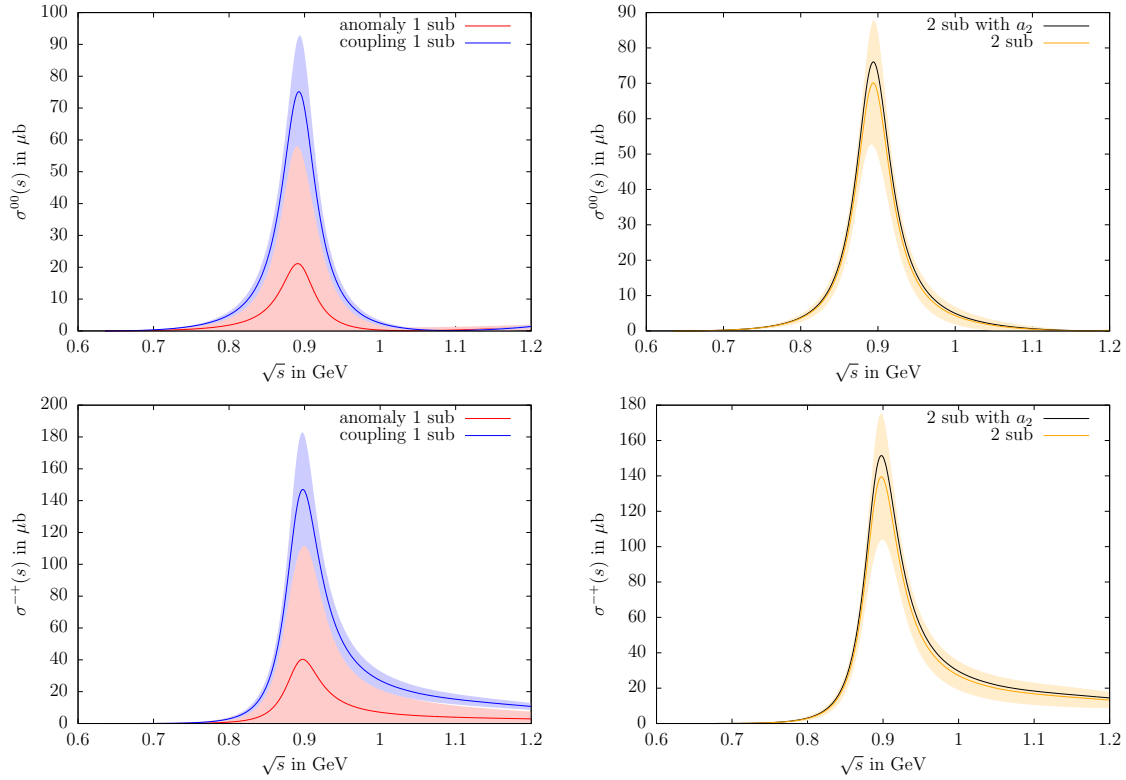

Figure 6.3: Cross section results for $\gamma\bar{K}^0 \to \bar{K}^0\pi^0$ (top) and $\gamma\bar{K}^0 \to K^-\pi^+$ (bottom) including P-wave amplitudes. Remaining caption as in Fig. 6.2.

with and without a_2-exchange, we observe that this mechanism is very small below 1 GeV. We conclude that it is unnecessary to take D- and higher partial waves into account when considering the left-hand cuts at the current level of accuracy.

Using Eq. (6.3) and the respective partial-wave amplitudes, we can calculate the cross sections for all physical channels, see Figs. 6.2 and 6.3. While the differences between the various channels at low energies, very discernible in the amplitudes, are hardly observable due to the phase space factors—the onset of the visible cross sections only seems to be deferred by about 50 MeV for the charge-exchange reactions with their suppressed near-threshold amplitudes—, we see a significant difference between the π^0 and the charge-exchange channels above the $K^*(892)$, where we predict a strong suppression of the π^0 production cross sections around 1.1 GeV. As we expect D-wave corrections to become important only above those energies [298], such a suppression should be realistically observable in experiments. With incoming neutral kaons, the cross sections are enhanced by about a factor of two compared to their charged-kaon counterparts, while the outgoing-neutral-pion channels are suppressed by again roughly a factor of two in the peak region in comparison to the charge-exchange reactions.

6.7 Summary

In this chapter, we have constructed a dispersive representation for the reaction $\gamma K \to K\pi$ that can be measured with kaon beams using the Primakoff mechanism. Our formalism relies on isospin symmetry and describes all four physical charge channels simultaneously. We have solved Khuri–Treiman-type equations for the dominant s-(and u-)channel P-wave, based on fixed t-channel singularities that are constrained by data and phenomenology as far as possible. We have demonstrated that subtraction constants, the free parameters of the theory, can be matched to the low-energy prediction by the chiral anomaly, or the radiative couplings of the $K^*(892)$ resonance, or both. The dispersive amplitudes provide the correct, model-independent framework to continue data both to the subthreshold region, where it can be matched to chiral perturbation theory, and into the complex-energy plane, where resonance couplings are defined as pole residues on unphysical Riemann sheets.

Options for future theoretical improvement comprise in particular the calculation of the next-to-leading-order, or $\mathcal{O}(p^6)$, corrections to the chiral anomaly for this reaction. Furthermore, a reduction of the uncertainty in the $\omega \to K\bar{K}$ coupling, which affects our amplitude representation rather strongly, would be highly desirable. One prospect is to extract this coupling from the spacelike kaon form factor data. However, as shown in Chapter 8 the result of a global analysis of time- and spacelike data does not decrease the uncertainty.

Once high-precision, high-statistics experimental data is available, from AMBER or elsewhere, a simultaneous fit to the two observable charge configurations in γK^- fixes the subtraction constants, from where it is possible to extract the physical quantities of interest. The dispersive representation therefore allows future experiments to determine precise information on the anomaly in a photon–kaon reaction as well as the radiative couplings of the $K^*(892)$ resonance from the complete measured energy range up to $\sqrt{s} \approx 1.2\,\text{GeV}$.

Chapter 7

Polarizabilities from kaon Compton scattering

7.0 Prologue

The content of this chapter is based on the publication

- D. Stamen, J. L. Dammann, Y. Korte, and B. Kubis, *Polarizabilities from kaon Compton scattering*, Eur. Phys. J. C **84**, 1267 (2024) [arXiv:2409.05955 [hep-ph]] .

This project was started with Jan Luca Dammann's Master's thesis [349].

The electric and magnetic polarizabilities of hadrons, α and β, can be extracted from differential cross sections for Compton scattering near threshold, as they are defined via an expansion of the Born-term-subtracted Compton scattering amplitudes at threshold. However, for light pseudoscalar mesons Compton scattering cannot be measured directly from photon scattering experiments as there are no mesonic targets. For the charged pion amplitude the most recent measurement [350] extracts the Compton scattering amplitude from high-energy pion–nucleus bremsstrahlung $\pi Z \to \pi Z \gamma$. In principle, the corresponding measurement is possible for charged kaons at AMBER [318–320]; however, for kaons, it is affected by the presence of the $K^*(892)$ resonance not too far from threshold. The idea of this project is to propose a method to extend the energy range serviceable for this purpose by reconstructing the $K^*(892)$ contribution model-independently using dispersion theory from its $K\pi$ intermediate state.

The leading-order chiral perturbation theory (ChPT) calculation reproduces the results for kaon Compton scattering from scalar QED, which are the Born terms. Contributions to the polarizablities first appear at next-to-leading order and were calculated in Ref. [331]. This is in strict analogy to the pion case. At next-to-leading order, the loop corrections have cut contributions from the intermediate states that limit the range of convergence of the polynomial polarizability expansion. The kaon loops have a higher threshold and therefore do not limit the extraction in the proposed energy region. However, the pion threshold in the t-channel is already reached at energies close to the threshold. While the pion-loop contribution is of isospin $I = 0$ and a pure S-wave, there are sizable rescattering corrections due to the $f_0(500)$. Therefore, we propose a dispersion-theoretical treatment of $\gamma\gamma \to \pi\pi \to K^+K^-$. It is built on a coupled-channel formalism, and while the insertion into this project was worked out by the author of this thesis, the solutions of the coupled-channel formalism were provided by Yannis Korte. Note that the consideration of these rescattering corrections does not influence the extraction of the kaon polarizabilities on a meaningful level.

The contribution from the K^* resonance can be calculated with an effective Lagrangian assuming vector-meson dominance (VMD). This calculation was carried out by Jan Luca Dammann and cross-checked by the author of this thesis. From these amplitudes, one can

extract the polarizablities induced by the K^* resonance, which only contribute to the magnetic polarizability. In contrast to the ρ resonance in the pion case, the relative strength of the resonance contribution compared to the leading ChPT result is much larger for the K^* resonance. To better constrain the K^* contribution, we employ a dispersive treatment for the $K\pi$ intermediate states. Here, the $\gamma K \to K\pi$ amplitudes from Chapter 6 are used. A once-subtracted dispersion relation is needed in order to render the integral convergent. The subtraction constant can be directly related to the VMD polarizabilities calculated with the effective Lagrangian. This calculation was carried out by the author of this thesis. Code for the calculation of the dispersion integral and the $\gamma K \to K\pi$ amplitudes from Chapter 6 can be found at github.com/HISKP-ph/kaon_polarizabilities [351]. Note that there are two versions for the $\gamma K \to K\pi$ amplitudes. First, the solutions for the partial waves of Chapter 6 are stored in /gammaKKpi_amp. Secondly, the basis functions are stored in /gammaKKpi_amp/basisfunctions, which allow for a variation of the subtraction constants calculated in Ref. [4]. The code provides a class that allows calculating the first from the second.[1] Furthermore, the k^0_{++} amplitude for the dispersive t-channel calculation is provided in /dispersive_t_channel.

In analogy to the experimental analysis of Ref. [350], we define ratios of differential cross sections. These ratios can either be used for a fixed scattering angle or an integrated range thereof. The latter is more advantageous for the experiment, since the former will not produce meaningful statistics. However, choosing $z_s = -1$, the linear combination $\alpha_1 + \beta_1$ drops out and the ratio solely depends on $\alpha_1 - \beta_1$. Since there is no strong hierarchy between the sum and difference of the kaon polarizabilities, we discuss the sensitivity to disentangling both by improved experimental angular coverage. To depict possible outcomes from the experiment, we choose a range limited by the ChPT and VMD polarizabilities. This strategy of extracting the polarizabilities from experiment was developed by the author of this thesis in collaboration with Bastian Kubis. Again, the numerical calculation was performed and the plots were created by the author of this thesis.

Furthermore, it might become possible to investigate kaon Compton scattering for neutral kaons at the K-Long Facility (KLF) [297]. The same methods as above can be applied, however, with the key difference that there are no Born terms for the neutral kaon Compton scattering. Therefore, the cross section is directly proportional to the polarizabilities near threshold, but it tends to zero and is therefore heavily suppressed compared to the charged kaon case. The total cross section for both scenarios is calculated and we conclude that, due to the low statistics, measurements for the neutral kaon polarizabilities will become very challenging.

The text contained in this chapter was written by the author of this thesis in collaboration with Bastian Kubis.

7.1 Introduction

In classical electrodynamics, electric and magnetic polarizabilities characterize the deformation response of a composite system in an external electromagnetic field. They appear as the coefficients of proportionality between fields and induced dipole moments [352]. In quantum field theory, the electric and magnetic polarizabilities, α and β, are defined from

[1] This is only true for the mean values; the uncertainties for the partial waves are only provided via the first version.

an expansion of the (Born-term-subtracted) Compton scattering amplitudes at threshold. Since there are no mesonic targets available, the Compton cross sections for mesons cannot be measured directly from photon scattering experiments.

Instead, in the charged-pion channel, high-energy pion–nucleus bremsstrahlung $\pi Z \to \pi Z \gamma$ [350, 353, 354], radiative pion photoproduction off the proton $\gamma p \to \gamma \pi^+ n$ [355, 356], and the crossed-channel two-photon reaction $\gamma\gamma \to \pi^+\pi^-$ [357–361] have been measured. Historically, there have been tensions between the experimental extractions of the charged-pion polarizabilities and the theoretical predictions from chiral perturbation theory (ChPT) [362–367], which have been extensively discussed in the literature [368]. The most recent measurement by the COMPASS experiment [350] is in perfect agreement with the ChPT prediction, and model dependencies for the extraction of pion polarizabilities may be sufficient to explain the tension with respect to earlier measurements. A dispersive calculation of the pion polarizabilities is in good agreement with the ChPT result [369]; cf. also the new dispersive analysis in Ref. [370]. Furthermore, new experiments are planned in order to clarify the current situation. For an extensive review, see Ref. [368].

In principle, analogous reactions to all these can also be investigated for kaons. The photon–photon fusion processes $\gamma\gamma \to \bar{K}K$ have already been measured in the near-threshold region [371, 372]. The data however cannot realistically be used in order to extract polarizabilities, as the physical region is too far removed from the kinematical point that defines the polarizabilities to allow for a reliable expansion. A promising setup for the extraction of the Compton scattering cross section for charged kaons from the Primakoff reaction [305] is the proposed AMBER experiment located at CERN [318–320]. Using an intensified charged-kaon beam[2] allows for a measurement of the $\gamma K^- \to \gamma K^-$ process. However, the different masses will render the extraction of polarizabilities more challenging than in the pion case: the definition of the polarizabilities amounts to a polynomial expansion at threshold, whose range of applicability is clearly limited, in particular by the lowest lying (vector) resonances. As $M_\rho/M_\pi \approx 5.5$, but $M_{K^*}/M_K \approx 1.8$, a way to extend the range of applicability of the kaon Compton scattering amplitude to higher energies and thereby extract these quantities with increased accuracy is clearly desirable. This is similar in spirit (although not in practical implementation) to the extraction of the chiral anomaly from Primakoff reactions [4, 117, 118], including data from the first resonance region. In this chapter we propose such a method.

In order to dispersively reconstruct the K^* resonance in the kaon Compton amplitude we use the solutions from the Primakoff reactions calculated in Ref. [4]. Therefore, with these two studies we in principle allow for a simultaneous data analysis of the charged-kaon polarizabilities, the chiral anomaly, and the radiative couplings of the K^* resonance at AMBER.

This chapter is structured as follows: in Sec. 7.2, we introduce the relevant definitions for the helicity amplitudes as well as their expansion in terms of dipole and higher-order polarizabilities. The Born terms and next-to-leading-order corrections in ChPT are discussed in Sec. 7.3. Therein we also investigate a dispersive strategy to improve on the pion loops beyond the chiral expansion. In Sec. 7.4, effects of the vector $K^*(892)$ resonance are discussed: a vector-meson-dominance (VMD) model is used to estimate higher-order corrections to the polarizabilities; and in addition, $\gamma K \to K\pi$ amplitudes are used to re-

[2]The statistics using kaons is expected to be lower than in the pion case by a factor of 8 [296].

construct the K^* resonance dispersively. Numerical results are presented in Sec. 7.5, and we propose a method to experimentally extract the kaon polarizabilities. A short discussion of neutral-kaon Compton scattering is provided in Sec. 7.6. In Sec. 7.7 we summarize our findings.

7.2 Definitions

The S-matrix element for the kaon Compton scattering process reads [341]

$$\langle\gamma(q_2,\lambda_2)K(p_2)|\gamma(q_1,\lambda_1)K(p_1)\rangle = (2\pi)^4\delta^{(4)}(q_2+p_2-q_1-p_1) \cdot\left(\delta_{\lambda_1\lambda_2}+ie^2\mathcal{F}_{\lambda_1\lambda_2}(s,t)e^{i(\lambda_1-\lambda_2)\phi}\right), \quad (7.1)$$

with the two helicities λ_1 and λ_2 of the in- and outgoing photons, respectively. Furthermore, the azimuthal angle ϕ is explicitly separated. The Mandelstam variables read $s=(q_1+p_1)^2$, $t=(q_1-q_2)^2$, and $u=(q_1-p_2)^2$. They fulfill the on-shell condition $s+t+u=2M_K^2$. The Mandelstam variable t can be expressed via s and the cosine of the s-channel scattering angle $z_s=\cos\theta_s$ according to

$$t(s,z_s)=\frac{z_s-1}{2s}(s-M_K^2)^2\,. \quad (7.2)$$

We can separate the polarization vectors from the helicity amplitude $\mathcal{F}_{\lambda_1\lambda_2}$ via

$$\mathcal{F}_{\lambda_1\lambda_2}(s,t)=\epsilon_\mu(q_1,\lambda_1)\epsilon_\nu^*(q_2,\lambda_2)W^{\mu\nu}(s,t)\,, \quad (7.3)$$

and use the Bardeen–Tung–Tarrach procedure [373, 374] to define scalar amplitudes $\mathcal{A}(s,t)$ and $\mathcal{B}(s,t)$ without kinematic singularities. This results in [341, 375]

$$W^{\mu\nu}(s,t)=\mathcal{A}(s,t)\left(\frac{t}{2}g^{\mu\nu}+q_2^\mu q_1^\nu\right) +\mathcal{B}(s,t)\left(2t\Delta^\mu\Delta^\nu-(s-u)^2g^{\mu\nu}+2(s-u)(\Delta^\mu q_1^\nu+\Delta^\nu q_2^\mu)\right), \quad (7.4)$$

where $\Delta_\mu=(p_1+p_2)_\mu$. The amplitude is manifestly gauge and Lorentz invariant and fulfills the Ward identities $q_{1\mu}W^{\mu\nu}(s,t)=0=W^{\mu\nu}(s,t)q_{2\nu}$. Using the explicit form of the polarization vectors[3]

$$\epsilon(q_1,\pm)=\mp\frac{1}{\sqrt{2}}\begin{pmatrix}0\\1\\\pm i\\0\end{pmatrix},\quad \epsilon(q_2,\pm)=\mp\frac{1}{\sqrt{2}}\begin{pmatrix}0\\\cos\theta_s\\\pm i\\-\sin\theta_s\end{pmatrix}, \quad (7.5)$$

and the four-momentum vectors

$$q_1=\frac{s-M_K^2}{2\sqrt{s}}\begin{pmatrix}1\\0\\0\\1\end{pmatrix},\quad q_2=\frac{s-M_K^2}{2\sqrt{s}}\begin{pmatrix}1\\\sin\theta_s\\0\\\cos\theta_s\end{pmatrix}, \quad (7.6)$$

[3]Here we use the phase convention of Ref. [376].

we obtain the helicity amplitudes in terms of the scalar ones by

$$\begin{aligned}\mathcal{F}_{++}(s,t) &= \mathcal{F}_{--}(s,t) = 4(M_K^4 - su)\mathcal{B}(s,t)\,,\\ \mathcal{F}_{+-}(s,t) &= \mathcal{F}_{-+}(s,t) = -\frac{t}{2}\mathcal{A}(s,t) + t(t-4M_K^2)\mathcal{B}(s,t)\,.\end{aligned} \tag{7.7}$$

One can also construct the amplitude in the center-of-mass system with Coloumb gauge, cf. Refs. [377, 378], according to[4]

$$\mathcal{F}(s,t) = 2\left[-\vec{\epsilon}_1\cdot\vec{\epsilon}_2\mathcal{A}^{\mathrm{KF}}(s,t) + \vec{\epsilon}_1\cdot\vec{q}_2\,\vec{\epsilon}_2\cdot\vec{q}_1\frac{2}{t}\big(\mathcal{A}^{\mathrm{KF}}(s,t)+\mathcal{B}^{\mathrm{KF}}(s,t)\big)\right], \tag{7.8}$$

where the different scalar amplitudes are mapped onto each other by

$$\begin{aligned}\mathcal{A}^{\mathrm{KF}}(s,t) &= \frac{t}{4}\mathcal{A}(s,t) - \frac{(s-u)^2}{2}\mathcal{B}(s,t)\,,\\ \mathcal{B}^{\mathrm{KF}}(s,t) &= 2(s-M_K^2)^2\mathcal{B}(s,t)\,.\end{aligned} \tag{7.9}$$

The total differential cross section is given by

$$\frac{\mathrm{d}\sigma}{\mathrm{d}\Omega} = \frac{\alpha_{\mathrm{em}}^2}{4s}\left(|\mathcal{F}_{++}(s,t)|^2 + |\mathcal{F}_{+-}(s,t)|^2\right), \tag{7.10}$$

where α_{em} is the fine-structure constant. This chapter uses the isospin limit with $M_K = 0.496\,\mathrm{GeV}$ and $M_\pi = M_{\pi^\pm}$.[5]

Polarizabilities specify corrections to the Born terms. Electric and magnetic dipole, quadrupole, and higher-order polarizabilities are defined as the expansion coefficients of the Born-term-subtracted amplitudes in powers of t at fixed $s = M_K^2$ [341, 379],

$$\begin{aligned}\pm\frac{2\alpha_{\mathrm{em}}}{M_K t}\widehat{\mathcal{F}}_{+\pm}(M_K^2,t) &= (\alpha_1 \pm \beta_1)_{K^\pm} + \frac{t}{12}(\alpha_2\pm\beta_2)_{K^\pm} + \mathcal{O}\big(t^2\big),\\ \widehat{\mathcal{F}}_{+\pm}(s,t) &= \mathcal{F}_{+\pm}(s,t) - \mathcal{F}_{+\pm}^{\mathrm{Born}}(s,t)\,.\end{aligned} \tag{7.11}$$

To illustrate the contributions of the polarizabilities that are most relevant in the forward or backward direction, respectively, one may define $z_\pm = 1 \pm z_s$ and expand the differential cross section to linear order in the polarizablities [350, 380]

$$\left(\frac{\mathrm{d}\sigma}{\mathrm{d}\Omega}\right)_{P\gamma} = \left(\frac{\mathrm{d}\sigma}{\mathrm{d}\Omega}\right)_{\mathrm{Born}} - \frac{\alpha_{\mathrm{em}}M_P^3(s-M_P^2)^2}{4s^2\left(sz_+ + M_P^2 z_-\right)}\left(z_-^2(\alpha_1-\beta_1)_P + z_+^2\frac{s^2}{M_P^4}(\alpha_1+\beta_1)_P\right), \tag{7.12}$$

where P is an arbitrary (charged) pseudoscalar meson.

[4] Note that the T-matrix element defined in Refs. [377, 378] is related to $\mathcal{F}$ via $T = e^2\mathcal{F}$.

[5] This convention was used in the pion–kaon scattering analysis of Refs. [60, 337] and the $\gamma K \to K\pi$ analysis of Ref. [4].

7.3 ChPT amplitudes and t-channel cuts

At leading order in the chiral expansion, the ChPT amplitudes for charged-kaon Compton scattering reproduce the results of scalar quantum electrodynamics, hence they consist precisely of the Born terms only. Nonvanishing contributions to the polarizabilities first appear at next-to-leading or one-loop order. Including these corrections, the scalar amplitudes read [331][6]

$$\begin{aligned}\mathcal{A}(s,t) &= \frac{1}{M_K^2 - s} + \frac{1}{M_K^2 - u} + \frac{8}{F_K^2}\,(L_9 + L_{10}) + \mathcal{A}^{\text{loop}}(t)\,,\\ \mathcal{B}(s,t) &= \frac{1}{2t}\left(\frac{1}{M_K^2 - s} + \frac{1}{M_K^2 - u}\right)\,,\end{aligned} \tag{7.13}$$

where

$$\begin{aligned}\mathcal{A}^{\text{loop}}(t) &= -\frac{1}{8\pi^2 F_K^2}\left[\frac{3}{2} - \frac{2M_\pi^2}{t}\arctan^2\left(\frac{1}{\sigma^\pi(t)}\right) - \frac{4M_K^2}{t}\arctan^2\left(\frac{1}{\sigma^K(t)}\right)\right],\\ \sigma^P(t) &= \sqrt{\frac{4M_P^2}{t} - 1}\,.\end{aligned} \tag{7.14}$$

Using this result and Eq. (7.11), one can calculate the contribution to the polarizabilities, which yields [331, 383]

$$\begin{aligned}(\alpha_1 + \beta_1)^{\text{ChPT}}_{K^\pm} &= 0\,,\\ (\alpha_1 - \beta_1)^{\text{ChPT}}_{K^\pm} &= \frac{8\alpha_{\text{em}}}{M_K F_K^2}(L_9 + L_{10}) = \frac{M_\pi F_\pi^2}{M_K F_K^2}(\alpha_1 - \beta_1)^{\text{ChPT}}_{\pi^\pm} + \mathcal{O}(M_K)\\ &= 1.1(2)\cdot 10^{-4}\,\text{fm}^3\Big\{1 + \mathcal{O}\big(M_K^2/\Lambda_\chi^2\big)\Big\}\,,\end{aligned} \tag{7.15}$$

where $\Lambda_\chi \approx 1\,\text{GeV}$ is the chiral symmetry breaking scale. The result is in strict analogy to the pion polarizabilities, with the appropriate replacement of mass and decay constant, and hence can be expressed as a low-energy theorem in terms of the latter, up to $SU(3)$-breaking effects. Note that for this specific combination it is advantageous to measure the cross section in the backward direction, cf. Eq. (7.12). For the numerical estimate, we have employed the next-to-leading-order chiral prediction for the pion polarizabilities from Ref. [367]. The uncertainty therein is a chiral $SU(2)$ uncertainty, while the kaon polarizabilities are affected by (unknown) chiral $SU(3)$ corrections as indicated in Eq. (7.15). We will neglect the uncertainty on the pion polarizabilities in the following, and instead give estimates for the kaon ones.

The loop contributions in Eq. (7.14) show nontrivial analytic structures: they include cuts due to two-pion and two-kaon intermediate states, with branch points at $t = 4M_\pi^2$ and $t = 4M_K^2$, respectively. These obviously limit the range of convergence of the polynomial polarizability expansion around $t = 0$, Eq. (7.11): a representation of the Compton amplitude (beyond Born terms) in terms of a polynomial is bound to fail beyond those thresholds. In the extraction of polarizabilities from charged-pion Compton scattering,

[6] Note the missing factor of 4 in Eq. (2) of Ref. [331] in comparison to Refs. [363, 381, 382]. Additionally the loop correction has a wrong normalization by a factor of 2, cf. Appendix B of Ref. [330].

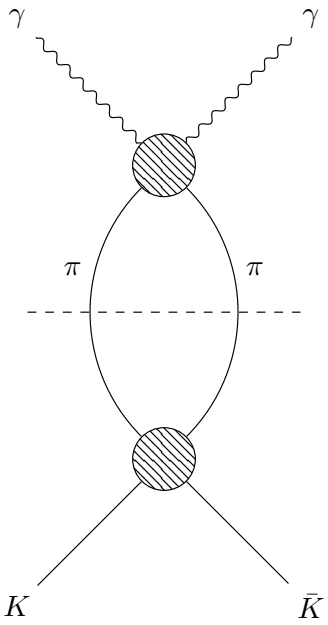

Figure 7.1: Dispersive reconstruction of the t-channel contribution to kaon Compton scattering, including the $\pi\pi$ intermediate states. The blobs denote the full $\gamma\gamma \to \pi\pi$ and $\pi\pi \to \bar{K}K$ S-wave amplitudes.

the pionic one-loop corrections have therefore been retained [350, 378], and the same is clearly advisable in the investigation of kaon Compton scattering: according to Eq. (7.2), the maximum value of $|t|$ probed at fixed s is given by $(s - M_K^2)^2/s$, which reaches $4M_\pi^2$ already for $\sqrt{s} \approx 0.65\,\text{GeV}$. In contrast, a polynomial expansion of the kaon loops, with their much higher threshold, is well justified. We will discuss a further improvement of the t-channel cut in the following.

The t-channel pion-loop contribution to kaon Compton scattering is of total isospin $I = 0$, and, at next-to-leading order, a pure S-wave. It is well known that the $I = 0$ S-wave pion–pion system is particularly prone to sizeable rescattering corrections due to the proximity of the $f_0(500)$ resonance (cf., e.g., Ref. [182] and references therein). In order to control this effect reliably and prevent the non-analyticities from perturbing the extraction of polarizability effects, we improve on the description of the pion–pion intermediate state by employing a dispersion-theoretical description of $\gamma\gamma \to \pi\pi \to K^+K^-$. This is shown diagrammatically in Fig. 7.1.

One may wonder why we concentrate on the lowest cut due to $\pi\pi$ intermediate states only, and do not resum all t-channel rescattering completely, given that the formalism is based on a coupled-channel treatment of $\gamma\gamma \to \pi\pi$ and $\gamma\gamma \to (\bar{K}K)_{I=0}$ [375] anyway. As we are (mainly) interested in charged-kaon Compton scattering, the corresponding amplitude does not only consist of t-channel isospin $I = 0$, but also contains $I = 1$, which is the coupled-channel system of $\gamma\gamma \to \pi\eta$ and $\gamma\gamma \to (\bar{K}K)_{I=1}$ [329, 330, 384]. The reason is that both $\pi\eta$ and $\bar{K}K$ cuts are much further away from $t = 0$, and do not affect the radius of convergence in a t-expansion for energies up to the $K^*(892)$ resonance. Furthermore, the $\pi\eta$ singularity affects the amplitude far less, as $\gamma\gamma \to \pi\eta$ is famously suppressed in the chiral expansion [385–387]. Finally, including the kaon loops dispersively would lead

to intricate dependencies, as their reconstruction depends on subtraction constants given by the very kaon polarizabilities we aim to extract, see Eq. (7.17) below.

The $\gamma\gamma \to (\bar{K}K)_{I=0}$ S-wave amplitude k^0 contributes to the helicity amplitudes according to [375, 388]

$$\begin{aligned} \mathcal{F}_{+-}^{\pi\text{-disp}}(s,t) &= -\frac{t}{2}\mathcal{A}^{\pi\text{-disp}}(t) = \frac{1}{\sqrt{2}}k_{++}^0(t)\,, \\ \mathcal{F}_{++}^{\pi\text{-disp}}(s,t) &= 0\,. \end{aligned} \tag{7.16}$$

Note that the helicity indices on the crossed-channel amplitudes denote the photon helicities in that channel. Furthermore, the factor $-1/\sqrt{2}$ is needed to relate the $I = 0$ amplitude to the charge basis. The Born-term-subtracted coupled-channel amplitudes are given by [375, 388, 389]

$$\begin{aligned} \begin{pmatrix} h_{++}^0(t) \\ k_{++}^0(t) \end{pmatrix} = \mathbf{\Omega}(t) \Bigg\{ \begin{pmatrix} a_t^\pi \\ a_t^K \end{pmatrix} t + \frac{t^2}{\pi} \Bigg(\sum_V \int_{-\infty}^{t_V} \mathrm{d}x \frac{\mathbf{\Omega}^{-1}(x)}{x^2(x-t)} \mathrm{Im} \begin{pmatrix} h_{++}^{0,V}(x) \\ k_{++}^{0,V}(x) \end{pmatrix} \\ - \int_{4M_\pi^2}^{\infty} \mathrm{d}x \frac{\mathrm{Im}\,\mathbf{\Omega}^{-1}(x)}{x^2(x-t)} \begin{pmatrix} h_{++}^{0,\mathrm{Born}}(x) \\ k_{++}^{0,\mathrm{Born}}(x) \end{pmatrix} \Bigg) \Bigg\}\,, \end{aligned} \tag{7.17}$$

where

$$t_V = -\frac{1}{M_V^2}(M_V^2 - M_\pi^2)^2\,, \tag{7.18}$$

and h^0 denotes the $\gamma\gamma \to (\pi\pi)_{I=0}$ S-wave amplitudes. The vector-exchange and Born-term contributions can be found in the literature, cf. Ref. [375]. Thereby, suppressing the isospin index (since all elements have $I = 0$), the Omnès matrix has the following components [148, 390]

$$\mathbf{\Omega}(t) = \begin{pmatrix} \Omega_{\pi\pi\to\pi\pi}(t) & \Omega_{\pi\pi\to\bar{K}K}(t) \\ \Omega_{\bar{K}K\to\pi\pi}(t) & \Omega_{\bar{K}K\to\bar{K}K}(t) \end{pmatrix}\,. \tag{7.19}$$

We now decouple and reduce it to only the $\pi\pi$ intermediate state explicitly, as shown diagrammatically in Fig. 7.1. Therefore, we set $a_t^K = k_{++}^{0,V} = k_{++}^{0,\mathrm{Born}} = 0$. The system is now independent of the subtraction constant a_t^K, fixed from kaon polarizablities, and only depends on a_t^π, which is related to pion polarizabilities by

$$a_t^\pi = -\frac{M_\pi}{2\alpha_{\mathrm{em}}}\frac{1}{\sqrt{3}}\left[2(\alpha_1-\beta_1)_{\pi^\pm} + (\alpha_1-\beta_1)_{\pi^0}\right]\,. \tag{7.20}$$

We now compare $\mathcal{A}^{\pi\text{-disp}}(t)$ to the ChPT result for the pion loops,

$$\mathcal{A}^\pi(t) = -\frac{1}{8\pi^2 F_K^2}\left(\frac{1}{2} - \frac{2M_\pi^2}{t}\arctan^2\left(\frac{1}{\sigma^\pi(t)}\right)\right)\,, \tag{7.21}$$

in Fig. 7.2. There the derivative at small t can be related to the quadrupole polarizabilities via Eq. (7.11). It is known that the next-to-next-to-leading order ChPT result gives sizable corrections for the pion quadrupole polarizabilities [367]. As there is no calculation at that order for the kaons, we cannot make a quantitative comparison. However, corrections on

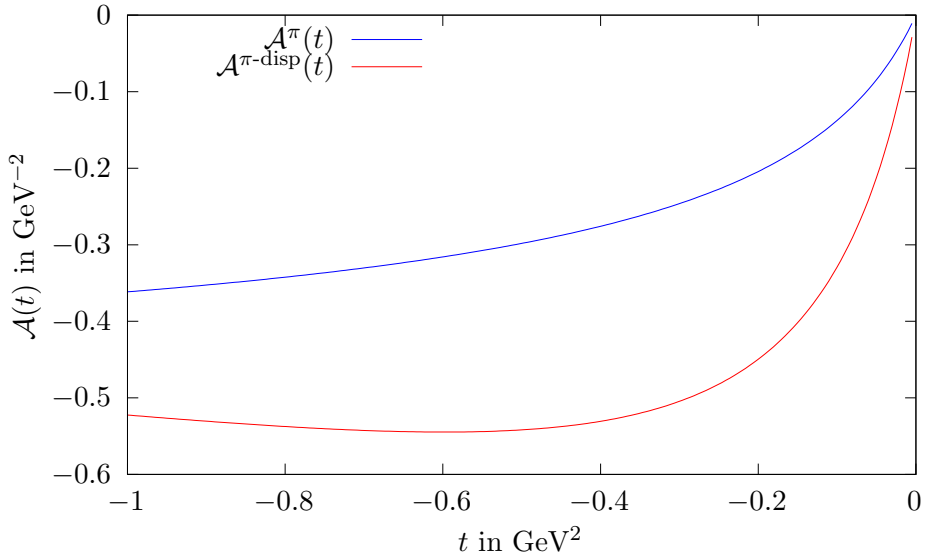

Figure 7.2: Comparison of the pion loop in Eq. (7.21) and the corresponding dispersive solution given by $\mathcal{A}^{\pi\text{-disp}}(t)$. The relevant physical range for $\sqrt{s} < 0.85\,\text{GeV}$ is $-0.31\,\text{GeV}^2 < t \leq 0\,\text{GeV}^2$.

the order shown in Fig. 7.2 are certainly not unexpected. The scalar function $\mathcal{A}$ including the dispersively reconstructed pion–pion intermediate state, but the $\bar{K}K$ one in the one-loop approximation, finally reads

$$\mathcal{A}^{\text{disp}}(t) = -\frac{\sqrt{2}}{t} k^0_{++}(t) - \frac{1}{8\pi^2 F_K^2}\left[1 - \frac{4M_K^2}{t}\arctan^2\left(\frac{1}{\sigma^K(t)}\right)\right].$$

Note that the size of $\mathcal{A}^{\text{disp}}(t)$ does not play a major role for the extraction of the kaon polarizabilities presented in this chapter, as the figures in Sec. 7.5 look the same for both the ChPT and the dispersive solution.

7.4 K^* resonance

The effects of vector resonances (in the spirit of resonance saturation of chiral low-energy constants [391]) only appear at next-to-next-to-leading-order ChPT [363–367]. Assuming VMD and using an effective interaction Lagrangian for the vertex of the kaon, the photon, and the K^* [330, 375]

$$\mathcal{L}_{\text{int}} = eC_{K^*}\epsilon^{\mu\nu\alpha\beta} F_{\mu\nu}(\partial_\alpha K)K^*_\beta\,, \tag{7.22}$$

we find the helicity amplitudes [330] (cf. also Ref. [363] for the analogous pion case)

$$\begin{aligned}
\mathcal{F}^V_{++}(s,t) &= C^2_{K^*}\left(M_K^4 - su\right)\left[\frac{1}{M^2_{K^*}-s} + \frac{1}{M^2_{K^*}-u}\right],\\
\mathcal{F}^V_{+-}(s,t) &= C^2_{K^*} t\left[\frac{s}{M^2_{K^*}-s} + \frac{u}{M^2_{K^*}-u}\right].
\end{aligned} \tag{7.23}$$

The coupling C_{K^*} can be fixed with the $K^* \to K\gamma$ width using the values from the Review of Particle Physics [22] via

$$\Gamma_{K^*\to K\gamma} = \alpha_{\rm em}\frac{C_{K^*}^2}{6}\left(\frac{M_{K^*}^2 - M_K^2}{M_{K^*}}\right)^3 . \tag{7.24}$$

An expansion of Eq. (7.23) according to Eq. (7.11) leads to the magnetic polarizability

$$(\beta_1)_{K^\pm}^{\rm VMD} = \frac{4\alpha_{\rm em}C_{K^*}^2 M_K}{M_{K^*}^2 - M_K^2} = \frac{24M_{K^*}^3 M_K}{(M_{K^*}^2 - M_K^2)^4}\Gamma_{K^*\to K\gamma} = 0.36\cdot 10^{-4}\,{\rm fm}^3 , \tag{7.25}$$

while no contribution to the electric one $(\alpha_1)_{K^\pm}^{\rm VMD}$ is found. This is in accordance with the fact that a pseudoscalar-to-vector transition requires a spin flip in the quark model, and hence a magnetic photon coupling. Quantitatively, we observe that the vector-exchange correction reduces the $\mathcal{O}(p^4)$ ChPT result for $(\alpha_1-\beta_1)_{K^\pm}$, cf. Eq. (7.15), by roughly 30%. In addition, the hierarchy $(\alpha_1+\beta_1) \ll (\alpha_1-\beta_1)$, still valid at full $\mathcal{O}(p^6)$ in ChPT for charged pions [367], is modified very significantly: the ratio $(\alpha_1+\beta_1)/(\alpha_1-\beta_1)$ is increased to almost 50%, while it remains at the level of around 3% for the pions. As a result, the $(\alpha_1+\beta_1)_{K^\pm}$ contribution can in general not be neglected for kaon Compton scattering.

As the detailed studies of charged-pion polarizabilities at $\mathcal{O}(p^6)$ ChPT demonstrate [363, 365, 367], vector-exchange contributions alone only yield a fair estimate of the order of magnitude of such effects, but not a reliable quantitative assessment. From the point of view of resonance saturation, axial-vector exchanges reduce the vector effects on $(\alpha_1-\beta_1)$, but add to them for $(\alpha_1+\beta_1)$, as they only contribute to α_1 via

$$(\alpha_1)_{K^\pm}^{\rm axial} = \frac{4\alpha_{\rm em}C_{K_1}^2 M_K}{M_{K_1}^2 - M_K^2} = \frac{24M_{K_1}^3 M_K}{(M_{K_1}^2 - M_K^2)^4}\Gamma_{K_1\to K\gamma} , \tag{7.26}$$

where the Lagrangian for axial-vector to pseudoscalar and photon transitions reads [375]

$$\mathcal{L}_{\rm axial} = 2eC_{K_1}F_{\mu\nu}\partial^\mu K_1^\nu K . \tag{7.27}$$

The main difficulty is to access the radiative charged axial-vector coupling, since there is no experimental data available. Using nonet symmetry one can relate the strange couplings to the non-strange ones via [375, 392]

$$C_{K_1^+(1270)}^2 + C_{K_1^+(1400)}^2 = C_{b_1^+(1235)}^2 + C_{a_1^+(1260)}^2 , \tag{7.28}$$

where one further needs to assume the Lipkin mechanism [393] in order to extract the physical $K_1^+(1270)$ coupling. Moreover, the branching ratio for the $a_1^+(1260)$ is disputed in the literature [394–397], with no precise modern experimental value available. A similar symmetry relation to Eq. (7.28) can be tested for the radiative neutral strange axial-vector couplings,

$$C_{K_1^0(1270)}^2 + C_{K_1^0(1400)}^2 = 4C_{b_1^+(1235)}^2 , \tag{7.29}$$

which are overestimated by more than a factor of 2. Hence, we do not attempt to quantify the axial-vector contributions here. Furthermore, loop corrections are sizable, as are the uncertainties due to variations of the scale at which resonance saturation is assumed to hold. We take this into account below by associating a 50% uncertainty with the VMD

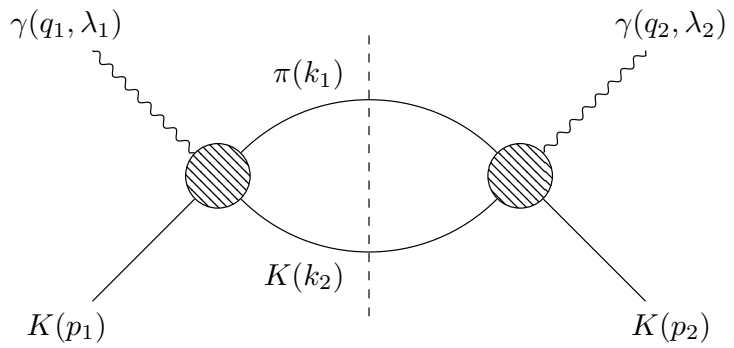

Figure 7.3: Compton scattering of kaons via an $K\pi$ intermediate state. The two photons have momenta q_i and helicity λ_i, while the in- and outgoing kaon momenta are labeled by p_i. The internal momenta are k_1 for the pion and k_2 for the kaon.

estimates for the polarizabilities, which is probably not even overly conservative. The main difference between the kaon and pion cases is the size of the respective masses: higher orders in the polarizabilities are suppressed only by M_K^2 instead of M_π^2, making the former more susceptible to corrections by a factor of about 12.

Apart from corrections to the polarizabilities, however, the appearance of resonances in the Compton amplitude limits the energy range that can sensibly be employed for the experimental extraction thereof. For this specific problem, there is still a clear hierarchy in mass scales between the $K^*(892)$ and the first axial-vector state, the $K_1(1270)$. We will therefore reconstruct the K^* contribution dispersively via its two possible $K\pi$ intermediate states.

We show the exact form of the partial-wave expansion of the Compton helicity amplitudes in Appendix 7.A. There, we also derive the imaginary parts of the P-waves due to $K\pi$ intermediate states, see Fig. 7.3, for the $+\pm$ helicities, which read

$$\mathrm{Im}\left(f_{1,\pm}(s)\right) = \pm\frac{1}{8\pi e^2}\frac{\lambda^{3/2}(s, M_\pi^2, M_K^2)}{72 s^2}\left(|g_1^c(s)|^2 + |g_1^n(s)|^2\right)\theta\big(s - (M_K + M_\pi)^2\big)\,, \quad (7.30)$$

where $\lambda(a, b, c)$ is the Källén function defined in Eq. (2.15).[7] Here g_1^c and g_1^n are the $\gamma K \to K\pi$ amplitudes with the charged and neutral kaons in the final state, respectively.[8] Using an n-times subtracted dispersion integral we obtain the $\gamma K \to \gamma K$ P-wave amplitude

$$f_{1,\pm}(s) = P_{n-1}(s) + \frac{\big(s - M_K^2\big)^n}{\pi}\int_{M_K^2}^{\infty} \mathrm{d}s' \frac{\mathrm{Im}\left(f_{1,\pm}(s')\right)}{\big(s' - M_K^2\big)^n\,(s' - s)}\,, \quad (7.31)$$

where we have subtracted at $s = M_K^2$. We use the twice subtracted result from Ref. [4] for the $\gamma K \to K\pi$ amplitudes, which approach a constant for $s \to \infty$. Since we only need $g_1^i(s)$ in the low-energy region close to the K^* resonance and are not interested in the high-energy behavior of this amplitude, we set $g_1^i(s) \to 1/s$ for large s, starting at 1 GeV. With one subtraction the partial-wave amplitude then reads

$$f_{1,\pm}^1(s) = a_1^\pm \pm \bar{f}_1^1(s)\,, \quad (7.32)$$

[7] Note that we include the factor of e^2 due to the amplitude definition in Ref. [4].
[8] This form holds for both charged- and neutral-kaon Compton scattering, with $g_1^{c,n}$ replaced accordingly.

where

$$\bar{f}_1^1(s) = \frac{(s-M_K^2)}{\pi}\int_{M_K^2}^{\infty} \mathrm{d}s' \frac{\mathrm{Im}\,(f_{1,+}(s'))}{(s'-M_K^2)(s'-s)}\,. \tag{7.33}$$

The subtraction can be fixed via $a_1^{\pm} = f_{1,\pm}^1(M_K^2)$.

Reinserting the P-waves into the partial-wave decomposition for the helicity amplitudes leads to the dispersively reconstructed K^* contributions

$$\begin{aligned}\mathcal{F}_{++}^{K^*}(s,t) &= \frac{3}{4}\left(M_K^4 - su\right)\left[f_{1,+}^1(s) + f_{1,+}^1(u)\right]\,,\\ \mathcal{F}_{+-}^{K^*}(s,t) &= -\frac{3}{4}t\left[sf_{1,-}^1(s) + uf_{1,-}^1(u)\right]\,.\end{aligned} \tag{7.34}$$

The u-channel pieces are added by hand in order to render the amplitude crossing symmetric. Comparing to Eq. (7.23), we note that the VMD model can be brought into exactly the same form. Applying Eq. (7.11) then allows us to identify the connection between the subtraction constants and the polarizabilities extracted from the VMD model,

$$a_1^{\pm} = \frac{1}{3M_K\alpha_{\mathrm{em}}}\left(\alpha_1 \pm \beta_1\right)_{K^{\pm}}^{\mathrm{VMD}} = \pm\frac{4}{3}\frac{C_{K^*}^2}{M_{K^*}^2 - M_K^2}\,. \tag{7.35}$$

To understand to what extent these subtraction constants can be replaced by the phenomenological polarizabilties that, ultimately, ought to serve as free parameters to be extracted from experiment, we need to discuss the structure of our complete amplitude representation, which is of the following form. In addition to the Born terms, we retain

1. the dipole polarizabilities;
2. dispersive representations of the leading singularities in s-, t-, and u-channels, which comprises the $K\pi$ P-waves (or the $K^*(892)$) in s- and u-channels, as well as the $\pi\pi$ S-wave (or the $f_0(500)$) in the t-channel;
3. and the perturbative t-channel kaon loop to account for the missing piece in the above to reproduce the complete next-to-leading-order chiral representation.

The Born-term-subtracted helicity amplitudes are therefore of the form

$$\begin{aligned}\widehat{\mathcal{F}}_{+-}(s,t) &= -\frac{t}{2}\left[\frac{M_K}{\alpha_{\mathrm{em}}}(\alpha_1-\beta_1)_{K^{\pm}} + \mathcal{A}^{\mathrm{disp}}(t) - \frac{3}{2}\left(ta_1^- + s\bar{f}_1^1(s) + u\bar{f}_1^1(u)\right)\right]\,,\\ \widehat{\mathcal{F}}_{++}(s,t) &= \frac{3}{4}(M_K^4 - su)\left[\frac{2}{3M_K\alpha_{\mathrm{em}}}(\alpha_1+\beta_1)_{K^{\pm}} + \bar{f}_1^1(s) + \bar{f}_1^1(u)\right]\,.\end{aligned} \tag{7.36}$$

Note that the dipole polarizabilities $(\alpha_1 \pm \beta_1)_{K^{\pm}}$ now subsume the contributions induced by the subtraction constants of the dispersive P-wave. For the $+-$ helicity amplitude, however, a term proportional to $t^2 a_1^-$ is explicitly kept, since it induces a contribution to the quadrupole polarizabilities. These only come from the K^* resonance. Here, a_1^- is fixed by Eq. (7.35). Furthermore, in the $++$ helicity we keep the kinematic structure in front of the scalar amplitude, cf. Eq. (7.7).

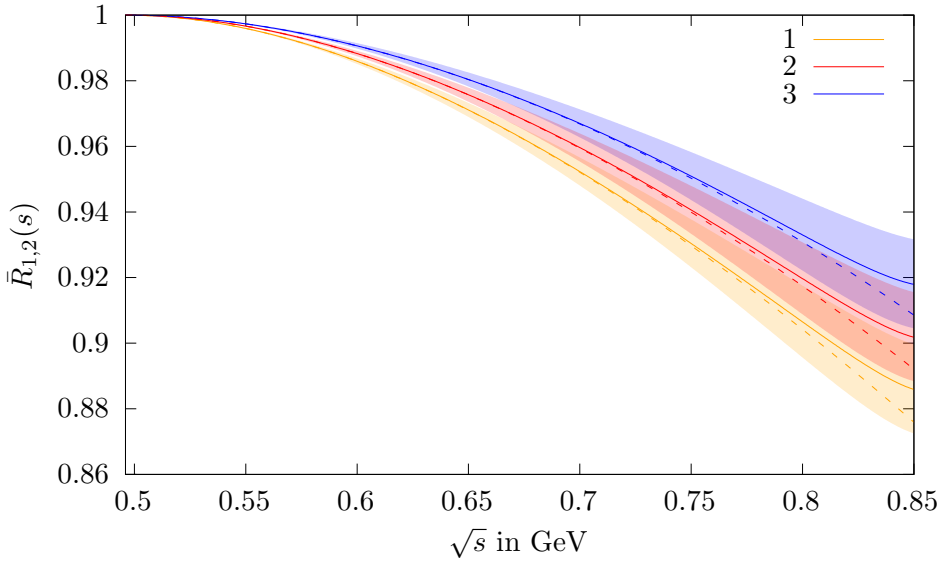

Figure 7.4: Energy dependence of the integrated ratio of the differential cross sections over the backward half angle $\bar{R}_1(s)$ as defined in Eq. (7.38). The colors indicate the scenarios 1 to 3, which are described in the main text. The dashed lines represent the same input for the kaon polarizabilities as indicated by their color, but for the unphysical integrated ratio $\bar{R}_2(s)$.

7.5 Results

In analogy to Ref. [350], we now define ratios of differential cross sections to extract the kaon polarizabilities and test the sensitivity to the latter. Here, the experimentally measured quantity is normalized and compared to a theoretical one. We add the Born terms and calculate the differential cross sections via Eq. (7.10). The ratio optimized for sensitivity to polarizability effects, retaining all other parts of the amplitude, then reads

$$R_1(s,t) = \frac{\mathrm{d}\sigma/\mathrm{d}\Omega(s,t)}{\mathrm{d}\sigma/\mathrm{d}\Omega(s,t)\Big|_{\alpha_1=\beta_1=0}}\,, \tag{7.37}$$

where the label indicates that α_1 and β_1 are set to zero in Eq. (7.36), while all other terms are kept. For an analysis focusing on the extraction of the kaon polarizability *difference*, this ratio can be integrated over backward angles, leading to

$$\bar{R}_1(s) = \int_{-1}^{z_{\mathrm{cut}}} \mathrm{d}z_s R_1(s, t(s, z_s))\,. \tag{7.38}$$

This backward-integrated ratio $\bar{R}_1(s)$, with cutoff angle $z_{\mathrm{cut}} = 0$, is shown in Fig. 7.4. For the difference of kaon polarizabilities $(\alpha_1 - \beta_1)_{K^\pm}$ we use three different scenarios. We employ the ChPT prediction, Eq. (7.15), and add 0.5, 1, and 1.5 times the VMD induced corrections, Eq. (7.25), labeled by scenario 1 to 3, respectively.[9] This corresponds

[9]Note that due to Eq. (7.25) the two linear combinations have a different sign for the VMD contribution to the polarizabilities. Therefore, adding 1.5 times the VMD result leads to a smaller polarizability for $(\alpha_1 - \beta_1)_{K^\pm}$ than 0.5 times the VMD result.

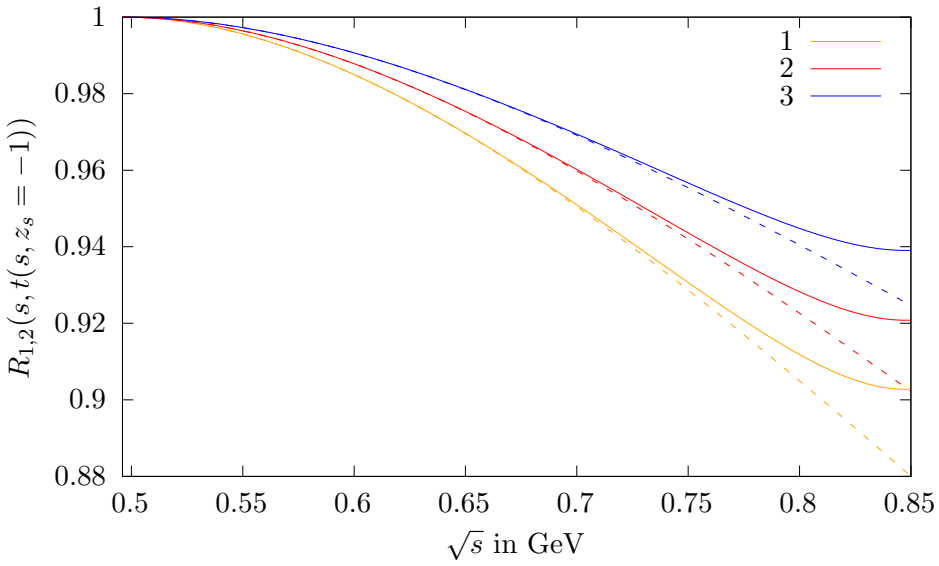

Figure 7.5: Energy dependence of the ratio of the differential cross sections, Eq. (7.37), for $z_s = -1$. Line styles as in Fig. 7.4.

to varying $(\alpha_1 - \beta_1)_{K^\pm}$ by approximately $\pm 20\%$ around the central value, given by the ChPT result with higher-order corrections estimated by VMD; in other words, the different full lines in Fig. 7.4 indicate the required accuracy to extract $(\alpha_1 - \beta_1)_{K^\pm}$ at the 20% level.

On the other hand, the colored bands around the three central full curves depict a variation in $(\alpha_1 + \beta_1)_{K^\pm}$ from 0.5 to 1.5 times the VMD result. While we will discuss strategies to actually disentangle $(\alpha_1 \pm \beta_1)_{K^\pm}$ below, in the context of the extraction of the polarizability difference in backward directions, we regard the sum merely as a source of uncertainty. We observe that these bands grow wider with increasing energy, start to overlap significantly around $\sqrt{s} \approx 700\,\text{MeV}$, and around 800 MeV are so wide that the 50% variation in $(\alpha_1 + \beta_1)_{K^\pm}$ roughly makes up for the 20% variation in $(\alpha_1 - \beta_1)_{K^\pm}$: the impact of the *sum* of polarizabilities on the extraction of the *difference* is by far not negligible. This is in notable contrast to the charged-pion case. This effect can be reduced by choosing the angle more narrowly ($z_{\text{cut}} < 0$), which will on the other hand limit the statistics. The extreme case is illustrated in Fig. 7.5: in strict backward direction, for fixed $z_s = -1$, the amplitude is independent of the linear combination $(\alpha_1 + \beta_1)_{K^\pm}$ and therefore does not show any bands. However, it is unrealistic that an experiment will gather enough statistics for such a fixed angle. Therefore, it will become crucial in the experimental analysis to optimize the interplay of both these quantities.

We can define different ratios of differential cross sections to illustrate the necessity to retain the K^* resonance in the polarizability extraction; all of them are similarly studied

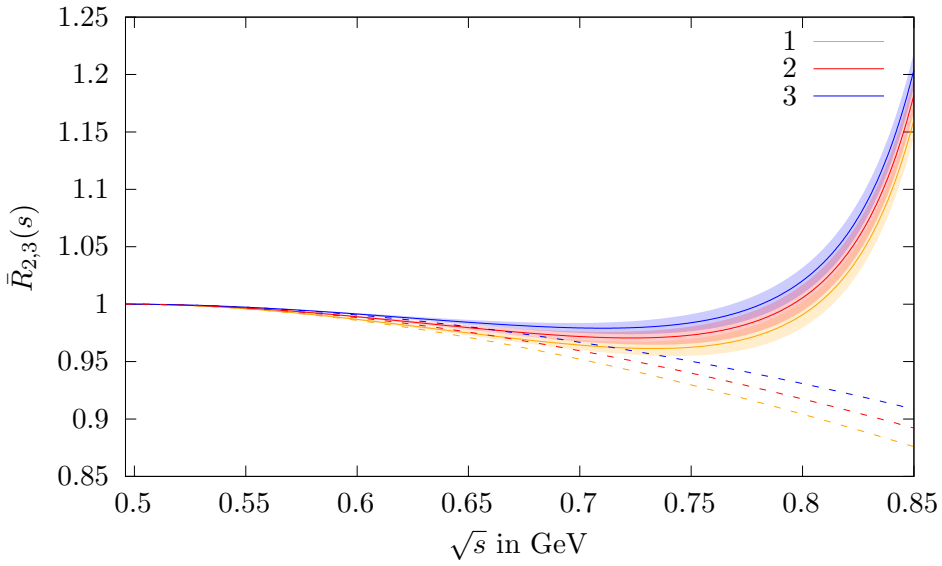

Figure 7.6: Energy dependence of the integrated ratio of the differential cross sections over the backward half angle $\bar{R}_3(s)$ as defined in Eq. (7.40), neglecting the dispersively reconstructed K^* in the denominator. Line styles as in Fig. 7.4.

in forms integrated over backward angles. We define

$$R_2(s,t) = \frac{\mathrm{d}\sigma/\mathrm{d}\Omega(s,t)\Big|_{K^*=0}}{\mathrm{d}\sigma/\mathrm{d}\Omega(s,t)\Big|_{\alpha_1=\beta_1=K^*=0}}\,,$$
$$\bar{R}_2(s) = \int_{-1}^{z_{\mathrm{cut}}} \mathrm{d}z_s R_2(s,t(s,z_s))\,, \tag{7.39}$$

where $K^* = 0$ denotes that we neglect the K^* resonance and therefore do not include $\bar{f}_1^1$ and a_1^- in Eq. (7.36). This is a purely theoretical or unphysical ratio (as the K^* is omitted also in the numerator, which is impossible to measure experimentally), but it serves to illustrate the analogy to the pion case, where the ρ resonance is outside of the relevant energy region: its influence is suppressed because the energy range is chosen to be $\sqrt{s} < 3.5M_\pi$ [350], where the ρ is far enough away ($M_\rho \approx 5.5M_\pi$, or $3.5M_\pi \approx M_\rho - 2\Gamma_\rho$). However, this still leads to an available energy range above threshold of approximately 350 MeV. $\bar{R}_2(s)$ hence shows the sensitivity of a charged-kaon polarizability extraction in a world where no s-channel resonance disturbs the range of validity of the expansion.

This ratio is also included for comparison in Fig. 7.4 for the same three different values of $(\alpha_1 - \beta_1)_{K^\pm}$ (but neglecting the variation in $(\alpha_1 + \beta_1)_{K^\pm}$, which leads to extremely similar bands as for $\bar{R}_1(s)$), denoted by dashed lines. We find that full and dashed lines, corresponding to $\bar{R}_1(s)$ and $\bar{R}_2(s)$, are extremely close up to roughly $\sqrt{s} \approx 800$ MeV: our effort to stabilize the ratio by inclusion of the K^* is entirely successful, and data for higher energies can be made available for the polarizability extraction that way. Note that the energy range displayed in Figs. 7.4–7.6 corresponds rather precisely to the 350 MeV used for the pion polarizability extraction [350].

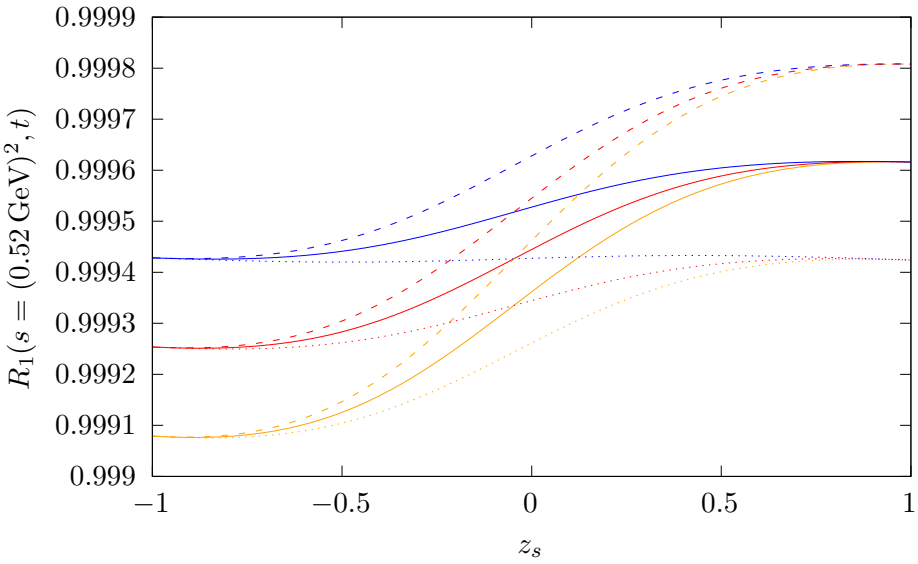

Figure 7.7: Angular dependence of the ratio of differential cross sections $R_1(s,t)$ as defined in Eq. (7.37) for $s = (0.52\,\mathrm{GeV})^2$. As before we employ the ChPT prediction for the polarizabilities and add 0.5 (orange; dashed), 1 (red; solid), and 1.5 (blue; dotted) times the VMD induced corrections. Different colors indicate the variation in $(\alpha_1 - \beta_1)_{K^\pm}$, whereas different dash-types denote the varied values for $(\alpha_1 + \beta_1)_{K^\pm}$.

Finally, we investigate the ratio

$$R_3(s,t) = \frac{\mathrm{d}\sigma/\mathrm{d}\Omega(s,t)}{\mathrm{d}\sigma/\mathrm{d}\Omega(s,t)\Big|_{\alpha_1=\beta_1=K^*=0}}\,,$$
$$\bar{R}_3(s) = \int_{-1}^{z_\mathrm{cut}} \mathrm{d}z_s R_3(s,t(s,z_s))\,, \tag{7.40}$$

where the full, experimentally accessible, differential cross section is employed in the numerator, but normalized to a denominator omitting the K^* effects. This corresponds to the attempt to extract polarizabilities from real data, but ignoring the K^* in the normalization expression. We obviously expect R_3 to show strong deviations from unity when increasing s towards the K^* resonance energy, which are indeed visible in Fig. 7.6: the onset of the resonant rise in $\bar{R}_3(s)$ obscures the polarizability sensitivity at the 20% level already for energies as low as $\sqrt{s} \approx 650\,\mathrm{MeV}$, and quickly deteriorates even further above. We therefore strongly suggest to use $\bar{R}_1$ for the extraction of kaon polarizabilities.

AMBER might be able to extend the angular range to forward directions, or positive z_s [398]. In Figs. 7.7, 7.8, and 7.9 we show the z_s dependence of the ratio $R_1(s,t)$, cf. Eq. (7.37), for different s and variations of the polarizabilities. In accordance with Eq. (7.12), at backwards angle $z_s = -1$ only $(\alpha_1 - \beta_1)_{K^\pm}$ affects the ratio, while at forward angle $z_s = +1$ only $(\alpha_1 + \beta_1)_{K^\pm}$ can be extracted. Clearly, good sensitivity at forward angles would enable one to determine $(\alpha_1+\beta_1)_{K^\pm}$ much more precisely, and hence ultimately disentangle electric and magnetic dipole polarizabilities. Obviously, the same variation of the VMD contribution to $(\beta_1)_{K^\pm}$ has a larger relative impact on $(\alpha_1 + \beta_1)_{K^\pm}$

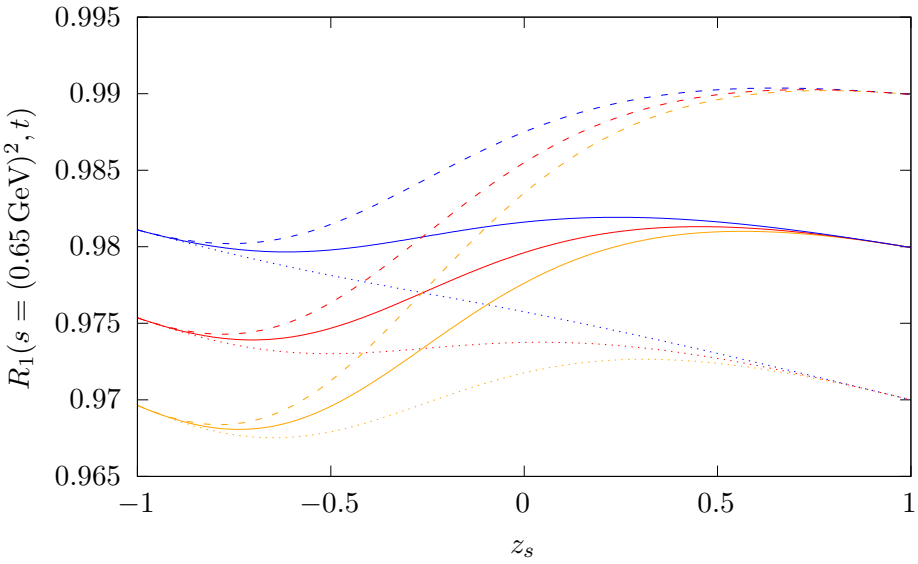

Figure 7.8: Angular dependence of the ratio of differential cross sections $R_1(s,t)$ as defined in Eq. (7.37) for $s = (0.65\,\mathrm{GeV})^2$. Legend is the same as in Fig. 7.7.

than on $(\alpha_1 - \beta_1)_{K^\pm}$. Additionally, the variation in $(\alpha_1 - \beta_1)_{K^\pm}$ seems to only have impact for all relevant s starting at $z_s \lesssim 0.5$, while $(\alpha_1 + \beta_1)_{K^\pm}$ affects the ratio visibly already for $z_s \gtrsim -0.75$.

Furthermore, we checked the stability of all these ratios by varying the input $\gamma K \to K\pi$ amplitudes in the dispersion integral within their uncertainty bands. Figs. 7.4, 7.5, 7.7, 7.8, and 7.9 do not change at all, since the dispersion integral is included in both the numerator and denominator of the ratios. However, this will obviously be different once the numerator is fixed from experiment. Additionally, Fig. 7.6 shows a dependence on the different inputs as the dispersion integral is only used in the numerator.

Note that an experimental extraction of the accompanying pion-production process $\gamma K \to K\pi$ is necessary to properly constrain the amplitudes that are used in the dispersion integral for the resonant P-wave. This is also achievable with the AMBER experiment [4]. Furthermore, note that for the analysis of the charged-pion polarizabilities [350], also radiative corrections have been taken into account. These can easily be adapted for charged kaons [377], which ought to be done for the experimental analysis.

7.6 Neutral-kaon Compton scattering

Compton scattering can also be discussed for *neutral* kaons, and measurements of this kind might become feasible in the future at the planned K-Long Facility (KLF) at Jefferson Lab [297]. Due to the absence of Born terms, the near-threshold amplitude is directly proportional to the dipole polarizabilities, leading to a cross section of the form

$$\sigma(s) = \frac{\pi(s - M_K^2)^4}{12 M_K^2 s^3}\left(M_K^4\,(\alpha_1 - \beta_1)_{K^0}^2 + s^2\,(\alpha_1 + \beta_1)_{K^0}^2\right). \tag{7.41}$$

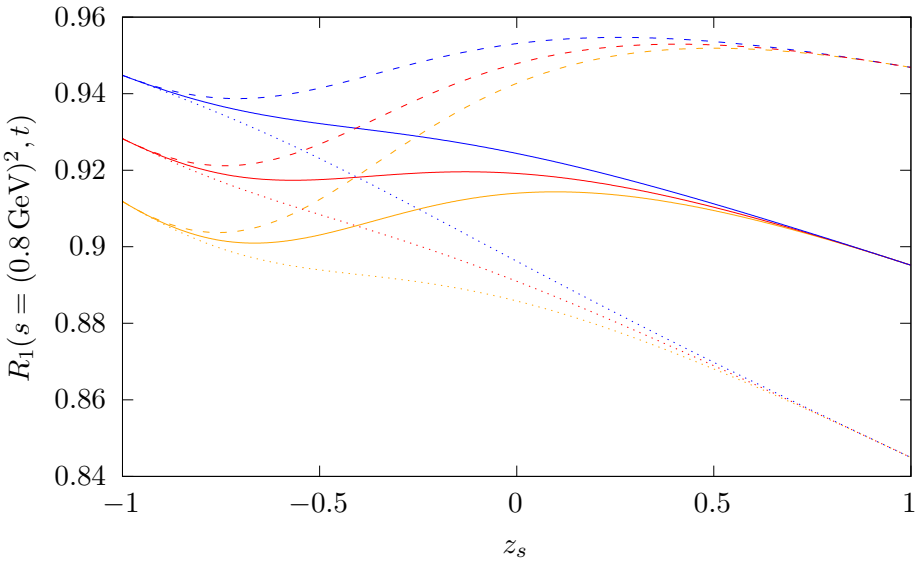

Figure 7.9: Angular dependence of the ratio of differential cross sections $R_1(s,t)$ as defined in Eq. (7.37) for $s = (0.8\,\mathrm{GeV})^2$. Legend is the same as in Fig. 7.7.

This would in principle allow for a much more straightforward extraction of these; the downside, obviously, is that the corresponding cross sections are smaller by orders of magnitude.

In ChPT, the first contribution to the neutral-kaon Compton amplitude arises at one-loop order and is given by [331]

$$\begin{aligned}\mathcal{A}^n(s,t) &= -\frac{1}{8\pi^2 F_K^2}\left[1 - \frac{2M_\pi^2}{t}\arctan^2\left(\frac{1}{\sigma^\pi(t)}\right) - \frac{2M_K^2}{t}\arctan^2\left(\frac{1}{\sigma^K(t)}\right)\right],\\ \mathcal{B}^n(s,t) &= 0\,.\end{aligned} \tag{7.42}$$

Both polarizabilities in fact vanish at this order. We therefore model them, in the spirit of the preceding analysis for charged kaons, by K^*-exchange, leading to a nonvanishing magnetic polarizability given by the same expression as in Eq. (7.25). With radiative width and masses adjusted to the neutral channel, this results in $(\beta_1)_{K^0}^{\mathrm{VMD}} = 0.8 \cdot 10^{-4}\,\mathrm{fm}^3$. The resonant lineshape of the K^* is dispersively reconstructed in direct analogy to the charged case.

The dispersive t-channel $\gamma\gamma \to \pi\pi \to \bar{K}K$ amplitude replaces the pion loops $\mathcal{A}^\pi(t)$ in Eq. (7.42) following the discussion in Sec. 7.3. This results in

$$\mathcal{A}^n(t) = -\frac{\sqrt{2}}{t}k_{++}^0(t) - \frac{1}{8\pi^2 F_K^2}\left[\frac{1}{2} - \frac{2M_K^2}{t}\arctan^2\left(\frac{1}{\sigma^K(t)}\right)\right].$$

The cross section dominated by the polarizablities in the low-energy region is shown in Fig. 7.10. The solid red line represents the full neutral solution with polarizabilities, loop corrections, and the K^* resonance. The dashed line denotes the result based solely on polarizabilities according to Eq. (7.41). We observe that the polarizabilities dominate up to

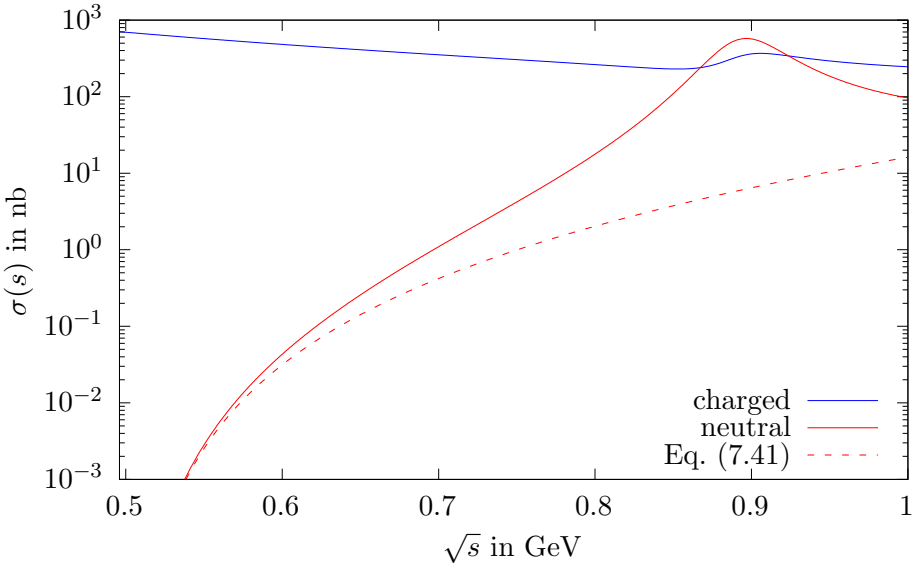

Figure 7.10: Cross section for the charged (blue) and neutral (red) kaon Compton scattering. The dashed red line represents Eq. (7.41).

about $\sqrt{s} = 0.7\,\text{GeV}$; in this range, the total cross section amounts to less than a nanobarn. Compared to the approximately 700 nb in the charged-kaon case, one looses many orders of magnitude of events. Therefore, experimental observation close to threshold will be very challenging. However, in the region of the K^* resonance the neutral cross section exceeds the charged one due to the larger radiative width of the K^{*0}.

7.7 Conclusion

We proposed a method to extract kaon polarizabilities from differential cross sections of kaon Compton scattering. To this end, we used the ChPT amplitudes up to next-to-leading order as a starting point. Therein, the t-channel pion loop contribution that limits the range of applicability of the polarizability expansion can be dispersively improved, employing solutions of a coupled-channel analysis of $\gamma\gamma \to \{\pi\pi, \bar{K}K\}$. The dominant K^* resonance in the s-channel is dispersively reconstructed using amplitudes from the pion photoproduction reaction on kaons, $\gamma K \to K\pi$. In contrast to the pion case the hierarchy $(\alpha_1 + \beta_1) \ll (\alpha_1 - \beta_1)$ is not viable for kaon polarizabilities and both linear combinations need to be considered. We then suggested a ratio, optimized for sensitivity to the kaon polarizabilities, by incorporating all of the former effects. We showed that this ratio enlarges the energy range to be similar to the pion case. In addition, the relative size of polarizability difference and sum is such in the charged-kaon case that an extension of the experimental analysis of Compton scattering towards forward angles may realistically allow for the disentanglement of $(\alpha_1)_{K^\pm}$ and $(\beta_1)_{K^\pm}$. For neutral kaons the cross section close to threshold is directly proportional to the square of the polarizabilities, however, experimental extraction will become challenging due to the small overall cross section, since there are no corresponding Born terms.

This chapter provides all necessary theoretical methods for a combined analysis of kaon

Primakoff data for both kaon–photon and kaon–pion [4] final states, giving combined access to the chiral anomaly in a kaon reaction, the radiative width of the $K^*(892)$ resonance, and to kaon polarizabilities. Once experimental data on these reactions is available, e.g., from AMBER, such an analysis ought to be performed to minimize theoretical bias and model dependence.

7.A Dispersive reconstruction of the $K\pi$ intermediate state

In this appendix, we derive the discontinuity equation for a $K\pi$ intermediate state of the kaon Compton scattering amplitude. The definitions of the momenta are shown in Fig. 7.3. We start from the unitarity of the S-matrix, which leads to

$$\mathrm{disc}\,(\mathcal{M}_{if}) = i\sum_n (2\pi)^4 \delta^{(4)}(q_1 + p_1 - k_n)\mathcal{M}_{in}\mathcal{M}^*_{nf}\,. \tag{7.43}$$

The sum in general runs over all possible hadronic intermediate states. Replacing the sum by the appropriate integrations results in

$$\mathrm{disc}\,(\mathcal{M}_{if}) = \frac{i}{(2\pi)^2}\int \frac{\mathrm{d}^3k_1}{2k_1^0}\frac{\mathrm{d}^3k_2}{2k_2^0}\delta^{(4)}(q_1 + p_1 - k_1 - k_2)\mathcal{M}_{in}\mathcal{M}^*_{nf}\,. \tag{7.44}$$

The initial-to-final Compton scattering amplitude can be expanded into partial waves via [145]

$$\mathcal{F}_{+\pm}(s,t,u) = \sum_{J=1}^{\infty}(2J+1)\left(\frac{(s-M_K^2)^2}{4}\right)^J f_{J,\pm}(s)d^J_{1,\pm}(z_s)\,, \tag{7.45}$$

where the small Wigner d-functions are given by

$$d^J_{1,\pm} = \frac{1\mp z}{J(J+1)}P'_J(z_s) \pm P_J(z_s)\,. \tag{7.46}$$

P_J and P'_J are the Legendre polynomials and their derivatives, respectively. The amplitudes involving $K\pi$ intermediate states are of odd intrinsic parity and can be related to scalar amplitudes $\mathcal{G}(s,t,u)$[10]

$$\mathcal{M}_{\gamma K\to K\pi,\pm} = i\varepsilon_{\mu\nu\alpha\beta}\epsilon^\mu_{j,\pm}p_i^\nu k_1^\alpha k_2^\beta \mathcal{G}(s,t,u)\,, \tag{7.47}$$

where $j = 1$ for initial to intermediate and $j = 2$ for intermediate to final state. The partial-wave expansion of the scalar amplitudes is given by

$$\mathcal{G}(s,t,u) = \sum_J g_J(s)P'_J(z_s)\,. \tag{7.48}$$

S-waves are forbidden and the D-wave and higher contributions only become relevant outside of the kinematical region we are interested in, where the $K_2^*(1430)$ is the lowest

[10] For simplicity, we refrain from distinguishing the two possible $K\pi$ charge configurations notation-wise, which will simply be summed over in the final result.

lying resonance starting well beyond 1 GeV. Therefore, we only consider P-waves and the discontinuity relation reads

$$3\frac{(s-M_K^2)^2}{4}\frac{1\pm z_s}{2}\mathrm{disc}\left(f_{1,\pm}(s)\right)=\frac{i}{(2\pi)^2}\frac{\lambda^{1/2}(s,M_\pi^2,M_K^2)}{8s}|g_1(s)|^2\mathcal{I}_\pm\,, \tag{7.49}$$

where

$$\mathcal{I}_\pm=\int \mathrm{d}\cos\left(z_s'\right)\mathrm{d}\phi'\varepsilon_{\mu\nu\alpha\beta}\varepsilon_{\sigma\rho\gamma\delta}\epsilon_{1,+}^{\mu}\epsilon_{2,\pm}^{\sigma}p_1^{\nu}p_2^{\rho}k_1^{\alpha}k_1^{\gamma}k_2^{\beta}k_2^{\delta}\,. \tag{7.50}$$

Since $\mathcal{I}_\pm$ is fully contracted, we can evaluate it in the center-of-mass system and choose an explicit representation for the momenta [349]. This results in

$$\mathcal{I}_\pm=\pm\pi\frac{1\pm z_s}{24s}\lambda(s,M_\pi^2,M_K^2)(s-M_K^2)^2\,. \tag{7.51}$$

Therefore the discontinuity of the P-wave for the $+\pm$ helicities reads

$$2i\mathrm{Im}\left(f_{1,\pm}(s)\right)=\mathrm{disc}\left(f_{1,\pm}(s)\right)=\pm\frac{i}{4\pi}\frac{\lambda^{3/2}(s,M_\pi^2,M_K^2)}{72s^2}|g_1(s)|^2\,. \tag{7.52}$$

Chapter 8

Kaon electromagnetic form factors in dispersion theory

8.0 Prologue

The content of this chapter is based on the publication

- D. Stamen, D. Hariharan, M. Hoferichter, B. Kubis, and P. Stoffer, *Kaon electromagnetic form factors in dispersion theory*, Eur. Phys. J. C **82**, 432 (2022) [arXiv:2202.11106 [hep-ph]] .

Furthermore, results of this chapter are used in

- M. Hoferichter, G. Colangelo, B.-L. Hoid, B. Kubis, J. Ruiz de Elvira, D. Stamen, and P. Stoffer, *Chiral extrapolation of hadronic vacuum polarization and isospin-breaking corrections*, PoS **LATTICE2022**, 316 (2022) [arXiv:2210.11904 [hep-ph]] ,
- M. Hoferichter, G. Colangelo, B.-L. Hoid, B. Kubis, J. Ruiz de Elvira, D. Schuh, D. Stamen, and P. Stoffer, *Phenomenological Estimate of Isospin Breaking in Hadronic Vacuum Polarization*, Phys. Rev. Lett. **131**, 161905 (2023) [arXiv:2307.02532 [hep-ph]] .

This project started in the context of Deepti Hariharan's Master's thesis [399].

The electromagnetic form factors of charged and neutral kaons are strongly constrained by their low-energy singularities, in the isovector part from two-pion intermediate states and the isoscalar contribution in terms of ω and ϕ residues. The former can be predicted using the respective $\pi\pi \to \bar{K}K$ partial-wave amplitude and the pion electromagnetic form factor. The pion electromagnetic form factor uses the same $\pi\pi \to \bar{K}K$ phase shift to ensure a real-valued imaginary part in the unitarity relation. The free parameters are fixed by a fit to $e^+e^- \to \pi^+\pi^-$ data from BaBar [400]. Using the imaginary part from the unitarity relation in an unsubtracted dispersion integral yields the isovector part of the kaon electromagnetic form factor. We fix the normalization by including intermediate states beyond $\pi\pi$ in a minimal way via the ρ' resonance. The result can be compared to data from $\tau^- \to K^-K_S\nu_\tau$ decays. This analysis was carried out by the author of this thesis.

For the isoscalar part, parameters need to be determined from electromagnetic reactions involving kaons. For this, we use a vector-meson dominance ansatz, where the residues, masses, and widths are free parameters.

We present a global analysis of timelike and spacelike data that implements all of these constraints. The analysis needs to account for multiple effects such as final-state radiation, vacuum-polarization effects, and systematic uncertainties leading to the d'Agostini bias [401]. Furthermore, one data set provides binned data that needs to be accounted

for. These fits were carried out by the author of this thesis including the creation of all plots in this chapter and the analysis of the uncertainties and correlations. The global fit to $\bar{K}K$ gives $\bar{M}_\phi = 1019.479(5)\,\text{MeV}$, $\bar{\Gamma}_\phi = 4.207(8)\,\text{MeV}$ for the parameters of the ϕ resonance including vacuum-polarization effects.

The results enable manifold applications: kaon charge radii, elastic contributions to the kaon electromagnetic self energies and corrections to Dashen's theorem, kaon boxes in hadronic light-by-light (HLbL) scattering, and the ϕ region in hadronic vacuum polarization (HVP). The kaon charge radii are calculated via the derivative of the form factor at zero energy. Our results are $\langle r^2\rangle_\text{c} = 0.359(3)\,\text{fm}^2$, $\langle r^2\rangle_\text{n} = -0.060(4)\,\text{fm}^2$ for the charged and neutral radii. The calculation was performed by the author of this thesis.

Using a variant of the Cottingham formula and our result for the kaon electromagnetic form factor, along with the pion electromagnetic form factor from Ref. [146], we find $\epsilon = 0.63(40)$ for the elastic contribution to the violation of Dashen's theorem. This application was, again, carried out by the author of this thesis.

Next, we calculate the charged kaon box in HLbL scattering to be $a_\mu^{K\text{-box}} = -0.48(1)\cdot 10^{-11}$. This was carried out by Peter Stoffer and Martin Hoferichter, who already had an existing numerical code for the calculation of the box-diagram contribution to HLbL.

As the last application, we are able to calculate the HVP integrals around the ϕ resonance to yield $a_\mu^\text{HVP}[K^+K^-, \leq 1.05\,\text{GeV}] = 184.5(2.0)\cdot 10^{-11}$, $a_\mu^\text{HVP}[K_SK_L, \leq 1.05\,\text{GeV}] = 118.3(1.5)\cdot 10^{-11}$. We find a small tension to the analysis using data combination, since the ϕ resonance shape is modified due to tensions in the underlying data sets. This analysis was again carried out by the author of this thesis.

Note that all the previous results were cross-checked by Peter Stoffer and Martin Hoferichter.

Currently, the tension between lattice QCD and the results from the $e^+e^- \to \text{hadrons}$ cross-section data for the HVP determination hinders interpreting the precision measurement of the muon's anoumalous magnetic moment. Since isospin-breaking effects are calculated separately in lattice QCD, we identify them for the data-driven framework in multiple channels. This framework and the results of this chapter are used in Refs. [7, 8] to estimate the isospin-breaking effects in HVP induced by the kaon mass difference. These aspects are included in Appendix 8.A.

8.1 Introduction

The simplest, most stringently constrained matrix element that describes the interaction of hadrons with the electromagnetic current j_μ is the pion vector form factor (VFF)

$$\left\langle \pi^+(p_1)\pi^-(p_2)\right| j_\mu(0)\left|0\right\rangle = (p_1 - p_2)_\mu F_\pi^V(s)\,, \tag{8.1}$$

where $s = (p_1 + p_2)^2$. By far the dominant contribution to its unitarity relation arises from $\pi\pi$ intermediate states above the threshold $s_\text{th} = 4M_\pi^2$,

$$\operatorname{Im} F_\pi^V(s) = F_\pi^V(s)\sin\delta(s)e^{-i\delta(s)}\theta(s - s_\text{th})\,, \tag{8.2}$$

which strongly constrains the functional form of $F_\pi^V(s)$ in terms of the P-wave phase shift $\delta(s)$ for $\pi\pi$ scattering. Up to isospin-breaking and inelastic corrections, the unitarity

relation can be solved in terms of the Omnès function [45, 46]

$$\Omega(s) = \exp\left(\frac{s}{\pi}\int_{s_{\text{th}}}^{\infty} \mathrm{d}s' \frac{\delta(s')}{s'(s'-s)}\right), \tag{8.3}$$

up to a real polynomial $P(s)$,

$$F_\pi^V(s) = P(s)\Omega(s)\,. \tag{8.4}$$

Such dispersive constraints are ubiquitous in the literature as basis for increasingly precise representations of $F_\pi^V(s)$ [146, 402–411], often motivated by the two-pion contribution to HVP.

In this chapter, we apply the same strategy to the electromagnetic form factors of the kaon, with several key differences to the case of the pion. First, while the electromagnetic form factor of the π^0 vanishes due to C parity, both charged and neutral kaons can couple to j_μ, so that isoscalar and isovector components need to be considered. The isovector part possesses a unitarity relation similar to Eq. (8.2) [412], in that $\pi\pi$ intermediate states yield by far the biggest contribution, but the reaction is no longer elastic and $F_\pi^V(s)$ as well as the respective partial-wave amplitude for $\pi\pi \to \bar{K}K$ need to be provided as input. The unitarity relation for the isoscalar part receives dominant contributions from 3π and $\bar{K}K$ intermediate states, but in practice the corresponding spectral function is well approximated by the narrow ω and ϕ resonances, i.e., their pole parameters and residues. These key ideas are spelled out in more detail in Sec. 8.2, to establish the formalism upon which the remainder of this work will be based.

While the isovector part can thus be predicted (and validated by data for $\tau^- \to K^-K_S\nu_\tau$ [413]), the representation for the isoscalar part involves free parameters, most notably the residues of the ω and ϕ contributions. To determine these, we perform fits to cross-section data for the charged and neutral timelike reactions $e^+e^- \to K^+K^-$ [414–417] and $e^+e^- \to K_SK_L$ [414, 418, 419], respectively, as well as spacelike data for charged-kaon–electron scattering [420, 421]. The results of these fits are presented in Sec. 8.3, including the comparison to the ϕ resonance parameters from Refs. [125, 347, 422, 423].

The resulting form factors can then be used to study a number of applications.

1. The derivative at $s = 0$ determines the charge radii, see Sec. 8.4.1. For the charged kaon, the averages from Ref. [347] are based on the spacelike data [420, 421] only, such that the comparison illustrates the impact of the timelike data sets, as well as the dispersion-theoretical constraints on the isovector part. For the neutral kaon, constraints on the charge radius can be extracted from $K_L \to \pi^+\pi^-e^+e^-$ [424, 425] and electron scattering experiments [426–428], allowing for another cross check.

2. The kaon form factors determine the elastic contribution to Compton scattering off the kaon, which, in turn, gives the bulk of the electromagnetic self energy via the Cottingham formula [429]. Together with the analog formula for the pion, we can thus provide an estimate of the corrections to Dashen's theorem [430]—which maintains that the electromagnetic mass difference for the kaon coincides with the one for the pion in the chiral limit—at least for the (dominant) part that arises from elastic intermediate states. This estimate and the comparison to results from lattice QCD as well as extractions from $\eta \to 3\pi$ are presented in Sec. 8.4.2.

3. The spacelike form factors determine the kaon-box contributions to HLbL scattering in the anomalous magnetic moment of the muon $a_\mu = (g-2)_\mu/2$, corroborating previous estimates using vector-meson dominance (VMD) [325] and Dyson–Schwinger (DS) equations [431, 432], see Sec. 8.4.3.

4. The timelike form factors reflect HVP in the vicinity of the ϕ resonance, in fact, we used precisely the same data sets that enter in the direct integration of $e^+e^- \to$ hadrons cross sections [411, 433–435]. Since our representation does not include excited states above the ϕ, we cannot provide a complete account of the contribution up to a typical matching point to inclusive descriptions around 1.8 GeV, but we can study the consistency of the various $\bar{K}K$ data sets around the ϕ region among themselves as well as with other hadronic reactions in which the ϕ parameters are measured. These aspects are studied in Sec. 8.4.4.

Finally, we summarize our findings and conclusions in Sec. 8.5. The results that are used in Refs. [7, 8] can be found in Appendix 8.A.

8.2 Formalism

While the electromagnetic form factors of charged and neutral kaons, $F_{K^{\pm,0}}(s)$, are defined in strict analogy to Eq. (8.1), it is more convenient for a dispersion-theoretical analysis to decompose them into isovector (v) and isoscalar (s) components according to

$$\begin{aligned} F_{K^\pm}(s) &= F_K^s(s) + F_K^v(s)\,, \\ F_{K^0}(s) &= F_K^s(s) - F_K^v(s)\,. \end{aligned} \tag{8.5}$$

We will discuss both of these in turn in the following.

8.2.1 Isovector part

The unitarity relation for the isovector kaon form factor reads [412]

$$\operatorname{Im} F_K^v(s) = \frac{s}{4\sqrt{2}}\sigma_\pi^3(s)\big(g_1^1(s)\big)^* F_\pi^V(s)\,. \tag{8.6}$$

Here, $g_1^1(s)$ refers to the $\pi\pi \to \bar{K}K$ P-wave, which is defined from the $\pi\pi \to \bar{K}K$ scattering amplitude according to [336, 337, 345]

$$\begin{aligned} G^I(s,t,u) &= 16\pi\sqrt{2}\sum_\ell (2\ell+1)(q_\pi q_K)^\ell P_\ell(z) g_I^\ell(s)\,, \\ q_P(s) &= \frac{\sqrt{s-4M_P^2}}{2} = \frac{\sqrt{s}}{2}\sigma_P(s)\,, \end{aligned} \tag{8.7}$$

where $P_\ell(z)$ are the Legendre polynomials and z refers to the cosine of the scattering angle. We specifically employ the phase of the $\pi\pi \to \bar{K}K$ amplitude in the Omnès representation for the pion VFF to render the imaginary part of Eq. (8.6) real by construction; this phase agrees with the pion–pion P-wave phase shift in the elastic region, hence this choice only

affects the continuation of $\delta(s)$ above. The polynomial is fixed by a fit to the BaBar data [400], parameterizing the ρ–ω mixing via a Breit–Wigner function [96],

$$P(s) = 1 + \alpha s + \kappa \frac{s}{M_\omega^2 - s - iM_\omega \Gamma_\omega}\,, \tag{8.8}$$

where the κ-term is dropped for the kaon form factor analysis, since the latter is performed in the isospin limit. Furthermore, the polynomial is set to a constant above $\sqrt{s} = 2\,\text{GeV}$ to ensure convergence. Reference [337] offers two alternative parameterizations of $g_1^1(s)$, an *unconstrained fit to data* (UFD) of that partial wave only, as well as a variant that implements various dispersion-theoretical constraints (CFD). The fit parameters in the pion form factor are $\alpha_{\text{UFD}} = 0.15(9)\,\text{GeV}^{-2}$, $\alpha_{\text{CFD}} = 0.18(8)\,\text{GeV}^{-2}$, where the uncertainty is dominated by the input for g_1^1. In the following, the error analysis will be performed by propagating the uncertainties in the parameterization of g_1^1 and by linearly adding up the resulting variations, since these parameters are, in general, expected to be strongly correlated [183]. Since the correlations between the parameters in g_1^1 are not provided in Ref. [337], this procedure should produce a conservative but realistic estimate of the isovector uncertainties. The full isovector kaon form factor can be calculated using an unsubtracted dispersion integral

$$F_K^v(s) = \frac{1}{\pi} \int_{s_{\text{th}}}^\infty \mathrm{d}s' \frac{\operatorname{Im} F_K^v(s')}{s' - s}\,. \tag{8.9}$$

Effects of higher $\rho' = \rho(1450)$ and $\rho'' = \rho(1700)$ states are visible in g_1^1, but only affect the form factor minimally, so that the integral is dominated by the ρ resonance. This, however, only captures the effect of, e.g., the ρ' partially, which is known to couple strongly to 4π [347] (see also the discussion in Ref. [436]). To account for intermediate states beyond $\pi\pi$ in a minimal way, we therefore add an explicit ρ' resonance via a Breit–Wigner parameterization, with the coupling adjusted to fix the form factor normalization to $F_K^v(0) = 1/2$. It is introduced in the form

$$F_K^{\rho'}(s) = \lambda_{\rho'} \frac{M_{\rho'}^2}{M_{\rho'}^2 - s - i\sqrt{s}\Gamma_{\rho'}(s)}\,, \tag{8.10}$$

with the energy-dependent width chosen in accordance with the parameterization employed for g_1^1 [336, 337, 345][1]

$$\Gamma_{\rho'}(s) = \frac{\Gamma_{\rho'}\sqrt{s}\left(2\hat{\sigma}_\pi^3(s) + \hat{\sigma}_K^3(s)\right)}{2M_{\rho'}\sigma_\pi^3(M_{\rho'}^2)}\,, \tag{8.11}$$

where $\hat{\sigma}_P(s) = \sigma_P(s)\theta(s - 4M_P^2)$. The resulting ρ' couplings are $\lambda_{\rho',\text{UFD}} = 0.01(6)$ and $\lambda_{\rho',\text{CFD}} = -0.04(7)$, respectively, which demonstrates that the $\pi\pi$ intermediate states alone saturate the sum rule for the isovector charge to at least 15% accuracy, in line with similar sum rules in Refs. [117, 438]. The use of an unsubtracted dispersion relation, Eq. (8.9), with the addition of effective poles to satisfy the normalization constraint, guarantees a reasonable high-energy behavior of the form factor representation, $F_K^v(s) \asymp s^{-1}$ for $s \to \infty$ [403, 439–445].

[1] We stress that 2π and $\bar{K}K$ are not the dominant decay channels for ρ', ρ'', see Ref. [437] for more realistic spectral functions.

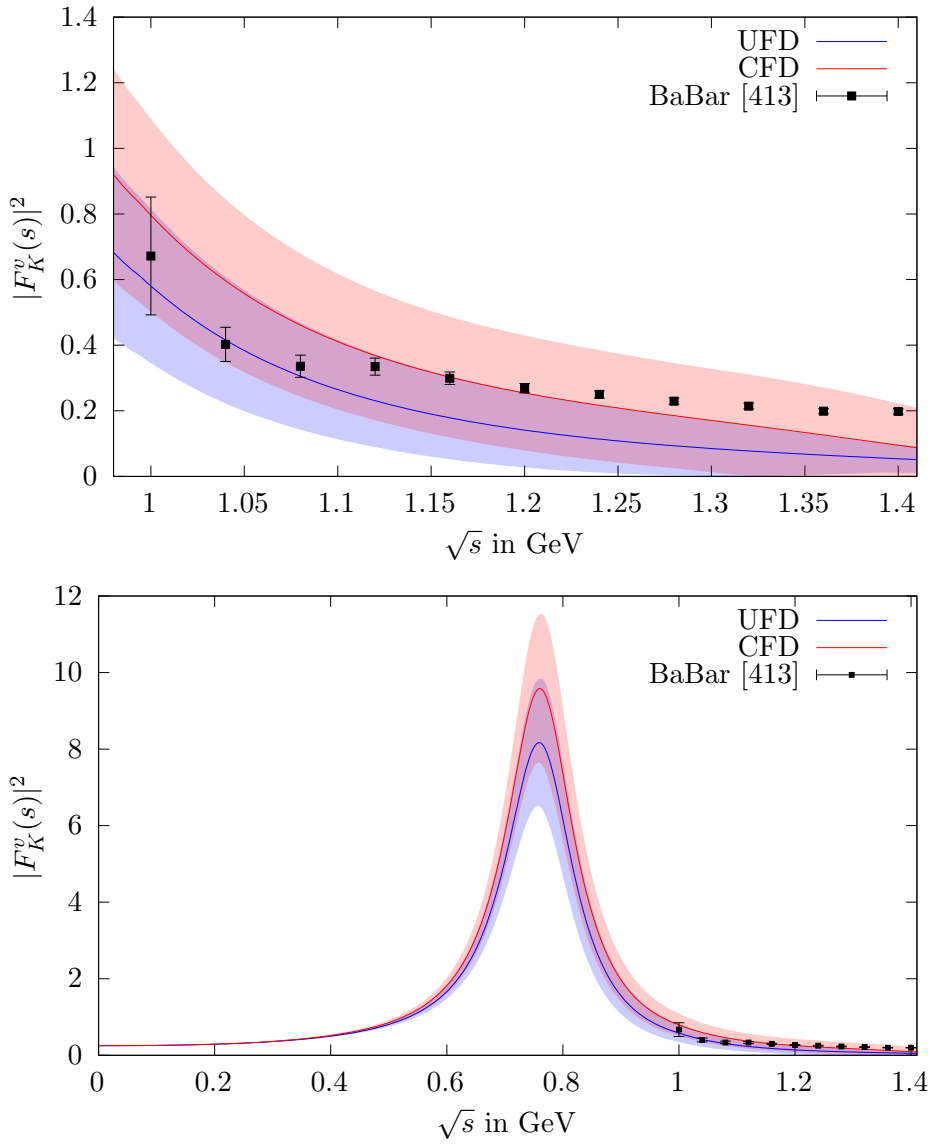

Figure 8.1: The kaon isovector form factor with input from the UFD (blue) and CFD (red) parameterizations from Ref. [337], compared to the BaBar data [413] for the $\tau^- \to K^- K_S \nu_\tau$ decay (top) and in the full kinematic range including the ρ resonance (bottom).[2]

Information on the isovector kaon form factor below m_τ can be obtained from $\tau^- \to K^- K_S \nu_\tau$ decays. There the spectral function $v_1(s)$ is related to the isovector form factor by

$$v_1(s) = \frac{\sigma_K^3(s)}{12\pi} |F_K^v(s)|^2 \,, \tag{8.12}$$

up to isospin-breaking corrections, which, contrary to a determination of the 2π HVP contribution from τ decays, are not relevant at the present level of accuracy. A joined analysis of the $\tau^- \to K^- K_S \nu_\tau$ and $\tau^- \to \pi^- \pi^0 \nu_\tau$ decays was performed in Ref. [446] using

[2]Note that these plots differ from the ones in Ref. [6].

resonance chiral theory in combination with dispersion relations to extract information on the ρ' and ρ'' parameters. While the details of these higher ρ excitations are not incorporated into our dispersive formalism, we expect the resulting representation to be reliable at least near threshold. In Fig. 8.1 we plot the recent data from BaBar [413] against the two form factors obtained with the different inputs for g_1^1. We observe that the result using the UFD input shows better agreement with the data than the CFD result in the region below 1.1 GeV. These shifts reflect the degree of consistency among the data base used in Ref. [337], indicating a preference for the UFD variant. Given that the UFD and CFD inputs agree within uncertainties, we thus opt for the more data-driven approach and adopt the UFD result in the following, to ensure better agreement with the $\tau^- \to K^- K_S \nu_\tau$ data in the energy region of the fits.

8.2.2 Isoscalar part

For the isoscalar part of the kaon form factors, we employ a VMD ansatz based on the lowest-lying isoscalar vector resonances $\omega(782)$ and $\phi(1020)$, as an efficient way to capture the main singularities due to $\bar{K}K$ and 3π intermediate states. While such a description is only strictly model-independent on the poles, the small widths of both resonances ensure that corrections beyond these dominant contributions will be appreciably suppressed. In analogy to the isovector case, we supplement this with one effective heavier pole, here chosen as the $\omega' = \omega(1420)$, to guarantee the correct form factor normalization as well as a reasonable large-s behavior. This results in

$$\begin{aligned} F_K^s(s) = \frac{c_\phi}{3} \frac{M_\phi^2}{M_\phi^2 - s - i\sqrt{s}\Gamma_\phi(s)} + \frac{c_\omega}{6} \frac{M_\omega^2}{M_\omega^2 - s - iM_\omega \Gamma_\omega} \\ + \left(\frac{1}{2} - \frac{c_\phi}{3} - \frac{c_\omega}{6} \right) \frac{M_{\omega'}^2}{M_{\omega'}^2 - s - iM_{\omega'}\Gamma_{\omega'}} , \end{aligned} \tag{8.13}$$

in such a way that the $SU(3)$-symmetric limit with lowest-meson dominance corresponds to $c_\omega = c_\phi = 1$. The energy-dependent width for the ϕ resonance is parameterized as [122]

$$\begin{aligned} \Gamma_\phi(s) = \sum_{K=K^+,K^0} \frac{\gamma_{\phi\to\bar{K}K}(s)}{\gamma_{\phi\to\bar{K}K}(M_\phi^2)} \Gamma'_{\phi\to\bar{K}K} \theta\big(s - 4M_K^2\big) \\ + \frac{f_{\phi\to\pi\rho+3\pi}(s)}{f_{\phi\to\pi\rho+3\pi}(M_\phi^2)} \Gamma'_{\phi\to\pi\rho+3\pi} \theta\big(s - (M_\rho + M_\pi)^2\big) , \end{aligned} \tag{8.14}$$

where the Γ' refer to the partial widths rescaled to compensate for all other decay channels not included explicitly, and

$$\begin{aligned} \gamma_{\phi\to\bar{K}K}(s) &= \frac{\big(s - 4M_K^2\big)^{3/2}}{s} , \\ f_{\phi\to\pi\rho+3\pi}(s) &= \left(\frac{\lambda\left(s, M_\rho^2, M_\pi^2\right)}{s} \right)^{3/2} , \end{aligned} \tag{8.15}$$

where $\lambda(a,b,c)$ is the Källén function defined in Eq. (2.15). The widths of ω and ω' are kept constant in the timelike region for simplicity, since they only serve as smooth

background terms around the ϕ peak and therefore cannot be further resolved in any of the data sets considered in the fit. The parameterization of the spectral functions could be further improved along the lines described in Ref. [122], e.g., by a proper description of the energy dependence from the 3π channel beyond ρ dominance (8.15) or a dispersively improved variant of Eq. (8.13), but in the energy regions included in the fit, i.e., the spacelike region and the timelike region around the ϕ peak, none of these variants would lead to any visible changes.

8.3 Fits to data

After establishing the formalism we now fit the resulting representations of the kaon form factors to the available data in the timelike and spacelike regions. The timelike data are fit with the total Born cross section [94]

$$\sigma^{(0)}(s) = \frac{\pi\alpha^2}{3s}\sigma_K^3(s)|F_K(s)|^2\,, \tag{8.16}$$

multiplied by a correction factor $1 + \frac{\alpha}{\pi}\eta(s)$ [447–450] to account for final-state radiation (FSR). Sometimes the Sommerfeld–Gamow–Sakharov factor [451–453]

$$Z(s) = \frac{\pi\alpha}{\sigma_K(s)}\frac{1+\alpha^2/\big(4\sigma_K^2(s)\big)}{1-\exp\left(-\pi\alpha/\sigma_K(s)\right)} \tag{8.17}$$

is used instead to resum higher orders in α, but we checked that those effects are irrelevant for the application to the K^+K^- channel, and smaller than the non-Coulomb corrections contained in $\eta(s)$. The spacelike region is fit with the same form factor function (with all widths set to zero). We use two sets of data obtained by eK scattering for charged kaons in the spacelike region [420, 421]. Data for neutral kaons in the spacelike region only exist indirectly via the scattering off atomic electrons [426–428], leading to constraints on the neutral-kaon charge radius, and are not included in our fit. In the timelike region, data for charged kaons are taken from CMD-2 [415],[3] CMD-3 [417], SND [414], and BaBar [416]. Data for neutral kaons are from CMD-2 [418], CMD-3 [419], and SND [414].[4] SND has two data sets depending on the mode of detection for the K_S, distinguishing charged ($K_S \to \pi^+\pi^-$, referred to as SND_{nc}) and neutral mode ($K_S \to \pi^0\pi^0$, SND_{nn}).[5] All the timelike data sets except for BaBar_{c} and CMD-2_{n} have vacuum-polarization (VP) effects

[3] We show results for CMD-2 [415] for completeness, but emphasize that these data are affected by an overestimation of the trigger efficiency for slow kaons, which leads to a systematic bias that requires a reanalysis [454]. Therefore, the corresponding results will be indicated by dashed lines and not included in global fits.

[4] Note that BaBar [422] do not provide cross-section data for the neutral channel in the ϕ region, only for the resulting ϕ parameters, so that their analysis cannot be included in our fit. However, the ϕ parameters are shown for comparison in Fig. 8.3.

[5] Note that the recently published SND data set [455] for the neutral kaon form factor is not included in the fits discussed in this chapter. Precisely as SND_{nn} it is measured in the neutral mode. We show the cross section in Fig. 8.6 in comparison to our results. The uncertainties in the data set are linearly added systematic and statistical uncertainties quoted therein. Note that VP corrections are applied and the bare cross section is used. The data set is in good agreement with our fit, however, due to the very small uncertainties, compared to the older data sets, it can probably slightly decrease the uncertainties in the neutral channel. A new analysis including Ref. [455] is planned for the future.

included in the cross section. Therefore, we remove these using the routine from Ref. [434], which outputs the running fine structure constant $\Delta\alpha(s)$. It relates the bare cross section $\sigma^{(0)}(s)$ to the dressed one $\sigma(s)$ via

$$\sigma^{(0)}(s) = \sigma(s)\big|1 - \Delta\alpha(s)\big|^2 . \tag{8.18}$$

Removal of VP effects leads to a downward shift in the mass of the ϕ resonance by 0.260(3) MeV [125, 423]. Crucially, this unfolding is only consistent as long as the ϕ masses are, which therefore needs to be monitored in the analysis below. In order to account for the binning in the BaBar experiment [416], which, in contrast to energy-scan experiments, measures the integrated signal over the bin, we take the bare cross section including FSR integrated over the bin as our fit function

$$f(x_i) = \frac{1}{s_i^{\max} - s_i^{\min}} \int_{s_i^{\min}}^{s_i^{\max}} \mathrm{d}s \left(1 + \frac{\alpha}{\pi}\eta(s)\right) \sigma^{(0)}(s) . \tag{8.19}$$

We include the systematic uncertainties in our fits after accounting for the d'Agostini bias [401]. In the case of strongly correlated data (most prominently observed for those of normalization-type origin), this bias leads to lower fit values in a chi-square minimization defined as

$$\chi^2 = \sum_{i,j} \big(f(x_i) - y_i\big) V(i,j)^{-1} \big(f(x_j) - y_j\big) , \tag{8.20}$$

where $f(x)$ is the fit function, y are the data points, and V is the covariance matrix. The systematic uncertainties are taken to be 100% correlated for each experiment,[6] and in addition fully correlated between the two detection modes $\mathrm{SND_{nc}}$ and $\mathrm{SND_{nn}}$ [456].

We follow the iterative method developed in Ref. [457] to remove the bias. The modified covariance matrix is defined as

$$V_{n+1}(i,j) = V^{\mathrm{stat}}(i,j) + \frac{V^{\mathrm{syst}}(i,j)}{y_i y_j} f_n(x_i) f_n(x_j) , \tag{8.21}$$

where the fit function and the full covariance matrix are updated in each iteration step n. The iteration procedure very quickly converges to the final result. Finally, the uncertainties of the fit parameters are inflated by the scale factor

$$S = \sqrt{\chi^2/\mathrm{dof}} , \tag{8.22}$$

in case that $\chi^2/\mathrm{dof} > 1$, following the Review of Particle Physics (RPP) prescription [347], to account, in a minimal way, for unknown systematic errors as indicated by the χ^2.

Fits in the timelike region were constrained to energies close to the ϕ resonance (as shown in Figs. 8.5 and 8.6), since we do not include higher vector resonances in the energy region above the ϕ with couplings adjustable to cross-section data [344]. We considered several variants of the timelike input:

1. individual fits to a single experiment (charged or neutral channel), referred to by the name of the respective experiment;

[6] $\mathrm{BaBar_c}$ [416] quote 9 different sources for the systematic uncertainty, to be taken as 100% correlated individually.

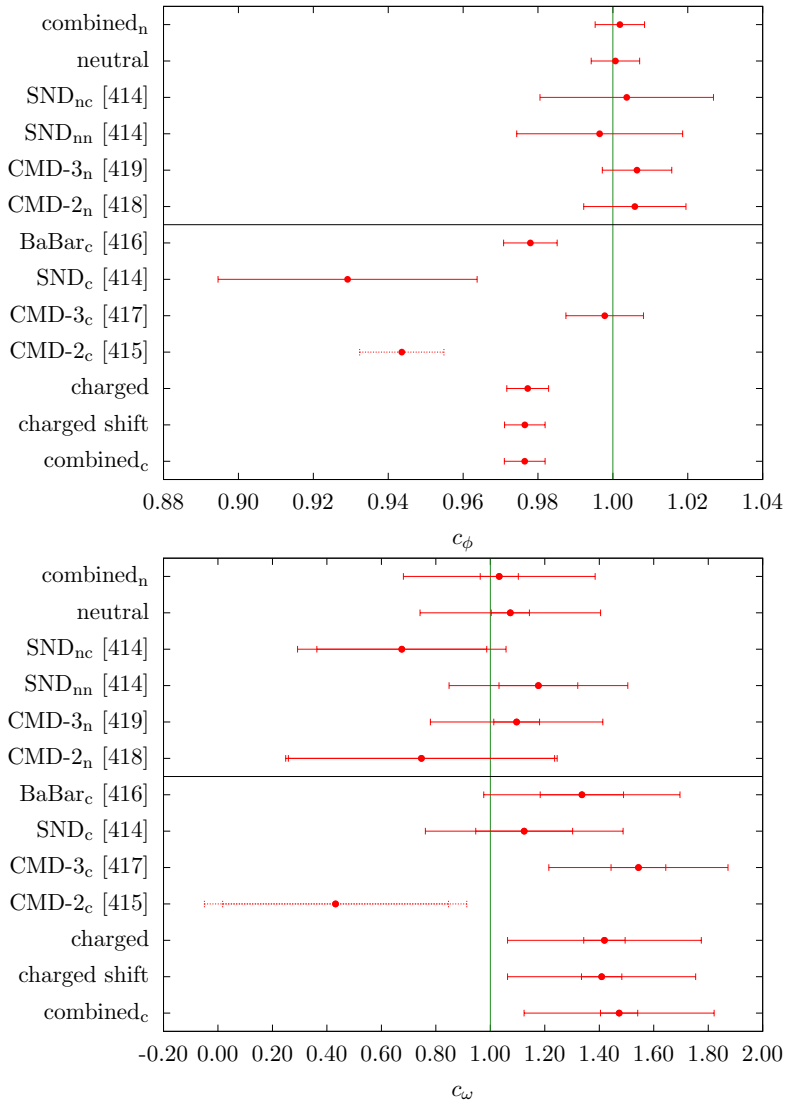

Figure 8.2: Results of the individual and the combined neutral and charged data sets for c_ϕ (top) and c_ω (bottom), with the neutral/charged-channel-residues in the upper/lower panel. The green line denotes the $SU(3)$-prediction. "combined$_n$" and "combined$_c$" refer to the scenarios in which the ϕ resonance parameters and all couplings are fit simultaneously, "neutral" and "charged" to the ones in which only the timelike neutral and charged data are considered, respectively, and "charged shift" to the variant in which a shift in the BaBar$_c$ energy calibration is allowed, see main text for details. The inner errors for c_ω refer to the fit uncertainties, the total ones are obtained by adding the systematic error from the variation of the UFD input in quadrature (a negligible effect for c_ϕ, M_ϕ, and Γ_ϕ).

2. combined fits to charged or neutral data sets, referred to as "charged" and "neutral";

3. a full combination of charged and neutral data, referred to as "combined" (or "combined$_c$" and "combined$_n$" for the residues).

In each scenario, the ϕ parameters M_ϕ, Γ_ϕ, and c_ϕ, as well as the residue of the ω pole

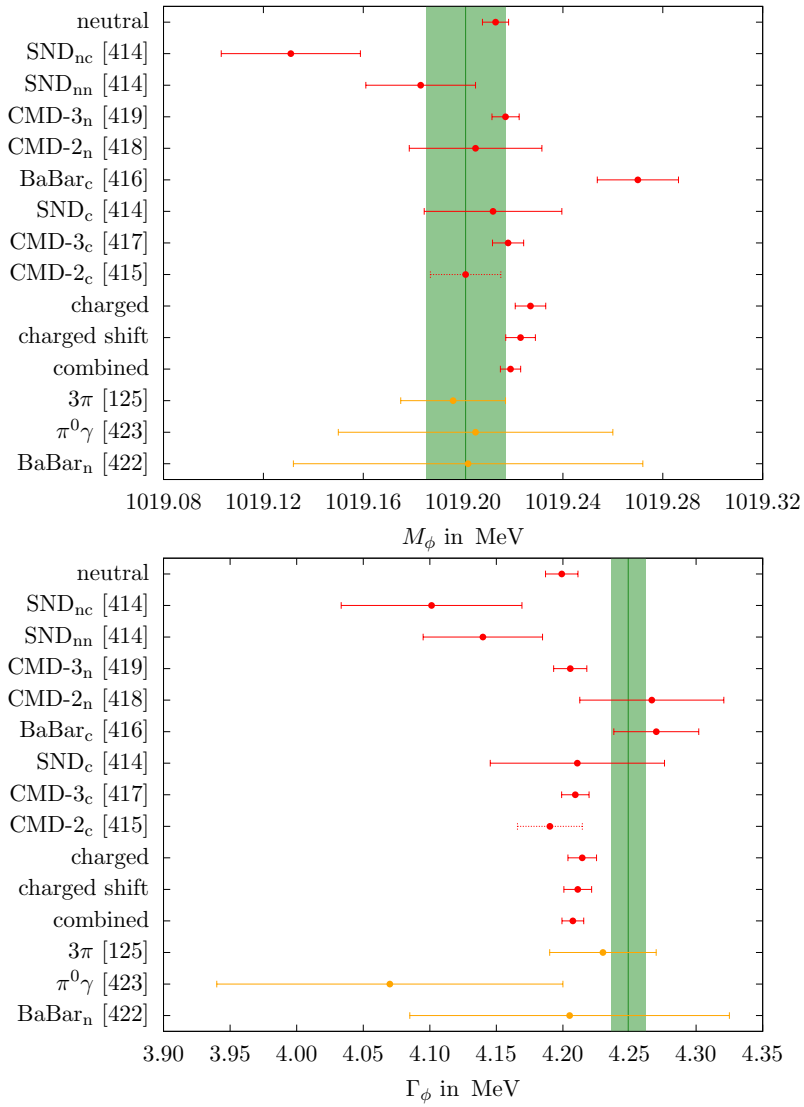

Figure 8.3: Results of the individual and the combined neutral and charged data sets for M_ϕ (left) and Γ_ϕ (right) in red. "combined" refers to the scenario in which the ϕ resonance parameters and all couplings are fit simultaneously, corresponding to "combined$_n$" and "combined$_c$" in Fig. 8.2, otherwise, the notation is as in that figure. The green band corresponds to the RPP mass average [347] shifted by the prescription from Ref. [423] to remove the VP effect. In orange the results for the $e^+e^- \to 3\pi$ and $e^+e^- \to \pi^0\gamma$ channels are given, as is the result for the neutral channel from BaBar [422].

c_ω are allowed to float, while masses and widths of ω and ω' are kept fixed (as the fits are entirely insensitive to them). The spacelike data are included in all three variants, since, even though they are relatively crude in precision compared to the timelike cross-section measurements, they do help stabilize the extracted values of c_ω to some extent. We have checked that the extracted ϕ parameters only change within uncertainties when the $SU(3)$ constraint $c_\omega = c_\phi$ is imposed. They are insensitive to the complete omission of the spacelike data from the fits and largely unaffected by the uncertainties from the

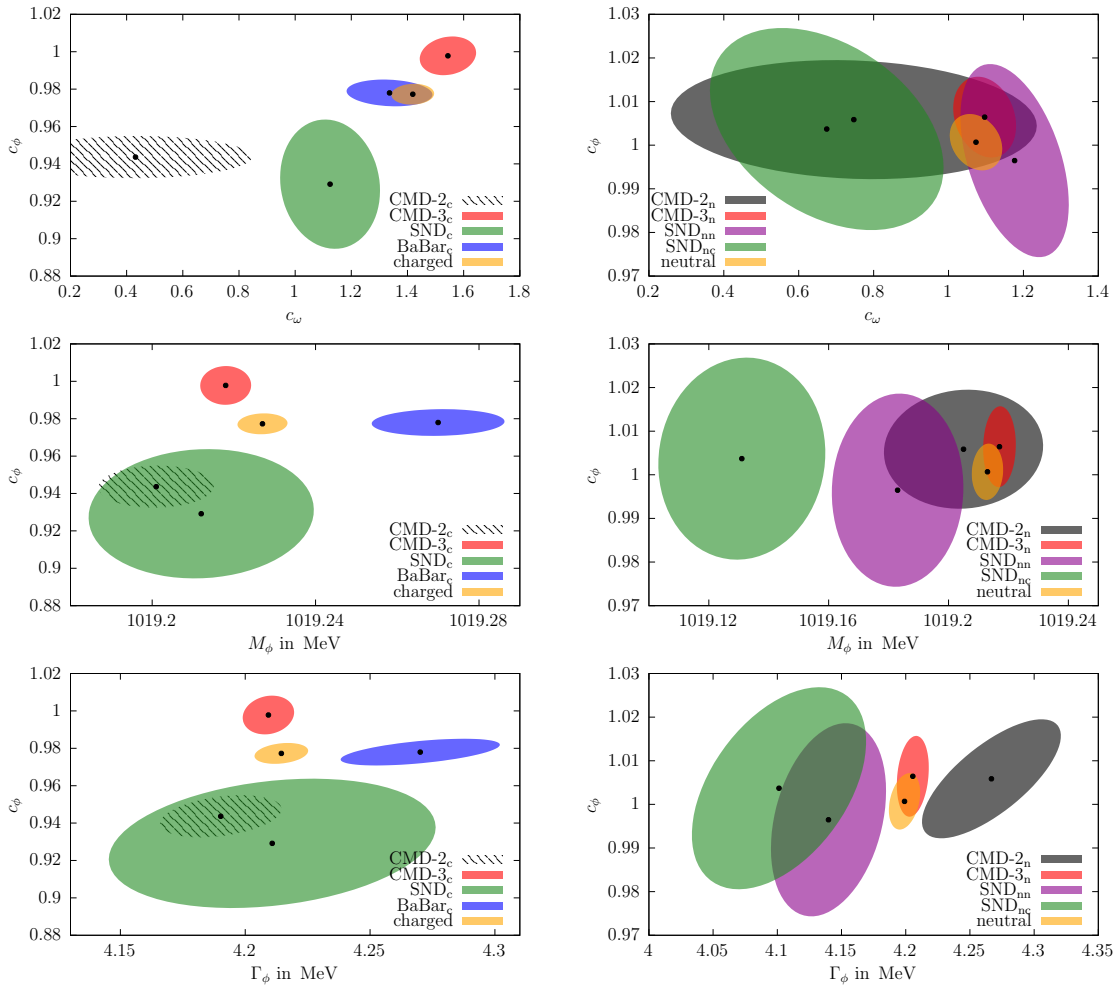

Figure 8.4: Correlations among c_ϕ and c_ω (top), M_ϕ (middle), and Γ_ϕ (bottom), for the "charged" (left) and "neutral" (right) scenarios in comparison to the respective individual fits. The ellipses correspond to the $\Delta\chi^2 = 1$ contours (39% confidence level) inflated by the scale factor, in such a way that the projections reproduce the 1σ errors of the parameters. For c_ω only the fit uncertainties are shown.

isovector part. However, the fit value of c_ω does become sensitive to the UFD input, which we take into account by an additional systematic uncertainty, see Fig. 8.2 and Table 8.1.

In the full combination 3 we allow c_ω and c_ϕ to differ in the charged and neutral channels, leading to 6 free parameters overall, since we do observe indications for isospin breaking in these parameters, see Fig. 8.2. Isospin violation has been studied in the past in the context of the ratio $\Gamma(\phi \to K^+K^-)/\Gamma(\phi \to K_S K_L)$ [458–460], finding rather small effects, with dynamical explanations tending to increase the charged-kaon coupling rather than decrease it [458]. In principle, isospin breaking would also need to be considered when using the charged spacelike data as constraint in the fits to the neutral channel only, but in this case the data are clearly not precise enough to resolve such effects.

The results for the ϕ resonance parameters are shown in Fig. 8.3. In general, there is reasonable agreement among all data sets and fit variants, the exception being the BaBar$_c$

	neutral	charged	charged shift	combined
$\frac{\chi^2}{\text{dof}}$	$\frac{168}{150} = 1.12$	$\frac{139}{111} = 1.25$	$\frac{130}{110} = 1.18$	$\frac{293}{238} = 1.23$
p-value	15%	3.7%	9.4%	0.9%
M_ϕ [MeV]	1019.213(5)	1019.227(6)	1019.223(6)	1019.219(4)
Γ_ϕ [MeV]	4.199(12)	4.215(11)	4.211(10)	4.207(8)
c_ϕ	1.001(6)	0.977(6)	0.976(5)	0.976(5) 1.002(7)
c_ω	1.07(7)(42)	1.42(8)(35)	1.41(7)(34)	1.47(7)(34) 1.03(7)(35)
$\xi \cdot 10^3$			$-1.3(5)$	

Table 8.1: Parameters for the fit variants 2 and 3 discussed in the main text. In the combined fit, the upper/lower values for c_ϕ, c_ω refer to the charged/neutral channel, respectively. The second bracket for c_ω indicates the uncertainty induced by the UFD input, it is fully correlated with the corresponding variation in the isovector form factor and thus affects the neutral and charged residues in the opposite directions.

data [416], which favor both a larger mass and width than the remainder of the data base, as reflected also by the tension to the RPP average. This observation motivates the consideration of a variant of fit scenario 2 in which the energy calibration in this data set is allowed to vary, referred to as "charged shift." Following Ref. [146], we implement such an energy shift via

$$\sqrt{s} \to \sqrt{s} + \xi\left(\sqrt{s} - 2M_K\right) \tag{8.23}$$

to leave the threshold invariant. On the level of the form factor this translates to a small correction [146]

$$\begin{aligned} |F_K(s)|^2 &\to |F_K(s)|^2\left(1 + \xi A(s) + \mathcal{O}(\xi^2)\right), \\ A(s) &= \frac{2(s - 10M_K^2)}{s + 2\sqrt{s}M_K}, \end{aligned} \tag{8.24}$$

to leave the cross section (8.16) invariant, but in practice we use directly Eq. (8.19) in the fit. Since Ref. [416] already provides the bare cross section, the only case in which a potential mismatch of the ϕ parameters when removing VP effects using the routine from Ref. [434] could have played a role thus remains uncritical.

The fit parameters illustrated in Figs. 8.2 and 8.3 (and for the combined fits listed in Table 8.1) display some interesting features. First, we see that there is good consistency among the neutral data sets, whose residue comes out in very good agreement with the $SU(3)$ prediction $c_\phi = 1$. In contrast, for the charged channel there is considerable spread in the fit parameters, not only in the ϕ mass and width, leading to the increased χ^2/dof as given in Table 8.1. Moreover, the combined value of c_ϕ almost coincides with the BaBar_c value, not the naive average with CMD-3_c, hinting towards an important role of correlations in the combination. The origin of this effect is illustrated in Fig. 8.4. First, the

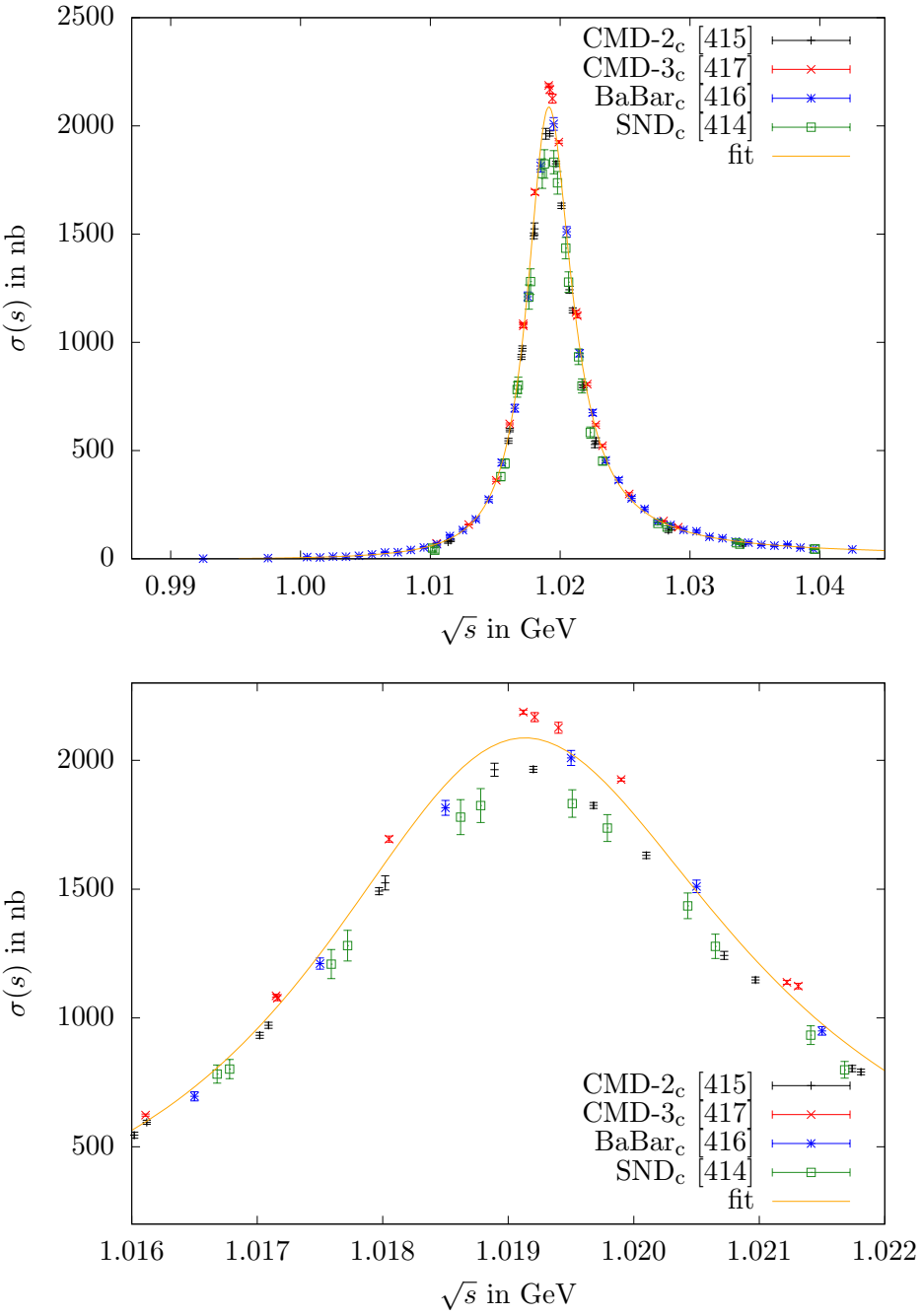

Figure 8.5: Cross-section data as well as our combined fit to all data sets using the "combined$_c$" residue for $e^+e^- \to K^+K^-$. They are shown in the complete fit energy ranges (top) and focused on the ϕ peak region (bottom). The fit of the charged channel is indistinguishable from the "fit" curves shown here.

figure reiterates the fact that consistency among the neutral data sets is much better than in the charged case, but also explains why the charged-fit value of c_ϕ is pulled downward compared to its naive average: c_ϕ is correlated with Γ_ϕ (and, to a lesser extent, M_ϕ), and

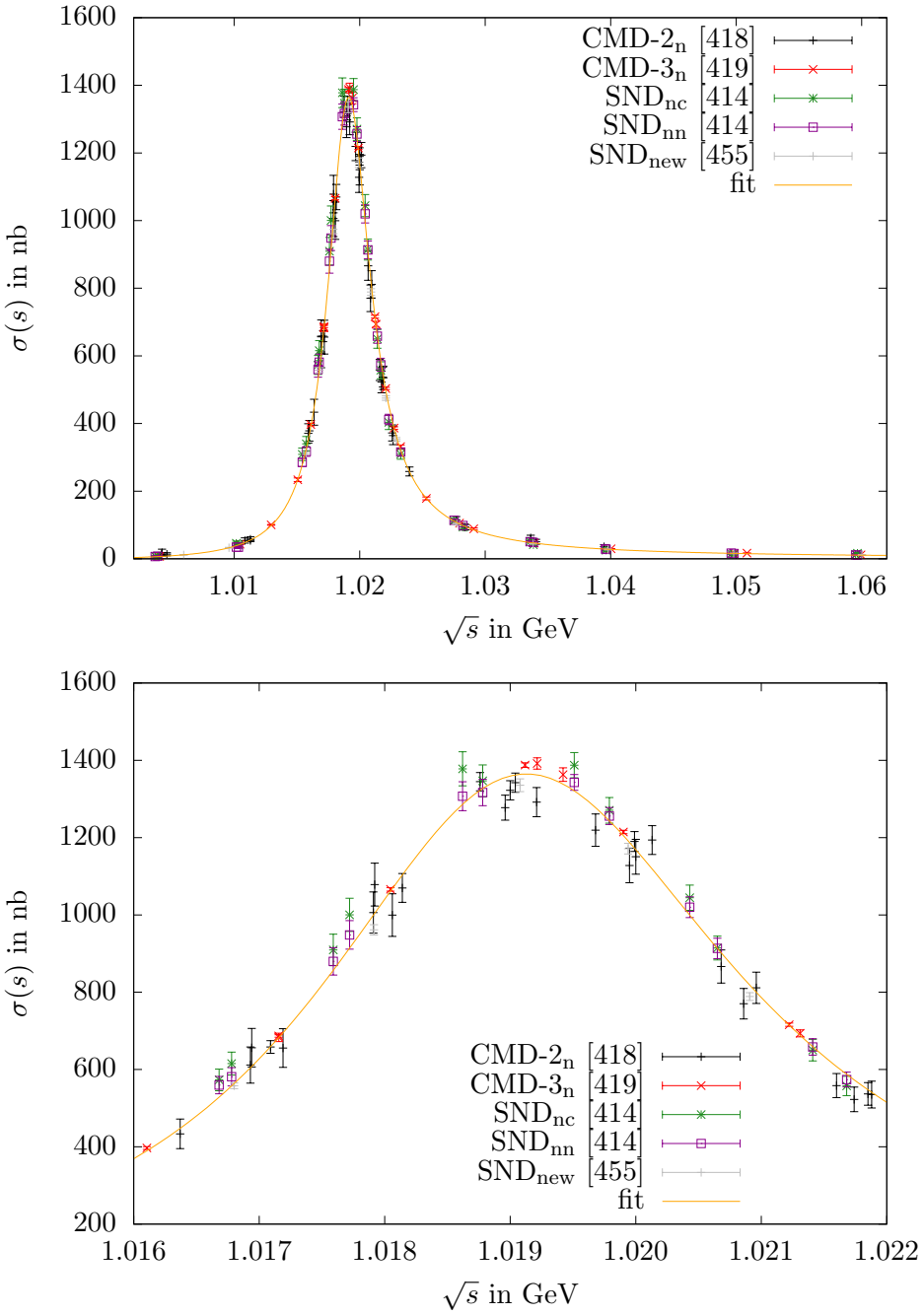

Figure 8.6: Cross-section data as well as our combined fit to all data sets using the "combined$_n$" residue for $e^+e^- \to K_S K_L$ (right). They are shown in the complete fit energy ranges (top) and focused on the ϕ peak region (bottom). The fit of the neutral channel is indistinguishable from the "fit" curves shown here.

the corresponding correlations can indeed be used to reproduce the behavior of the charged fit. In this way, the tension visible in the ϕ resonance parameters also propagates to the extracted value of the residue. As expected, the consistency of the fit does improve slightly

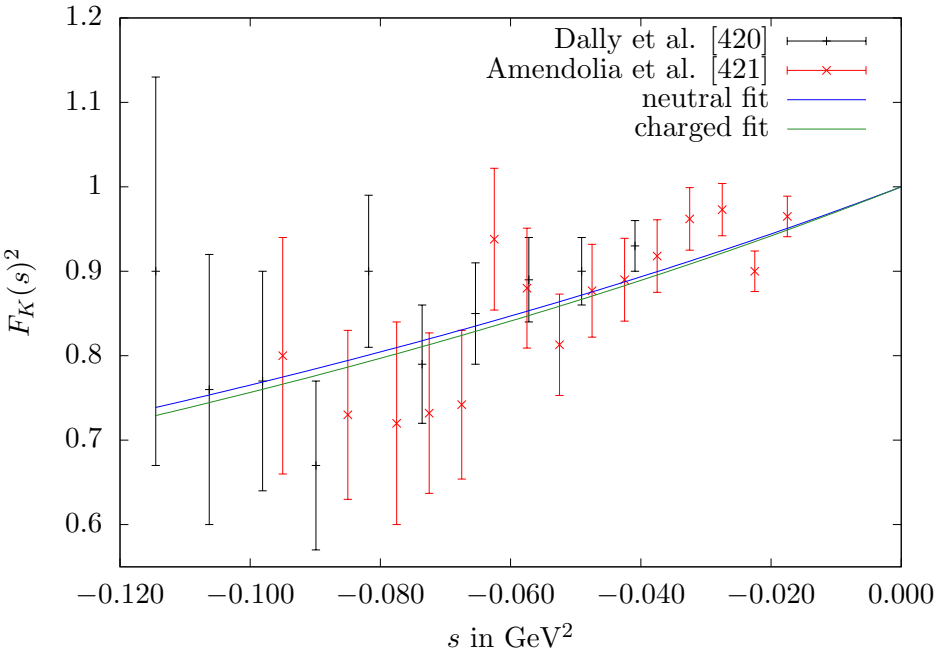

Figure 8.7: Spacelike charged-kaon form factor (squared) data compared to the fits for all neutral or charged data sets combined.

in the "charged shift" variant, with the new χ^2/dof given in Table 8.1.[7] We observe that the residues are not affected by this shift and the mass M_ϕ is only shifted slightly towards the RPP value (cf. Figs. 8.2 and 8.3). Finally, we also show the outcome of the fits in the spacelike region, see Fig. 8.7. In particular, there is no visible difference in the neutral and charged fit, which indicates the weak dependence on the fit parameters on this region and justifies, a posteriori, neglecting isospin breaking in the neutral fit.

An improved determination of c_ω could, in combination with the ω–photon coupling constant well known from $\omega \to e^+e^-$ [118, 343], be used to extract the coupling of the ω to kaons. As pointed out in Chapter 6, the latter constitutes one of the dominant uncertainties in an analysis of the reaction $\gamma K \to K\pi$, where a value deduced from a VMD analysis of kaon form factors in a wider (timelike) energy range [344] was employed, corresponding to $c_\omega = 1.29(15)$. From our analysis, we conclude that the inclusion of spacelike data does not reduce the uncertainty in this coupling constant appreciably, cf. Table 8.1; to the contrary, the uncertainties propagated from the isovector part of the form factor imply a larger uncertainty than quoted in Ref. [344].

Adding back VP effects, our combined fit 3 gives

$$\begin{aligned} \bar{M}_\phi\big|_{\text{our fit}} &= 1019.479(5)\,\text{MeV}\,, \\ \bar{\Gamma}_\phi\big|_{\text{our fit}} &= 4.207(8)\,\text{MeV}\,, \end{aligned} \tag{8.25}$$

[7] We note that the inclusion of the lower-precision spacelike data partly conceals the extent of the tension: without spacelike data, the p-value drops to 0.9% in the "charged" fit and to 3.1% in the "charged shift" fit, while the fit parameters remain essentially unchanged.

to be compared with the RPP averages

$$\begin{aligned} \bar{M}_\phi\big|_{[347]} &= 1019.461(16)\,\text{MeV}\,, \\ \bar{\Gamma}_\phi\big|_{[347]} &= 4.249(13)\,\text{MeV}\,, \end{aligned} \tag{8.26}$$

see also Fig. 8.3. The ϕ mass comes out consistent within errors, but our global fit suggests a sizable reduction in uncertainty, as a result of fitting all available cross sections in a combined analysis, instead of averaging only the resonance parameters as quoted by each experiment. For the width, the resulting uncertainty comes out similarly as in Ref. [347], but with a central value that is lower by 2.8σ. In both cases, our results from $\bar{K}K$ are consistent with previous extractions from the 3π and $\pi^0\gamma$ channels [125, 423].

8.4 Applications

8.4.1 Charge radii of the kaon

As first application of the results from Sec. 8.3 we consider the kaon charge radii, which are defined by the derivative at $s = 0$

$$\langle r^2 \rangle = 6 \frac{\mathrm{d}F(s)}{\mathrm{d}s}\bigg|_{s=0}\,. \tag{8.27}$$

The RPP averages of the neutral and charged kaon charge radii are [347]

$$\begin{aligned} \langle r^2 \rangle_\text{n}\big|_{[347]} &= -0.077(10)\,\text{fm}^2 && [424,\,425,\,428]\,, \\ \langle r^2 \rangle_\text{c}\big|_{[347]} &= 0.314(35)\,\text{fm}^2 && [420,\,421]\,, \end{aligned} \tag{8.28}$$

which are shown as green bands in Fig. 8.8 and compared to our computed results, including the values from the combined fit 3

$$\begin{aligned} \langle r^2 \rangle_\text{n}\big|_\text{our fit} &= -0.060(3)(2)\,\text{fm}^2 = -0.060(4)\,\text{fm}^2\,, \\ \langle r^2 \rangle_\text{c}\big|_\text{our fit} &= 0.359(3)(2)\,\text{fm}^2 = 0.359(3)\,\text{fm}^2\,. \end{aligned} \tag{8.29}$$

Here and below, we quote the results from the combined fit as our main result, given that this implements the maximum amount of independent constraints, in particular, universality of the ϕ pole parameters. The first error refers to the fit uncertainties, the second one to the uncertainties due to the UFD input (fully propagated, including the indirect effect via c_ω). Both sources of error can therefore be considered uncorrelated and added in quadrature.

In the charged channel, the results are compatible within 1.3σ, which is expected given that the result quoted in Ref. [347] is calculated from the same spacelike experiments that are used in our analysis. However, the inclusion of the timelike data as well as the dispersive constraints on the isovector component allow us to improve the precision by an order of magnitude.

For the neutral kaon we also observe a sizable reduction in uncertainty, here our result lies 1.6σ higher than Ref. [347], whose average is dominated by the extraction [425] from $K_L \to \pi^+\pi^- e^+ e^-$. The latter requires some assumptions on the other decay mechanisms

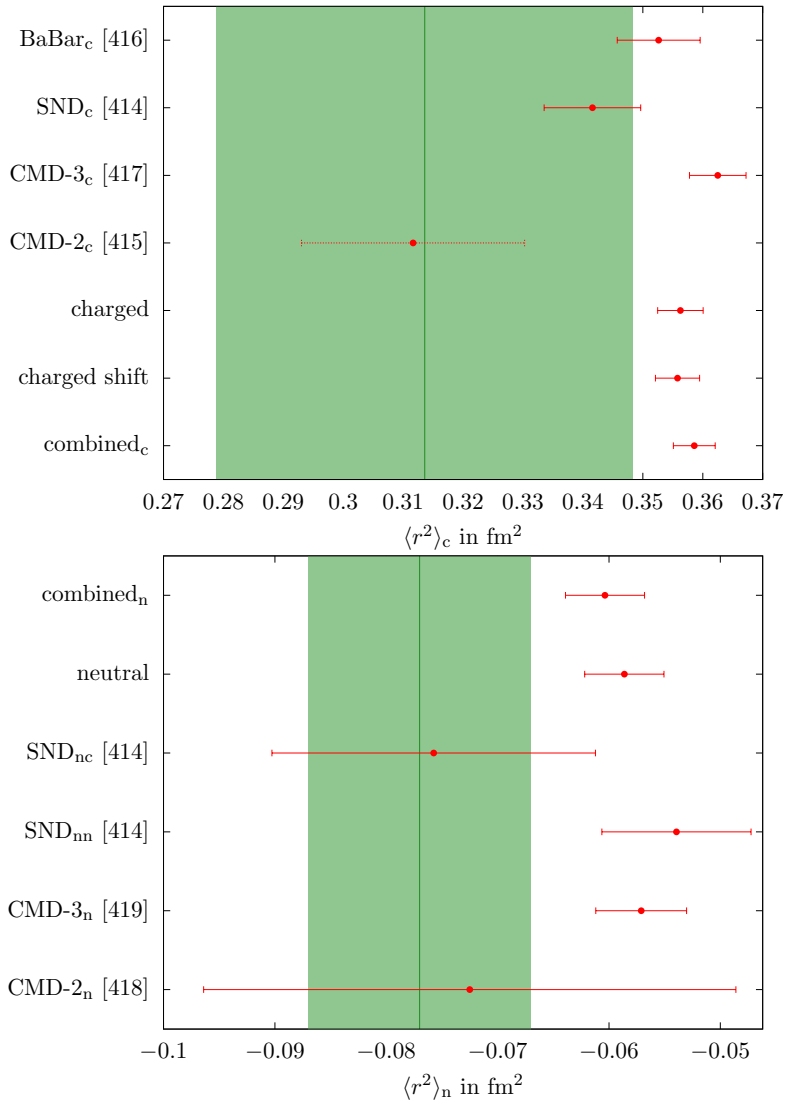

Figure 8.8: Results of the individual and the combined charged (left) and neutral (right) data sets of the squared mean charge radius for the charged (left) and neutral (right) kaon, for all fit variants in the same convention as in Fig. 8.2. The uncertainty is obtained by adding the fit uncertainty and the systematic error from the UFD input in quadrature. The green band denotes the value quoted in Ref. [347].

not involving the kaon form factor, and it is noteworthy that the best determination from K^0–electron scattering [428] finds a central value even higher than ours, albeit with a large uncertainty. Given the slight tension with Ref. [425], we also studied variants of our fit in which the neutral radius from Ref. [347] is imposed as another constraint, with minimal changes to the fit outcome.

Finally, we can also compare to the strict VMD predictions

$$\begin{aligned}\langle r^2\rangle_{\rm n}\big|_{\rm VMD} &= \frac{2}{M_\phi^2}+\frac{1}{M_\omega^2}-\frac{3}{M_\rho^2}\simeq -0.06\,\text{fm}^2\,,\\ \langle r^2\rangle_{\rm c}\big|_{\rm VMD} &= \frac{2}{M_\phi^2}+\frac{1}{M_\omega^2}+\frac{3}{M_\rho^2}\simeq 0.33\,\text{fm}^2\,,\end{aligned} \tag{8.30}$$

which shows, a posteriori, that at least in the charge radii the deviations from VMD are small. In the same way, the related low-energy constants in chiral perturbation theory will come out close to the expectation from resonance saturation [461, 462].

8.4.2 Corrections to Dashen's theorem

A precise determination of the electromagnetic mass difference for kaons

$$(\Delta M_K^2)_{\rm EM} = \left(M_{K^\pm}^2 - M_{K^0}^2\right)_{\rm EM} \tag{8.31}$$

is important for extractions of the quark mass difference $\delta = m_d - m_u$ from meson masses. The combination

$$Q^2 = \frac{M_K^2}{M_\pi^2}\frac{M_K^2-M_\pi^2}{(M_{K^0}^2-M_{K^\pm}^2)_{\rm str}}\Big\{1+\mathcal{O}\big(m_q^2,\delta,e^2\big)\Big\}\,, \tag{8.32}$$

which determines the major semi-axis in Leutwyler's ellipse [463]

$$\left(\frac{m_u}{m_d}\right)^2+\frac{1}{Q^2}\left(\frac{m_s}{m_d}\right)^2=1\,, \tag{8.33}$$

is particularly stable with respect to strong higher-order corrections [177], but to make use of this relation the masses need to be corrected for their electromagnetic contributions. Dashen's theorem predicts [430]

$$(\Delta M_K^2)_{\rm EM} = (\Delta M_\pi^2)_{\rm EM} + \mathcal{O}\big(e^2 m_q\big)\,, \tag{8.34}$$

but corrections are large, as shown in Refs. [464–467]. To quantify these corrections, one commonly defines the parameter

$$\epsilon = \frac{(\Delta M_K^2)_{\rm EM}}{(\Delta M_\pi^2)_{\rm EM}} - 1\,. \tag{8.35}$$

The most recent lattice-QCD averages are [468]:

$$\begin{aligned} N_f = 2+1+1: &\qquad \epsilon = 0.79(6) &&\qquad [469\text{–}471]\,,\\ N_f = 2+1: &\qquad \epsilon = 0.73(17) &&\qquad [472]\,. \end{aligned} \tag{8.36}$$

Phenomenologically, the electromagnetic contributions can be estimated via the Cottingham formula [429, 473], which establishes a connection between the electromagnetic self energies and the forward Compton tensor. This approach has been used extensively to separate the proton–neutron mass difference into strong and electromagnetic pieces [474–481], but applies to any self-energy-type matrix element that arises from the contraction

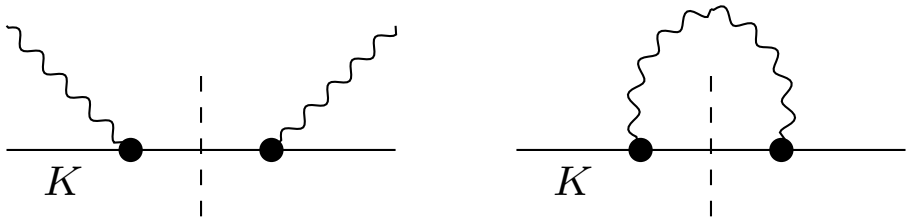

Figure 8.9: Forward scattering amplitude (left) and self-energy contraction (right). The thick black dots denote kaon electromagnetic form factor insertions, the dashed line indicates the kaon pole. Crossed diagrams are omitted.

of two external currents, including meson masses [391, 465, 466, 482, 483] or even contact-term contributions in neutrinoless double β decays [484, 485]. In particular, the dominant contributions are typically generated by the elastic intermediate states, e.g., for the pion, in which case strong contributions to the mass difference are suppressed by δ^2, one can check that the pion pole gives more than 90% of the total, with small axial-vector corrections expected to make up the remainder. Since these elastic contributions are fully determined by the respective electromagnetic form factor, we can thus apply our result to obtain an estimate of the electromagnetic self energies of the kaons, and, in combination with the analog result for the pion, derive the corresponding value of ϵ.

To this end, we need a variant of the Cottingham formula that includes strong higher-order corrections, while the expressions in the literature are typically given in the chiral limit. Starting point is the relation

$$(M_P^2)_{\rm EM} = \frac{ie^2}{2}\int \frac{\mathrm{d}^4k}{(2\pi)^4}\frac{T_\mu^\mu}{k^2+i\epsilon}\,, \tag{8.37}$$

where T_μ^μ is the contracted Compton tensor in forward direction, see Fig. 8.9. The elastic contribution reads

$$T_\mu^\mu\big|_{\rm el} = \frac{2k^2(3k^2-4M_P^2)-16(k\cdot p)^2}{(k^2)^2-4(k\cdot p)^2}\big[F_P(k^2)\big]^2\,, \tag{8.38}$$

where $F_P(k^2)$ refers to the electromagnetic form factor of the meson P and p is its on-shell momentum. Wick-rotating k^0 onto the imaginary axis, the integral yields

$$(M_P^2)_{\rm EM} = \frac{\alpha}{8\pi}\int_0^\infty \mathrm{d}s\,\big[F_P(-s)\big]^2\Big(4W+\frac{s}{M_P^2}\,(W-1)\Big)\,, \tag{8.39}$$

with $W=\sqrt{1+4M_P^2/s}$, and the limit $M_P\to 0$ reproduces the corresponding expressions in the literature.[8] Strictly speaking, to identify the elastic contributions in Eq. (8.38) one needs to analyze a dispersion relation and evaluate the single-particle poles, but in contrast to the nucleon case this does not lead to any subtleties and results in the scalar-QED expression multiplied with the electromagnetic form factor, see Ref. [486]. As the

[8] For $M_P^2 \ll s$ one has $4W+(W-1)s/M_P^2\to 6$. However, at finite M_P this kernel behaves as $8M_P/\sqrt{s}$ for $s\to 0$, which explains why the kaon self-energy integral receives a larger contribution from low energies than the one for the pion.

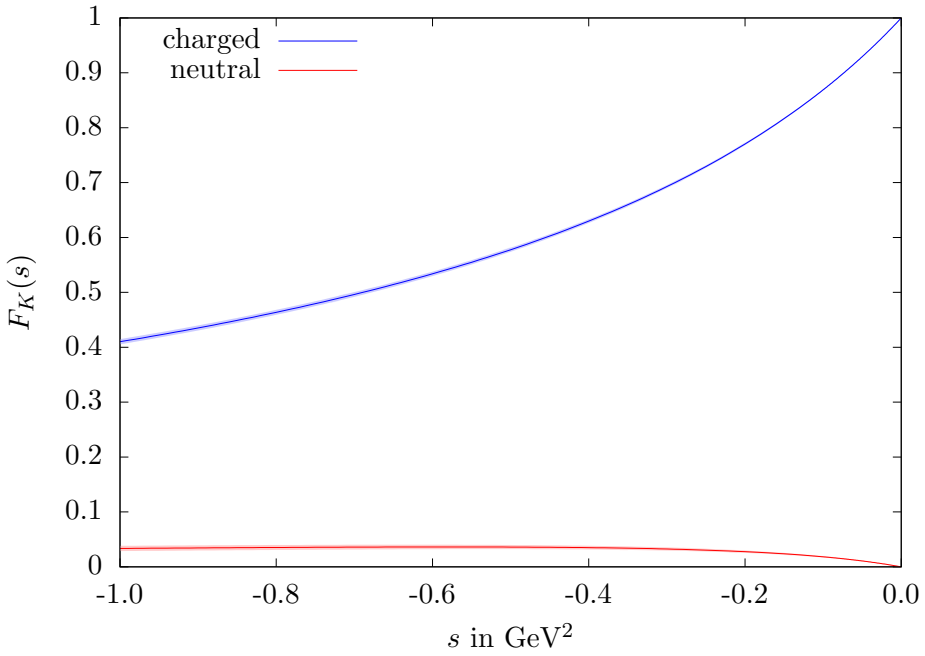

Figure 8.10: The charged (blue) and neutral (red) kaon form factors in the spacelike region as determined in Sec. 8.3.

elastic contribution to $(M^2_{\pi^0})_{\rm EM}$ vanishes, $(\Delta M^2_\pi)_{\rm EM} = (M^2_{\pi^\pm})_{\rm EM}$ at this order, while the electromagnetic kaon mass difference may be rewritten according to

$$(\Delta M^2_K)_{\rm EM} = \frac{\alpha}{2\pi}\int_0^\infty {\rm d}s\, F_K^v(-s)F_K^s(-s)\Big(4W + \frac{s}{M_K^2}\,(W-1)\Big)\,, \tag{8.40}$$

illustrating the role of the isovector kaon form factor that is theoretically particularly well constrained by the present analysis. Since we allow for residual isospin-breaking effects in our fits, which affect the isoscalar form factor, we still rely on Eq. (8.39) for the numerical evaluation.

Using our result for the kaon form factors in the spacelike region, see Fig. 8.10, as well as the pion form factor from Ref. [146], we find

$$\begin{aligned}
(M^2_{K^\pm})_{\rm EM} &= 2.12(2)(17)\cdot 10^{-3}\,{\rm GeV}^2 = 2.12(18)\cdot 10^{-3}\,{\rm GeV}^2\,,\\
(M^2_{K^0})_{\rm EM} &= 7(2)(17)\cdot 10^{-6}\,{\rm GeV}^2 \quad\;\; = 7(17)\cdot 10^{-6}\,{\rm GeV}^2\,,\\
(\Delta M^2_K)_{\rm EM} &= 2.12(2)(17)\cdot 10^{-3}\,{\rm GeV}^2 = 2.12(18)\cdot 10^{-3}\,{\rm GeV}^2\,,\\
(\Delta M^2_\pi)_{\rm EM} &= 1.3(3)\cdot 10^{-3}\,{\rm GeV}^2\,,\\
\epsilon &= 0.63(40)\,.
\end{aligned} \tag{8.41}$$

The errors cover only the uncertainty in the elastic contributions, not the additional uncertainty from inelastic corrections. The second uncertainty for the kaons contains the variation of the UFD parameters as well as an uncertainty from the asymptotic continuation, all added linearly to account for possible correlations between the UFD and asymptotic uncertainties. The latter gives the dominant effect in this application, and has been estimated

by varying the input for the pion VFF above $s = (2\,\mathrm{GeV})^2$, changing the matching point to an asymptotic form of the isovector kaon form factor $F_K^v(-s) \asymp a/(b+s) \cdot (s/(b+s))^n$ for virtualities between $1\,\mathrm{GeV}^2$ and $10\,\mathrm{GeV}^2$, and varying the exponent $n = 0, 1$ to assess the impact of terms beyond the asymptotic $F_K(-s) \asymp 1/s$ behavior. Moreover, the final uncertainty from the asymptotic continuation has been inflated by a factor 2 to account for a similar effect that could arise in the isoscalar contribution. For the pion the uncertainty is obtained from the error bands provided in Ref. [146] and also covers the uncertainty due to the asymptotic continuation.

In the end, the uncertainty in ϵ is dominated by the pion contribution. In part, this is due to the fact that the integration kernel gives a larger contribution from low virtualities for the kaon, resulting in a smaller relative uncertainty, but the more precise timelike data for the pion VFF also allow for a more detailed study of inelastic effects in the unitarity relation and thus a more robust error estimate for the continuation into the spacelike region.

Equation (8.41) corresponds to the linear pion mass difference $\left(M_{\pi^\pm} - M_{\pi^0}\right)_{\mathrm{EM}} = 4.8(1.1)\,\mathrm{MeV}$, which numerically saturates the experimental value $M_{\pi^\pm} - M_{\pi^0} = 4.59\,\mathrm{MeV}$ (the strong mass difference is estimated to give only a small contribution $\left(M_{\pi^\pm} - M_{\pi^0}\right)_{\mathrm{str}} = 0.17(3)\,\mathrm{MeV}$ [177]).

Comparison to Eq. (8.36) shows that this elastic estimate fully agrees with the lattice results, demonstrating that inelastic effects have to be smaller than the precision with which the elastic contributions can currently be evaluated.

From Eq. (8.41), we can extract the *strong* kaon mass difference

$$\left(M_{K^0}^2 - M_{K^\pm}^2\right)_{\mathrm{str}} = 6.02(18) \cdot 10^{-3}\,\mathrm{GeV}^2\,, \tag{8.42}$$

which is perfectly compatible with the result extracted from a dispersive analysis of $\eta \to 3\pi$ decays, $\left(M_{K^0}^2 - M_{K^\pm}^2\right)_{\mathrm{str}} = 6.24(38) \cdot 10^{-3}\,\mathrm{GeV}^2$ [111]. Similarly, if we convert our result for the strong kaon mass difference into a value for the quark mass ratio Q according to Eq. (8.32),[9] we find

$$Q = 22.4(3)\,, \tag{8.43}$$

again compatible with the value deduced from $\eta \to 3\pi$, $Q = 22.1(7)$ [111], as well as from several other analyses of the same decay [106–108, 387, 487]. We wish to emphasize again that our errors here merely reflect the ones in the kaon and pion form factors, but not the omission of inelastic intermediate states in the Cottingham formula. In view of the large uncertainties, however, we expect that the assigned uncertainties also cover the omitted inelastic contributions, as is indeed the case for the pion mass difference.

8.4.3 Kaon-box contribution to HLbL scattering

The last two applications concern the anomalous magnetic moment of the muon, whose experimental world average [488–492]

$$a_\mu^{\mathrm{exp}} = 116\,592\,061(41) \cdot 10^{-11} \tag{8.44}$$

[9] For the isospin-symmetric masses M_K^2 and M_π^2 in Eq. (8.32), we use the average of charged and neutral squared kaon masses, subtracting the electromagnetic contribution as calculated here, and the neutral pion mass corrected for the strong mass shift [177].

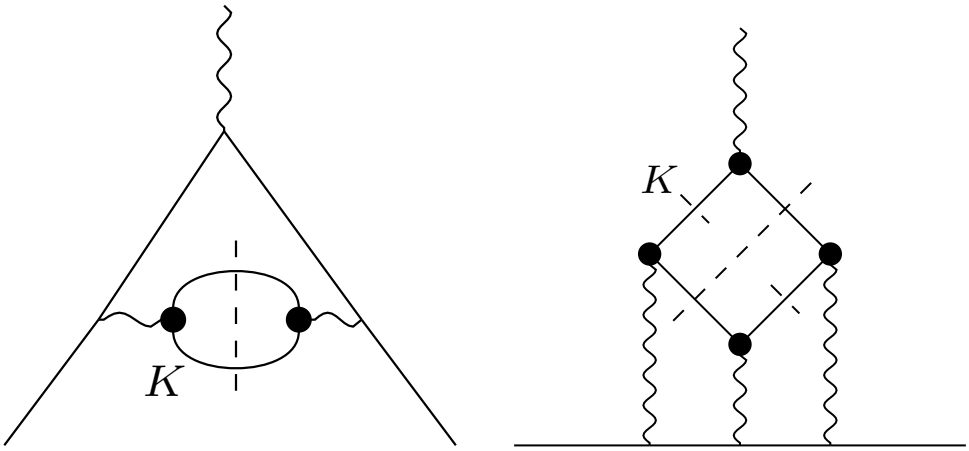

Figure 8.11: Diagrammatic representation of the kaon contributions to HVP (left) and HLbL (right). The thick black dots denote kaon electromagnetic form factor insertions. Dashed lines indicate the $\bar{K}K$ cuts and, for HLbL scattering, the kaon pole in the $\gamma^*\gamma^{(*)} \to \bar{K}K$ subamplitudes.

currently displays a 4.2σ discrepancy to the Standard-Model (SM) prediction [123–125, 146, 324, 325, 411, 423, 433–435, 486, 493–509]

$$a_\mu^{\mathrm{SM}} = 116\,591\,810(43) \cdot 10^{-11}\,. \tag{8.45}$$

Improvements are most pressing for the HVP contribution, for which the evaluation from $e^+e^- \to$ hadrons cross-section data that enters Eq. (8.45) stands in 2.1σ tension with the recent lattice-QCD calculation [510], especially since the uncertainty in the leading-order HVP contribution [125, 146, 325, 411, 423, 433–435]

$$a_\mu^{\mathrm{HVP,\,LO}} = 6\,931(40) \cdot 10^{-11} \tag{8.46}$$

emerges as the limiting factor in the total SM prediction. A large part of the uncertainty arises from systematic tensions among the 2π data sets, most notably between the BaBar [511] and KLOE [512] data. It is therefore the 2π channel that receives most attention [513], including when scrutinizing the consequences of the tension with Ref. [510], see Refs. [514–517]. However, compared to the final precision anticipated at the Fermilab experiment, $\Delta a_\mu^{\mathrm{exp}}[\mathrm{E989}] = 16 \cdot 10^{-11}$ [518], also the subleading channels are sizable, among them $e^+e^- \to K^+K^-$ and $e^+e^- \to K_S K_L$; cf. Fig. 8.11 (left). We will study their contributions in the vicinity of the ϕ region in Sec. 8.4.4.

First, we turn to the HLbL contribution [123, 124, 324, 325, 431, 486, 498–507, 519–523]

$$a_\mu^{\mathrm{HLbL}} = 90(17) \cdot 10^{-11}\,, \tag{8.47}$$

in which case the uncertainty is dominated by subleading contributions beyond pseudoscalar poles and two-meson cuts, see Refs. [437, 524–532] for recent work in this direction. Meanwhile, $\bar{K}K$ states prove to be appreciably suppressed compared to their $\pi\pi$ analog, which is true for both the leading box contributions (estimated in VMD [325] or DS equations [431, 432]) and rescattering corrections [530], in the latter case despite the strong coupling between the $\pi\pi$ and $\bar{K}K$ channels via the $f_0(980)$. While the overall effect

	$a_\mu^{K^\pm\text{-box}} \cdot 10^{11}$	$a_\mu^{K^0\text{-box}} \cdot 10^{15}$
VMD [325]	−0.50	−1.2
DS [431]	−0.48(2)(4)	
DS [432]	−0.48(4)	
This work	−0.484(5)(10)	−0.5(2)(4)

Table 8.2: Results for the charged and neutral kaon-box contributions to HLbL scattering.

is thus known to be small, we can confirm these conclusions by means of our data-driven evaluation of the kaon form factors.

The pion-box contribution, defined dispersively in a double-spectral representation of HLbL scattering, was shown in Ref. [486] to coincide with the scalar-QED one-loop expression, multiplied by pion electromagnetic form factors for the three virtual photons. The same applies to kaon intermediate states, see Fig. 8.11 (right): in the master formula for the contribution to a_μ [502], the HLbL scalar functions are of the form

$$\bar{\Pi}_i^{K\text{-box}}(Q_1^2, Q_2^2, Q_3^2) = F_K(Q_1^2) F_K(Q_2^2) F_K(Q_3^2) \frac{1}{16\pi^2} \int_0^1 \mathrm{d}x \int_0^{1-x} \mathrm{d}y \, I_i^K(x, y) \,, \tag{8.48}$$

where Q_i^2 denote the spacelike photon virtualities and the scalar-QED Feynman integrals are analogous to the pion case [502]. Thus, the charged- and neutral-kaon boxes can be obtained from the expressions for the pion box by simply replacing the meson mass and electromagnetic form factors. Diagrammatically, the box contributions correspond to two-meson cuts in which the $\gamma^*\gamma^{(*)} \to \pi\pi/\bar{K}K$ subamplitudes [327, 328, 341, 533–535] are further reduced to the respective poles. As in the case of the Cottingham formula, these contributions are fully determined by the electromagnetic form factors.

The numerical results for the kaon boxes with our data-driven form-factor input, shown in the spacelike region in Fig. 8.10, are in good agreement with previous estimates, see Table 8.2. The uncertainties have been obtained in the same way as in Sec. 8.4.2. While in the case of the pion box about 95% of the contribution is generated for photon virtualities below 1 GeV, due to the heavier kaon mass the charged kaon box is saturated to only 74% by this energy region. For the neutral kaon box, this low-energy region is responsible for only about 25% of the contribution due to the vanishing of the form factors at $Q_i^2 = 0$. The sensitivity to larger virtualities explains the large relative uncertainty. While the neutral-kaon box is numerically irrelevant for $(g-2)_\mu$, even the charged-kaon box,

$$a_\mu^{K\text{-box}} = -0.48(1) \cdot 10^{-11} \,, \tag{8.49}$$

is of little importance in view of the overall uncertainty of the HLbL contribution, cf. Eq. (8.47).

	K^+K^-	K_SK_L
Refs. [434, 435]	181.2(1.7)	119.7(1.8)
charged/neutral	184.5(2.0)	118.3(1.5)
charged shift	184.3(2.0)	
combined	184.5(2.0)	118.3(1.5)
BaBar [416]	182.5(2.2)	
CMD-2 [418]		117.2(2.4)
CMD-3 [417, 419]	192.6(3.9)	119.5(2.2)
SND [414]	166.7(11.9)	119.0(5.1) 121.1(5.0)

Table 8.3: Results for the charged- and neutral-kaon contributions to HVP up to $\sqrt{s} \leq 1.05\,\text{GeV}$, in units of 10^{-11}.

8.4.4 HVP around the ϕ resonance

The HVP contribution to a_μ derives from the master formula [536, 537]

$$a_\mu^{\text{HVP, LO}} = \left(\frac{\alpha m_\mu}{3\pi}\right)^2 \int_{M_{\pi^0}^2}^{\infty} \mathrm{d}s \frac{\hat{K}(s)}{s^2} R_{\text{had}}(s)\,,$$
$$R_{\text{had}}(s) = \frac{3s}{4\pi\alpha^2}\sigma(e^+e^- \to \text{hadrons})\,, \tag{8.50}$$

where $\hat{K}(s)$ is a known kernel function and the hadronic cross section is understood to be photon inclusive, see Fig. 8.11 (left) for the contribution from the $\bar{K}K$ cut. For the neutral channel, the cross section thus follows directly from the form factor via Eq. (8.16), while for the charged kaons the FSR correction needs to be added back. The numerical results are shown in Table 8.3, in comparison to the direct integration from Refs. [434, 435].

For the neutral channel, the difference between the fit scenarios 2 and 3 is minimal, in both cases the integral comes out lower by less than 1σ in comparison to Refs. [434, 435]. This small difference mostly traces back to the use of a linear interpolation therein, given that the data points in the neutral channel are more clustered than in the charged one, see Figs. 8.5 and 8.6. Accordingly, the same effect does not play a role in the charged channel [538]. In this case, we observe that the outcomes of the fit variants 2 and 3 are still well compatible, but larger by more than 1σ in comparison to Refs. [434, 435].[10]

This difference is ultimately a manifestation of the tensions between the BaBar and CMD-3 data sets (2.3σ for the HVP integral): in our approach, the cross section is constrained to follow the shape of the ϕ resonance in all fit variants, in such a way that the combined HVP integral comes out very close to the naive average of the individual data sets, despite the underlying tension, and, as shown in Table 8.1, with a reasonable χ^2/dof even for the combined charged fit (albeit clearly worse than in the neutral channel, as

[10] Assuming uncorrelated errors, the difference would be 1.3σ, but this is likely an underestimate since, due to the use of the same timelike data sets, the uncertainties are expected to be strongly correlated.

long as no shift in energy calibration is allowed). Performing instead local averages of the data can obfuscate this global shape if inconsistencies are present among the data sets, and indeed a fit of our representation to the data combination of Refs. [434, 435] displays a $\chi^2/\text{dof} > 2$.[11] In particular, the increase in the χ^2/dof occurs because the peak cross section is no longer compatible with the cross-section values in the tails of the resonance, to the effect that a linear interpolation gives the HVP integral as in Refs. [434, 435], while enforcing our fit function does produce a larger value very close to our combined fit.

Our final results are

$$\begin{aligned} a_\mu^{\text{HVP}}[K^+K^-, \leq 1.05\,\text{GeV}] &= 184.5(2.0) \cdot 10^{-11}, \\ a_\mu^{\text{HVP}}[K_SK_L, \leq 1.05\,\text{GeV}] &= 118.3(1.5) \cdot 10^{-11}\,, \end{aligned} \tag{8.51}$$

quoted, as for the other applications before, from the combined fit 3. In this way, we implement the maximum amount of independent constraints available, emphasizing the complementarity of our results to the direct integration of the cross-section data [411, 433–435]. In particular, demanding universality of the ϕ pole parameters implies that part of the tension in the charged data base propagates into the result for the neutral channel via the scale factor of the fit, but the numerical impact is minimal, see Table 8.3. Since, in this fit scenario, the numbers for the two channels become correlated via the ϕ pole parameters, we also quote the sum

$$a_\mu^{\text{HVP}}[K^+K^- + K_SK_L, \leq 1.05\,\text{GeV}] = 302.8(2.5) \cdot 10^{-11}\,. \tag{8.52}$$

8.5 Summary and conclusions

In this chapter, we presented a comprehensive analysis of the electromagnetic form factors of the kaon, including all available constraints from dispersion relations and both timelike and spacelike data. This approach has the advantage that a host of experimental constraints can be considered simultaneously, including (i) input from the P-wave of $\pi\pi \to \bar{K}K$ and the pion electromagnetic form factor, which together yield the bulk of the spectral function of the isovector kaon form factor, with a result that can be validated by data for $\tau^- \to K^-K_S\nu_\tau$, (ii) timelike data for $e^+e^- \to \bar{K}K$, which determine the residue of the ϕ resonance in the isoscalar part of the form factor, and (iii) spacelike data for charged-kaon–electron scattering, which help constrain the residue of the ω, as not directly accessible in the timelike region. Further (indirect) constraints on the charge radius of the neutral kaon could be imposed, but for the reasons given in Sec. 8.4.1 we opt to provide an independent determination instead. Dispersion relations are most useful for the isovector form factor, leading to a model-independent implementation of the ρ meson in terms of 2π intermediate states, while for the isoscalar spectral function, dominated by 3π and $\bar{K}K$ contributions, a parameterization in terms of the narrow ω and ϕ resonances proves sufficient. We considered several fit variants for the timelike data, described in 1–3 in Sec. 8.3, to account for tensions in the charged-channel data base. In particular, we studied to which extent the subsequent applications are affected.

[11] We thank Alex Keshavarzi for making the combined cross-section data from Refs. [434, 435] available to us.

The results obtained along these lines for the kaon electromagnetic form factors enter in a number of applications. Besides the ϕ resonance parameters—the global fit leads to the values given in Eq. (8.25)—these are:

1. Charge radii for charged and neutral kaon, see Sec. 8.4.1 and Eq. (8.29) for the main result: for the charged kaon, our result lies 1.3σ above the current RPP average, but is considerably more precise, thanks to the inclusion of timelike data and dispersive constraints on the isovector form factor. The same is true for the neutral kaon, in which case our result lies 1.6σ above the RPP average (dominated by $K_L \to \pi^+\pi^- e^+ e^-$), closer to the central value from K^0–electron scattering.

2. Corrections to Dashen's theorem, see Sec. 8.4.2 and Eq. (8.41) for the main result: the spacelike kaon form factor determines the elastic contribution to the electromagnetic mass shift via the Cottingham formula, and thus the comparison to the analog formula for the pion entails a prediction for the corrections to Dashen's theorem. Our result is in perfect agreement with lattice QCD and extractions from $\eta \to 3\pi$, demonstrating that the inelastic effects in the evaluation of the Cottingham formula are smaller than the current uncertainties in the elastic contribution.

3. Kaon-box contributions to HLbL scattering, see Sec. 8.4.3 and Eq. (8.49) for the main result: the spacelike form factor also arises in the evaluation of two-kaon intermediate states to HLbL scattering, so-called kaon-box contributions. Our result agrees with previous calculations, but provides a data-driven estimate of the uncertainty.

4. Two-kaon contributions to HVP, see Sec. 8.4.4 and Eq. (8.51) for the main result: the timelike data around the ϕ resonance, used to constrain the ϕ parameters in the isoscalar form factor, dominate the contribution to the HVP integral in the same energy region. Our evaluation delineates the potential impact of dispersive constraints and input from other kinematic regions, and also allows for a more detailed study of the consequences of the tensions in the charged-channel data base. In general, our results are in good agreement with previous evaluations using a direct integration of the data, but we find that, in the charged channel, the HVP integral increases by more than 1σ if the global shape of the ϕ resonance is enforced as it is in our dispersive representation. This difference ultimately reflects a tension between the BaBar and CMD-3 data for the $e^+e^- \to K^+K^-$ channel.

8.A Isospin breaking in hadronic vacuum polarization

In this appendix, we present the results that were included in Refs. [7, 8]. Since Ref. [510] differs for the entire HVP integral by 2.1σ from e^+e^- data, we focus on the comparison to lattice QCD as the reason of this deviation is still not understood. A point that can be scrutinized in lattice-QCD calculations concerns the separation into an isosymmetric part and isospin-breaking (IB) corrections, the latter further separated into QED, $\mathcal{O}(e^2)$, and strong IB, $\mathcal{O}(\delta = m_u - m_d)$, effects. Attempts to estimate such corrections from phenomenology have been made before [521, 539], but using the results of this chapter one of the main IB contributions for which enhancement is expected can be calculated. Therefore, we provide a valuable point of comparison to lattice QCD for the IB corrections.

Note that Refs. [7, 8] also consider other important channels and this might help to better understand the source of this deviation.

To calculate the HVP contribution on a $T \times L^3$ lattice one defines correlators in Euclidean time [540]

$$C_L(t) = \frac{a^3}{3} \sum_{i=1}^{3} \sum_{\vec{x}} \langle J_i(x) J_i(0) \rangle \,, \tag{8.53}$$

where a is the lattice spacing and J_i are the antihermitian spatial components of the electromagnetic current. Using a known kernel function $\tilde{K}(t)$ and taking the appropriate limits one finds

$$a_\mu^{\text{HVP, LO}} = \lim_{a \to 0} \lim_{L,T \to \infty} \left(\frac{\alpha}{\pi}\right)^2 \left(\frac{a}{m_\mu^2}\right) \sum_{t=0}^{T/2} \tilde{K}(t m_\mu) \operatorname{Re} C_L(t) \,, \tag{8.54}$$

which is the HVP contribution from lattice QCD and can be directly compared to the quantity in Eq. (8.50).

To disentangle different regions in the CM energy $\sqrt{s}$, one can study so-called Euclidean-time windows [541]. These are defined in Euclidean time by

$$\begin{aligned} \Theta^{\text{SD}}(t) &= 1 - \Theta(t, t_0, \Delta) \,, \\ \Theta^{\text{int}}(t) &= \Theta(t, t_0, \Delta) - \Theta(t, t_1, \Delta) \,, \\ \Theta^{\text{LD}}(t) &= \Theta(t, t_1, \Delta) \,, \\ \Theta(t, t', \Delta) &= \frac{1}{2} \left(1 + \tanh \frac{t - t'}{\Delta}\right) \,, \end{aligned} \tag{8.55}$$

where the standard parameter choice is $t_0 = 0.4\,\text{fm}$, $t_1 = 1.0\,\text{fm}$, and $\Delta = 0.15\,\text{fm}$. This defines a short-distance (SD), intermediate (int), and long-distance (LD) window, where the intermediate window behaves particularly well with regards to systematic effects in lattice QCD. To insert them in Eq. (8.50) directly, the weight functions can be transformed to CM energy by [542]

$$\begin{aligned} \tilde{\Theta}(s) &= \frac{3 s^{5/2}}{8 m_\mu^4 \hat{K}(s)} \int_0^\infty \mathrm{d}t\, \Theta(t) e^{-t\sqrt{s}} \int_0^\infty \mathrm{d}s' w\left(\frac{s'}{m_\mu^2}\right) \left(t^2 - \frac{4}{s'} \sin^2 \frac{t\sqrt{s'}}{2}\right) \,, \\ w(r) &= \frac{\left(r + 2 - \sqrt{r(r+4)}\right)^2}{\sqrt{r(r+4)}} \,. \end{aligned} \tag{8.56}$$

These are shown in Fig. 8.12 and allow us to split up the IB contributions into the different window quantities, which simplifies the comparison with lattice QCD.

The first class of contributions is from FSR that combines the virtual-photon and bremsstrahlung diagrams. These effects are captured by $\eta(s)$ defined in Sec. 8.3 and are a pure $\mathcal{O}(e^2)$ effect. Consequently, we compare the variation with respect to the inclusion of $\eta(s)$ for the charged kaons.

The second class comes from the IB in the kaon mass and we can use the electromagnetic kaon mass difference in Eq. (8.41) and the strong kaon mass difference in Eq. (8.42) to find

$$M_{K^\pm} = (494.58 - 3.05_\delta + 2.14_{e^2})\ \text{MeV} \quad \text{and} \quad M_{K^0} = (494.58 + 3.03_\delta)\ \text{MeV} \,, \tag{8.57}$$

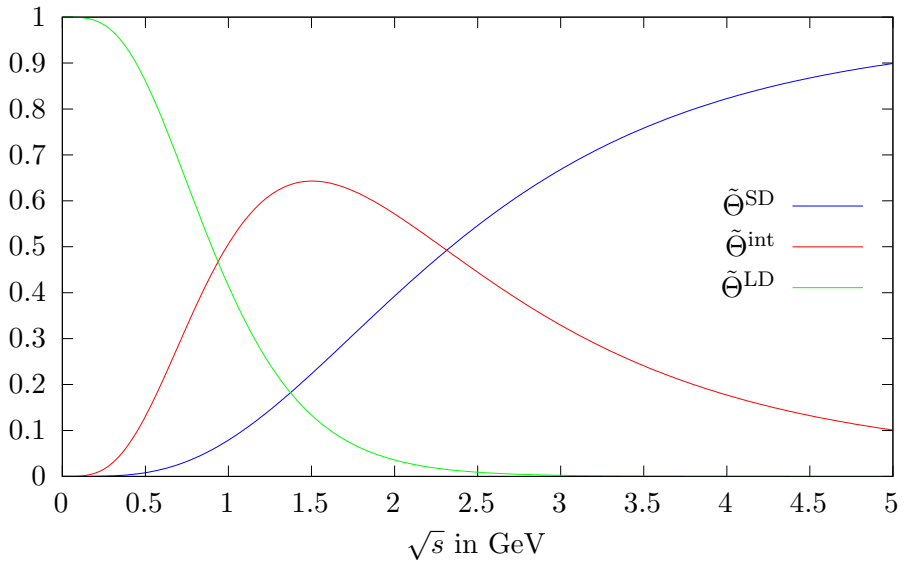

Figure 8.12: Weight function for short-distance (SD), intermediate (int), and long-distance (LD) window in terms of the CM energy.

	SD		int		LD	
	$\mathcal{O}(e^2)$	$\mathcal{O}(\delta)$	$\mathcal{O}(e^2)$	$\mathcal{O}(\delta)$	$\mathcal{O}(e^2)$	$\mathcal{O}(\delta)$
FSR (K^+K^-)	0.06(0)	–	0.39(2)	–	0.30(2)	–
mass (K^+K^-)	−0.27(1)	0.42(2)	−1.68(9)	2.57(13)	−1.29(7)	1.98(10)
mass ($\bar{K}^0K^0$)	0.00(0)	−0.39(2)	−0.01(0)	−2.39(12)	−0.01(0)	−1.84(9)

Table 8.4: IB effects to a_μ^{HVP} separated into $\mathcal{O}(e^2)$ and $\mathcal{O}(\delta)$ contributions as well as short-distance (SD), intermediate (int), and long-distance (LD) windows. All entries in units of 10^{-10}. Note that these values slightly vary from the ones used in Refs. [7, 8], because a wrong $\tilde{\Theta}(s)$ was used therein.

where the charged and neutral sum is fixed to the RPP value. Varying the masses around the isospin limit yields the IB corrections for the HVP integral.

The charged and neutral $\phi \to K\bar{K}$ couplings from Table 8.1 are

$$c_\phi^{K^+K^-} = 1.001(6) \quad \text{and} \quad c_\phi^{K^0\bar{K}^0} = 0.977(6)\,, \tag{8.58}$$

but it is not clear how to define the coupling in the isospin limit and therefore this IB effect is not included in the results. Instead, we used the charged- (neutral-)kaon residue in the K^+K^- ($K^0\bar{K}^0$) channel. The opposite assignment produces a shift in the integral, and we will assign this value (and its decomposition onto the windows, cf. Table 8.4) as a source of uncertainty that should give an indication of missing effects in the exclusive channels that otherwise have been explicitly included.

Our results for the full HVP, with the same cutoff in $\sqrt{s}$ as used in Sec. 8.4.4, are

$$a_\mu^{\mathrm{HVP}}[K^+K^-, e^2] = 0.75(4)\,,$$

for the FSR and

$$\begin{aligned} a_\mu^{\rm HVP}[K^+K^-, e^2] &= -3.24(17)\,, & a_\mu^{\rm HVP}[K^0\bar{K}^0, e^2] &= -0.02(0)\,, \\ a_\mu^{\rm HVP}[K^+K^-, \delta] &= 4.98(26)\,, & a_\mu^{\rm HVP}[K^0\bar{K}^0, \delta] &= -4.62(23)\,, \\ a_\mu^{\rm HVP}[K^+K^-, e^2\delta] &= -0.33(1)\,, \end{aligned} \tag{8.59}$$

for the mass variation in units of 10^{-10}, while the decomposition in the window quantities is shown in Table 8.4. Note that the $\mathcal{O}(e^2\delta)$ contribution is estimated from the difference of the charged and neutral channel using the isospin kaon mass. Furthermore, there is a small contribution to $\mathcal{O}(e^2)$ for the neutral kaons, since the charged kaon mass enters through the energy dependent width of the ϕ resonance in Eq. (8.14).

Epilogue

Chapter 9

Conclusions and outlook

While the standard model remains the most successful description of particle physics, with its main problems as already mentioned in the introduction still being unsolved, this thesis helped to gradually improve the understanding of the strong interaction. Thereby, different aspects were investigated that we will briefly summarize in this chapter and give an outlook on future research that can be conducted based on these results. All of these calculations were performed to test the precision frontier, i.e., precise calculations of low-energy phenomena in the non-perturbative regime of the strong interaction.

The currently most prominent example to test this frontier is the anomalous magnetic moment of the moun, which is discussed in Chapter 8 as an application of the kaon electromagnetic form factor. We performed a combined fit of the kaon electromagnetic form factor to the $e^+e^- \to K\bar{K}$ cross section in the timelike region and eK scattering in the spacelike region from all available experiments. This constrained the free parameters in the theoretical parameterization of the form factor. Using the form factor and its uncertainties, we were able to extract several physical quantities. For the electromagnetic charge radii of the charged and neutral kaons, the uncertainty was heavily decreased due to the inclusion of the timelike data. Moreover, we could test Dashen's theorem by employing the Cottingham formula to extract the strong kaon mass difference. For applications to the anomalous magnetic moment of the muon, we were able to calculate the kaon-box contribution to hadronic light-by-light scattering, which we found to be in perfect agreement with previous analyses. For the hadronic-vacuum-polarization contribution around the ϕ resonance our result is in slight tension with the analysis using data combination, which was due to the underlying tension in the cross-section data from different experiments. While the most important and heavily disputed hadronic contribution to the anomalous magnetic moment of the muon is connected to the $\pi\pi$ channel, our results were used in Ref. [7] to estimate isospin breaking for hadronic vacuum polarization and might be needed in the future for a precise calculation of the deviation from the experimental value. Additionally, this analysis allows the straightforward inclusion of new data sets.

In Chapter 6, we applied dispersion-theoretical methods to predict the cross sections for the Primakoff reaction $\gamma K \to K\pi$ using the chiral anomaly and the currently available experimental radiative couplings of the $K^*(892)$ resonance. We included full crossed-channel rescattering via Khuri–Treiman-type equations and, in the future, a precision measurement of this cross section will allow us to extract these quantities with small theoretical uncertainties using our framework. Moreover, in Chapter 7, the kaon Compton amplitude was used to derive a method to experimentally extract the kaon dipole polarizabilities. Therein, the results from Chapter 6 were used to dispersively reconstruct the K^* resonance. A combined analysis of $\gamma K \to \gamma K$ and $\gamma K \to K\pi$ can therefore be used to extract the chiral anomaly, the radiative couplings, and the kaon polarizabilities once experimental data, e.g., from AMBER, becomes available. This allows for a high-precision extraction of these quantities with small model dependencies. The ex-

tracted chiral anomaly can be tested with the leading-order chiral perturbation theory prediction—which is currently available—or with a full next-to-leading-order calculation to be performed in the future. Furthermore, we provided tools to extract fundamental electromagnetic properties of kaons, i.e., the kaon dipole polarizabilities and the electromagnetic charge radius from the previous paragraph, and to investigate the inner structure of these strongly bound particles. The radiative K^* couplings and kaon polarizabilities extracted here can then be used as an input in the dispersive determination of the photon–photon fusion coupled-channel reactions $\gamma\gamma \to \pi\pi/K\bar{K}$ and $\gamma\gamma \to \pi\eta/K\bar{K}$, which in turn are used in calculations of the hadronic light-by-light contribution to the anomalous magnetic moment of the muon. A similar analysis to Chapter 7 could also be done for the pion polarizabilities, taking into account the effects of the $\rho(770)$ resonance explicitly, which might allow for a more accurate measurement than currently available [350] due to the smaller theoretical uncertainties.

In Chapter 4, we investigated the effect of rescattering in 3π final states for different angular-momentum quantum numbers of the decaying particle. This is an important result, since typical experimental analyses neglect these effects, and with increasing statistics, they might be needed in the future. Therefore, we calculated the number of events in a Dalitz plot that is needed to distinguish simple isobar models from full rescattering effects via Khuri–Treiman dispersion relations. Unfortunately, this analysis was only possible in very limited scenarios, as it needed to be conducted without prior knowledge on the different processes. This limits the number of different channels that could be computed, since only one overall constant could be fixed via the normalization. A generalized code was made available, which will simplify the numerical solution of Khuri–Treiman equations in future applications.

One possible application is the decay $\omega \to 3\pi$, since the experimental situation for its Dalitz plot is heavily disputed. While dispersive analyses with a single subtraction [81, 102] are not compatible with the experimental Dalitz-plot data, a second subtraction is needed to reproduce the experimental values [113]. Using a pion–pion phase shift that includes the dominating $\omega\pi$ inelasticities in a Khuri–Treiman analysis might clarify the situation [543]. Additionally, making the full (binned) Dalitz-plot data available instead of only the polynomial fit values would help to understand these intricacies better. Furthermore, a subset of upcoming high-statistics $J/\psi \to 3\pi$ Dalitz-plot data from BESIII can be used to precisely study ρ–ω mixing as well as the ω mass and width in the $\pi^+\pi^-$ invariant mass spectrum. The ω resonance parameters extracted from isospin-conserving and isospin-violating settings are not compatible, cf. Refs. [127, 532, 544], and this analysis would allow for another test of the isospin-violating setting via ρ–ω mixing. Moreover, one can get insights into the production mechanism, since the strong production—via three gluons—is strongly suppressed due to the OZI mechanism [545–547], and therefore, the photon exchange is quantitatively competitive. Since this will be high-precision data, rescattering effects in the region around the ρ-resonance bands must be calculated with the use of Khuri–Treiman equations. In the vector charmonium sector, the "$\rho\pi$ puzzle" (cf. Refs. [548–551] and references therein) refers to the phenomenon that the ratio of $\psi(2S) \to \rho\pi$ and $J/\psi \to \rho\pi$ branching ratios is heavily suppressed compared to perturbative QCD predictions. While Khuri–Treiman analyses for $J/\psi \to 3\pi$ are available [103, 115]—albeit they do not study the experimental Dalitz plot—the $\psi(2S) \to 3\pi$ decay has not been analyzed. Clearly, a simple analysis that assumes a dominant $\rho\pi$ decay of the $\psi(2S)$ will not be useful and

higher partial waves need to be incorporated. Further, it would be interesting to understand the interference of production mechanisms in charged-meson scattering experiments, i.e., $\pi^- p \to \pi^-\pi^-\pi^+ p$ at COMPASS, since the Deck effect [552] will contribute. Therefore, the analysis of these Dalitz plots is more complicated and cannot be described by only using Khuri–Treiman equations; however, one might be able to suppress the Deck effect contributions by choosing specific kinematic regions. As different reconstruction theorems were derived here or in the literature, other more complex scenarios are possible. These include processes that need different partial waves and isospins or unequal particle content in the final state, similar to $\eta' \to \eta\pi\pi$ but with spin.

Khuri–Treiman equations are clearly limited at higher energies, as they are derived from truncated partial-wave expansions. A possible extension to this was investigated in Chapter 5, where a hypergeometric isobar model with Regge trajectories was constructed. Here, the range is not limited anymore as it takes the infinite tower of partial waves into account and exhibits the expected Regge behavior at high energies. Furthermore, it fulfills many necessary theoretical constraints and connects the low-energy region, governed by resonances, with the high-energy region via Regge trajectories. As an initial numerical application, we benchmarked our formalism on the ρ and $\sigma/f_0(500)$ resonances in $\pi\pi$ scattering. While the partial waves could be described nicely, also the pole parameters could be extracted. The Regge trajectory additionally contains information about resonances far outside the fit region, and we could extract the pole positions of excited resonances. The main difficulties with this model are that unitary can only be imposed approximately and one needs to solve non-linear integral equations. Since the first numerical calculations of the homogeneous solution (for which crossed-channel effects are neglected) were tested successfully, further improvements will be explored in the future. The obvious next step is the inclusion of crossed channels and a simultaneous fit to the $\pi\pi$ partial waves. This then allows one to study the scattering process also at high energies. If this proves to be solvable, possible extensions include decay processes, coupled channels, unequal masses, and the inclusion of particles with spins, which will increase the applicability of this model.

In summary, a lot of future research is possible based on the results presented in this thesis. It will hopefully allow to disentangle more secrets of the strong interaction.

Bibliography

[1] J. R. R. Tolkien, *The Return of the King*, George Allen & Unwin, 1955.

[2] D. Stamen, T. Isken, B. Kubis, M. Mikhasenko, and M. Niehus, *Analysis of rescattering effects in* 3π *final states*, Eur. Phys. J. C **83**, 510 (2023) [arXiv:2212.11767 [hep-ph]], [Erratum: Eur. Phys. J. C **83**, 586 (2023)].

[3] D. Stamen, D. Winney, A. Rodas, C. Fernández-Ramírez, V. Mathieu, G. Montaña, A. Pilloni, and A. P. Szczepaniak, *Towards a unified description of hadron scattering at all energies*, (2024) [arXiv:2409.09172 [hep-ph]].

[4] M. Dax, D. Stamen, and B. Kubis, *Dispersive analysis of the Primakoff reaction* $\gamma K \to K\pi$, Eur. Phys. J. C **81**, 221 (2021) [arXiv:2012.04655 [hep-ph]].

[5] D. Stamen, J. L. Dammann, Y. Korte, and B. Kubis, *Polarizabilities from kaon Compton scattering*, Eur. Phys. J. C **84**, 1267 (2024) [arXiv:2409.05955 [hep-ph]].

[6] D. Stamen, D. Hariharan, M. Hoferichter, B. Kubis, and P. Stoffer, *Kaon electromagnetic form factors in dispersion theory*, Eur. Phys. J. C **82**, 432 (2022) [arXiv:2202.11106 [hep-ph]].

[7] M. Hoferichter, G. Colangelo, B.-L. Hoid, B. Kubis, J. Ruiz de Elvira, D. Schuh, D. Stamen, and P. Stoffer, *Phenomenological Estimate of Isospin Breaking in Hadronic Vacuum Polarization*, Phys. Rev. Lett. **131**, 161905 (2023) [arXiv:2307.02532 [hep-ph]].

[8] M. Hoferichter, G. Colangelo, B.-L. Hoid, B. Kubis, J. Ruiz de Elvira, D. Stamen, and P. Stoffer, *Chiral extrapolation of hadronic vacuum polarization and isospin-breaking corrections*, PoS **LATTICE2022**, 316 (2022) [arXiv:2210.11904 [hep-ph]].

[9] D. Stamen, M. Dax, and B. Kubis, *Dispersive analysis of the Primakoff reaction* $\gamma K \to K\pi$, PoS **CD2021**, 048 (2021).

[10] T. Clifton, P. G. Ferreira, A. Padilla, and C. Skordis, Phys. Rept. **513**, 1–189 (2012) [arXiv:1106.2476 [astro-ph.CO]].

[11] J. Alexander *et al.*, (2016) [arXiv:1608.08632 [hep-ph]].

[12] M. Dine, W. Fischler, and M. Srednicki, Phys. Lett. B **104**, 199–202 (1981).

[13] C.-N. Yang and R. L. Mills, Phys. Rev. **96**, 191–195 (1954).

[14] S. L. Glashow, Nucl. Phys. **22**, 579–588 (1961).

[15] P. W. Higgs, Phys. Lett. **12**, 132–133 (1964).

[16] F. Englert and R. Brout, Phys. Rev. Lett. **13**, 321–323 (1964).

[17] P. W. Higgs, Phys. Rev. Lett. **13**, 508–509 (1964).

[18] S. Weinberg, Phys. Rev. Lett. **19**, 1264–1266 (1967).

[19] A. Salam, Conf. Proc. C **680519**, 367–377 (1968).

[20] H. Fritzsch, M. Gell-Mann, and H. Leutwyler, Phys. Lett. B **47**, 365–368 (1973).

[21] F. Gross *et al.*, Eur. Phys. J. C **83**, 1125 (2023) [arXiv:2212.11107 [hep-ph]].

[22] R. L. Workman *et al.* [Particle Data Group], PTEP **2022**, 083C01 (2022).

[23] R. N. Mohapatra *et al.*, Rept. Prog. Phys. **70**, 1757–1867 (2007) [arXiv:hep-ph/0510213].

[24] K. Ottnad, B. Kubis, U.-G. Meißner, and F.-K. Guo, Phys. Lett. B **687**, 42–47 (2010) [arXiv:0911.3981 [hep-ph]].

[25] B. Kubis, (2007) [arXiv:hep-ph/0703274].

[26] S. L. Adler, Phys. Rev. **177**, 2426–2438 (1969).

[27] S. L. Adler and W. A. Bardeen, Phys. Rev. **182**, 1517–1536 (1969).

[28] W. A. Bardeen, Phys. Rev. **184**, 1848–1857 (1969).

[29] J. S. Bell and R. Jackiw, Nuovo Cim. A **60**, 47–61 (1969).

[30] G. 't Hooft, Phys. Rev. Lett. **37**, 8–11 (1976).

[31] H. Weyl, Z. Phys. **46**, 1 (1927).

[32] E. Wigner, *Gruppentheorie und ihre Anwendungen auf die Quantenmechanik der Atomspektren*, Vieweg+Teubner Verlag, 1931.

[33] Y. Nambu and G. Jona-Lasinio, Phys. Rev. **122**, 345–358 (1961).

[34] Y. Nambu and G. Jona-Lasinio, Phys. Rev. **124**, 246–254 (1961).

[35] J. Goldstone, Nuovo Cim. **19**, 154–164 (1961).

[36] C. Vafa and E. Witten, Nucl. Phys. B **234**, 173–188 (1984).

[37] S. Mizera, Phys. Rept. **1047**, 1–92 (2024) [arXiv:2306.05395 [hep-th]].

[38] R. J. Eden, P. V. Landshoff, D. I. Olive, and J. C. Polkinghorne, *The analytic S-matrix*, Cambridge Univ. Press, 1966.

[39] H. Lehmann, K. Symanzik, and W. Zimmermann, Nuovo Cim. **1**, 205–225 (1955).

[40] S. Mandelstam, Phys. Rev. **112**, 1344–1360 (1958).

[41] G. Källén, *Elementary particle physics*, Addison-Wesley, 1964.

[42] T. Isken, PhD thesis, Bonn University (2021).

[43] D. I. Olive, Nuovo Cim. **26**, 73–102 (1962).

[44] M. Niehus, Master's thesis, Bonn University (2017).

[45] R. Omnès, Nuovo Cim. **8**, 316–326 (1958).

[46] N. I. Muskhelishvili, *Singular Integral Equations*, Wolters-Noordhoff Publishing, 1958.

[47] J. Stern, H. Sazdjian, and N. H. Fuchs, Phys. Rev. D **47**, 3814–3838 (1993) [arXiv:hep-ph/9301244].

[48] M. Knecht, B. Moussallam, J. Stern, and N. H. Fuchs, Nucl. Phys. B **457**, 513–576 (1995) [arXiv:hep-ph/9507319].

[49] B. Ananthanarayan, G. Colangelo, J. Gasser, and H. Leutwyler, Phys. Rept. **353**, 207–279 (2001) [arXiv:hep-ph/0005297].

[50] A. Martin and T. Spearman, *Elementary Particle Theory*, North-Holland Publishing Company, 1970.

[51] P. D. B. Collins, *An Introduction to Regge Theory and High Energy Physics*, Cambridge University Press, 1977.

[52] V. N. Gribov, *The theory of complex angular momenta: Gribov lectures on theoretical physics*, Cambridge University Press, 2003.

[53] D. Sivers and J. Yellin, Rev. Mod. Phys. **43**, 125–188 (1971).

[54] A. I. Bugrij, G. Cohen-Tannoudji, L. L. Jenkovszky, and N. A. Kobylinsky, Fortsch. Phys. **21**, 427–506 (1973).

[55] L. L. Jenkovszky, Riv. Nuovo Cim. **10N12**, 1–108 (1987).

[56] T. Regge, Nuovo Cim. **14**, 951–976 (1959).

[57] G. F. Chew and S. C. Frautschi, Phys. Rev. Lett. **8**, 41–44 (1962).

[58] R. García-Martín, R. Kamiński, J. R. Peláez, J. Ruiz de Elvira, and F. J. Ynduráin, Phys. Rev. D **83**, 074004 (2011) [arXiv:1102.2183 [hep-ph]].

[59] I. Caprini, G. Colangelo, and H. Leutwyler, Eur. Phys. J. C **72**, 1860 (2012) [arXiv:1111.7160 [hep-ph]].

[60] J. R. Peláez and A. Rodas, Phys. Rev. D **93**, 074025 (2016) [arXiv:1602.08404 [hep-ph]].

[61] P. Di Vecchia, Lect. Notes Phys. **737**, 59–118 (2008) [arXiv:0704.0101 [hep-th]].

[62] H. Lehmann, Nuovo Cim. **10**, 579–589 (1958).

[63] A. Martin, Nuovo Cim. A **42**, 930–953 (1965).

[64] G. N. Watson, Proc. R. Soc. Lond. A **95**, 83–99 (1918).

[65] A. Sommerfeld, *Partial Differential Equations in Physics*, Academic Press, 1949.

[66] A. Erdélyi *et al.*, *Higher Transcendental Functions. Vol. 1*, McGraw Hill, 1953.

[67] F. Carlson, PhD thesis, Uppsala University (1914).

[68] S. Mandelstam, Annals Phys. **19**, 1–24 (1962).

[69] G. F. Chew and S. C. Frautschi, Phys. Rev. Lett. **7**, 394–397 (1961).

[70] I. Y. Pomeranchuk, Sov. Phys. JETP **7**, 499 (1958).

[71] R. J. Eden, Rev. Mod. Phys. **43**, 15–35 (1971).

[72] M. Froissart, Phys. Rev. **123**, 1053–1057 (1961).

[73] A. Martin, Phys. Rev. **129**, 1432–1436 (1963).

[74] V. N. Gribov and I. Y. Pomeranchuk, Zh. Eksp. Teor. Fiz. **43**, 308 (1962).

[75] V. N. Gribov, I. Y. Pomeranchuk, and K. A. Ter-Martirosian, Phys. Rev. **139**, B184–B202 (1965).

[76] G. Veneziano, Nuovo Cim. A **57**, 190–197 (1968).

[77] C. Lovelace, Phys. Lett. B **28**, 264–268 (1968).

[78] J. A. Shapiro, Phys. Rev. **179**, 1345–1353 (1969).

[79] K. Kawarabayashi, S. Kitakado, and H. Yabuki, Phys. Lett. B **28**, 432–435 (1969).

[80] H. Akdag, T. Isken, and B. Kubis, JHEP **02**, 137 (2022) [arXiv:2111.02417 [hep-ph]], [Erratum: JHEP 12, 156 (2022)].

[81] F. Niecknig, B. Kubis, and S. P. Schneider, Eur. Phys. J. C **72**, 2014 (2012) [arXiv:1203.2501 [hep-ph]].

[82] S. Schneider, PhD thesis, Bonn University (2012).

[83] F. Niecknig, PhD thesis, Bonn University (2016).

[84] T. Isken, Master's thesis, Bonn University (2015).

[85] J. Gasser and A. Rusetsky, Eur. Phys. J. C **78**, 906 (2018) [arXiv:1809.06399 [hep-ph]].

[86] M. Niehus, M. Hoferichter, and B. Kubis, PoS **CD2018**, 076 (2019) [arXiv:1902.10150 [hep-ph]].

[87] M. Niehus, PhD thesis, Bonn University (2022).

[88] W. Jakob, J. Rhinelander, and D. Moldovan, "pybind11 – seamless operability between c++11 and python," 2017.

[89] H. Akdag, B. Kubis, M. Niehus, and D. Stamen, Zenodo (2023).

[90] C. Amsler, Rev. Mod. Phys. **70**, 1293–1340 (1998) [arXiv:hep-ex/9708025].

[91] D. V. Bugg, Phys. Rept. **397**, 257–358 (2004) [arXiv:hep-ex/0412045].

[92] E. Klempt and A. Zaitsev, Phys. Rept. **454**, 1–202 (2007) [arXiv:0708.4016 [hep-ph]].

[93] B. Ketzer, B. Grube, and D. Ryabchikov, Prog. Part. Nucl. Phys. **113**, 103755 (2020) [arXiv:1909.06366 [hep-ex]].

[94] S.-s. Fang, B. Kubis, and A. Kupść, Prog. Part. Nucl. Phys. **120**, 103884 (2021) [arXiv:2102.05922 [hep-ph]].

[95] K. M. Watson, Phys. Rev. **95**, 228–236 (1954).

[96] G. Breit and E. Wigner, Phys. Rev. **49**, 519–531 (1936).

[97] N. N. Khuri and S. B. Treiman, Phys. Rev. **119**, 1115–1121 (1960).

[98] G. Colangelo, E. Passemar, and P. Stoffer, Eur. Phys. J. C **75**, 172 (2015) [arXiv:1501.05627 [hep-ph]].

[99] G. Colangelo, J. Gasser, and H. Leutwyler, Nucl. Phys. B **603**, 125–179 (2001) [arXiv:hep-ph/0103088].

[100] J. Kambor, C. Wiesendanger, and D. Wyler, Nucl. Phys. B **465**, 215–266 (1996) [arXiv:hep-ph/9509374].

[101] A. V. Anisovich and H. Leutwyler, Phys. Lett. B **375**, 335–342 (1996) [arXiv:hep-ph/9601237].

[102] I. V. Danilkin *et al.*, Phys. Rev. D **91**, 094029 (2015) [arXiv:1409.7708 [hep-ph]].

[103] B. Kubis and F. Niecknig, Phys. Rev. D **91**, 036004 (2015) [arXiv:1412.5385 [hep-ph]].

[104] P. Guo *et al.*, Phys. Rev. D **92**, 054016 (2015) [arXiv:1505.01715 [hep-ph]].

[105] F. Niecknig and B. Kubis, JHEP **10**, 142 (2015) [arXiv:1509.03188 [hep-ph]].

[106] P. Guo, I. V. Danilkin, C. Fernández-Ramírez, V. Mathieu, and A. P. Szczepaniak, Phys. Lett. B **771**, 497–502 (2017) [arXiv:1608.01447 [hep-ph]].

[107] G. Colangelo, S. Lanz, H. Leutwyler, and E. Passemar, Phys. Rev. Lett. **118**, 022001 (2017) [arXiv:1610.03494 [hep-ph]].

[108] M. Albaladejo and B. Moussallam, Eur. Phys. J. C **77**, 508 (2017) [arXiv:1702.04931 [hep-ph]].

[109] T. Isken, B. Kubis, S. P. Schneider, and P. Stoffer, Eur. Phys. J. C **77**, 489 (2017) [arXiv:1705.04339 [hep-ph]].

[110] F. Niecknig and B. Kubis, Phys. Lett. B **780**, 471–478 (2018) [arXiv:1708.00446 [hep-ph]].

[111] G. Colangelo, S. Lanz, H. Leutwyler, and E. Passemar, Eur. Phys. J. C **78**, 947 (2018) [arXiv:1807.11937 [hep-ph]].

[112] M. Dax, T. Isken, and B. Kubis, Eur. Phys. J. C **78**, 859 (2018) [arXiv:1808.08957 [hep-ph]].

[113] M. Albaladejo *et al.* [JPAC], Eur. Phys. J. C **80**, 1107 (2020) [arXiv:2006.01058 [hep-ph]].

[114] E. Kou, T. Moskalets, and B. Moussallam, JHEP **12**, 177 (2023) [arXiv:2303.12015 [hep-ph]].

[115] M. Albaladejo *et al.* [JPAC], Phys. Rev. D **108**, 014035 (2023) [arXiv:2304.09736 [hep-ph]].

[116] V. Bernard, S. Descotes-Genon, M. Knecht, and B. Moussallam, Eur. Phys. J. C **84**, 744 (2024) [arXiv:2403.17570 [hep-ph]].

[117] M. Hoferichter, B. Kubis, and D. Sakkas, Phys. Rev. D **86**, 116009 (2012) [arXiv:1210.6793 [hep-ph]].

[118] M. Hoferichter, B. Kubis, and M. Zanke, Phys. Rev. D **96**, 114016 (2017) [arXiv:1710.00824 [hep-ph]].

[119] M. Albaladejo *et al.* [JPAC], Eur. Phys. J. C **78**, 574 (2018) [arXiv:1803.06027 [hep-ph]].

[120] M. Niehus, M. Hoferichter, and B. Kubis, JHEP **12**, 038 (2021) [arXiv:2110.11372 [hep-ph]].

[121] M. Zdráhal and J. Novotný, Phys. Rev. D **78**, 116016 (2008) [arXiv:0806.4529 [hep-ph]].

[122] M. Hoferichter, B. Kubis, S. Leupold, F. Niecknig, and S. P. Schneider, Eur. Phys. J. C **74**, 3180 (2014) [arXiv:1410.4691 [hep-ph]].

[123] M. Hoferichter, B.-L. Hoid, B. Kubis, S. Leupold, and S. P. Schneider, Phys. Rev. Lett. **121**, 112002 (2018) [arXiv:1805.01471 [hep-ph]].

[124] M. Hoferichter, B.-L. Hoid, B. Kubis, S. Leupold, and S. P. Schneider, JHEP **10**, 141 (2018) [arXiv:1808.04823 [hep-ph]].

[125] M. Hoferichter, B.-L. Hoid, and B. Kubis, JHEP **08**, 137 (2019) [arXiv:1907.01556 [hep-ph]].

[126] D. Schuh, Master's thesis, Bonn University (2023).

[127] M. Hoferichter, B.-L. Hoid, B. Kubis, and D. Schuh, JHEP **08**, 208 (2023) [arXiv:2307.02546 [hep-ph]].

[128] P. Adlarson *et al.* [WASA-at-COSY Collaboration], Phys. Lett. B **770**, 418–425 (2017) [arXiv:1610.02187 [nucl-ex]].

[129] M. Ablikim *et al.* [BESIII Collaboration], Phys. Rev. D **98**, 112007 (2018) [arXiv:1811.03817 [hep-ex]].

[130] A. Aloisio *et al.* [KLOE Collaboration], Phys. Lett. B **561**, 55–60 (2003) [arXiv:hep-ex/0303016], [Erratum: Phys. Lett. B **609**, 449 (2005)].

[131] R. R. Akhmetshin *et al.*, Phys. Lett. B **642**, 203–209 (2006).

[132] T. W. B. Kibble, Phys. Rev. **117**, 1159–1162 (1960).

[133] D. Schott [CLAS Collaboration], PoS **ConfinementX**, 106 (2012).

[134] C. Adolph *et al.* [COMPASS Collaboration], Phys. Lett. B **740**, 303–311 (2015) [arXiv:1408.4286 [hep-ex]], [Erratum: Phys. Lett. B **811**, 135913 (2020)].

[135] A. Rodas *et al.* [JPAC], Phys. Rev. Lett. **122**, 042002 (2019) [arXiv:1810.04171 [hep-ph]].

[136] M. Albrecht *et al.* [Crystal Barrel Collaboration], Eur. Phys. J. C **80**, 453 (2020) [arXiv:1909.07091 [hep-ex]].

[137] B. Kopf *et al.*, Eur. Phys. J. C **81**, 1056 (2021) [arXiv:2008.11566 [hep-ph]].

[138] M. Aghasyan *et al.* [COMPASS Collaboration], Phys. Rev. D **98**, 092003 (2018) [arXiv:1802.05913 [hep-ex]].

[139] S. Weinberg, Phys. Rev. Lett. **17**, 616–621 (1966).

[140] S. Gardner and J. Shi, Phys. Rev. D **101**, 115038 (2020) [arXiv:1903.11617 [hep-ph]].

[141] H. Akdag, PhD thesis, Bonn University (2023).

[142] R. L. Jaffe, K. Johnson, and Z. Ryzak, Annals Phys. **168**, 344–367 (1986).

[143] J. J. Dudek, Phys. Rev. D **84**, 074023 (2011) [arXiv:1106.5515 [hep-ph]].

[144] I. J. General, S. R. Cotanch, and F. J. Llanes-Estrada, Eur. Phys. J. C **51**, 347–358 (2007) [arXiv:hep-ph/0609115].

[145] M. Jacob and G. C. Wick, Annals Phys. **7**, 404–428 (1959).

[146] G. Colangelo, M. Hoferichter, and P. Stoffer, JHEP **02**, 006 (2019) [arXiv:1810.00007 [hep-ph]].

[147] S. Kullback and R. A. Leibler, Annals Math. Stat. **22**, 79–86 (1951).

[148] S. Ropertz, C. Hanhart, and B. Kubis, Eur. Phys. J. C **78**, 1000 (2018) [arXiv:1809.06867 [hep-ph]].

[149] M. Ablikim *et al.* [BESIII Collaboration], Phys. Lett. B **710**, 594–599 (2012) [arXiv:1202.2048 [hep-ex]].

[150] C. Adolph *et al.* [COMPASS Collaboration], Phys. Rev. Lett. **115**, 082001 (2015) [arXiv:1501.05732 [hep-ex]].

[151] M. Mikhasenko, B. Ketzer, and A. Sarantsev, Phys. Rev. D **91**, 094015 (2015) [arXiv:1501.07023 [hep-ph]].

[152] G. D. Alexeev *et al.* [COMPASS Collaboration], Phys. Rev. Lett. **127**, 082501 (2021) [arXiv:2006.05342 [hep-ph]].

[153] M. Albaladejo *et al.* [JPAC], Phys. Rev. D **101**, 054018 (2020) [arXiv:1910.03107 [hep-ph]].

[154] F. Niecknig, Diploma thesis, Bonn University (2011).

[155] R. H. Dalitz, Phil. Mag. Ser. 7 **44**, 1068–1080 (1953).

[156] E. Fabri, Nuovo Cim. **11**, 479–491 (1954).

[157] S. Weinberg, Phys. Rev. Lett. **4**, 87–89 (1960), [Erratum: Phys. Rev. Lett. **4**, 585 (1960)].

[158] G. F. Chew, Rev. Mod. Phys. **34**, 394–401 (1962).

[159] G. F. Chew, Science **161**, 762–765 (1968).

[160] G. F. Chew, Phys. Rev. D **4**, 2330–2335 (1971).

[161] L. Castillejo, R. H. Dalitz, and F. J. Dyson, Phys. Rev. **101**, 453–458 (1956).

[162] F. J. Dyson, Phys. Rev. **106**, 157–159 (1957).

[163] D. Atkinson and R. L. Warnock, Phys. Rev. **188**, 2098–2111 (1969).

[164] M. Gell-Mann, Phys. Rev. **125**, 1067–1084 (1962).

[165] M. Gell-Mann, Phys. Lett. **8**, 214–215 (1964).

[166] S. Scherer, Prog. Part. Nucl. Phys. **64**, 1–60 (2010) [arXiv:0908.3425 [hep-ph]].

[167] S. J. Brodsky, G. F. de Teramond, H. G. Dosch, and J. Erlich, Phys. Rept. **584**, 1–105 (2015) [arXiv:1407.8131 [hep-ph]].

[168] M. R. Shepherd, J. J. Dudek, and R. E. Mitchell, Nature **534**, 487–493 (2016) [arXiv:1802.08131 [hep-ph]].

[169] A. Esposito, A. Pilloni, and A. D. Polosa, Phys. Rept. **668**, 1–97 (2017) [arXiv:1611.07920 [hep-ph]].

[170] F.-K. Guo *et al.*, Rev. Mod. Phys. **90**, 015004 (2018) [arXiv:1705.00141 [hep-ph]], [Erratum: Rev. Mod. Phys. **94**, 029901 (2022)].

[171] R. A. Briceño, J. J. Dudek, and R. D. Young, Rev. Mod. Phys. **90**, 025001 (2018) [arXiv:1706.06223 [hep-lat]].

[172] F.-K. Guo, X.-H. Liu, and S. Sakai, Prog. Part. Nucl. Phys. **112**, 103757 (2020) [arXiv:1912.07030 [hep-ph]].

[173] M. Albaladejo *et al.* [JPAC], Prog. Part. Nucl. Phys. **127**, 103981 (2022) [arXiv:2112.13436 [hep-ph]].

[174] M. Mai, U.-G. Meißner, and C. Urbach, Phys. Rept. **1001**, 1–66 (2023) [arXiv:2206.01477 [hep-ph]].

[175] M. T. Hansen and S. R. Sharpe, Ann. Rev. Nucl. Part. Sci. **69**, 65–107 (2019) [arXiv:1901.00483 [hep-lat]].

[176] J. Gasser and H. Leutwyler, Annals Phys. **158**, 142–210 (1984).

[177] J. Gasser and H. Leutwyler, Nucl. Phys. B **250**, 465–516 (1985).

[178] G. Ecker, Prog. Part. Nucl. Phys. **35**, 1–80 (1995) [arXiv:hep-ph/9501357].

[179] V. Bernard, N. Kaiser, and U.-G. Meißner, Int. J. Mod. Phys. E **4**, 193–346 (1995) [arXiv:hep-ph/9501384].

[180] U.-G. Meißner, Phys. Rept. **161**, 213–361 (1988).

[181] M. Neubert, Phys. Rept. **245**, 259–396 (1994) [arXiv:hep-ph/9306320].

[182] J. R. Peláez, Phys. Rept. **658**, 1–111 (2016) [arXiv:1510.00653 [hep-ph]].

[183] M. Hoferichter, J. Ruiz de Elvira, B. Kubis, and U.-G. Meißner, Phys. Rept. **625**, 1–88 (2016) [arXiv:1510.06039 [hep-ph]].

[184] A. C. Irving and R. P. Worden, Phys. Rept. **34**, 117–231 (1977).

[185] V. Gribov, *Strong Interactions of Hadrons at High Energies: Gribov Lectures on Theoretical Physics*, Oxford University Press, 2009.

[186] R. Dolen, D. Horn, and C. Schmid, Phys. Rev. **166**, 1768–1781 (1968).

[187] F. Huang *et al.*, Eur. Phys. J. A **40**, 77–87 (2009) [arXiv:0810.2680 [hep-ph]].

[188] A. Sibirtsev, J. Haidenbauer, F. Huang, S. Krewald, and U.-G. Meißner, Eur. Phys. J. A **40**, 65–75 (2009) [arXiv:0903.0535 [hep-ph]].

[189] A. Sibirtsev, J. Haidenbauer, S. Krewald, U.-G. Meißner, and A. W. Thomas, Eur. Phys. J. A **41**, 71–84 (2009) [arXiv:0902.1819 [hep-ph]].

[190] J. Ruiz de Elvira, J. R. Peláez, M. R. Pennington, and D. J. Wilson, Phys. Rev. D **84**, 096006 (2011) [arXiv:1009.6204 [hep-ph]].

[191] J. T. Londergan, J. Nebreda, J. R. Peláez, and A. Szczepaniak, Phys. Lett. B **729**, 9–14 (2014) [arXiv:1311.7552 [hep-ph]].

[192] E. Del Giudice, P. Di Vecchia, and S. Fubini, Annals Phys. **70**, 378–398 (1972).

[193] R. Jengo, Phys. Lett. B **28**, 606–610 (1969).

[194] S. M. Roy, Phys. Lett. B **36**, 353–356 (1971).

[195] F. Steiner, Fortsch. Phys. **19**, 115–159 (1971).

[196] S. Mandelstam, Phys. Rev. **115**, 1741–1751 (1959).

[197] A. D. Martin and T. D. Spearman, *Elementary Particle Theory*, North-Holland Publishing Co., 1970.

[198] M. G. Donnelly and R. E. Kreps, Phys. Rev. D **6**, 2009–2014 (1972).

[199] J. C. Botke, Nucl. Phys. B **40**, 141–150 (1972).

[200] R. C. Brower, C. E. DeTar, and J. H. Weis, Phys. Rept. **14**, 257–367 (1974).

[201] T. Shimada, A. D. Martin, and A. C. Irving, Nucl. Phys. B **142**, 344–364 (1978).

[202] G. Montaña *et al.*, (2024) [arXiv:2407.19577 [hep-ph]].

[203] J. B. Bronzan and C. Kacser, Phys. Rev. **132**, 2703 (1963).

[204] I. J. R. Aitchison, (2015) [arXiv:1507.02697 [hep-ph]].

[205] A. V. Barnes *et al.*, Phys. Rev. Lett. **37**, 76–79 (1976).

[206] F. A. Cerulus and A. Martin, Phys. Lett. **8**, 80–82 (1964).

[207] R. W. Childers, Phys. Rev. Lett. **21**, 868–871 (1968).

[208] A. A. Trushevsky, Ukr. Fiz. Zh. (Ukr. Ed.) **22**, 353–362 (1977).

[209] A. Degasperis and E. Predazzi, Nuovo Cim. A **65**, 764–782 (1970).

[210] J. C. Botke and R. Blankenbecler, Phys. Rev. **186**, 1536–1539 (1969).

[211] A. V. Anisovich, V. V. Anisovich, and A. V. Sarantsev, Phys. Rev. D **62**, 051502 (2000) [arXiv:hep-ph/0003113].

[212] A. P. Szczepaniak and M. R. Pennington, Phys. Lett. B **737**, 283–288 (2014) [arXiv:1403.5782 [hep-ph]].

[213] J. A. Silva-Castro *et al.* [JPAC], Phys. Rev. D **99**, 034003 (2019) [arXiv:1809.01954 [hep-ph]].

[214] M. L. Paciello, L. Sertorio, and B. Taglienti, Nuovo Cim. A **63**, 1026–1034 (1969).

[215] L. van Hove, Phys. Lett. **24**, 183–184 (1967).

[216] R. W. Childers, Phys. Rev. Lett. **23**, 357–360 (1969).

[217] M. Gell-Mann, M. Goldberger, and F. Low, Rev. Mod. Phys. **36**, 640–649 (1964).

[218] S. Donnachie, H. G. Dosch, O. Nachtmann, and P. Landshoff, *Pomeron physics and QCD*, Cambridge University Press, 12, 2004.

[219] V. Mathieu, N. Kochelev, and V. Vento, Int. J. Mod. Phys. E **18**, 1–49 (2009) [arXiv:0810.4453 [hep-ph]].

[220] W. Ochs, J. Phys. G **40**, 043001 (2013) [arXiv:1301.5183 [hep-ph]].

[221] I. Szanyi, L. Jenkovszky, R. Schicker, and V. Svintozelskyi, Nucl. Phys. A **998**, 121728 (2020) [arXiv:1910.02494 [hep-ph]].

[222] F. J. Llanes-Estrada, Eur. Phys. J. ST **230**, 1575–1592 (2021) [arXiv:2101.05366 [hep-ph]].

[223] P. G. O. Freund, Phys. Rev. Lett. **20**, 235–237 (1968).

[224] H. Harari, Phys. Rev. Lett. **20**, 1395–1398 (1968).

[225] R. C. Badatya and P. K. Patnaik, Phys. Rev. D **29**, 2582–2588 (1984).

[226] S. Mandelstam, Phys. Rev. **166**, 1539–1552 (1968).

[227] G. Epstein, Phys. Rev. **166**, 1633–1637 (1968).

[228] S.-Y. Chu, G. Epstein, P. Kaus, R. C. Slansky, and F. Zachariasen, Phys. Rev. **175**, 2098–2105 (1968).

[229] D. Atkinson and K. Dietz, Phys. Rev. **177**, 2579–2581 (1969).

[230] R. Fiore, L. L. Jenkovszky, V. Magas, F. Paccanoni, and A. Papa, Eur. Phys. J. A **10**, 217–221 (2001) [arXiv:hep-ph/0011035].

[231] K. Quirion *et al.* [JPAC], (2024) [arXiv:2405.09517 [hep-ph]].

[232] P. D. B. Collins, R. C. Johnson, and E. J. Squires, Phys. Lett. B **26**, 223–225 (1968).

[233] J. R. Peláez and F. J. Ynduráin, Phys. Rev. D **69**, 114001 (2004) [arXiv:hep-ph/0312187].

[234] F. Halzen, K. Igi, M. Ishida, and C. S. Kim, Phys. Rev. D **85**, 074020 (2012) [arXiv:1110.1479 [hep-ph]].

[235] M. M. Brisudova, L. Burakovsky, and J. T. Goldman, Phys. Lett. B **460**, 1–7 (1999) [arXiv:hep-ph/9810296].

[236] A. V. Kholodkov, F. Paccanoni, S. S. Stepanov, and R. S. Tutik, J. Phys. G **18**, 985–992 (1992).

[237] P. Desgrolard, M. Giffon, E. Martynov, and E. Predazzi, Eur. Phys. J. C **18**, 555–561 (2001) [arXiv:hep-ph/0006244].

[238] G. F. Chew and S. Mandelstam, Phys. Rev. **119**, 467–477 (1960).

[239] G. F. Chew, S. C. Frautschi, and S. Mandelstam, Phys. Rev. **126**, 1202–1208 (1961).

[240] R. García-Martín, R. Kamiński, J. R. Peláez, and J. Ruiz de Elvira, Phys. Rev. Lett. **107**, 072001 (2011) [arXiv:1107.1635 [hep-ph]].

[241] M. Hoferichter, J. Ruiz de Elvira, B. Kubis, and U.-G. Meißner, Phys. Lett. B **853**, 138698 (2024) [arXiv:2312.15015 [hep-ph]].

[242] L. A. Heuser *et al.*, Eur. Phys. J. C **84**, 599 (2024) [arXiv:2403.15539 [hep-ph]].

[243] H. J. Lipkin, Nucl. Phys. B **9**, 349–363 (1969).

[244] S. L. Adler, Phys. Rev. **137**, B1022–B1033 (1965).

[245] S. L. Adler, Phys. Rev. **139**, B1638–B1643 (1965).

[246] K. Huang, Phys. Rev. Lett. **23**, 903–906 (1969).

[247] D. Y. Wong, Phys. Rev. **181**, 1900–1901 (1969).

[248] I. Danilkin, V. Biloshytskyi, X.-L. Ren, and M. Vanderhaeghen, Phys. Rev. D **107**, 074021 (2023) [arXiv:2206.15223 [hep-ph]].

[249] S. Mandelstam, Comments Nucl. Part. Phys. **3**, 65–72 (1969).

[250] I. Danilkin, O. Deineka, and M. Vanderhaeghen, Phys. Rev. D **103**, 114023 (2021) [arXiv:2012.11636 [hep-ph]].

[251] M. Albaladejo and J. A. Oller, Phys. Rev. D **86**, 034003 (2012) [arXiv:1205.6606 [hep-ph]].

[252] A. Rodas, J. J. Dudek, and R. G. Edwards [Hadron Spectrum Collaboration], Phys. Rev. D **109**, 034513 (2024) [arXiv:2304.03762 [hep-lat]].

[253] Z. Xiao and H. Q. Zheng, Nucl. Phys. A **695**, 273–294 (2001) [arXiv:hep-ph/0011260].

[254] I. Caprini, Phys. Rev. D **77**, 114019 (2008) [arXiv:0804.3504 [hep-ph]].

[255] J. R. Peláez, A. Rodas, and J. Ruiz de Elvira, Eur. Phys. J. ST **230**, 1539–1574 (2021) [arXiv:2101.06506 [hep-ph]].

[256] H. Bateman, *Higher Transcendental Functions, Volume I*, McGraw–Hill Book Company, 1953.

[257] R. Blankenbecler, S. J. Brodsky, J. F. Gunion, and R. Savit, Phys. Rev. D **8**, 4117 (1973).

[258] D. D. Coon, J. F. Gunion, J. Tran Thanh Van, and R. Blankenbecler, Phys. Rev. D **18**, 1451 (1978).

[259] S. J. Brodsky and G. R. Farrar, Phys. Rev. Lett. **31**, 1153–1156 (1973).

[260] S. J. Brodsky and G. R. Farrar, Phys. Rev. D **11**, 1309 (1975).

[261] V. A. Matveev, R. M. Muradian, and A. N. Tavkhelidze, Lett. Nuovo Cim. **7**, 719–723 (1973).

[262] M. G. Schmidt, Phys. Lett. B **43**, 417–421 (1973).

[263] A. I. Bugrii, Z. E. Chikovani, L. L. Jenkovszky, and M. Z. Maksimov, Z. Phys. C **4**, 45–52 (1980).

[264] R. Fiore, L. L. Jenkovszky, V. K. Magas, and F. Paccanoni, Phys. Rev. D **60**, 116003 (1999) [arXiv:hep-ph/9904202].

[265] P. D. B. Collins and P. J. Kearney, Z. Phys. C **22**, 277–288 (1984).

[266] G. F. Chew and A. Pignotti, Phys. Rev. Lett. **20**, 1078–1081 (1968).

[267] C. Schmid, Phys. Rev. Lett. **20**, 689–691 (1968).

[268] V. A. Alessandrini, D. Amati, and E. J. Squires, Phys. Lett. B **27**, 463–465 (1968).

[269] V. Barger and L. Durand, Phys. Lett. B **26**, 588–590 (1968).

[270] V. Alessandrini and D. Amati, Phys. Lett. B **29**, 193–197 (1969).

[271] B. H. Kellett, Nucl. Phys. B **18**, 173–181 (1970).

[272] D. B. Lichtenberg, R. G. Newton, and E. Predazzi, Phys. Rev. Lett. **22**, 1215–1217 (1969).

[273] G. Venturi and W. J. Zakrzewski, Nuovo Cim. A **69**, 431–443 (1970).

[274] G. Cohen-Tannoudji, F. Henyey, G. L. Kane, and W. J. Zakrzewski, Phys. Rev. Lett. **26**, 112–115 (1971).

[275] A. I. Bugrij, L. L. Jenkovszky, and N. A. Kobylinsky, Lett. Nuovo Cim. **5S2**, 393–397 (1972).

[276] M. Suzuki, Phys. Rev. Lett. **23**, 205–208 (1969).

[277] L. Schlessinger, Phys. Rev. **167**, 1411 (1968).

[278] R.-A. Tripolt, I. Haritan, J. Wambach, and N. Moiseyev, Phys. Lett. B **774**, 411–416 (2017) [arXiv:1610.03252 [hep-ph]].

[279] D. Binosi and R.-A. Tripolt, Phys. Lett. B **801**, 135171 (2020) [arXiv:1904.08172 [hep-ph]].

[280] D. Binosi, A. Pilloni, and R.-A. Tripolt, Phys. Lett. B **839**, 137809 (2023) [arXiv:2205.02690 [hep-ph]].

[281] J. R. Peláez, A. Rodas, and J. Ruiz de Elvira, Phys. Rev. Lett. **130**, 051902 (2023) [arXiv:2206.14822 [hep-ph]], [Erratum: Phys. Rev. Lett. **132**, 239901 (2024)].

[282] F. J. Ynduráin, R. García-Martín, and J. R. Peláez, Phys. Rev. D **76**, 074034 (2007) [arXiv:hep-ph/0701025].

[283] A. Švarc *et al.*, Phys. Rev. C **88**, 035206 (2013) [arXiv:1307.4613 [hep-ph]].

[284] A. Švarc *et al.*, Phys. Rev. C **89**, 065208 (2014) [arXiv:1404.1544 [nucl-th]].

[285] A. Švarc, M. Hadžimehmedović, H. Osmanović, J. Stahov, and R. L. Workman, Phys. Rev. C **91**, 015207 (2015) [arXiv:1405.6474 [nucl-th]].

[286] P. Masjuan and J. J. Sanz-Cillero, Eur. Phys. J. C **73**, 2594 (2013) [arXiv:1306.6308 [hep-ph]].

[287] P. Masjuan, J. Ruiz de Elvira, and J. J. Sanz-Cillero, Phys. Rev. D **90**, 097901 (2014) [arXiv:1410.2397 [hep-ph]].

[288] I. Caprini, P. Masjuan, J. Ruiz de Elvira, and J. J. Sanz-Cillero, Phys. Rev. D **93**, 076004 (2016) [arXiv:1602.02062 [hep-ph]].

[289] J. R. Peláez, A. Rodas, and J. Ruiz de Elvira, Eur. Phys. J. C **77**, 91 (2017) [arXiv:1612.07966 [hep-ph]].

[290] J. L. Basdevant, Fortsch. Phys. **20**, 283–331 (1972).

[291] D. L. Hunter and G. A. Baker, Phys. Rev. B **7**, 3346–3376 (1973).

[292] K. D. Jordan, Int. J. Quantum Chem. **9**, 325–336 (1975).

[293] M. Dax, Master's thesis, Bonn University (2020).

[294] D. Stamen, Master's thesis, Bonn University (2020).

[295] D. Ecker, Nuovo Cim. C **47**, 217 (2024) [arXiv:2310.09138 [hep-ph]].

[296] J. M. Friedrich. Private communication, 2023.

[297] M. Amaryan *et al.* [KLF Collaboration], (2020) [arXiv:2008.08215 [nucl-ex]].

[298] B. Bacho, Bachelor's thesis, Bonn University (2021).

[299] J. Wess and B. Zumino, Phys. Lett. B **37**, 95–97 (1971).

[300] E. Witten, Nucl. Phys. B **223**, 422–432 (1983).

[301] J. Bijnens, A. Bramon, and F. Cornet, Phys. Lett. B **237**, 488–494 (1990).

[302] S. L. Adler, B. W. Lee, S. B. Treiman, and A. Zee, Phys. Rev. D **4**, 3497–3501 (1971).

[303] M. V. Terent'ev, Phys. Lett. B **38**, 419–422 (1972).

[304] R. Aviv and A. Zee, Phys. Rev. D **5**, 2372 (1972).

[305] H. Primakoff, Phys. Rev. **81**, 899 (1951).

[306] Y. M. Antipov *et al.*, Phys. Rev. D **36**, 21 (1987).

[307] J. A. Seyfried, Master's thesis, TU München (2017).

[308] A. Halprin, C. M. Andersen, and H. Primakoff, Phys. Rev. **152**, 1295–1303 (1966).

[309] C. Bemporad *et al.*, Nucl. Phys. B **51**, 1–15 (1973).

[310] W. C. Carithers, P. Mühlemann, D. Underwood, and D. G. Ryan, Phys. Rev. Lett. **35**, 349–352 (1975).

[311] D. Berg *et al.*, Phys. Lett. B **98**, 119–122 (1981).

[312] S. Cihangir *et al.* [Fermilab–Minnesota–Rochester Collaboration], Phys. Lett. B **117**, 123–125 (1982).

[313] C. Chandlee *et al.*, Phys. Rev. Lett. **51**, 168–171 (1983).

[314] D. Carlsmith *et al.*, Phys. Rev. Lett. **56**, 18–21 (1986).

[315] A. Alavi-Harati *et al.* [KTeV Collaboration], Phys. Rev. Lett. **89**, 072001 (2002) [arXiv:hep-ex/0110016].

[316] V. S. Burtovoy, Phys. Atom. Nucl. **78**, 1470–1473 (2015).

[317] V. S. Burtovoy, Phys. Part. Nucl. **48**, 932–934 (2017).

[318] P. Abbon *et al.* [COMPASS Collaboration], Nucl. Instrum. Meth. A **779**, 69–115 (2015) [arXiv:1410.1797 [physics.ins-det]].

[319] B. Adams *et al.*, (2018) [arXiv:1808.00848 [hep-ex]].

[320] J. Bernhard *et al.*, AIP Conf. Proc. **2249**, 030035 (2020) [arXiv:1911.01498 [hep-ex]].

[321] R. A. Briceño *et al.*, Phys. Rev. Lett. **115**, 242001 (2015) [arXiv:1507.06622 [hep-ph]].

[322] R. A. Briceño *et al.*, Phys. Rev. D **93**, 114508 (2016) [arXiv:1604.03530 [hep-ph]].

[323] C. Alexandrou *et al.*, Phys. Rev. D **98**, 074502 (2018) [arXiv:1807.08357 [hep-lat]].

[324] G. Colangelo, M. Hoferichter, B. Kubis, M. Procura, and P. Stoffer, Phys. Lett. B **738**, 6–12 (2014) [arXiv:1408.2517 [hep-ph]].

[325] T. Aoyama *et al.*, Phys. Rept. **887**, 1–166 (2020) [arXiv:2006.04822 [hep-ph]].

[326] D. M. Berg, PhD thesis, Rochester University (1983).

[327] R. García-Martín and B. Moussallam, Eur. Phys. J. C **70**, 155–175 (2010) [arXiv:1006.5373 [hep-ph]].

[328] I. Danilkin, O. Deineka, and M. Vanderhaeghen, Phys. Rev. D **101**, 054008 (2020) [arXiv:1909.04158 [hep-ph]].

[329] I. Danilkin, O. Deineka, and M. Vanderhaeghen, Phys. Rev. D **96**, 114018 (2017) [arXiv:1709.08595 [hep-ph]].

[330] J. Lu and B. Moussallam, Eur. Phys. J. C **80**, 436 (2020) [arXiv:2002.04441 [hep-ph]].

[331] F. Guerrero and J. Prades, Phys. Lett. B **405**, 341–346 (1997) [arXiv:hep-ph/9702303].

[332] M. Moinester [COMPASS Collaboration], Czech. J. Phys. **53**, B169–B187 (2003) [arXiv:hep-ex/0301024].

[333] M. I. Vysotsky and E. V. Zhemchugov, Phys. Rev. D **93**, 094029 (2016) [arXiv:1512.04438 [hep-ph]], [Erratum: Phys. Rev. D **94**, 019901 (2016)].

[334] T. Ebertshäuser, PhD thesis, Mainz University (2002).

[335] C. Hacker, PhD thesis, Mainz University (2008).

[336] P. Büttiker, S. Descotes-Genon, and B. Moussallam, Eur. Phys. J. C **33**, 409–432 (2004) [arXiv:hep-ph/0310283].

[337] J. R. Peláez and A. Rodas, Phys. Rept. **969**, 1–126 (2022) [arXiv:2010.11222 [hep-ph]].

[338] A. Radhakrishnan, J. J. Dudek, and R. G. Edwards [Hadron Spectrum Collaboration], Phys. Rev. D **106**, 114513 (2022) [arXiv:2208.13755 [hep-lat]].

[339] G. F. Chew, M. L. Goldberger, F. E. Low, and Y. Nambu, Phys. Rev. **106**, 1345–1355 (1957).

[340] O. Hanstein, D. Drechsel, and L. Tiator, Nucl. Phys. A **632**, 561–606 (1998) [arXiv:nucl-th/9709067].

[341] M. Hoferichter, D. R. Phillips, and C. Schat, Eur. Phys. J. C **71**, 1743 (2011) [arXiv:1106.4147 [hep-ph]].

[342] B. Kubis and J. Plenter, Eur. Phys. J. C **75**, 283 (2015) [arXiv:1504.02588 [hep-ph]].

[343] F. Klingl, N. Kaiser, and W. Weise, Z. Phys. A **356**, 193–206 (1996) [arXiv:hep-ph/9607431].

[344] K. I. Beloborodov, V. P. Druzhinin, and S. I. Serednyakov, J. Exp. Theor. Phys. **129**, 386–390 (2019).

[345] J. R. Peláez and A. Rodas, Eur. Phys. J. C **78**, 897 (2018) [arXiv:1807.04543 [hep-ph]].

[346] G. Ecker and C. Zauner, Eur. Phys. J. C **52**, 315–323 (2007) [arXiv:0705.0624 [hep-ph]].

[347] P. A. Zyla *et al.* [Particle Data Group], PTEP **2020**, 083C01 (2020).

[348] C. Adolph *et al.* [COMPASS Collaboration], Eur. Phys. J. A **50**, 79 (2014) [arXiv:1403.2644 [hep-ex]].

[349] J. L. Dammann, Master's thesis, Bonn University (2023).

[350] C. Adolph *et al.* [COMPASS Collaboration], Phys. Rev. Lett. **114**, 062002 (2015) [arXiv:1405.6377 [hep-ex]].

[351] D. Stamen, Zenodo (2024).

[352] B. R. Holstein and S. Scherer, Ann. Rev. Nucl. Part. Sci. **64**, 51–81 (2014) [arXiv:1401.0140 [hep-ph]].

[353] Y. M. Antipov *et al.*, Phys. Lett. B **121**, 445–448 (1983).

[354] Y. M. Antipov *et al.*, Z. Phys. C **26**, 495–497 (1985).

[355] T. A. Aibergenov *et al.*, Czech. J. Phys. B **36**, 948–951 (1986).

[356] J. Ahrens *et al.*, Eur. Phys. J. A **23**, 113–127 (2005) [arXiv:nucl-ex/0407011].

[357] C. Berger *et al.* [PLUTO Collaboration], Z. Phys. C **26**, 199–207 (1984).

[358] A. Courau *et al.*, Nucl. Phys. B **271**, 1–20 (1986).

[359] J. Boyer *et al.*, Phys. Rev. D **42**, 1350–1367 (1990).

[360] H. J. Behrend *et al.* [CELLO Collaboration], Z. Phys. C **56**, 381–390 (1992).

[361] T. Mori *et al.* [Belle Collaboration], J. Phys. Soc. Jap. **76**, 074102 (2007) [arXiv:0704.3538 [hep-ex]].

[362] J. Bijnens and F. Cornet, Nucl. Phys. B **296**, 557–568 (1988).

[363] S. Bellucci, J. Gasser, and M. E. Sainio, Nucl. Phys. B **423**, 80–122 (1994) [arXiv:hep-ph/9401206], [Erratum: Nucl. Phys. B **431**, 413 (1994)].

[364] U. Bürgi, Phys. Lett. B **377**, 147–152 (1996) [arXiv:hep-ph/9602421].

[365] U. Bürgi, Nucl. Phys. B **479**, 392–426 (1996) [arXiv:hep-ph/9602429].

[366] J. Gasser, M. A. Ivanov, and M. E. Sainio, Nucl. Phys. B **728**, 31–54 (2005) [arXiv:hep-ph/0506265].

[367] J. Gasser, M. A. Ivanov, and M. E. Sainio, Nucl. Phys. B **745**, 84–108 (2006) [arXiv:hep-ph/0602234].

[368] M. Moinester and S. Scherer, Int. J. Mod. Phys. A **34**, 1930008 (2019) [arXiv:1905.05640 [hep-ph]].

[369] B. Pasquini, D. Drechsel, and S. Scherer, Phys. Rev. C **77**, 065211 (2008) [arXiv:0805.0213 [hep-ph]].

[370] V. Ermolina, I. Danilkin, and M. Vanderhaeghen, EPJ Web Conf. **303**, 01007 (2024) [arXiv:2407.21471 [hep-ph]].

[371] H. Albrecht *et al.* [ARGUS Collaboration], Z. Phys. C **48**, 183–190 (1990).

[372] S. Uehara *et al.* [Belle Collaboration], PTEP **2013**, 123C01 (2013) [arXiv:1307.7457 [hep-ex]].

[373] W. A. Bardeen and W. K. Tung, Phys. Rev. **173**, 1423–1433 (1968), [Erratum: Phys. Rev. D **4**, 3229 (1971)].

[374] R. Tarrach, Nuovo Cim. A **28**, 409 (1975).

[375] R. García-Martín and B. Moussallam, Eur. Phys. J. C **70**, 155–175 (2010) [arXiv:1006.5373 [hep-ph]].

[376] A. R. Edmonds, *Angular momentum in quantum mechanics*, Princeton University Press, 1960.

[377] N. Kaiser and J. M. Friedrich, Nucl. Phys. A **812**, 186–200 (2008) [arXiv:0806.2614 [nucl-th]].

[378] N. Kaiser and J. M. Friedrich, Eur. Phys. J. A **36**, 181–188 (2008) [arXiv:0803.0995 [nucl-th]].

[379] I. Guiasu and E. E. Radescu, Annals Phys. **120**, 145–174 (1979).

[380] D. Drechsel and L. V. Filkov, Z. Phys. A **349**, 177–184 (1994).

[381] J. Bijnens, A. Fayyazuddin, and J. Prades, Phys. Lett. B **379**, 209–218 (1996) [arXiv:hep-ph/9512374].

[382] J. Bijnens and J. Prades, Nucl. Phys. B **490**, 239–271 (1997) [arXiv:hep-ph/9610360].

[383] J. F. Donoghue and B. R. Holstein, Phys. Rev. D **40**, 3700 (1989).

[384] H. Schäfer, M. Zanke, Y. Korte, and B. Kubis, Phys. Rev. D **108**, 074025 (2023) [arXiv:2307.10357 [hep-ph]].

[385] L. Ametller, J. Bijnens, A. Bramon, and F. Cornet, Phys. Lett. B **276**, 185–190 (1992).

[386] M. Jetter, Nucl. Phys. B **459**, 283–310 (1996) [arXiv:hep-ph/9508407].

[387] L. Gan, B. Kubis, E. Passemar, and S. Tulin, Phys. Rept. **945**, 1–105 (2022) [arXiv:2007.00664 [hep-ph]].

[388] Y. Korte and B. Kubis. In preparation, 2024.

[389] L.-Y. Dai and M. R. Pennington, Phys. Rev. D **90**, 036004 (2014) [arXiv:1404.7524 [hep-ph]].

[390] J. T. Daub, C. Hanhart, and B. Kubis, JHEP **02**, 009 (2016) [arXiv:1508.06841 [hep-ph]].

[391] G. Ecker, J. Gasser, A. Pich, and E. de Rafael, Nucl. Phys. B **321**, 311–342 (1989).

[392] L. Roca, J. E. Palomar, and E. Oset, Phys. Rev. D **70**, 094006 (2004) [arXiv:hep-ph/0306188].

[393] H. J. Lipkin, Phys. Lett. B **72**, 249–250 (1977).

[394] M. Zielinski *et al.*, Phys. Rev. Lett. **52**, 1195 (1984).

[395] G. T. Condo *et al.*, Phys. Rev. D **48**, 3045–3047 (1993).

[396] M. Nozar *et al.* [CLAS Collaboration], Phys. Rev. Lett. **102**, 102002 (2009) [arXiv:0805.4438 [hep-ex]].

[397] C. Adolph *et al.* [COMPASS Collaboration], Eur. Phys. J. A **50**, 79 (2014) [arXiv:1403.2644 [hep-ex]].

[398] J. M. Friedrich and D. Ecker. Private communication, 2024.

[399] D. Hariharan, Master's thesis, Bonn University (2021).

[400] B. Aubert *et al.* [BaBar Collaboration], Phys. Rev. Lett. **103**, 231801 (2009) [arXiv:0908.3589 [hep-ex]].

[401] G. D'Agostini, Nucl. Instrum. Meth. A **346**, 306–311 (1994).

[402] J. F. De Trocóniz and F. J. Ynduráin, Phys. Rev. D **65**, 093001 (2002) [arXiv:hep-ph/0106025].

[403] H. Leutwyler, (2002) [arXiv:hep-ph/0212324].

[404] G. Colangelo, Nucl. Phys. B Proc. Suppl. **131**, 185–191 (2004) [arXiv:hep-ph/0312017].

[405] J. F. de Trocóniz and F. J. Ynduráin, Phys. Rev. D **71**, 073008 (2005) [arXiv:hep-ph/0402285].

[406] B. Ananthanarayan, I. Caprini, D. Das, and I. Sentitemsu Imsong, Phys. Rev. D **89**, 036007 (2014) [arXiv:1312.5849 [hep-ph]].

[407] B. Ananthanarayan, I. Caprini, D. Das, and I. Sentitemsu Imsong, Phys. Rev. D **93**, 116007 (2016) [arXiv:1605.00202 [hep-ph]].

[408] M. Hoferichter, B. Kubis, J. Ruiz de Elvira, H.-W. Hammer, and U.-G. Meißner, Eur. Phys. J. A **52**, 331 (2016) [arXiv:1609.06722 [hep-ph]].

[409] C. Hanhart *et al.*, Eur. Phys. J. C **77**, 98 (2017) [arXiv:1611.09359 [hep-ph]], [Erratum: Eur. Phys. J. C **78**, 450 (2018)].

[410] B. Ananthanarayan, I. Caprini, and D. Das, Phys. Rev. D **98**, 114015 (2018) [arXiv:1810.09265 [hep-ph]].

[411] M. Davier, A. Hoecker, B. Malaescu, and Z. Zhang, Eur. Phys. J. C **80**, 241 (2020) [arXiv:1908.00921 [hep-ph]], [Erratum: Eur. Phys. J. C **80**, 410 (2020)].

[412] S. Blatnik, J. Stahov, and C. B. Lang, Lett. Nuovo Cim. **24**, 39–44 (1979).

[413] J. P. Lees *et al.* [BaBar Collaboration], Phys. Rev. D **98**, 032010 (2018) [arXiv:1806.10280 [hep-ex]].

[414] M. N. Achasov *et al.*, Phys. Rev. D **63**, 072002 (2001) [arXiv:hep-ex/0009036].

[415] R. R. Akhmetshin *et al.* [CMD-2 Collaboration], Phys. Lett. B **669**, 217–222 (2008) [arXiv:0804.0178 [hep-ex]].

[416] J. P. Lees *et al.* [BaBar Collaboration], Phys. Rev. D **88**, 032013 (2013) [arXiv:1306.3600 [hep-ex]].

[417] E. A. Kozyrev *et al.*, Phys. Lett. B **779**, 64–71 (2018) [arXiv:1710.02989 [hep-ex]].

[418] R. R. Akhmetshin *et al.* [CMD-2 Collaboration], Phys. Lett. B **578**, 285–289 (2004) [arXiv:hep-ex/0308008].

[419] E. A. Kozyrev *et al.* [CMD-3 Collaboration], Phys. Lett. B **760**, 314–319 (2016) [arXiv:1604.02981 [hep-ex]].

[420] E. B. Dally *et al.*, Phys. Rev. Lett. **45**, 232–235 (1980).

[421] S. R. Amendolia *et al.*, Phys. Lett. B **178**, 435–440 (1986).

[422] J. P. Lees *et al.* [BaBar Collaboration], Phys. Rev. D **89**, 092002 (2014) [arXiv:1403.7593 [hep-ex]].

[423] B.-L. Hoid, M. Hoferichter, and B. Kubis, Eur. Phys. J. C **80**, 988 (2020) [arXiv:2007.12696 [hep-ph]].

[424] A. Lai *et al.* [NA48 Collaboration], Eur. Phys. J. C **30**, 33–49 (2003).

[425] E. Abouzaid *et al.* [KTeV Collaboration], Phys. Rev. Lett. **96**, 101801 (2006) [arXiv:hep-ex/0508010].

[426] H. Foeth *et al.*, Phys. Lett. B **30**, 276–281 (1969).

[427] F. Dydak *et al.*, Nucl. Phys. B **102**, 253–274 (1976).

[428] W. R. Molzon *et al.*, Phys. Rev. Lett. **41**, 1213–1216 (1978), [Errata: Phys. Rev. Lett. **41**, 1523 (1978); 1835 (1978)].

[429] W. N. Cottingham, Annals Phys. **25**, 424–432 (1963).

[430] R. F. Dashen, Phys. Rev. **183**, 1245–1260 (1969).

[431] G. Eichmann, C. S. Fischer, and R. Williams, Phys. Rev. D **101**, 054015 (2020) [arXiv:1910.06795 [hep-ph]].

[432] A. Miramontes, A. Bashir, K. Raya, and P. Roig, Phys. Rev. D **105**, 074013 (2022) [arXiv:2112.13916 [hep-ph]].

[433] M. Davier, A. Hoecker, B. Malaescu, and Z. Zhang, Eur. Phys. J. C **77**, 827 (2017) [arXiv:1706.09436 [hep-ph]].

[434] A. Keshavarzi, D. Nomura, and T. Teubner, Phys. Rev. D **97**, 114025 (2018) [arXiv:1802.02995 [hep-ph]].

[435] A. Keshavarzi, D. Nomura, and T. Teubner, Phys. Rev. D **101**, 014029 (2020) [arXiv:1911.00367 [hep-ph]].

[436] C. Hanhart, Phys. Lett. B **715**, 170–177 (2012) [arXiv:1203.6839 [hep-ph]].

[437] M. Zanke, M. Hoferichter, and B. Kubis, JHEP **07**, 106 (2021) [arXiv:2103.09829 [hep-ph]].

[438] S. P. Schneider, B. Kubis, and F. Niecknig, Phys. Rev. D **86**, 054013 (2012) [arXiv:1206.3098 [hep-ph]].

[439] V. L. Chernyak and A. R. Zhitnitsky, JETP Lett. **25**, 510 (1977), [Zh. Eksp. Teor. Fiz. **25**, 544 (1977)].

[440] V. L. Chernyak and A. R. Zhitnitsky, Sov. J. Nucl. Phys. **31**, 544–552 (1980), [Yad. Fiz. **31**, 1053 (1980)].

[441] A. V. Efremov and A. V. Radyushkin, Theor. Math. Phys. **42**, 97–110 (1980), [Teor. Mat. Fiz. **42**, 147 (1980)].

[442] A. V. Efremov and A. V. Radyushkin, Phys. Lett. B **94**, 245–250 (1980).

[443] G. R. Farrar and D. R. Jackson, Phys. Rev. Lett. **43**, 246–249 (1979).

[444] G. P. Lepage and S. J. Brodsky, Phys. Lett. B **87**, 359–365 (1979).

[445] G. P. Lepage and S. J. Brodsky, Phys. Rev. D **22**, 2157 (1980).

[446] S. Gonzàlez-Solís and P. Roig, Eur. Phys. J. C **79**, 436 (2019) [arXiv:1902.02273 [hep-ph]].

[447] A. Hoefer, J. Gluza, and F. Jegerlehner, Eur. Phys. J. C **24**, 51–69 (2002) [arXiv:hep-ph/0107154].

[448] J. Gluza, A. Hoefer, S. Jadach, and F. Jegerlehner, Eur. Phys. J. C **28**, 261–278 (2003) [arXiv:hep-ph/0212386].

[449] H. Czyż, A. Grzelińska, J. H. Kühn, and G. Rodrigo, Eur. Phys. J. C **39**, 411–420 (2005) [arXiv:hep-ph/0404078].

[450] Y. M. Bystritskiy, E. A. Kuraev, G. V. Fedotovich, and F. V. Ignatov, Phys. Rev. D **72**, 114019 (2005) [arXiv:hep-ph/0505236].

[451] A. Sommerfeld, *Atombau und Spektrallinien*, F. Vieweg & Sohn, 1921.

[452] G. Gamow, Z. Phys. **51**, 204–212 (1928).

[453] A. D. Sakharov, Zh. Eksp. Teor. Fiz. **18**, 631–635 (1948).

[454] S. Eidelman, F. Ignatov, and E. Kozyrev. Private communication, 2017. As quoted in Ref. [434].

[455] M. N. Achasov *et al.* [SND Collaboration], Phys. Rev. D **110**, 072001 (2024) [arXiv:2407.15140 [hep-ex]].

[456] S. Eidelman and F. Ignatov. Private communication, 2017. As quoted in Ref. [434].

[457] R. D. Ball *et al.* [NNPDF Collaboration], JHEP **05**, 075 (2010) [arXiv:0912.2276 [hep-ph]].

[458] A. Bramon, R. Escribano, J. L. Lucio M., and G. Pancheri, Phys. Lett. B **486**, 406–413 (2000) [arXiv:hep-ph/0003273].

[459] F. V. Flores-Baéz and G. López Castro, Phys. Rev. D **78**, 077301 (2008) [arXiv:0810.4349 [hep-ph]].

[460] M. Benayoun, P. David, L. DelBuono, and F. Jegerlehner, Eur. Phys. J. C **72**, 1848 (2012) [arXiv:1106.1315 [hep-ph]].

[461] J. Gasser and H. Leutwyler, Nucl. Phys. B **250**, 517–538 (1985).

[462] J. Bijnens and P. Talavera, JHEP **03**, 046 (2002) [arXiv:hep-ph/0203049].

[463] H. Leutwyler, Phys. Lett. B **378**, 313–318 (1996) [arXiv:hep-ph/9602366].

[464] J. Bijnens, Phys. Lett. B **306**, 343–349 (1993) [arXiv:hep-ph/9302217].

[465] J. F. Donoghue, B. R. Holstein, and D. Wyler, Phys. Rev. D **47**, 2089–2097 (1993).

[466] R. Baur and R. Urech, Phys. Rev. D **53**, 6552–6557 (1996) [arXiv:hep-ph/9508393].

[467] B. Ananthanarayan and B. Moussallam, JHEP **06**, 047 (2004) [arXiv:hep-ph/0405206].

[468] Y. Aoki *et al.* [Flavour Lattice Averaging Group (FLAG)], Eur. Phys. J. C **82**, 869 (2022) [arXiv:2111.09849 [hep-lat]].

[469] S. Borsanyi *et al.*, Science **347**, 1452–1455 (2015) [arXiv:1406.4088 [hep-lat]].

[470] D. Giusti *et al.*, Phys. Rev. D **95**, 114504 (2017) [arXiv:1704.06561 [hep-lat]].

[471] S. Basak *et al.* [MILC Collaboration], Phys. Rev. D **99**, 034503 (2019) [arXiv:1807.05556 [hep-lat]].

[472] Z. Fodor *et al.*, Phys. Rev. Lett. **117**, 082001 (2016) [arXiv:1604.07112 [hep-lat]].

[473] H. Harari, Phys. Rev. Lett. **17**, 1303–1306 (1966).

[474] J. Gasser and H. Leutwyler, Nucl. Phys. B **94**, 269–310 (1975).

[475] J. Gasser and H. Leutwyler, Phys. Rept. **87**, 77–169 (1982).

[476] A. Walker-Loud, C. E. Carlson, and G. A. Miller, Phys. Rev. Lett. **108**, 232301 (2012) [arXiv:1203.0254 [nucl-th]].

[477] A. Thomas, X. Wang, and R. Young, Phys. Rev. C **91**, 015209 (2015) [arXiv:1406.4579 [nucl-th]].

[478] F. Erben, P. Shanahan, A. Thomas, and R. Young, Phys. Rev. C **90**, 065205 (2014) [arXiv:1408.6628 [nucl-th]].

[479] J. Gasser, M. Hoferichter, H. Leutwyler, and A. Rusetsky, Eur. Phys. J. C **75**, 375 (2015) [arXiv:1506.06747 [hep-ph]], [Erratum: Eur. Phys. J. C **80**, 353 (2020)].

[480] J. Gasser, H. Leutwyler, and A. Rusetsky, Phys. Lett. B **814**, 136087 (2021) [arXiv:2003.13612 [hep-ph]].

[481] J. Gasser, H. Leutwyler, and A. Rusetsky, Eur. Phys. J. C **80**, 1121 (2020) [arXiv:2008.05806 [hep-ph]].

[482] W. A. Bardeen, J. Bijnens, and J. M. Gérard, Phys. Rev. Lett. **62**, 1343–1346 (1989).

[483] J. F. Donoghue and A. F. Pérez, Phys. Rev. D **55**, 7075–7092 (1997) [arXiv:hep-ph/9611331].

[484] V. Cirigliano, W. Dekens, J. de Vries, M. Hoferichter, and E. Mereghetti, Phys. Rev. Lett. **126**, 172002 (2021) [arXiv:2012.11602 [nucl-th]].

[485] V. Cirigliano, W. Dekens, J. de Vries, M. Hoferichter, and E. Mereghetti, JHEP **05**, 289 (2021) [arXiv:2102.03371 [nucl-th]].

[486] G. Colangelo, M. Hoferichter, M. Procura, and P. Stoffer, JHEP **09**, 074 (2015) [arXiv:1506.01386 [hep-ph]].

[487] K. Kampf, M. Knecht, J. Novotný, and M. Zdráhal, Phys. Rev. D **84**, 114015 (2011) [arXiv:1103.0982 [hep-ph]].

[488] G. W. Bennett *et al.* [Muon $g-2$ Collaboration], Phys. Rev. D **73**, 072003 (2006) [arXiv:hep-ex/0602035].

[489] B. Abi *et al.* [Muon $g-2$ Collaboration], Phys. Rev. Lett. **126**, 141801 (2021) [arXiv:2104.03281 [hep-ex]].

[490] T. Albahri *et al.* [Muon $g-2$ Collaboration], Phys. Rev. D **103**, 072002 (2021) [arXiv:2104.03247 [hep-ex]].

[491] T. Albahri *et al.* [Muon $g-2$ Collaboration], Phys. Rev. A **103**, 042208 (2021) [arXiv:2104.03201 [hep-ex]].

[492] T. Albahri *et al.* [Muon $g-2$ Collaboration], Phys. Rev. Accel. Beams **24**, 044002 (2021) [arXiv:2104.03240 [physics.acc-ph]].

[493] T. Aoyama, M. Hayakawa, T. Kinoshita, and M. Nio, Phys. Rev. Lett. **109**, 111808 (2012) [arXiv:1205.5370 [hep-ph]].

[494] T. Aoyama, T. Kinoshita, and M. Nio, Atoms **7**, 28 (2019).

[495] A. Czarnecki, W. J. Marciano, and A. Vainshtein, Phys. Rev. D **67**, 073006 (2003) [arXiv:hep-ph/0212229], [Erratum: Phys. Rev. D **73**, 119901 (2006)].

[496] C. Gnendiger, D. Stöckinger, and H. Stöckinger-Kim, Phys. Rev. D **88**, 053005 (2013) [arXiv:1306.5546 [hep-ph]].

[497] A. Kurz, T. Liu, P. Marquard, and M. Steinhauser, Phys. Lett. B **734**, 144–147 (2014) [arXiv:1403.6400 [hep-ph]].

[498] K. Melnikov and A. Vainshtein, Phys. Rev. D **70**, 113006 (2004) [arXiv:hep-ph/0312226].

[499] G. Colangelo, M. Hoferichter, M. Procura, and P. Stoffer, JHEP **09**, 091 (2014) [arXiv:1402.7081 [hep-ph]].

[500] P. Masjuan and P. Sánchez-Puertas, Phys. Rev. D **95**, 054026 (2017) [arXiv:1701.05829 [hep-ph]].

[501] G. Colangelo, M. Hoferichter, M. Procura, and P. Stoffer, Phys. Rev. Lett. **118**, 232001 (2017) [arXiv:1701.06554 [hep-ph]].

[502] G. Colangelo, M. Hoferichter, M. Procura, and P. Stoffer, JHEP **04**, 161 (2017) [arXiv:1702.07347 [hep-ph]].

[503] A. Gérardin, H. B. Meyer, and A. Nyffeler, Phys. Rev. D **100**, 034520 (2019) [arXiv:1903.09471 [hep-lat]].

[504] J. Bijnens, N. Hermansson-Truedsson, and A. Rodríguez-Sánchez, Phys. Lett. B **798**, 134994 (2019) [arXiv:1908.03331 [hep-ph]].

[505] G. Colangelo, F. Hagelstein, M. Hoferichter, L. Laub, and P. Stoffer, Phys. Rev. D **101**, 051501 (2020) [arXiv:1910.11881 [hep-ph]].

[506] G. Colangelo, F. Hagelstein, M. Hoferichter, L. Laub, and P. Stoffer, JHEP **03**, 101 (2020) [arXiv:1910.13432 [hep-ph]].

[507] T. Blum *et al.*, Phys. Rev. Lett. **124**, 132002 (2020) [arXiv:1911.08123 [hep-lat]].

[508] G. Colangelo, M. Hoferichter, A. Nyffeler, M. Passera, and P. Stoffer, Phys. Lett. B **735**, 90–91 (2014) [arXiv:1403.7512 [hep-ph]].

[509] M. Hoferichter and T. Teubner, Phys. Rev. Lett. **128**, 112002 (2022) [arXiv:2112.06929 [hep-ph]].

[510] S. Borsanyi *et al.*, Nature **593**, 51–55 (2021) [arXiv:2002.12347 [hep-lat]].

[511] J. P. Lees *et al.* [BaBar Collaboration], Phys. Rev. D **86**, 032013 (2012) [arXiv:1205.2228 [hep-ex]].

[512] A. Anastasi *et al.* [KLOE-2 Collaboration], JHEP **03**, 173 (2018) [arXiv:1711.03085 [hep-ex]].

[513] G. Abbiendi *et al.*, (2022) [arXiv:2201.12102 [hep-ph]].

[514] A. Crivellin, M. Hoferichter, C. A. Manzari, and M. Montull, Phys. Rev. Lett. **125**, 091801 (2020) [arXiv:2003.04886 [hep-ph]].

[515] A. Keshavarzi, W. J. Marciano, M. Passera, and A. Sirlin, Phys. Rev. D **102**, 033002 (2020) [arXiv:2006.12666 [hep-ph]].

[516] B. Malaescu and M. Schott, Eur. Phys. J. C **81**, 46 (2021) [arXiv:2008.08107 [hep-ph]].

[517] G. Colangelo, M. Hoferichter, and P. Stoffer, Phys. Lett. B **814**, 136073 (2021) [arXiv:2010.07943 [hep-ph]].

[518] J. Grange *et al.* [Muon $g-2$ Collaboration], (2015) [arXiv:1501.06858 [physics.ins-det]].

[519] V. Pauk and M. Vanderhaeghen, Eur. Phys. J. C **74**, 3008 (2014) [arXiv:1401.0832 [hep-ph]].

[520] I. Danilkin and M. Vanderhaeghen, Phys. Rev. D **95**, 014019 (2017) [arXiv:1611.04646 [hep-ph]].

[521] F. Jegerlehner, *The Anomalous Magnetic Moment of the Muon*, Springer, 2017.

[522] M. Knecht, S. Narison, A. Rabemananjara, and D. Rabetiarivony, Phys. Lett. B **787**, 111–123 (2018) [arXiv:1808.03848 [hep-ph]].

[523] P. Roig and P. Sánchez-Puertas, Phys. Rev. D **101**, 074019 (2020) [arXiv:1910.02881 [hep-ph]].

[524] S. Holz *et al.*, Eur. Phys. J. C **81**, 1002 (2021) [arXiv:1509.02194 [hep-ph]].

[525] M. Hoferichter and P. Stoffer, JHEP **05**, 159 (2020) [arXiv:2004.06127 [hep-ph]].

[526] J. Lüdtke and M. Procura, Eur. Phys. J. C **80**, 1108 (2020) [arXiv:2006.00007 [hep-ph]].

[527] J. Bijnens, N. Hermansson-Truedsson, L. Laub, and A. Rodríguez-Sánchez, JHEP **10**, 203 (2020) [arXiv:2008.13487 [hep-ph]].

[528] J. Bijnens, N. Hermansson-Truedsson, L. Laub, and A. Rodríguez-Sánchez, JHEP **04**, 240 (2021) [arXiv:2101.09169 [hep-ph]].

[529] E.-H. Chao *et al.*, Eur. Phys. J. C **81**, 651 (2021) [arXiv:2104.02632 [hep-lat]].

[530] I. Danilkin, M. Hoferichter, and P. Stoffer, Phys. Lett. B **820**, 136502 (2021) [arXiv:2105.01666 [hep-ph]].

[531] G. Colangelo, F. Hagelstein, M. Hoferichter, L. Laub, and P. Stoffer, Eur. Phys. J. C **81**, 702 (2021) [arXiv:2106.13222 [hep-ph]].

[532] S. Holz, C. Hanhart, M. Hoferichter, and B. Kubis, Eur. Phys. J. C **82**, 434 (2022) [arXiv:2202.05846 [hep-ph]], [Addendum: Eur. Phys. J. C **82**, 1159 (2022)].

[533] B. Moussallam, Eur. Phys. J. C **73**, 2539 (2013) [arXiv:1305.3143 [hep-ph]].

[534] I. Danilkin and M. Vanderhaeghen, Phys. Lett. B **789**, 366–372 (2019) [arXiv:1810.03669 [hep-ph]].

[535] M. Hoferichter and P. Stoffer, JHEP **07**, 073 (2019) [arXiv:1905.13198 [hep-ph]].

[536] C. Bouchiat and L. Michel, J. Phys. Radium **22**, 121–121 (1961).

[537] S. J. Brodsky and E. de Rafael, Phys. Rev. **168**, 1620–1622 (1968).

[538] A. Keshavarzi. Private communication, 2022.

[539] S. Borsanyi *et al.* [Budapest–Marseille–Wuppertal Collaboration], Phys. Rev. Lett. **121**, 022002 (2018) [arXiv:1711.04980 [hep-lat]].

[540] D. Bernecker and H. B. Meyer, Eur. Phys. J. A **47**, 148 (2011) [arXiv:1107.4388 [hep-lat]].

[541] T. Blum *et al.* [RBC, UKQCD Collaboration], Phys. Rev. Lett. **121**, 022003 (2018) [arXiv:1801.07224 [hep-lat]].

[542] G. Colangelo *et al.*, Phys. Lett. B **833**, 137313 (2022) [arXiv:2205.12963 [hep-ph]].

[543] G. Chanturia, B. Kubis, D. Stamen *et al.* In preparation.

[544] G. Colangelo, M. Hoferichter, B. Kubis, and P. Stoffer, JHEP **10**, 032 (2022) [arXiv:2208.08993 [hep-ph]].

[545] S. Okubo, Phys. Lett. **5**, 165–168 (1963).

[546] G. Zweig. Unpublished, 1964.

[547] J. Iizuka, K. Okada, and O. Shito, Prog. Theor. Phys. **35**, 1061–1073 (1966).

[548] Y.-Q. Chen and E. Braaten, Phys. Rev. Lett. **80**, 5060–5063 (1998) [arXiv:hep-ph/9801226].

[549] X.-H. Mo, C.-Z. Yuan, and P. Wang, HEPNP **31**, 686–701 (2007) [arXiv:hep-ph/0611214].

[550] Q. Wang, G. Li, and Q. Zhao, Phys. Rev. D **85**, 074015 (2012) [arXiv:1201.1681 [hep-ph]].

[551] N. Kivel, Phys. Rev. D **107**, 094015 (2023) [arXiv:2301.03884 [hep-ph]].

[552] R. T. Deck, Phys. Rev. Lett. **13**, 169–173 (1964).

Acronyms

BW	Breit–Wigner
ChPT	chiral perturbation theory
CM	center-of-mass
CRP	constrained Regge pole
DAMA	dual amplitudes with Mandelstam analyticity
DHS	Dolen–Horn–Schmid
DS	Dyson–Schwinger
EFT	effective field theory
FESRs	finite-energy sum rules
FSR	final-state radiation
GKPY	García-Martín–Kamiński–Peláez–Ynduráin
HLbL	hadronic light-by-light
HVP	hadronic vacuum polarization
IB	isospin breaking
KL	Kullback–Leibler
KT	Khuri–Treiman
LHC	left-hand cut
pdf	probability density function
pQCD	perturbative quantum chromodynamics
PW	partial wave
QCD	quantum chromodynamics
QED	quantum electrodynamics
RHC	right-hand cut
RPP	Review of Particle Physics
RT	Regge trajectory
SM	standard model of particle physics
SPM	Schlessinger Point Method
SSB	spontaneous symmetry breaking
SVA	single-variable amplitude
VFF	vector form factor
VLS	Veneziano–Lovelace–Shapiro
VMD	vector-meson dominance
VP	vacuum polarization

Acknowledgements

As already indicated by the quote in the beginning I would have never finished this thesis alone. This chapter is dedicated to all the people that supported me on my way.

First and foremost I thank Bastian Kubis. From my first theoretical physics lecture to being the *Doktorvater* of this thesis he accompanied me for the major part of my academic career. I want to thank him for his continuous support during all the highs and lows. Moreover, I really appreciate his effort educating the next generation(s), while providing a comforting work atmosphere. It is a privilege to discuss ideas and solutions with him, since it feels like there are endless things one can learn from him. In addition, I am grateful for the opportunities to attend various workshops and conferences. I thank Christoph Hanhart for being the second referee of this thesis and for teaching me valuable concepts during (the early times of) my academic career. Additionally, I want to thank my collaborators on the numerous projects, who helped me with all the challenging aspects. Furthermore, I thank Bernhard Ketzer and Barbara Niethammer for agreeing to be the third and fourth member of my doctoral committee, respectively.

I thank Tobias Isken, Bastian Kubis, Simon Stamen, and Marvin Zanke for proofreading parts of this thesis.

I sincerely appreciate every college from the HISKP who made time in the office very worthwhile. My time in office 2.018 with Hakan Akdag, Yannis Korte, Simon Mutke, and Marvin Zanke will be a great memory together with the many discussions about work and other aspects of life. Additionally, I thank the research group "AG Kubis" for the occasional lunch break and interesting group seminars. During my time from starting a Bachelor's thesis to finishing this PhD thesis I encountered many interesting characters. For help with organizaitional topics I thank Heike Frömbgen-Penkert, Barbara Kraus, and Lara Lagemann.

A main contributor for my mental balance were the weekly board game nights with Frederik Brüning, David Heidler von Heilborn, Jan Heinrichs, Tobias Isken, Malwin Niehus, and Stefan Ropertz. I am very glad I found so many friends with whom I can share this great hobby. Further, the somewhat rarer board game nights and activities with the "Chaos Club", particularly the "Seniors" including Julia Breuer, Svenja Plinius, and Jana Schmitz, were equally much fun. Additionally, it provided me with much joy to rekindle my love for Badminton, especially due to the fun spirit of Team 10 from 1. BC Beuel. Furthermore, I want to thank Nassim Ainouz, Jan Heinrichs, Roman Küsters, and Patrick Schwäbig for the fun time spend away from university life and Len Brandes, Jan Heinrichs, and Maximilian Raaff for the yearly holiday trip.

Most importantly, I thank my parents Regina and Martin and my brother Simon. You are the reliable foundation of my life that allows me to thrive. I cannot put into words how grateful I am for all the things you have done for me. Without you, I would not be the person I am today, and for that I am forever thankful.

Financial support by the DFG through the funds provided to the Sino–German Collaborative Research Center TRR110 "Symmetries and the Emergence of Structure in QCD" (DFG Project-ID 196253076 – TRR 110) and by the MKW NRW under the funding code NW21-024-A is gratefully acknowledged.